

# Laminar Mixing: A Dynamical Systems Approach

EDIT S. SZALAI, MARIO M. ALVAREZ, and FERNANDO J. MUZZIO

*Rutgers University*

## 3-1 INTRODUCTION

Laminar mixing has been subject to formal study only recently, and it is safe to say that it is currently an “art” rather than a fully developed scientific discipline. The fundamentals evolved mainly from empiricism to a semiquantitative level, and a unifying framework that describes the dynamics of laminar mixing processes has only begun to emerge in the past decade. Our limited understanding of mixing fundamentals is a chief limiting factor in effective design of mixing equipment. Mixing, as an individual subject, is absent from most existing chemical engineering curricula. From a fundamental viewpoint, one of the main motivations to study of laminar mixing is that the underlying physics is amenable to direct analysis in a rigorous framework to develop meaningful theory. Additionally, mixing problems in laminar environments tend to be very difficult. In the context of pharmaceutical, food, polymer, and biotechnological processes, liquid mixing applications are frequently carried out at low speeds or involve high viscosity substances, such as detergents, ointments, creams, suspensions, antibiotic fermentations, and food emulsions. During the past few years there has been growing awareness of problems related to incomplete or inefficient mixing at various stages of these manufacturing processes. Some examples include dispersing particles or releasing bubbles from viscous liquids, oxygen or substrate limitation in high viscosity fermentation broths, preparation of sugar solutions for tablet or candy coatings, and difficulties controlling pH in batches of detergent (Muhr, 1995; Amanullah, 1998).

A full set of color figures for this chapter is provided on the Visual Mixing CD affixed to the back cover of the book.

---

*Handbook of Industrial Mixing: Science and Practice*, Edited by Edward L. Paul, Victor A. Atiemo-Obeng, and Suzanne M. Kresta  
ISBN 0-471-26919-0 Copyright © 2004 John Wiley & Sons, Inc.

In other instances, the concern for mechanical damage constrains mixing operations to the low-speed regime. Biological processes using shear-sensitive cell cultures (mammalian cells, plant cells, or mycelium) are prime examples where adequate mixing must be accomplished at low speeds to avoid compromising the metabolic and physical integrity of shear-sensitive cells and molecules. Increases in batch viscosity are also a common characteristic of these applications (e.g., production of antibiotics using mycelial fungus). As the biomass concentration increases at continued shearing, the fluid properties often become highly complex and strongly non-Newtonian, imposing new challenges on effective mixing.

## 3-2 BACKGROUND

### 3-2.1 Simple Mixing Mechanism: Flow Reorientation

Turbulent flows are intrinsically time-dependent. The velocity field is nonsteady, which implies a continuous reorientation of fluid particles along Lagrangian trajectories. However, steady laminar flows are often encountered when dealing with low fluid velocities or high viscosity materials. These types of processes can be poor mixing environments, because fluid motion is dominated by linear, viscous forces instead of nonlinear inertial forces. If the forcing is time-independent, fluid particles can follow concentric, closed streamlines. From a mixing standpoint, the lack of local time dependence often has a cost: poor performance.

Consider flow in a section of straight pipe, a typical example of steady, nonchaotic flows (often referred to as a regular flow). This problem is two dimensional, since the geometry possesses complete angular symmetry. It is well established that laminar flow of a Newtonian fluid produces a steady parabolic velocity profile within the pipe. To describe mixing in this flow, dye is injected at the inlet at different radial locations, as shown in Figure 3-1*a*. Consider how the dye streams behave as they are convected by the flow, if the flow regime is indeed steady. In the absence of diffusion, the material remains confined within streamlines that are forever parallel. Different streams do not mix with each other, and the surface separating representative streams (also known as the intermaterial contact area between two fluids) grows at most linearly in time. The pipe flow stretches the separating distance between neighboring particles at a constant rate, without any reorientation to the direction. The action of diffusion in viscous materials is minimal, because diffusivity is usually very low and the mixing time to achieve homogeneity via diffusion in most applications is prohibitively long. Should we conclude, then, that it is impossible to mix efficiently in laminar flows?

Quite the opposite is true, as mixing equipment such as stirred tanks (certainly the most widely used apparatus), static mixers, roller bottles, extruders, and so on, are employed commonly in laminar mixing applications with varying degrees of success. Such equipment, with the right choice of operational parameters and design, can disrupt continuous particle trajectories and create chaos (see Figure 3-1*b*). How are these systems different from our previous example, the straight pipe?

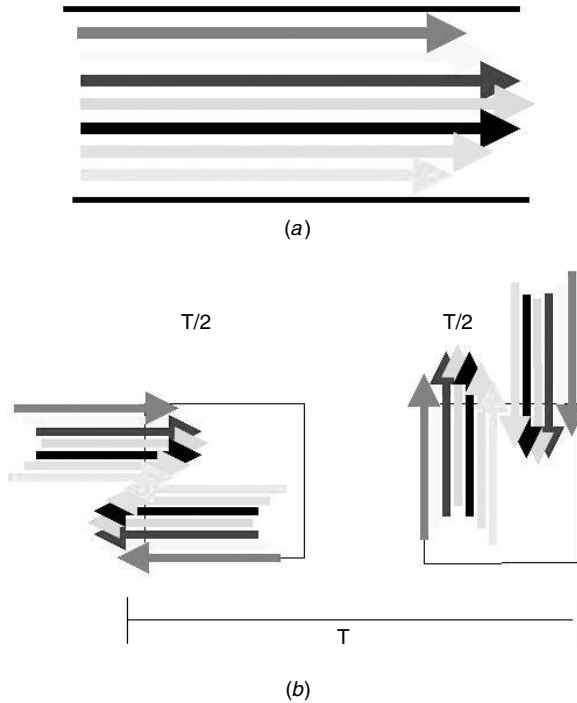


**Figure 3-1** Steady flows mix poorly. In a simple 2D flow, such as flow in a pipe (a), the intermaterial area between the colored streams does not grow in time. However, if two steady velocity fields are applied periodically in alternating directions to a stream of fluid (b), the interfaces between the dye streams grow exponentially in time.

These laminar mixing systems are effective because they make the mixing process time-dependent in a Lagrangian sense. The mechanism in all the equipment mentioned above is quite similar: a “periodic” forcing of the fluid. In the case of a stirred tank operated at a constant speed, each passage of the impeller blades disturbs the fluid periodically. In the case of a Kenics static mixer (Middlemann, 1977; Pahl and Muschelknautz, 1982; Ling and Zhang, 1995; Hobbs et al., 1997; Jaffer and Wood, 1998), the geometry of the system imposes spatial periodicity: Each element is a repetition of the preceding one twisting in the opposite direction, with a  $90^\circ$  rotation in between, forcing fluid elements to reorient in these transitional regions. Chaotic motion generated by periodic flows represents an important class of chaotic flows in general. Chaotic mixing is characterized by an exponential rate of stretching (as opposed to linear stretching in a nonchaotic flow) of fluid elements. As a fluid element travels through a chaotic flow, it is not only stretched, but also reoriented due to the repeated change in the direction of the flow field that acts on it. Reorientation leads to folding of material lines. The repetition of stretching and folding cycles increases the intermaterial area exponentially and reduces correspondingly the scale of segregation of the

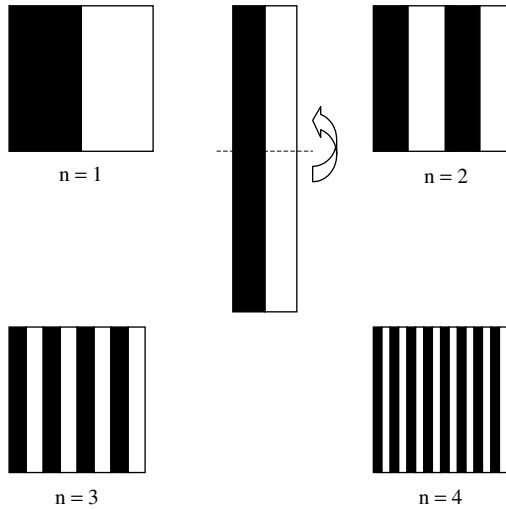


**Figure 3-2** Two components of chaotic mixing, stretching and folding, illustrated by a simple model. Baker's map defines a mixing protocol that stretches fluid elements to double length and folds them in each unit time  $n$ . The amount of intermaterial contact area (the interface between the light and the dark regions) grows at an exponential rate as the recipe is applied repeatedly.

system, also at an exponential rate (see Figure 3-2), following a general iterative "horseshoe" mechanism.

### 3-2.2 Distinctive Properties of Chaotic Systems

Although we have suggested a connection between chaos and laminar mixing, we have not established it formally. Two important properties of chaotic systems make them excellent candidates to mix in laminar conditions:

**3-2.2.1 Exponential Divergence of Nearby Particle Trajectories.** In a chaotic system, the distance separating two fluid particles initially located very close to one another will diverge exponentially in time. Considering that the objective of any mixing operation is to disperse clusters of material, exponential divergence of clusters of material that are initially close to each other is extremely desirable for mixing applications. Figure 3-3 illustrates some features of complex chaotic flows. Let us represent the initial distance between two particles as an infinitesimal vector of length  $l_0$ . Gradients in the velocity field continuously reorient and elongate the small material filament as it visits different regions in the flow. Its length at a later time  $t_n$  is denoted by  $l_n$ . In a chaotic flow, the ratio  $l_n/l_0$  (formally known as the *stretching* of a fluid element, denoted by  $\lambda$ ) grows as

$$\lambda = \frac{l_n}{l_0} = e^{\Lambda t} \quad (3-1)$$

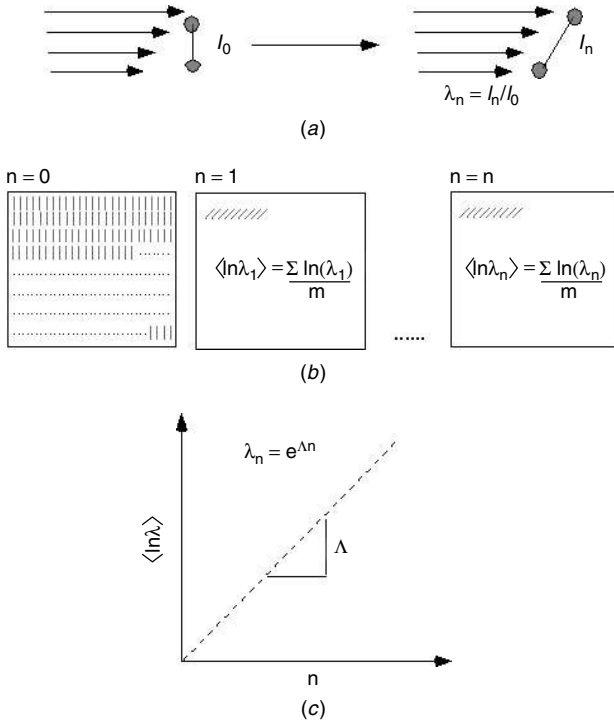


**Figure 3-3** Calculating the stretching field and the Lyapunov exponent. In (a) a small material filament, represented by a vector  $l_0$ , is convected by a flow. As a consequence, its length increases from the initial  $l_0$  to  $l_n$ . The stretching ( $\lambda$ ) experienced by the material line after each period  $n$  is the ratio  $l_0/l_n$ . In (b) an array of small vectors is placed in the flow, and the stretching of each is measured and an average  $\lambda$  can be calculated. In (c) a chaotic flow,  $\lambda$  grows exponentially, and the exponent characterizing the growth rate ( $\Lambda$ , the Lyapunov exponent) can be calculated from the slope of the curve  $\langle \ln \lambda \rangle$  versus  $n$ .

where  $l_n$  is the separation distance between the two particles at time  $t_n$ . The stretching  $\lambda$  represents the intensity of the mixing process experienced by the material element. The spectrum of mixing intensities in the flow can be measured using a large number of vectors to represent a collection of tiny material filaments populating the entire flow domain. The exponential rate of average growth of vector length is usually represented by the constant  $\Lambda$ , called the *Lyapunov exponent* of the flow (Oseledek, 1968), which is a volume-averaged measure of the average rate of stretching at a given flow period. Strictly speaking, the Lyapunov exponent is the asymptotic limit on stretching as time approaches infinity and  $l_0$  goes to zero. Chaotic flows are recognized by having positive Lyapunov exponents.

**3-2.2.2 Frequency Distribution of Stretching.** A single particle traveling along a chaotic trajectory can explore an entire chaotic region densely and

completely uniformly as time approaches infinity (i.e., in the asymptotic time limit). In a mixing context, this property of chaotic flows assures that every particle will eventually visit all areas in the chaotic region. The short-time frequency with which particles visit a particular region of the flow depends on their initial spatial position. The spatial position determines the amount of stretching and reorientation that a small fluid element experiences at that location. Eventually, the continuous stretching and reorientation process leads to the distribution of materials throughout the chaotic region.

The area visited by particles in a chaotic flow can be illustrated by the use of plots known as *Poincaré sections* or *maps*, a very common tool in dynamical systems theory. These plots show the long-time behavior of a mixing system by revealing whether the entire flow is chaotic or contains slow-mixing, segregated regions (*islands*). When preparing a Poincaré plot of a three dimensional dynamical system, such as a stirred tank or a static mixer, a two dimensional plane perpendicular to the main flow direction is typically chosen. This plane is intersected periodically by tracer particles following the flow. Some fluid tracer particles are marked in the flow and particle positions are recorded every time they cross the 2D plane. All these positions are superimposed on a single plot after many time periods.

An analogous definition of Poincaré sections can be applied to 2D time-dependent periodic systems. After some particles are marked in the flow, instantaneous snapshots of the system are taken at periodic intervals of time and overlapped on a single plot (Aref, 1984; Franjione and Ottino, 1987; Leong and Ottino, 1989; Muzzio and Swanson, 1991; Kusch and Ottino, 1992; Alvarez et al., 1997). The time period is usually chosen to be the period of the driving force that creates motion in the system. Poincaré plots simplify the analysis of a dynamical system, because the original system dimension is lowered by one, yet the characteristic dynamics are retained. In a Poincaré section, regions of chaotic motion appear as a cloud of points that will eventually fill the entire chaotic domain. Regions of regular motion (also known as islands or isolated regions) appear either as empty regions (if no particles were originally placed within) or as sets of closed curve (see Figure 3-4 for an example). The boundaries between the regular and chaotic regions are known as *KAM surfaces* [after Kolmogorov, Arnold, and Moser (Kolmogorov, 1954; Moser, 1962; Arnold, 1963)] and appear as closed curves in Poincaré sections. These surfaces pose a significant barrier to transport, because material exchange can occur across these boundaries only by diffusive mechanisms.

### 3-2.3 Chaos and Mixing: Some Key Contributions

The notion of complex, chaotic motion linked to simple dynamical systems is certainly not new. Aref introduced a set of ideas that led to major research efforts now spanning almost two decades (Aref, 1984). His main contribution was to incorporate concepts of dynamical systems theory to fluid mechanics, specifically in the context of laminar mixing. He was able to demonstrate that

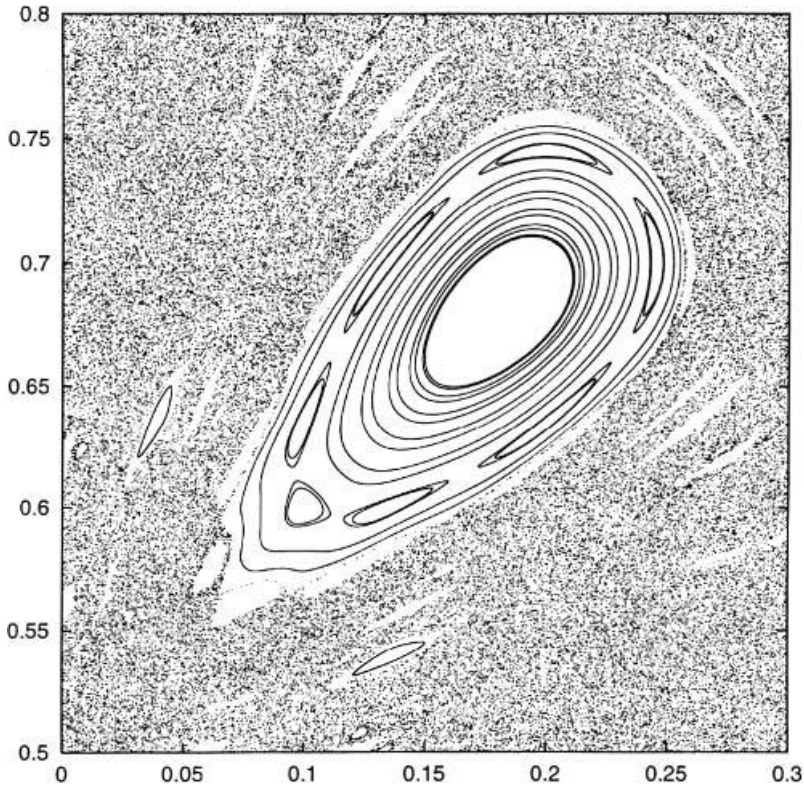


**Figure 3-4** Poincaré section of a model flow (the sine flow). Areas of chaotic motion appear as a random cloud of points, whereas segregated regions (i.e., islands) appear as empty regions, if no particles were originally placed inside. Tracers particles that are placed inside islands appear as sets of closed curves or KAM surfaces in quasi-periodic systems, and as points in a periodic system.

even very simple systems can exhibit chaos when operated in a time-periodic fashion. Working with a model 2D map, Aref's computations demonstrated that some time-periodic recipes could lead to chaotic motion almost everywhere in a flow domain.

The first experimental evidence of chaos in a 2D time-periodic flow was provided by Chien et al. (1986). The experimental system was a chamber filled with fluid, where two opposing surfaces could be moved independently. The shearing motion in the cavity causes flow and mixing in the system, otherwise referred to as *cavity flow*. If the direction and duration of motion for each surface is chosen carefully, the system can be fully chaotic or contain areas of regular flow (i.e., islands). Chaiken et al. (1986) provided strong evidence of chaotic motion in the journal bearing flow, a time-periodic flow between two eccentric cylinders. These three 2D systems—Aref's blinking vortex, Chien's cavity flow, and Chaiken's journal bearing—have since been investigated by many other

authors (Muzzio and Ottino, 1988; Leong and Ottino, 1989; Swanson and Ottino, 1990; Metcalfe and Ottino, 1994; Souvaliotis et al., 1995). As a result, a solid theoretical framework for chaotic mixing processes has been established for 2D systems, where the dynamics governing fluid and particle motion are simpler than in realistic 3D flows.

The idea that chaotic motion can exist in three dimensional (3D) systems was known among dynamical systems theorists when Aref began his studies on 2D maps. Poincaré was perhaps the first investigator to formally observe that deterministic systems can exhibit “erratic” trajectories, later called *chaotic trajectories*. Kusch presented the first formal experimental study of chaotic mixing in laminar regime in 3D systems (Kusch and Ottino, 1992). Using two different geometries, the eccentric helical annular mixer and the partitioned pipe mixer, he demonstrated the existence of isolated regions coexisting with chaotic regions in 3D physically realizable systems (although these systems are not used in industrial applications). It is now well established that chaotic motion is the cause of effective laminar mixing in industrially relevant 3D systems such as stirred tanks and static mixers (Dong et al., 1994; Lamberto et al., 1996; Hobbs et al., 1997; Hobbs and Muzzio, 1998). Due to chaotic fluid motion in these mixing devices, fluid elements elongate exponentially fast while the diffusive length scale reduces at the same rate.

### 3-3 HOW TO EVALUATE MIXING PERFORMANCE

#### 3-3.1 Traditional Approach and Its Problems

A long-standing issue in mixing theory (not only in the context of laminar mixing) has been how to characterize the state of a mixture. A largely debated issue is exactly what to measure and how to measure it. Resolving this problem is not a trivial task.

In Section 3-2 we described a common tool, Poincaré sections, which greatly simplify analysis of mixing in complex periodic systems since they reduce the dimensionality of the flow by one. Visualization of three dimensional mixing patterns becomes easier in two dimensional cross-sections, and some asymptotic characteristics such as permanently segregated areas in the flow can easily be revealed. However, important dynamics are lost when the evolution of mixing patterns is not considered on a shorter time scale. An inherent weakness of Poincaré sections is the loss of structure within the chaotic region of a flow. The fast, exponential separation between neighboring fluid particles severely limits the use of discrete points for representing continuous lamellar structures. Even if new points are added as mixing patterns develop, the complex spatial structure created by the flow is not retained with point tracers, because continuous material lines soon become a featureless, random cloud of points. See Figure 3-4, where large areas of the chaotic flow domain do not seem to possess any structure.

Some shortcomings of Poincaré sections are overcome when another measure, stretching, is used to analyze chaotic systems and exploit flow topology. However, this tool has not been the preferred approach among practitioners, probably



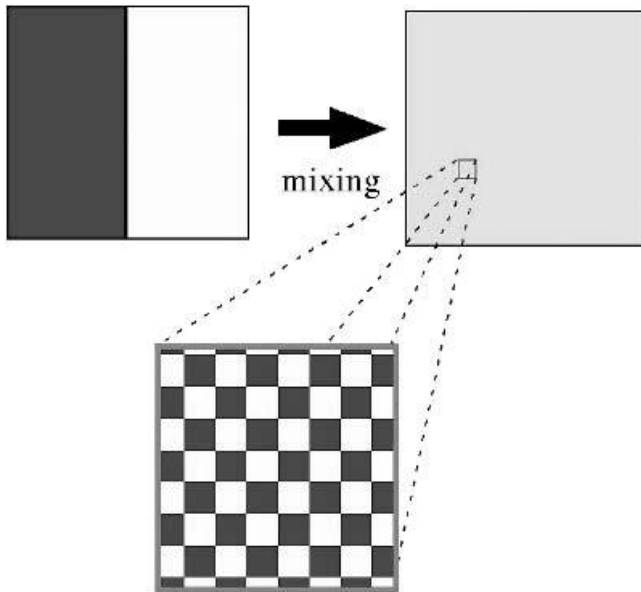
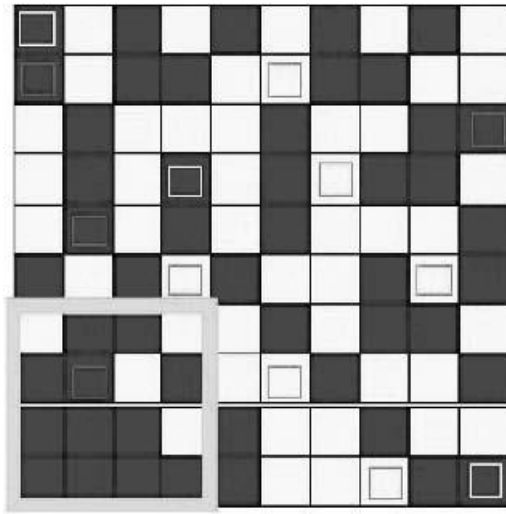


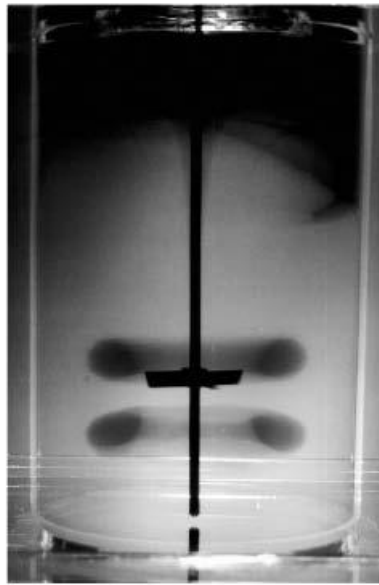
**Figure 3-5** Mixing is a process that increases the homogeneity of a system.

because it is not the most intuitive. When a mixing operation is performed, the ultimate objective is to achieve a target level of homogeneity within the mixture, and to do it in the fastest, cheapest, and if possible, the most elegant way. A simple mixing process is depicted in Figure 3-5, where the entire process volume is represented with a square domain. Starting from a highly segregated condition, dark fluid in one side of the square domain and light in the other, the mixing process generates a state at which the two colors are indistinguishable on the length scale of the system.

If the mixture is sampled in smaller quantities and examined on a smaller scale, there is always a level at which inhomogeneities can be detected. A first and obvious proposal to assess the state of a mixture would be to measure a property of interest throughout the system (e.g., concentration of a key component) and to determine the magnitude of deviations in the sample values from the target value desired for the entire mixture. On one hand, this is probably the most common approach to characterize mixtures both conceptually and in practice. On the other hand, this technique can lead to inconsistencies when trying to use it as an effective mixing measure. The definition of the size and location of samples and the total number taken are essential to establish the validity of any mixing measure. Thus, the placement and size of sampling probes must be matched if different experiments are to be compared. Consider sampling the mixture as depicted in Figure 3-6a. If different combinations of samples are analyzed from the same mixture the concentration estimation can deviate significantly from the “true” value of 0.5.



(a)



(b)

**Figure 3-6** Problems associated with some statistical methods of mixture characterization. If a different set of samples is selected from (a) than the one enclosed in the highlighted box, a different overall concentration is calculated each time. Real mixing systems, such as stirred tanks with laminar flow (b), exhibit such heterogeneity. If measured by a set of electrodes, the concentration of  $H^+$  depends strongly on the placement of the electrodes in the tank.

Clearly, a measure that is so dependent on the scale and mechanism of application is not sufficiently robust. An even more significant aspect of this approach is not its reliability or its reproducibility<sup>1</sup> but its physical significance. Laminar mixing processes can show systematic effects, such as the presence of islands that can bring into question the practice of repeatedly sampling at discrete locations. Consider measuring the mixing time in a stirred tank using a neutralization reaction when operated in the laminar regime. In principle, if a set of pH electrodes is inserted at different positions in the tank, pH measurements can be taken as the mixing process evolves to indicate the state of the reaction. At the starting condition, all electrodes will read the same value within an experimental uncertainty of about 1%. It is expected that the global variance will decrease to a near-zero value, and at that point, the mixing time can be established. In reality, the measurement does not give such a clear indicative answer (see Figure 3-6*b*). Some electrode readings approach the target value much faster than others: as soon as 20 min for some probes, or only after several hours for others.

A simple mixing visualization technique can tell us why. If we perform the same neutralization in a transparent vessel, pH indicator can be added to the viscous media to indicate the local H<sup>+</sup> concentration. In acid environments, the liquid turns yellow, whereas in basic environments it is blue. A picture of an initially basic system taken after mixing for 10 min is presented in Figure 3-6*b*. A laboratory scale mixing vessel, equipped with three standard Rushton impellers, was initially filled with viscous fluid containing NaOH base and pH indicator. The entire tank appeared initially blue due to the amount of base premixed with the process fluid. The impellers were then set in motion at a constant speed, and acidic solution was injected into the tank near the blades shortly afterward. As the concentrated acidic injection spreads through the vessel, the instantaneous neutralization reaction between the acid and base marks areas of contact between the two components. The change in pH causes a color change in well-mixed areas. The picture after 10 min shows two distinct colors, indicating well-mixed and poorly mixed areas in the tank. The islands, or segregated regions, remain blue, while all regions where the neutralization reaction goes to completion become yellow. The existence of large, blue doughnut-shaped toroidal regions below and above each impeller in the vessel is obvious even to the naked eye. These structures remain in the flow for extended periods of time and are destroyed only by slow diffusion after hours of processing. Obviously, any “average” mixing time calculated based on a few randomly placed, dispersed electrode readings would be meaningless for this system, because it misses such important behavior.

### 3-3.2 Measuring Microstructural Properties of a Mixture

Even more serious inconsistencies can occur when mixture quality is assessed exclusively based on concentration measurements. It is possible that the estimated concentration distribution may be the same for two mixtures that are very different

<sup>1</sup> For example, we can improve the statistical significance of the measured concentration estimate by increasing the number of samples.

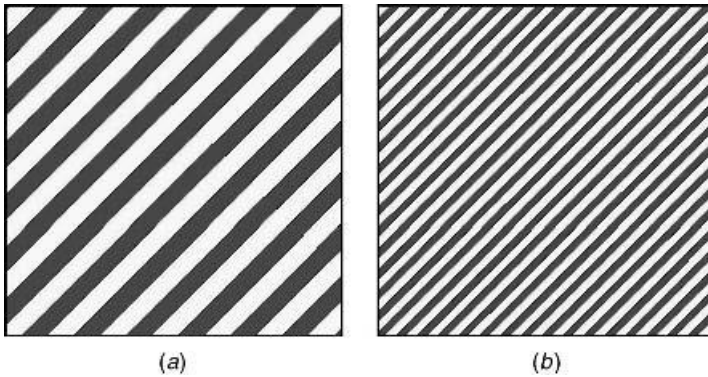
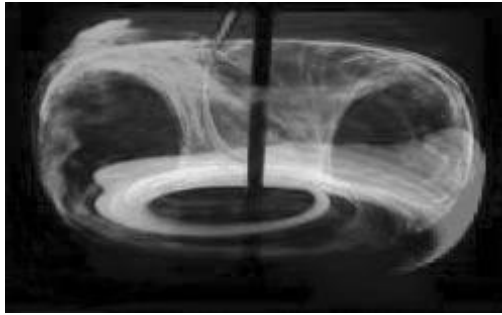


**Figure 3-7** Two mixtures with the same concentration (50% light and 50% dark component), but in (b) the intimacy of contact between the two materials is greater and the diffusional length scale is shorter. More surface area is available for transport in (b) than in (a). If a chemical reaction occurs in each of these systems, the observed reaction rates would be very different.

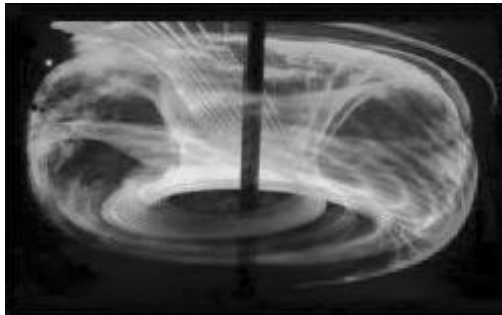
in nature. The two regions in Figure 3-7a and b have equal amounts of yellow material, 50%. However, the intermaterial contact area between the yellow and the blue constituents is higher in case (b). The parameters affecting mass transfer, the area available for transport and the diffusional distance, are both affected by the topology of the mixture. The area available for transport is greater and the diffusional distance is shorter in case (b). If this were a reactive mixture, these differences would result in a faster overall reaction rate in case (b). Similar situations occur in industrial mixtures (e.g., a polymerization reaction), which exhibit micromixing behavior that is strongly position-dependent.

Mixing processes involving miscible liquids (laminar and turbulent) generate complex striation patterns that are highly heterogeneous where mixing is much more intimate in some regions than in others. This topology is crucial to predicting the outcome of mass transfer and reactions. As an example of the complexity of lamellar structures generated by chaotic flows, refer to Figure 3-8. These photographs were taken at two different instances in time as two fluorescent dye streams are blended with a viscous liquid in a stirred tank. The shaft holding the impeller is visible at the center as a black line. The tank was equipped with a standard Rushton turbine, and green dye was injected above the impeller blades at the start of the experiment. Some time later, the red stream was added to follow the time evolution of the mixing structure in the tank. Within a small area, wide and thin striations coexist. Additionally, the intermaterial area density varies substantially between different regions of the system. This implies that the mixing quality—by any meaningful definition—is substantially different in different regions of the system.

Techniques for characterizing the evolving structural features in a mixing system need to be nonintrusive and robust. Some methods normally used (e.g.,



(a)



(b)

**Figure 3-8** The complex mixing patterns formed by chaotic flows are highly heterogeneous, and understanding the emerging structure is crucial to predicting heat and mass transfer in these systems. Here, some experimental pictures are shown of the mixing pattern formed by colored fluorescent dye in a stirred tank. The time evolution of the emerging structure can be monitored if a series of snapshots are taken in time, as in (a) and (b). See insert for a color representation of this figure.

probes) alter the structure that they intend to characterize. Optical methods are usually nonintrusive, but most of the mixing devices widely used in industry are opaque, which limits the applicability of these methods. Even if an optical method can be used, resolution of the most sophisticated optical equipment available today is not enough to resolve fine structural details.<sup>2</sup> As an alternative, recently developed numerical techniques can give insight to the statistics of flow and mixing in physical or model mixing systems. Simple 2D models are a valuable tool to represent and understand the behavior of industrially relevant 3D mixing systems. The analysis can be greatly simplified yet provide significant insight into the physics of realistic flows. It is well known that some characteristic features of real 3D chaotic systems are closely captured, at least qualitatively, by 2D time-periodic chaotic model flows. Namely, the coexistence of regular and chaotic

<sup>2</sup> As we will show in a later section, the distribution of length scales characteristic of chaotic flows spans more than four orders of magnitude.

regions, the shape of stretching distributions, and the scaling properties of those distributions are indicative of the similarity between 2D models and 3D flows.

Some methodologies of dynamical systems theory developed from model flows that can be extended to real 3D flows are introduced next. These new tools—stretching calculations, striation thickness distributions, and so on—are essential if one is to obtain detailed statistical information regarding the microstructure emerging in a mixing process and the dynamics of a mixing operation.

### 3-3.3 Study of Microstructure: A Brief Review

As many examples in the literature illustrate, the properties of the structure generated by chaotic flows have been studied by numerous methods in a list of different scientific disciplines. Mandelbrot introduced the concept of fractals, and with it, the notion of universality in the structure generated by chaotic systems (Mandelbrot, 1982). The structure generated by chaotic maps has been the subject of extensive analysis in mixing since dynamical system techniques have been applied to study the topology of mixing structures created by time-periodic stirring protocols (Aref, 1984). Many studies illustrating the complexity of these structures followed. Some numerical studies considering mixing structures in periodic flows include agglomeration in the blinking vortex flow (Muzzio and Ottino, 1988), or the evolution of mixing structure in time-periodic cavity flows (Leong and Ottino, 1989). Dye dispersion in the journal bearing flow was studied both computationally and experimentally (Swanson and Ottino, 1990). These studies recognized the creation of microstructure as an intrinsic characteristic of chaotic flows; nevertheless, the descriptions were primarily qualitative. Stretching and folding (Figure 3-2) were identified as the basic mechanisms that generate the complex structures observed in mixing experiments and simulations.

Since the flow topology governs local phenomena such as mass transfer and chemical reactions, its detailed characterization is the obvious next step. It is necessary to determine the distribution of length scales (or striation thicknesses) created during the stretching and folding process in a flow. Although the conceptual methods were already clear 10 years ago (Muzzio and Swanson, 1991), the limited resolution of image analysis techniques and the erosive effect of diffusion make experimental measurements of striation thickness distributions (STDs) nearly impossible. Currently, quantitative STDs cannot be resolved accurately using photographic techniques.

Until recently, numerical tools and resources were also underdeveloped relative to the magnitude of the striation measurement problem; Poincaré sections and tracer dispersion simulations were the primary techniques used to characterize mixing. To reconstruct striation patterns successfully by computational methods, it is necessary to track continuous material lines (i.e., dye blobs) injected in chaotic flows. The difficulty of such a numerical experiment is hidden in one word of the previous sentence: continuous. The feasibility of tracking material lines or surfaces numerically was explored by Franjione and Ottino, (Franjione and Ottino, 1987). These authors' estimations of time and disk space demands

showed that with the computational resources existing at that time, accurate simulation of this type was impossible even in the simplest chaotic flows. As a result, following the evolution of mixing patterns by means of direct tracking of interfaces was abandoned for an entire decade. Several papers examined the evolution of an assumed lamellar microstructure under the effects of diffusion and fast chemical reactions using simplified models of flow topology (Muzzio and Ottino, 1989, 1990; Sokolov and Blumen, 1991).

In parallel, the strong experimental evidence of self-similar geometric properties of mixing structures began to be explored using a statistical approach. The repetitive nature of time- or space-periodic flows was suspected to generate structures endowed with statistical self-similarity. Evidence of the validity of this hypothesis was provided by Muzzio et al. for the drop size distribution produced by breakup in chaotic flows (Muzzio et al., 1991). Since neither experimental nor direct numerical characterization of the striation thickness distribution could be achieved, the computation of stretching, which is related to the increase in interfacial area available for mass and energy transport (feasible for even 3D flows), was suggested as an alternative route to characterize microstructure (Muzzio and Swanson, 1991).

In the remaining sections of this chapter we discuss the characterization of mixing and the implementation of these statistical and computational techniques using a simple time-periodic flow as an example. Since the implementation of the algorithms used here is mostly sequential, it is natural to describe them in the order they are applied.

### 3-4 PHYSICS OF CHAOTIC FLOWS APPLIED TO LAMINAR MIXING

The physics of laminar mixing may be interpreted from several perspectives, each of which is discussed in this section. The key results are summarized in Table 3-1.

#### 3-4.1 Simple Model Chaotic System: The Sine Flow

The *sine flow*, a two dimensional model of a chaotic flow field, consists of two sinusoidal velocity fields which alternate for half a period ( $T/2$ ) carrying fluid in the X and Y directions sequentially:

$$\underline{v} = (V_x, V_y) = \begin{cases} (\sin 2\pi y, 0); & \text{for } nT < t \leq (n + 1/2)T \\ (0, \sin 2\pi x); & \text{for } (n + 1/2)T < t \leq (n + 1)T \end{cases} \quad (3-2)$$

$$(3-3)$$

A sketch of the velocity field is shown in Figure 3-9. This cycle can be repeated many times, where  $n$  denotes the number of periods. For most of the examples presented here, the sine flow is applied on a 2D domain. Periodic boundary conditions complete the definition of the system. Tracer particles that leave the domain through one side reenter the domain at the opposite side.

**Table 3-1** Measures of Mixing

Method of Analysis	Type	Brief Description	Advantages/Limitations	Section
Mixing patterns by particle tracking (Poincaré sections)	Experimental/computational	Colored fluid tracer particles are injected in a flow and their location is tracked during the mixing process by computational or experimental visualization methods. The efficiency of the mixing process is described by how fast and evenly the particles become dispersed	Segregated and slow-mixing regions can easily be identified. / Mixing patterns become indistinguishable as particles disperse in the flow.	3-4.1 eq. (3-4)
Stretching field ( $\lambda$ )	Computational	The elongation of fluid filaments in each region of a flow is measured by the stretching of small vectors, which are attached to fluid tracer particles.	Effective injection locations and fast-mixing areas can easily be identified. / The effect of diffusion is not measured by the stretching field.	3-4.2 eq. (3-1), eq. (3-7)
Lyapunov exponent ( $\Lambda$ )	Computational	This measure is the average stretching of fluid filaments after an infinite amount of time. The larger the Lyapunov exponent, the more efficient a mixing process is.	This measure can be used as a single number to compare the long-time efficiency of mixing processes. / $\Lambda$ does not give any indications about mixing patterns and dead zones in the flow.	3-4.6 eq. (3-11)



Topological entropy ( $\Theta$ )	Computational	This measure is the average stretching of fluid filaments in a finite amount of time. The larger the topological entropy, the more efficient a mixing process is.	This measure is appropriate to compare average mixing rates for shorter times. / $\Theta$ does not give any indications about mixing patterns and dead zones in the flow.	3-4.6 eq. (3-12)
Intermaterial area density ( $\rho$ )	Computational	This measure is the amount of contact area between mixture components in each region of a flow. Even and dense distribution of intermaterial area is desired for an efficient mixing process.	This measure can be used to characterize micromixing efficiency at all spatial locations. / $\rho$ cannot be obtained directly in complex flows, but it is predictable from the stretching field.	3-4.7 eq. (3-13), eq. (3-15)
Striation thickness distribution (STD)	Computational	The thickness of fluid filaments (i.e., striations) measures the diffusive length scale. The effectiveness of a mixing process is determined by how fast the striation thickness is reduced in each region of a flow. Uniform distribution of striations is desired everywhere for most effective mixing.	This measure can be used to characterize the diffusional length scale at all spatial locations. / STD cannot be obtained directly in complex flows, but it is predictable from the stretching field.	3-4.9 eq. (3-15), eq. (3-16)

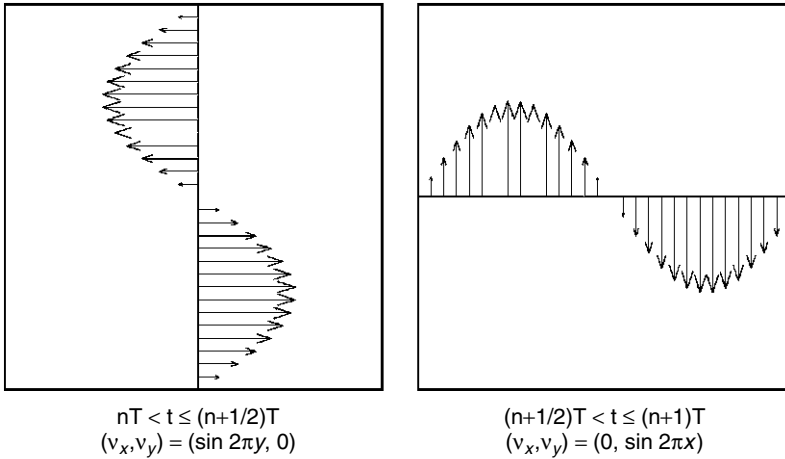


**Figure 3-9** The sine flow is a 2D model flow that shows many characteristics of physically realizable 3D chaotic flows. The flow is defined by sequentially applying two steady sinusoidal velocity fields to the unit square flow domain. The duration of time that each velocity field is applied is known as the flow period,  $T$ . It is the only parameter that controls the types of mixing behavior that can be observed in this system.

Even though the sine flow is not physically realizable, it is a suitable model to study chaotic flows, for several reasons. First, tracking tracer particles in time (to follow their position,  $\underline{X} = (x, y)$ , as a function of time) becomes very easy computationally. This is done by integrating the differential equation

$$\frac{d\underline{X}}{dt} = \underline{v} \quad (3-4)$$

With the analytical expression for the velocity field  $\underline{v}$  [eqs. (3-2) and (3-3)], there are no errors due to numerical approximations, and a closed-form solution for particle motion is attainable:

$$x_{n+1} = x_n + \frac{T}{2} [\sin(2\pi y_n)] \quad (3-5)$$

$$y_{n+1} = y_n + \frac{T}{2} [\sin(2\pi x_{n+1})] \quad (3-6)$$

The sinusoidal velocity profile and the periodic boundary conditions assure  $n$ th-order continuity, such that a particle leaving on one side of the system reenters on the opposite side with the same velocity. Using these expressions, the position of any tracer particle within the system can be calculated forward (or backward) for any time simply by knowing its initial (or final) position. Particle trajectories are a function of a single parameter ( $T$ ), the period of the flow. The simplicity of the solution [eqs. (3-5) and (3-6)] embodies the beautiful paradox of chaotic flows.

Although the application of these equations for one flow period is a very simple exercise, it cannot be used to obtain an explicit prediction of particle positions over many periods in a deterministic manner. The algebraic complexity grows exponentially with the number of flow periods as the current particle locations are taken into account.

The sine flow reveals different spatial distributions of chaotic and nonchaotic regions for different values of the parameter  $T$ , similar to real mixing flows. Figure 3-10 shows Poincaré sections for three parameter values:  $T = 0.8$ ,  $T = 1.2$ , and  $T = 1.6$ . Each section is computed by plotting the position of a single particle initially placed at  $(0.5, 0.5)$  after 10 000 iterations of the flow. The segregated regions initially contain no particles, so they appear as empty islands in the flow. At  $T = 0.8$ , four such large regions and many smaller ones are

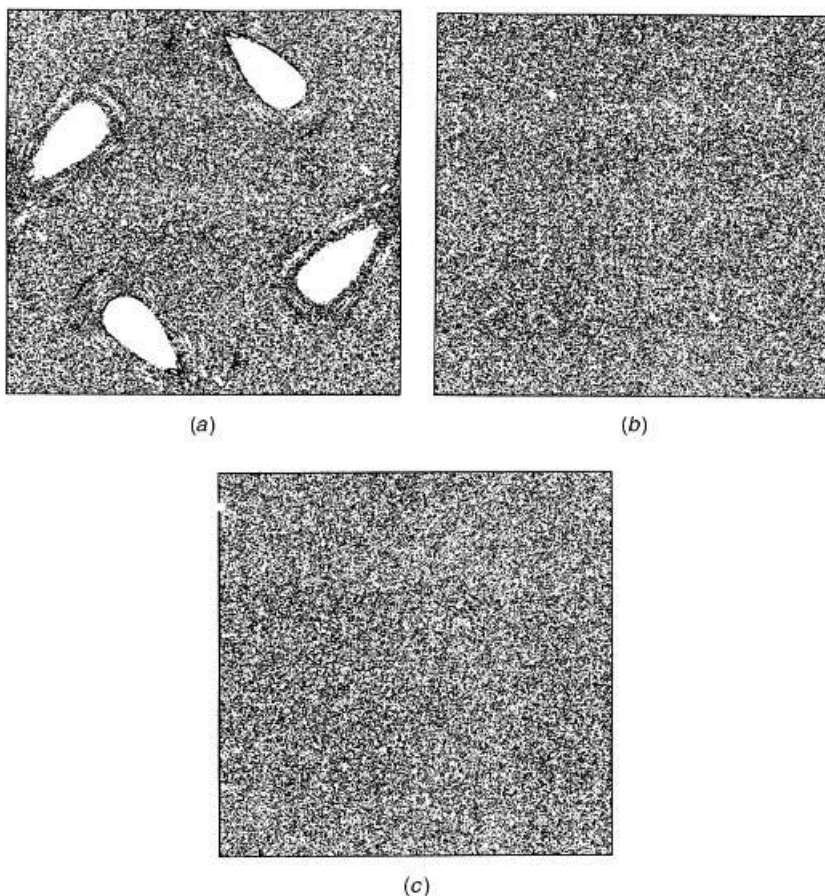


**Figure 3-10** Poincaré sections for three conditions in the sine flow: (a)  $T = 0.8$ , where large islands are visible; (b)  $T = 1.2$ , where only small islands are present; (c)  $T = 1.6$ , where particle motion is chaotic almost everywhere.

noticeable within the chaotic subdomain. (For a close-up, see Figure 3-4.) Islands significantly decrease in size for  $T = 1.2$ , and they nearly disappear at  $T = 1.6$ , thanks to the fact that this system is chaotic almost everywhere. These figures emphasize that the Poincaré analysis is valuable as an asymptotic diagnostic tool but not as a dynamical one. That is, the section shows the size and shape of the segregated regions in the flow, but it does not show the evolution to that asymptotic state, since the dynamic component (time dependence) is lost. Moreover, it creates an impression of “random, featureless mixing” that is entirely misleading and for many years deflected attention from an essential issue: the strong nonuniformity of mixing intimacy that is a prevailing feature of chaotic flows.

### 3-4.2 Evolution of Material Lines: The Stretching Field

More detailed information obtained by tracking the evolution of an arbitrary material line in a flow can be described by the stretching of a small vector attached to any particle in the flow:

$$\frac{dl}{dt} = (\nabla \underline{v})^T \cdot l \quad l_{t=0} = l_0 \quad (3-7)$$

where  $l_{t=0}$  is the initial stretching vector with a magnitude of 1 and random orientation in the flow field. Since filaments deform under the influence of the velocity gradient,  $\nabla \underline{v}$ , this equation is coupled with eq. (3-4) and must be integrated simultaneously.

Since the sine flow is continuous everywhere, it is differentiable within the entire flow domain. This property leads to a piecewise analytical expression for the stretching field in the flow domain:

$$l_{x,n+1} = l_{x,n} + 2\pi T[\cos(2\pi y_n)]l_{y,n} \quad (3-8)$$

$$l_{y,n+1} = l_{y,n} + 2\pi T[\cos(2\pi x_{n+1})]l_{x,n+1} \quad (3-9)$$

Here  $l_x$  and  $l_y$  are the two components of the small stretching vector  $l_{n+1}$ . Assuming that  $|l_0| = 1$ , the magnitude of the length stretch is given by

$$l_{n+1} = (l_{x,n+1}^2 + l_{y,n+1}^2)^{1/2} \quad (3-10)$$

The fact that the tracking of fluid particles and the calculation of stretching of material lines can be performed in closed form means that accurate calculations for the mixing microstructure are feasible.

### 3-4.3 Short-Term Mixing Structures

In practical applications we are often interested in the early stages of a mixing process, before the process becomes controlled by diffusion (i.e., when striations reach the length scale of diffusion). Short-term mixing dynamics have been extensively studied in the past by tracer dispersion simulations. Consider the sine flow

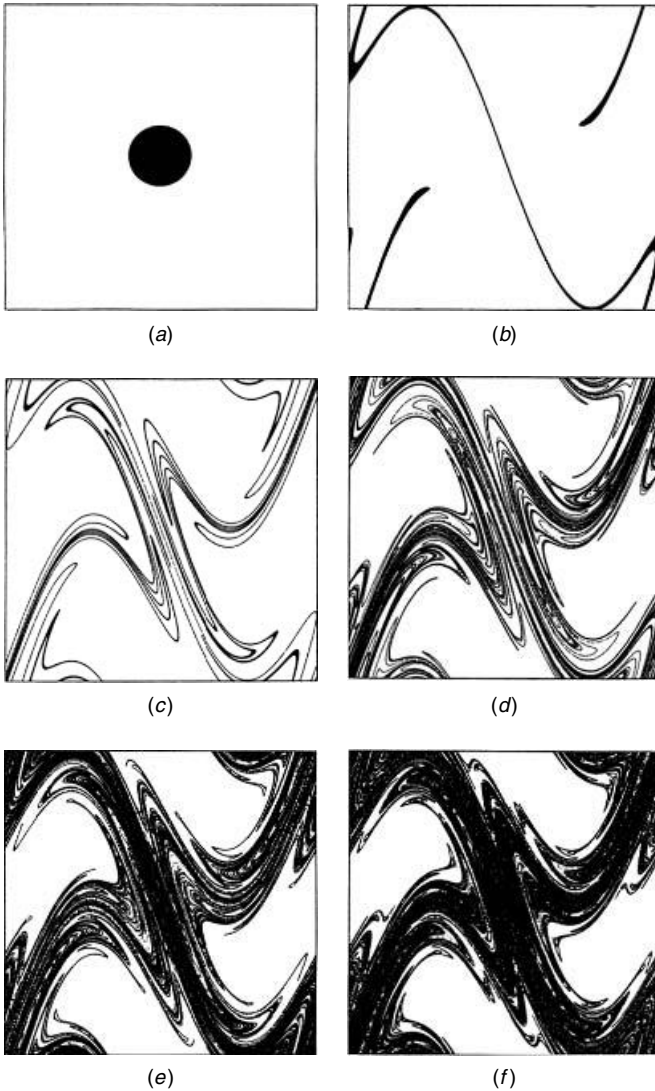


**Figure 3-11** Dispersion of a dye blob in the sine flow with  $T = 0.8$ : (a) Initially, the dye is at the center of the square flow domain and is spread throughout the chaotic region at times (b)  $n = 2$ ; (c)  $n = 4$ ; (d)  $n = 6$ ; (e)  $n = 8$ ; (f)  $n = 10$ .

with  $T = 0.8$ , where a circular blob of dye is placed at the center of the domain in Figure 3-11. The dye is represented as a collection of 100 000 massless tracer particles, and the position of each particle is plotted for  $n = 2, 4, 6, 8$ , and 10 flow periods. As the blob stretches and folds, it invades the flow domain at different rates in different areas, resulting in a highly nonuniform lamellar structure. However, an ability to resolve this structure is lost after a few iterations; as time

advances, the points that compose the blob are dispersed and the fine detail of the partially mixed structure fades. After just 10 flow iterations, it is no longer possible to distinguish striations in the center of the domain (see Figure 3-11*f*). As the material is dispersed throughout the entire domain in time, it becomes equivalent to a Poincarè structure. A specialized algorithm is needed to preserve continuity along the material interface by introducing new tracers whenever the distance between adjacent tracers exceeds a predefined limit.

#### 3-4.4 Direct Simulation of Material Interfaces

Material filaments are stretched and folded in a chaotic flow, but due to the Hamiltonian nature of incompressible flows (Aref, 1984), they never intersect. Thus, a dye blob can be represented by its surface in 3D or its perimeter in 2D to capture its structure and as a result, the computational effort to simulate the evolution of interfaces can be reduced significantly. The position and stretching of each point along the perimeter of the dye blob was calculated via eqs. (3-4) and (3-7), and the structure can be reconstructed after multiple iterations of the flow. The magnitude of the stretching experienced by the fluid along the original spatial distribution of points revealed continuous partially mixed structures such as the one presented in Figure 3-12. The dye blob was represented only by points tracing its perimeter initially, as in Figure 3-12*a*. This type of analysis reveals details that are “invisible” through conventional analysis of tracking point tracers. Compare the mixing structure that was computed via direct filament tracking (in Figure 3-12*b-d*) to the corresponding tracer spreading simulations in Figure 3-11*b-d*). The structure of the filament looks smooth and well dispersed in the particle tracking simulations, but it appears as a complex and nonuniform collection of material lines when the dynamics of the continuous filament is considered. The chaotic region at the center of the unit domain, packed very densely with material striations, attains a local orientation for all filaments.

Due to the nature of stretching in chaotic flows, an exponentially growing number of points is needed to sustain the continuity of material lines during the simulations, which makes these calculations extremely resource consuming. For example, for the case  $T = 1.2$ , after 10 iterations,  $10^8$  points are needed to properly reconstruct the filament. Performing such calculations for real 3D mixing systems is considerably beyond the realm of today’s computational power. A much more feasible alternative is to correlate measures of mixing intimacy, such as striation thickness distributions and intermaterial area density, to the stretching field. This correlation provides the necessary link to extend analysis to complex systems.

#### 3-4.5 Asymptotic Directionality in Chaotic Flows

After only a few flow periods in a chaotic flow, a remarkably symmetric and intricate lamellar structure composed of thousands of striations emerges. This structure is self-similar in time when recorded at a fixed frequency (conveniently

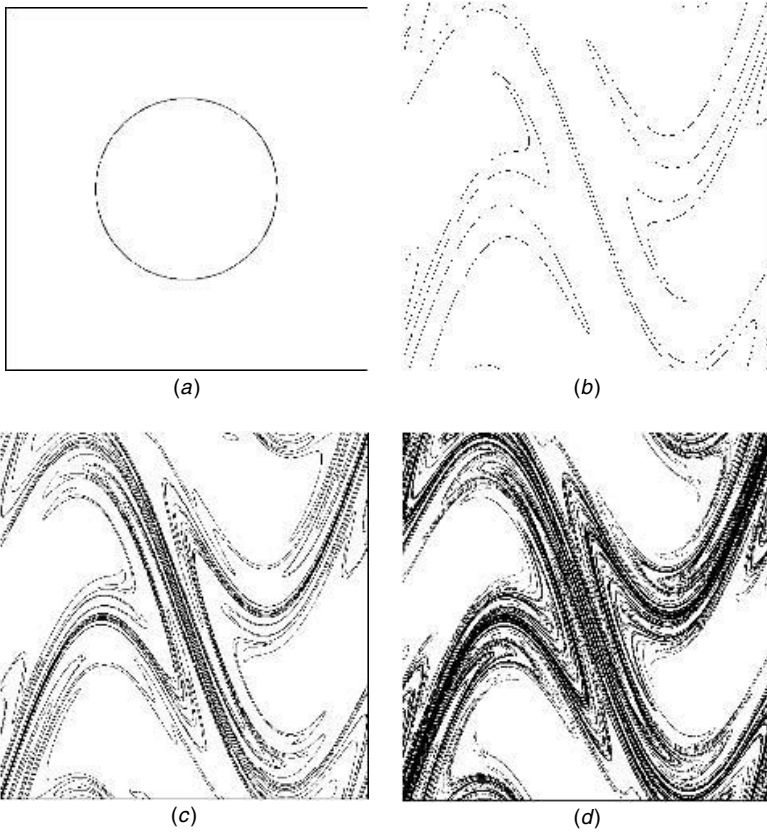


**Figure 3-12** Evolution of a continuous material filament in the sine flow for  $T = 0.8$ . The filament was initially placed at the center, and it is stretched throughout the chaotic region at times (a) initial filament; (b)  $n = 2$ ; (c)  $n = 4$ ; (d)  $n = 6$ . Dynamics of continuous material lines reveal details about the structure of the evolving mixing patterns that are “invisible” to the conventional analysis of tracking discrete points. Compare Figure 12b–d with Figure 11b–d.

after each flow period). As time evolves, the interface aligns to a template dictated by the flow, and more detail is added to the existing folds after each flow period. However, even though new striations appear at an exponential rate, the overall appearance of the structure remains the same. Asymptotically, as the material filament adapts to an invariant field of orientations in the flow, its structure becomes time-invariant (Muzzio et al., 2000).

The orientation process is very fast; the dependence on initial injection location is lost exponentially fast. After tracer fluid is injected at a specific location, the dye blob is stretched throughout the chaotic region of the flow; and dye filaments form an intricate and unique mixing pattern. This pattern is unique to the flow and becomes independent of the injection location after a short initial period.

Comparing the orientation of material lines that appear at the same location at different times in the flow field demonstrates that once a material line reaches a particular location of the flow, it adopts a characteristic local direction associated with that position in the flow. In other words, the orientation of a material filament in a periodic chaotic flow is determined by its instantaneous position, not by time.

The existence of an invariant field of orientations has important implications for the evolution of mixing patterns in chaotic flows. At each point in the chaotic domain there is a well-defined local orientation that is adopted by all material filaments in that region. The presence of an invariant field of orientations is referred to as asymptotic directionality in chaotic flows (Muzzio et al., 2000). In simple terms, when any portion of interface is in a particular region of the flow, it aligns to an orientation characteristic of that instantaneous spatial position. Thus, the evolution of mixing structures in chaotic flows is not a function of time but a function of instantaneous location. Asymptotic directionality (AD) explains the creation of self-similar mixing patterns in chaotic flows and provides a link to other properties of periodic chaotic flows in a general sense. For more details on AD property, see Giona et al. (1998, 1999), and Cerbelli (2000).

### 3-4.6 Rates of Interface Growth

Being able to measure or predict the rate of growth of interface and its area coverage is an important step toward understanding reactive processes. Intimate contact between mixture components is necessary to allow a chemical reaction to proceed. Although the spatial distribution of intermaterial area is unique in every chaotic flow, for all cases the interface grows exponentially fast in time and the rate of growth is known explicitly. In Figure 3-13 the natural logarithm of the total length of the interface is plotted versus number of iterations. One would expect that the rate of filament growth to be dictated by the Lyapunov exponent of the flow.

The Lyapunov exponent is the geometric average of the local stretching rates, which assigns equal weight to all local stretching values in the domain:

$$\Lambda \sim \lim_{n \rightarrow \infty} \left( \frac{1}{n} \langle \ln \lambda_i^n \rangle \right) = \frac{1}{nN_p} \sum_{i=1}^{N_p} \ln(\lambda_i^n) \quad (3-11)$$

However, if we examine the three cases of sine flow shown in Figure 3-13, it is evident that the length of the interface is consistently underpredicted by the Lyapunov exponent. Because the filament does not sample the low and high stretching regions with equal probability, high stretching regions contribute more to the integral sum of the geometric average. Recall that the sine flow with  $T = 1.6$  is a globally chaotic flow, whereas  $T = 0.8$  and  $T = 1.2$  are cases with mixed regimes containing both chaotic and regular flow regions. The deviation between the actual rate of elongation (along the filament) and the growth rate of the Lyapunov exponent is largest for  $T = 0.8$ . For this value of the period, the flow domain has large isolated regions of regular flow, which are not invaded by the stretching filament for long times.



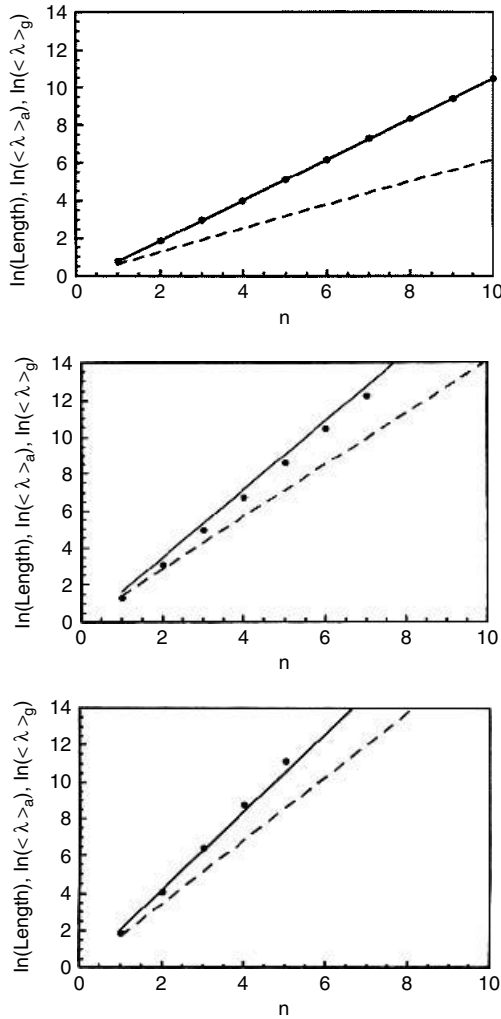


**Figure 3-13** Growth rate of material lines as measured by the Lyapunov exponent ( $\Lambda$ ) (dashed lines) and topological entropy ( $\Theta$ ) (solid lines). The three pictures represent three different flow conditions in the sine flow: (a)  $T = 0.8$ ; (b)  $T = 1.2$ ; (c)  $T = 1.6$ . In each case, the topological entropy closely predicts the length increase of the interface between mixture components (dots). The Lyapunov exponent underpredicts the mixing rate before the asymptotic time limit is reached.

The topological entropy,  $\Theta$ , is calculated from the logarithm of the arithmetic average of stretching:

$$\Theta \sim \lim_{n \rightarrow \infty} \left( \frac{1}{n} \ln \langle \lambda_i^n \rangle \right) = \frac{1}{nN_p} \ln \sum_{i=1}^{N_p} \lambda_i^n \tag{3-12}$$

This measure is a better predictor of the rate of elongation of interfaces because it incorporates the finding that high stretching regions are populated more densely; and it can capture the biased dynamics of the stretching process. The topological entropy,  $\Theta$ , provides a basis for comparison of different mixing protocols using a single parameter, but still overlooks an important aspect of mixing processes. Spatial distribution of the interface in a chaotic flow (whether it is globally chaotic or not) is highly nonuniform, and this inhomogeneity is a permanent feature of the flow. Next, we incorporate the topology of the flow into the global analysis of mixing.

### 3-4.7 Intermaterial Area Density Calculation

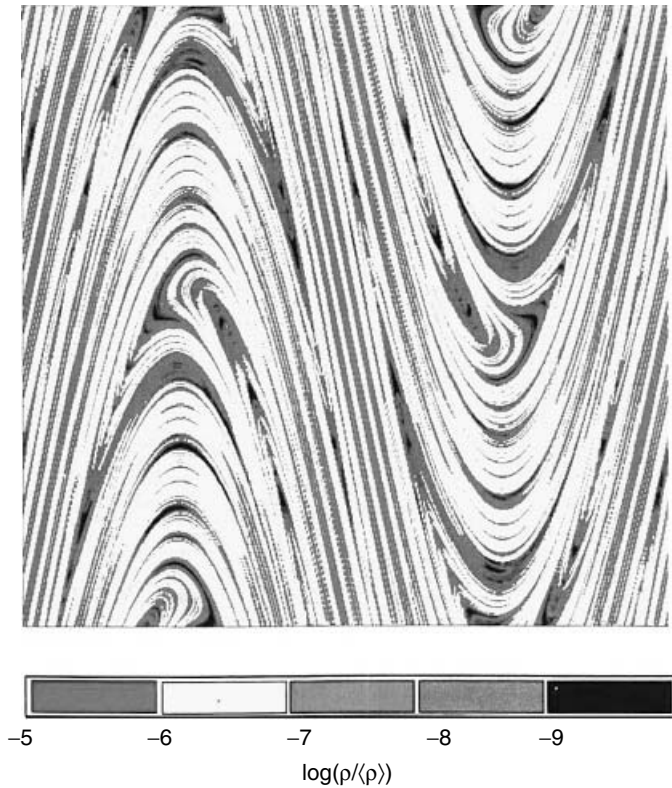
Consider quantifying the amount of interface covering different areas of the chaotic domain by a simple box-counting technique. To do this, we subdivide the entire domain into identical-sized boxes and measure the amount of material filament that falls in each box. Ergodicity assures that the same amount of material will eventually fill every box, but the time to approach such macroscopic homogeneity is dependent on the box size. The larger the box, the shorter the time needed to form a seemingly uniform mixture. The intermaterial area density ( $\rho$ ) is the length of filament in each cell ( $L_i$ ) divided by the area of the cell ( $\text{area}_i$ ). The average density in all boxes ( $\langle \rho \rangle$ ) is used to normalize each value to get a fraction of the total interface in each box. The spatial distribution of  $\rho/\langle \rho \rangle$  is displayed in Figure 3-14 for  $T = 1.6$ , after seven periods of the sine flow. Since the spectrum of intermaterial area densities spans more than five orders of magnitude, results are described on the logarithmic scale,  $\log(\rho/\langle \rho \rangle)$ . It is evident that while the system is homogeneous from a macroscopic standpoint (i.e., nearly the same amount of tracer is present in each box), micromixing is much more intense in some regions of the flow than in others. Furthermore, regions of high intermaterial area density correspond closely to high stretching regions in the flow. This is a key link to measuring striation thickness distributions in physically realizable flows.

In the statistical domain, the probability density function of  $\rho$  (PDF) is the quantitative characterization of this phenomenon. The frequency of  $\log \rho$  for different flow periods is

$$H(\log \rho) = \frac{1}{N_\rho} \frac{dN(\log \rho)}{d\rho} \quad (3-13)$$

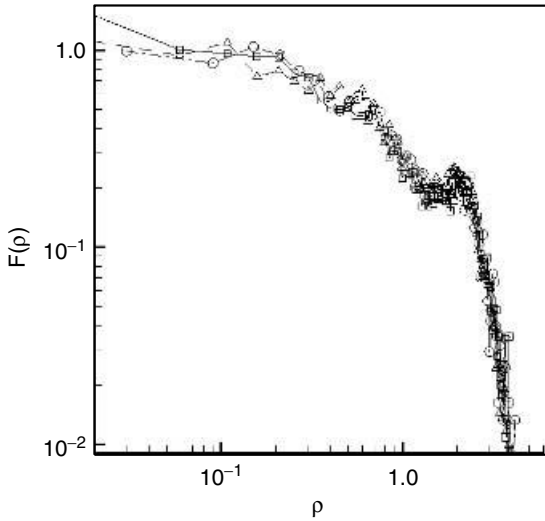
where  $N_\rho$  is the total number of boxes ( $512 \times 512$  grid) the flow region is divided into, and  $dN(\log \rho)$  is the number of boxes with densities between  $\rho$  and  $\rho + d\rho$ . Another manifestation of self-similarity of mixing structures generated by chaotic flows is that the normalized distributions of  $\log \rho$  can be collapsed onto a self-similar set of curves.

Figure 3-15 shows the time evolution of the intermaterial area density field, revealing that the nonuniform distribution of contact area is a permanent property of chaotic flows. Once the filament has sampled the flow domain for a few



**Figure 3-14** Spatial distribution of intermaterial area density ( $\rho$ ) in the sine flow without visible islands ( $T = 1.6$ ). The shades of gray represent values on the logarithmic scale, so in the black regions the material interface is four orders of magnitude denser than in the white regions. See a color version of the figure on the Visual Mixing CD.

periods, it sufficiently approaches the characteristic invariant spatial distribution and then evolves everywhere at the same rate. The overall length of the interface  $\langle \rho \rangle$  increases by several orders of magnitude, but its spatial distribution is preserved. Thus, the time evolution of micromixing intensity is expressed by a single value  $\langle \rho \rangle \approx e^{n\Theta}$ . It is important to realize that the scale  $e^{n\Theta}$  is not valid for arbitrarily long times. Small striations are erased by diffusion as they are reduced to the molecular scale. At this state, the model based on  $e^{n\Theta}$  both overpredicts the intensity of segregation and underpredicts the scale of segregation. Much of the interesting phenomena in practical laminar mixing applications occurs for much shorter times, before diffusion can have a significant influence on the overall rate of intermaterial area generation. Measuring intermaterial area density brings us closer to assessment of the rate of mass transfer and chemical reactions in laminar flows, since these processes occur through an interface. Still,  $\rho$  is a coarse-grained average quantity, not truly a local one.



**Figure 3-15** Intermaterial area density distribution for two cases of the sine flow at  $T = 1.6$  (almost globally chaotic). The figure compares the distribution computed from the coarse-grained stretching field to the distribution computed from direct tracking of a continuous material filament. Although the latter method cannot be applied to most chaotic flows, the first case is a fairly straightforward computation in both model and real chaotic flows. The distributions of  $\rho$  are shown as a function of initial position (square), as a function of final position (circles), and as computed from direct filament tracking (triangles). All three curves collapse onto a single distribution.

### 3-4.8 Calculation of Striation Thickness Distributions

The local micromixing intensity in chaotic flows is usually characterized by the distribution of striation thicknesses. This scale measures the thickness of material striations in the lamellar structure generated by chaotic flows along an arbitrary reference line. Practical implementation of this idea is not trivial, because chaotic flows generate a wide spectrum of length scales (striation thickness values). Consider that after only a few iterations of the sine flow map, values as low as  $10^{-12}$  are observed. In a physical context, if the length of the unit domain were 1 m, the striations are reaching molecular dimensions. Under such conditions, extreme care is necessary to prevent numerical errors from distorting the results; models need to be further developed to consider diffusion.

The striation thickness ( $s$ ) at a given flow period is based on taking a cross-sectional cut along a straight line in the flow domain and computing the intersections of the material filament with that reference line. The frequency distribution of  $\log s$  is defined as

$$H(\log s) = \frac{1}{N_s} \frac{dN_s(\log s)}{d(\log s)} \quad (3-14)$$

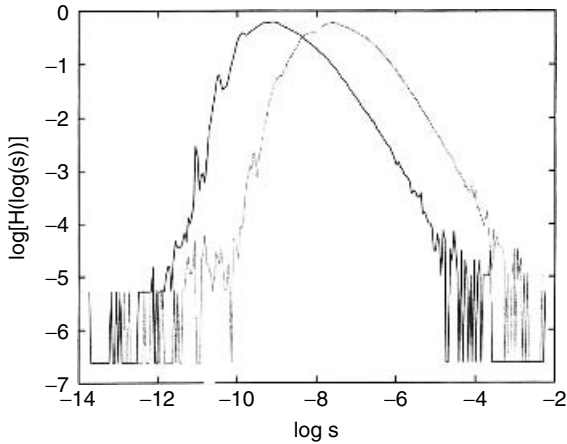


**Figure 3-16** Striation thickness distributions after nine time units in the sine flow,  $T = 1.2$ . The light- and dark-color curve is the distribution formed by the light and the dark mixture component. The horizontal shift in the mean is due to different amounts of light and dark material present in the mixture.

where  $N_s$  is the total number of intersections and  $dN_s(\log s)$  is the number of values of striation thickness between  $\log s$  and  $(\log s + d \log s)$ . Figure 3-16 shows the striation thickness distribution (STD) generated by the sine flow for  $T = 1.2$  after nine periods. The initial condition was similar to the one shown in Figure 3-11a. The distribution of the light-colored component in the binary mixture is the lighter curve; the distribution of the dark-colored component is the darker, continuous curve. The two are practically identical in shape. There is a difference in the mean of the two distributions (a horizontal shift along the axis), which is due to starting the mixing process with an excess amount of light-colored fluid. It is irrelevant where the reference line is placed in the chaotic flow domain, because after only a few periods the STDs along different reference lines are identical (Alvarez et al., 1997).

### 3-4.9 Prediction of Striation Thickness Distributions

In the preceding two sections, it was shown how to measure local micromixing intensity using intermaterial area distribution  $[H(\log \rho)]$  and length scale distributions  $[H(\log s)]$ . These tools are not directly applicable to 3D flows, because the resolution of the smallest length scales in 3D mixture structures is, to date, computationally prohibitive. In this section we present a predictive method for striation thickness distributions applicable to either 2D or 3D chaotic flows.

For incompressible 2D chaotic flows, the distribution of striation thicknesses was computed from the stretching distribution (Muzzio et al., 2000) using the idea that material filaments are stretched in one direction and simultaneously

compressed in another direction at the same rate. Formally stated,

$$s \sim \frac{1}{\rho} \sim \frac{1}{\lambda} \quad (3-15)$$

The time evolution, shape, and scaling of stretching distributions in globally chaotic flows is almost one-to-one with the same properties of striation thickness distributions. The proportionality is the intermaterial area density ( $\rho$ ) that links the stretching field with the number of striations influenced by each value of  $\lambda$ . If we consider that the *number* of stretching values is constant at each flow period, while the number of striations increases (i.e.,  $N_s \sim \langle \rho \rangle \sim \langle \lambda \rangle$ ), the striation thickness distribution as predicted from the stretching field is

$$H(\log s) = \frac{\lambda}{\langle \lambda \rangle} H(\log \lambda) \quad (3-16)$$

The real power of this relationship is that while the distribution on the left is unattainable directly in most flows, the second is obtainable from a fairly straightforward computation. Figure 3-17 provides evidence that  $\rho \sim \lambda$ , where the calculated and predicted intermaterial area density distributions are shown for the sine flow ( $T = 1.2$ ). With the use of eq. (3-16), an extremely accurate prediction of STD is obtained based on computing the stretching field alone. It is important to note here that this method applies to flows devoid of large segregated regions, which does not limit its applicability for a practical application, since mixtures with macroscopic segregations are almost always undesired.

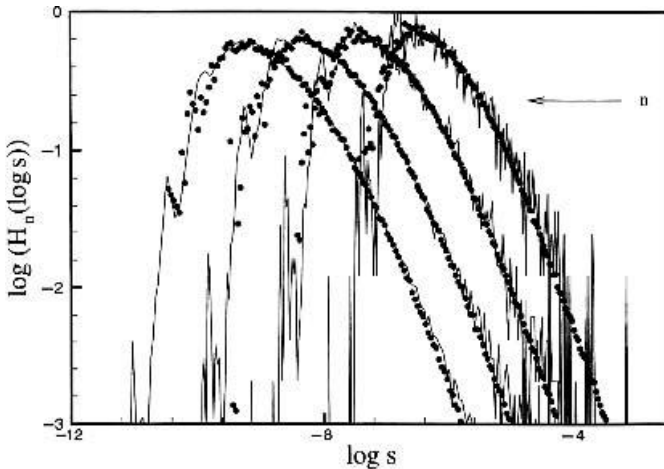


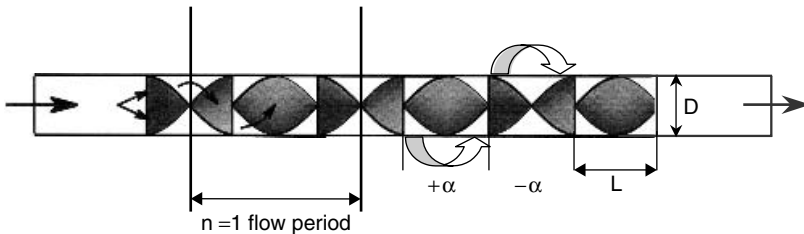
**Figure 3-17** Comparison of the striation thickness distribution calculated directly from simulating the evolution of material interfaces (as in Figure 3-12) and as predicted from the stretching field.

### 3-5 APPLICATIONS TO PHYSICALLY REALIZABLE CHAOTIC FLOWS

#### 3-5.1 Common 3D Chaotic System: The Kenics Static Mixer

In the preceding sections we summarized and described some common tools to characterize mixing in complex flows using a 2D model system. However, these tools are universal and are applicable to industrially relevant 3D chaotic mixing systems as well. Chaotic flows have been shown to exist in stirred tanks operated in the laminar regime, static mixers, or extruders (Kim and Kwon, 1996; Lamberto et al., 1996; Hobbs et al., 1997). The use and design of static mixers is reviewed in detail in Chapter 7. Only a brief description of the important characteristics of these continuous flow devices is given here, to illustrate the application of concepts from dynamical systems theory to physically realizable flows using the Kenics static mixer as an example.

Static mixers are often employed in industry for viscous mixing applications, as heat and mass transfer promoters, or even as chemical reactors in a variety of applications. The designs commonly consist of an empty tube with mixer elements inserted to perturb the flow and mix streams of material. Since they contain no moving parts, the energy for flow is derived from the pressure drop across the mixer. As an example of a 3D chaotic flow, we focus on flow in the Kenics static mixer. A schematic drawing of a six-element mixer in Figure 3-18 illustrates the geometry and important parameters in the Kenics. Different flow regimes are usually distinguished on the basis of the open-tube Reynolds number:



#### **Important Features:**

1. Spatial periodicity:  
2 Kenics elements = 1 flow period
2. Plane of symmetry: at center of each element
3. Parameters:  
Element length to diameter ratio =  $L/D$   
Twist angle per element =  $\alpha$   
Pitch per element = twist per unit length

**Figure 3-18** Geometry of a six-element Kenics static mixer. The element length-to-diameter ratio ( $L/D$ ) is 1.5 and the twist angle is  $180^\circ$  in the standard design.

$Re = (\rho_f \langle \underline{v} \rangle D) / \mu_f$ , where  $\langle \underline{v} \rangle$  is the average axial velocity,  $\rho_{\text{fluid}}$  and  $\mu_{\text{fluid}}$  are the fluid density and viscosity, and  $D$  is the diameter of the mixer housing.

### 3-5.2 Short-Term Mixing Structures

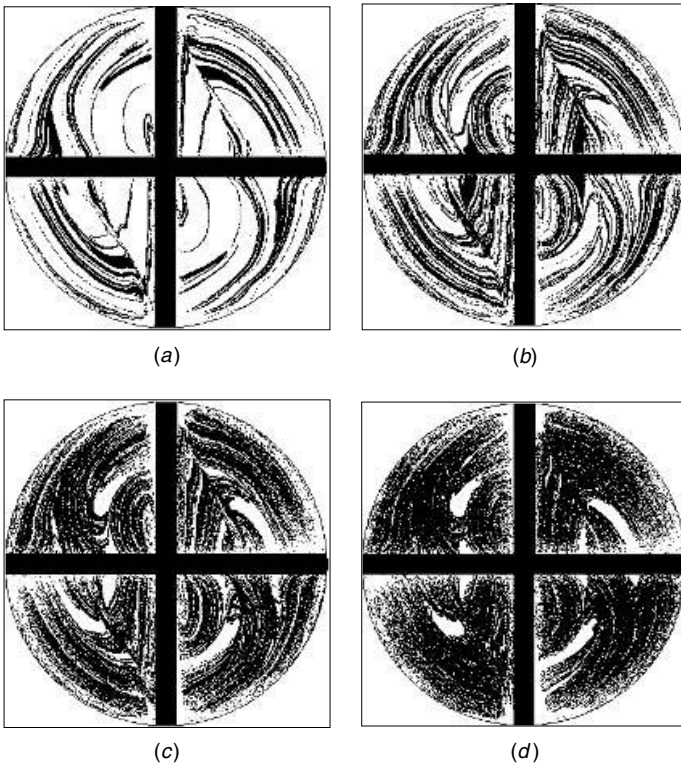
Mixing patterns in the Kenics are examined by simulating 10% (by volume) injection of a tracer with equal density and viscosity as the main fluid. A closed-form solution for particle trajectories, such as eqs. (3-5) and (3-6), does not exist for 3D flows. Tracer mixing patterns can be captured experimentally by dye injection patterns, or computationally by integrating along the velocity field. The trajectory of 200 000 tracer particles is computed according to eq. (3-4) after they have been injected 1 mm upstream of the first element at the center of the cross-sectional area. The software technology and computational algorithms have been validated by experimental data available in the literature (Zalc et al., 2001; Szalai and Muzzio, 2002). The tracer mixing patterns for  $Re = 10(\sqrt[3]{10})$  are revealed after 8, 12, 16, and 20 mixer elements in Figure 3-19a–d. Inertial effects on the flow at this  $Re$  are small. This figure reveals very similar mixing behavior in the Kenics that we have shown in the 2D model system in Figure 3-11. It is evident that the tracer, injected initially at the center of the pipe, does not spread uniformly throughout the flow domain. Quite the contrary—as it is convected, stretched, and folded by the flow, it gives rise to a lamellar system composed of thousands of striations with a wide distribution of local length scales. The structure continues evolving as the number of flow periods increases; the lamellae become increasingly thinner as the result of the iterative stretching and folding process. As the fluid travels through an increasing number of elements, the mixture displays increasingly finer striations organized in a self-preserving topology and a self-similar process dominates the evolution of the structure.

Figure 3-19 illustrates the intrinsic self-similarity in the mixing structure. As time increases, the chaotic flow produces a partially mixed structure that is essentially identical to the structure recorded a period earlier, except that a larger number of thinner striations is found in each region. It is important to remark here that such self-similar structures are independent of initial conditions. When the mixing structure is recorded at periodic intervals, it “always looks the same” regardless of the initial location of the dyed fluid in experiments or the location of the filament in simulations (unless tracer is injected in an island). Independence of initial conditions in flows that create self-similar mixing structures has been described qualitatively in a number of 2D and 3D chaotic mixing flows (Leong and Ottino, 1989; Swanson and Ottino, 1990; Muzzio et al., 1991; Lamberto et al., 1996; Hobbs and Muzzio, 1998; Gollub and Cross, 2000).

### 3-5.3 Asymptotic Directionality in the Kenics Mixer

The explanation of self-similarity in chaotic flows was given earlier, when the asymptotic directionality (AD) property was introduced through examples of the sine flow system. Recall that AD is a local property of chaotic flows that creates





**Figure 3-19** Injecting an equal viscosity additive (10% by volume) just upstream of the inlet region reveals nonuniform mixing in the standard Kenics. Tracer mixing patterns for  $Re = 10(10)^{1/3}$  are shown after (a) 8, (b) 12, (c) 16, and (d) 20 mixer elements. An animation of this mixing geometry is included on the Visual Mixing CD affixed to the back cover of the book.

an invariant spatial template of the mixture at different times. A material line that visits a certain region in the flow adopts an orientation that is characteristic of that position and independent of time. Therefore, periodic snapshots of a cross-section downstream look the same qualitatively, with more and more detail revealed in each picture.

This property, which controls the topology of chaotic flows, is readily observed in 3D industrially relevant flows. The technique used to reveal AD in the Kenics flow is similar to the method of stretching computations with a slight modification. If a small material element is represented as an infinitesimal vector attached to a fluid element in the flow, its position and stretching can be calculated from eqs. (3-4) and (3-7). However, instead of attaching only one such vector to a fluid particle, take a set of three orthogonal unit vectors (Figure 3-20). The evolution of the three vector components attached to the same trajectory reveals how the local spatial position affects the orientation of fluid filaments in a particular region. The three vectors could be thought of as material lines in close proximity to one

another having different initial orientations. The relative direction of each vector in the ensemble can be monitored by measuring the cosine of the angle between the vectors as they are convected by the flow. We randomly distributed the “vector tripods” at the inlet. The cosine of the angle between any two components is 0.0 initially, and the gradual alignment of the vectors along the same trajectory is expressed as the enclosed angle ( $\alpha_n$ ) decreases and the cosine tends to 1.0.

The reorientation and rapid alignment of vectors reveals how fluid filaments in a particular region tend to orient along a predetermined direction. Many sets of three vectors were dispersed at the inlet in the Kenics mixer, and the enclosed angle between the components of each set was recorded at consecutive downstream distances. The mean of the cosines ( $\langle \cos \alpha_n \rangle$ ), which is displayed in the main panel of Figure 3-20, starts from 0.0 at the inlet and rapidly approaches 1.0, indicating convergence to a single stretching direction at each spatial position in the flow. The direction to which all three vectors adapt is a function of the particular spatial position, and it is different for each set. Since the flow is spatially periodic, the field of orientations at a given phase angle is a stationary property of the system. Before the flow passes through a complete Kenics mixer element, the angle between the vector components is close to 0.0. This is an indication of strong directionality at all spatial locations in the flow. Material filaments, regardless of their previous orientation, arrive at a spatial position in the chaotic flow and they all adopt the local stretching direction. The probability density function of  $\cos \alpha_n$  is indicated in the inset of Figure 3-20. The initial distribution is a Dirac delta function centered at zero [ $\delta(0)$ ] since all sets of vectors initially have right angles between them. Each curve in the plot is the

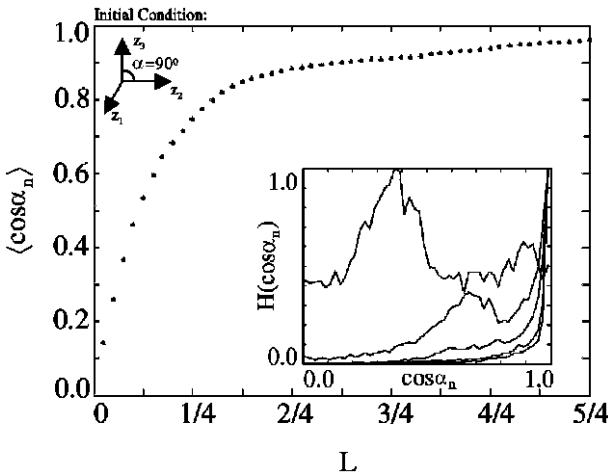


**Figure 3-20** Main panel: The mean of  $\cos \alpha_n$  converges to 1 as the initially orthogonal vectors become increasingly aligned.  $\alpha$  represents the angle enclosed by two of the vectors. Inset: The probability density function of  $\cos \alpha_n$  in the standard Kenics mixer for one-tenth of the total average residence time.

PDF( $\cos \alpha_n$ ) at consecutive time units in the flow. The important feature to note here is the rapid shift in the distribution from 0 to 1, showing the decrease in the enclosed angle from  $90^\circ$  toward  $0^\circ$ .

### 3-5.4 Computation of the Stretching Field

As stated earlier, the intensity of mixing and the intimacy between mixture components can be measured by computing the stretching of small vectors attached to fluid tracers. For 2D chaotic flows, closed-form solutions such as eqs. (3-8) and (3-9) can be obtained for the stretching field. Life is more complicated in 3D, where fluid filaments stretch and contract along multiple directions. The elongation (or stretching) of small vectors as they are convected by the flow is computed for 200 000 tracer elements in the Kenics. Numerical methods are used to solve eqs. (3-4) and (3-7) simultaneously in the entire 3D flow domain, and then the stretching magnitude is computed using eq. (3-10) with the third,  $z$ , component added. The accumulated stretching at several downstream distances is shown in Figure 3-21. The cross-sectional view of the mixer at each downstream distance is represented by circles, and the mixer element appears as a white line across the diameter. The initial orientation of the stretching vectors rapidly changes and they realign with the principal stretching direction of the flow within the first couple of mixer elements. After this realignment the initial vector orientations are no longer important.

The accumulated stretching of each tracer is plotted as a function of initial position and color-coded according to magnitude. Areas that experience high stretching correspond to high mixing intensities, where materials injected to the flow will spread rapidly over the domain. On the other hand, low-stretching areas correspond to poor mixing regions that exchange material slowly with the rest of the flow. Coherent structures that appear at every cross-section in the mixer are segregated regions, or islands, that are only destroyed by the slow action of diffusion. Two such large areas are noticeable at this flow condition ( $Re = 21.5$ ) in the Kenics, one on each side of the mixer element near the center of the tube (see Figure 3-21*d*). A higher flow rate in this mixer does not necessarily lead to better mixing. It has been documented that these segregated regions exist at  $Re = 100$  and cover nearly 10% of the total flow area. These figures reveal that these structures appear in the device at much lower flow rates and span a wider range of flow conditions than believed earlier.

It is important to point out that the range of stretching values is different in each cross-section, gradually increasing as the flow passes through more and more mixer elements. In Figure 3-21*a* after two mixer elements, the minimum stretching magnitude is  $4.80 \times 10^{-2}$ , the maximum is  $4.62 \times 10^8$ , and the arithmetic average accumulated stretching per tracer is  $4.84 \times 10^4$ . By the time the fluid elements pass through 22 elements, the range is much broader, spanning 17 orders of magnitude with a minimum at  $2.41 \times 10^{-1}$ , the maximum at  $2.01 \times 10^{15}$ , and the average at  $1.20 \times 10^{10}$ .

Asymptotic directionality and self-similarity, the cause and effect of universal dynamical behavior in chaotic flows, is immediately apparent in each set of three

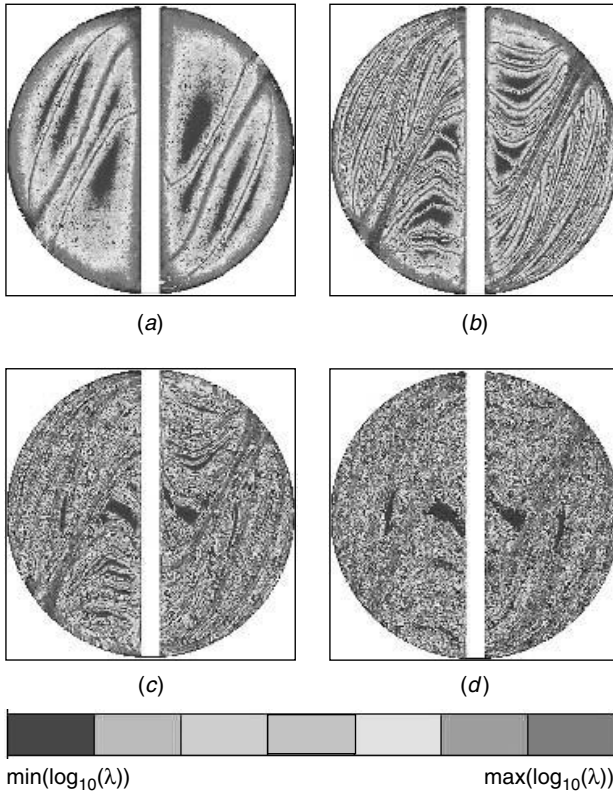


**Figure 3-21** Contours of the stretching field in the standard Kenics mixer at  $Re = 10(10)^{1/3}$ . The cross-sectional planes correspond to axial distances after (a) 2, (b) 6, (c) 10, and (d) 22 mixer elements. See insert for a color representation of this figure.

snapshots. Some features of the mixing structure appear early, after the fluid passes through just two mixer elements. New folds appear within existing ones in subsequent sections. The general features of each mixing pattern after 2, 6, or 10 elements (Figures 3-21a–c) are the same with more details added at each element. It should be pointed out at this point that dye mixtures in physical experiments would show the same pattern as observed in the stretching plots.

### 3-5.5 Rates of Interface Growth

We have shown in Figure 3-13 that intermaterial area density is created at an exponential rate in 2D chaotic flows. Figure 3-22 demonstrates that the same applies to 3D flows, where the average of the natural logarithm of stretching,  $\langle \log \lambda \rangle$ , is plotted as a function of downstream distance in the Kenics mixer for two flow rates. After some entrance effects, the mixing rate shows a uniform monotonic increase on a logarithmic scale, and the Lyapunov exponent

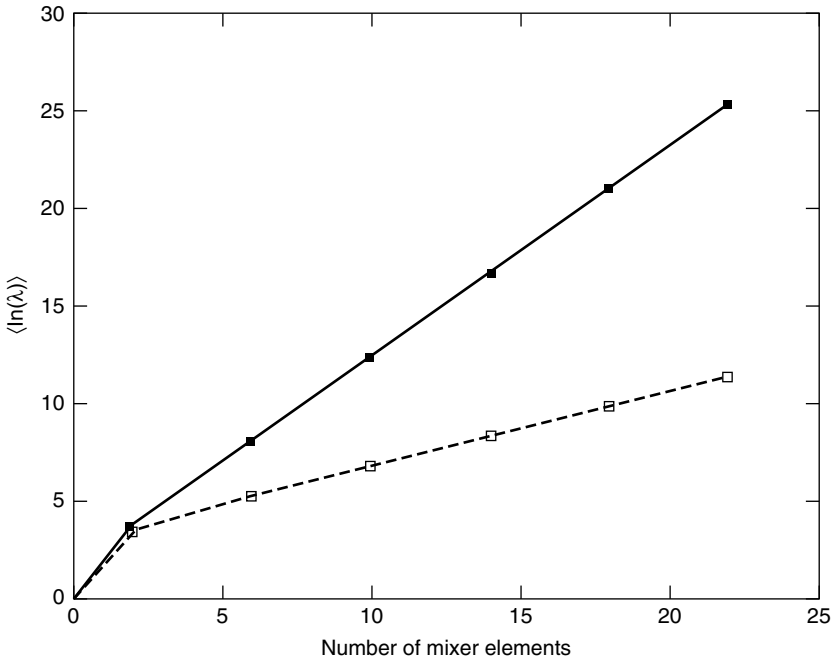


**Figure 3-22** Stretching in the standard Kenics mixer increases at an exponential rate, which is characteristic of chaotic flows. The rate of increase is higher at a higher flow rate  $Re = 1000$  (dark squares) than at  $Re = 10(10)^{1/3}$  (light squares) but the energy cost of maintaining such high average throughput is not reflected in  $\lambda$  alone.

is equal to the slope of the linear function. The rate of increase is higher at a higher flow rate  $Re = 1000$  than at  $Re = 10(10)^{1/3}$ . The different initial rate of increase (i.e., a kink in the slope after two elements) is due to the initial realignment of stretching vectors to the principal stretching direction during the first flow period.

### 3-5.6 Intermaterial Area Density Calculation

The real power of using stretching computations to characterize chaotic flows lies in the fact that stretching is the link between the macro- and micromixing intensities in laminar mixing flows. In this section we describe the method for computing striation thickness distribution in our 3D example, the Kenics mixer.

We used the direct relationship between intermaterial area density ( $\rho$ ) and stretching ( $\lambda$ ) stated in eq. (3-15) to compute the spatial structure of  $\rho$  in the Kenics flow. Approximately  $4 \times 10^6$  tracer particles were used in the stretching computations to assure statistically significant results. The specific method is as follows: First, the accumulated stretching of all the tracer filaments was recorded after 2, 6, 10, and 22 Kenics mixer elements. Then a uniform lattice of  $225 \times 225$

boxes was overlaid each mixer cross-section, and all the boxes that were fully or partially outside the flow area were discarded. This includes boxes that were placed on the tube perimeter or on the tube diameter along solid surfaces. A total of 37 130 boxes were retained from the original 50 625. Finally, the accumulated stretching of tracer particles in each box was summed and divided by the overall average  $\langle \lambda \rangle$ .

Figure 3-23 shows the spatial distribution of intermaterial contact area, scaled by the overall length of the interface  $\langle \rho \rangle$ , at each axial position in the mixer. As discussed earlier in the chapter, the distribution of intermaterial area is related directly to the stretching field through the relationship  $\lambda \sim \rho$ . Qualitatively, this relationship can be confirmed if one compares the stretching field in Figure 3-21 to the field of intermaterial area densities in Figure 3-23. Quantitative proof was given in Figures 3-14 and 3-15, where the direct computation and prediction of  $\rho$  were compared for the sine flow. Once the intermaterial area in each of the 37 130 cells is normalized by the overall average,  $\langle \rho \rangle$ , the distribution and scale are identical for all four cross-sectional positions. In other words, the function  $\hat{\rho} = \rho / \langle \rho \rangle$  is invariant and describes the intermaterial area density at each period everywhere in the domain (i.e., each color represents the same range of  $\rho$  in

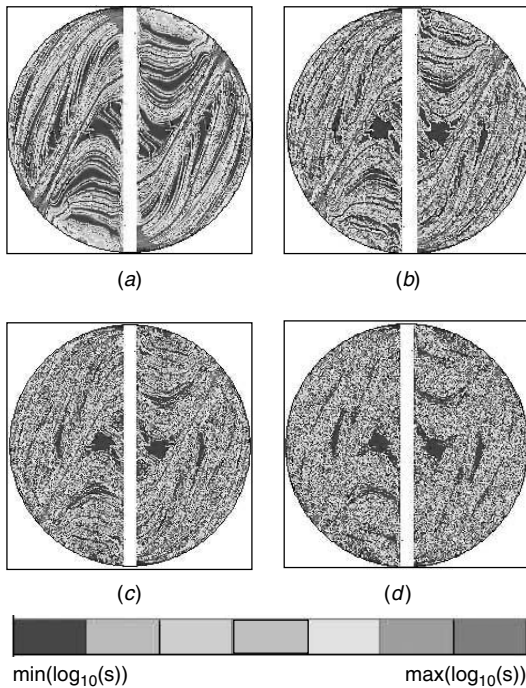


**Figure 3-23** Intermaterial area density ( $\rho$ ) from coarse-grained stretching average in the standard Kenics mixer at  $Re = 10(10)^{1/3}$  after (a) 8, (b) 12, (c) 16, and (d) 22 mixer elements. See insert for a color representation of this figure.

Figure 3-23a–d). This figure provides qualitative proof that the spatial structure of intermaterial area densities at different downstream distances is time-invariant. The spatial distribution of  $\rho$  exhibits strong fluctuations that are a *permanent* feature of the mixing process (i.e., the picture “looks the same” for the four flow periods). As shown in Figure 3-23, when the spatial distribution of  $\rho$  is computed after additional periods of the flow, although  $\langle \rho \rangle$  increases by several orders of magnitude, its spatial distribution remains essentially unchanged.

The time invariance in the spatial distribution of  $\rho$  is another manifestation of the self-similarity of the structures generated by time- and spatially periodic chaotic flows. Such invariant statistical properties can be demonstrated by computing the probability density  $H(\log \rho)$ . If the probability density function of the scaled variable  $(\rho/\langle \rho \rangle)$  is computed according to eq. (3-13), the distributions are scaled automatically by the mean density.

The distribution  $H(\log(\rho/\langle \rho \rangle))$  is shown in Figure 3-24 after  $n = 4, 6, 8,$  and  $11$  on a logarithmic scale.  $Re = 10(10)^{1/3}$  corresponds to a moderate flow rate of  $1.29 \text{ m}^3/\text{h}$ . From Figure 3-24 we see that the distributions approach an asymptotic shape characterized by a power law decay in the low- $\rho$  region as the number of elements increases, followed by a much steeper, possibly exponential decay in the high- $\rho$  region. The effective collapse of the scaled distribution over several orders of magnitude in  $\rho$  indicates that the above-mentioned nonuniformities in  $\rho$  are a permanent feature of periodic chaotic flows. As the number of elements increases, the intermaterial area density increases everywhere while preserving

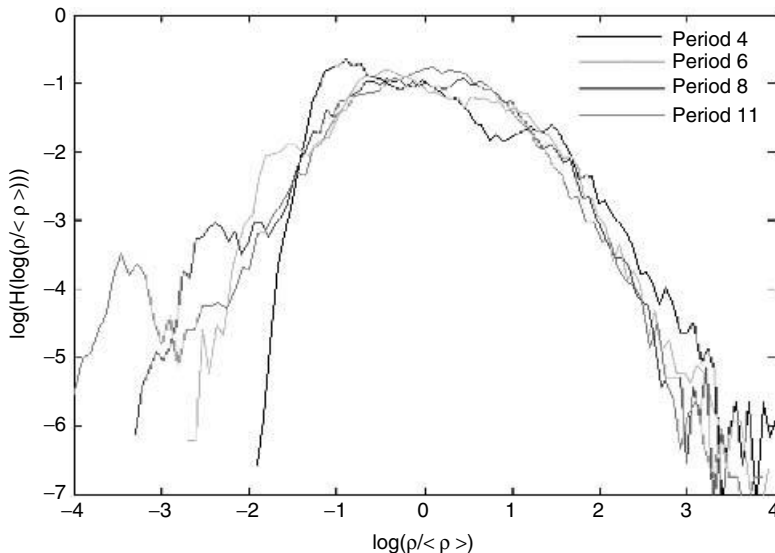


**Figure 3-24** The distribution of intermaterial area density ( $\rho$ ) in the standard Kenics mixer at four axial cross-sections at  $Re = 10(10)^{1/3}$ . The probability density function of  $\rho/\langle \rho \rangle$  reaches an invariant shape as the mixing process evolves.

the same distribution, meaning that the number of low- and high-density locations, and the relative magnitude of the density on such regions, remain unchanged. This behavior is not unique to flows with low or moderate inertia, nor is it limited to static mixers. The evolution of mixing intensities and microstructure shows similar characteristics in cases where the flow is on the verge of turbulence (Szalai and Muzzio, 2003) for both static mixers and stirred tanks.

The observed scaling of  $\rho$  has an important physical interpretation: Once  $\rho$  approaches the characteristic invariant and statistical distributions generated by the global invariant manifold, it then evolves everywhere at the same rate as the mean density. In other words, if the mean intermaterial area density is doubled, the *local* density is doubled *everywhere*. This is important, because it means that the time evolution of  $\langle \rho \rangle \approx e^{n\theta}$  determines the time evolution of  $\rho$  at all locations of the chaotic flow (i.e., intimacy of mixing improves everywhere by the same factor). Similarly, the striation thickness  $\langle s \rangle \approx \langle \rho \rangle^{-1}$  both locally and globally: The local average striation thickness decays everywhere at the same rate, as predicted by  $\langle s \rangle \approx e^{-n\theta}$ . Therefore, the mixing rate in periodic, chaotic mixing processes can be characterized by a single quantity, the growth of the average intermaterial area density  $\langle \rho \rangle$ . Moreover,  $\Theta$ , the topological entropy exponent, can be regarded as a mixing rate. While this observation is not true in nonchaotic regions, this distinction is immaterial in practical applications because flows with large nonchaotic regions are likely to generate such processing problems that in all likelihood such flows should be avoided in well-designed mixing applications.

As is clear from Figure 3-24,  $\rho$  in some regions is several orders of magnitude higher than in other regions. This observation means that even if the system is homogeneous from a macromixing standpoint, in some regions the flow achieves much more intimate mixing (much more intense micromixing) than in other regions. Such fluctuations in  $\rho$  can have huge effects on practical applications. For example, for systems that require dispersive mixing of a pigment or an additive (a common case in polymer processing applications), differences in  $\rho$  directly affect the optical quality and material properties of the finished product. For diffusion-controlled reactions, the local reaction rate depends both on the amount of contact area and the average intensity of the concentration gradient, which is usually proportional to the intermaterial area density. For systems with multiple reactions, the value of  $\rho$  determines the ratio of desired/undesired product generated in a given region of a reactor. Thus, strong fluctuations in interface density would have an enormous effect on reactive systems, resulting in different reaction rates and in different product distributions at each location. The micromixing properties of 3D chaotic flows are exploited in more detail in the next section.

### 3-5.7 Prediction of Striation Thickness Distributions in Realistic 3D Systems

The same iterative stretching-and-folding process that generates self-similar density distributions drives the evolution of striations and therefore controls the



dynamics of striation thickness distributions (STDs). STDs could be computed from the distributions of stretching values by realizing that as a portion of fluid is stretched, it generates striations with a thickness inversely proportional to the amount of stretching applied to the fluid. In other words, eqs. (3-15) and (3-16) can be extended to 3D systems such as the Kenics flow. The validity of eq. (3-16) was demonstrated in Figure 3-17, where more than  $10^9$  tracer particles and over  $10^6$  stretching values were required to compute the STD directly [by using eq. (3-14)] and were compared with the prediction of eq. (3-16). Such a level of numerical resolution is usually impossible and almost always impractical when dealing with realistic 3D flows. Equation (3-14) cannot be applied directly to 3D systems such as the example studied here.

Fortunately, additional theoretical developments allow one to circumvent the need for direct computation. Computing the distribution of stretching intensities and the overall stretching rate, as seen in Figures 3-21 and 3-22, is feasible in any deterministic chaotic flow. Subsequently,  $H(\log s)$  is predicted by eq. (3-16) in Figure 3-25 for two cases, after 6 and 22 elements, in the Kenics.  $H(\log s)$  versus  $(-\log s)$  calculated by assuming that  $s_0 \approx 1$  (i.e., the initial unmixed region is assumed to be of similar size as the entire system) is shown in Figure 3-25 for  $Re = 10(10)^{1/3}$ . Interestingly, the high stretching side of  $H(\log \lambda)$  generates essentially the entire distribution  $H(\log s)$ , and the mode of  $H(\log s)$  corresponds to stretching values far along the right tail of  $H(\log \lambda)$ . This observation has deep physical meaning. Figure 3-25 demonstrates that the overwhelming majority of

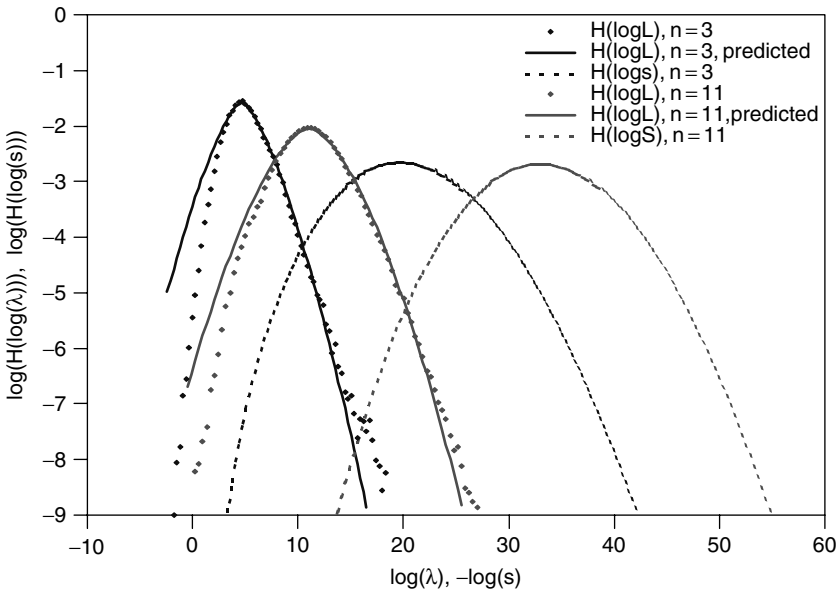


**Figure 3-25** The distribution of striation thicknesses,  $H(\log s)$ , is predicted from the right branch of the stretching distribution,  $H(\log \lambda)$ , for  $Re = 10(10)^{1/3}$ .

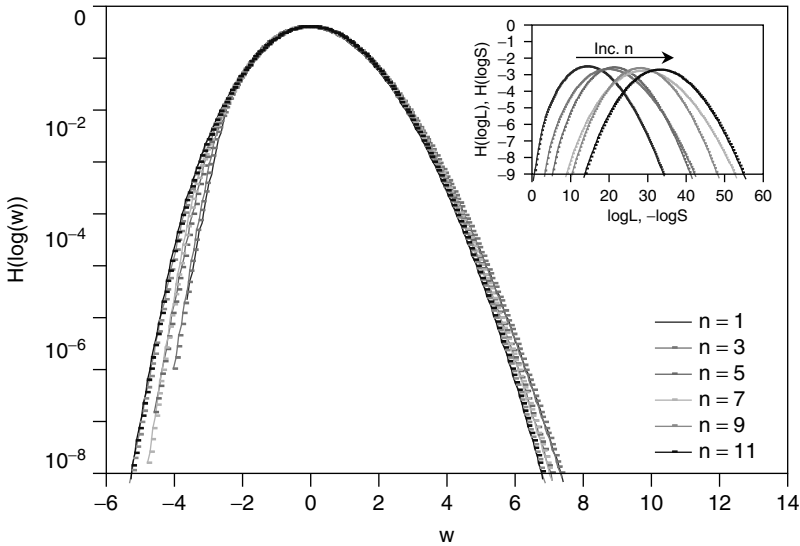


**Figure 3-26**  $H(\log s)$ , which represents the spectrum of diffusive length scales, is shown for  $n = 1-11$  for  $Re = 10(10)^{1/3}$ . The scale distributions in the main panel of each figure approach an invariant distribution as the period increases. The inset reveals the broadening distributions as striations are created by the flow.

striations, corresponding to most of the interfacial contact area in the system, is generated by a set of very rare but very intense stretching events (Szalai and Muzzio, 2003).

The evolution of  $H(\log s)$ , and its scaling properties, are illustrated in Figure 3-26 for  $Re = 10(10)^{1/3}$  for six cross-sections in the Kenics. The inset shows  $H(\log s)$  after 2, 6, 10, 14, 18, and 22 elements. In the main panel the same data are shown after the distributions have been re-scaled by subtracting the mean and dividing by the standard deviation. As revealed in Figure 3-26, the shape of the distribution gradually approaches a self-similar distribution where the curves increasingly overlap one another as  $n$  increases. Surprisingly, the convergence to a self-similar STD is much faster and much more complete for  $Re = 1000$  (figure not shown), where the distributions overlap over three decades of probability after the first few elements (Szalai and Muzzio, 2003).

### 3-6 REACTIVE CHAOTIC FLOWS

The effects of flow and mixing on reactive systems have been recognized for many decades, yet the interplay of convection and diffusion has traditionally been treated with overly simplistic approaches. The complexity of applications where both diffusion and mechanical stirring occur simultaneously with reactions has been overwhelming to the point that perhaps in despair, critical aspects of

convective flow have been altogether neglected. The classic approach of drawing a black box around the reactor and examining only the intrinsic kinetics of the reactive process is only meaningful when macroscopic inhomogeneities can no longer be detected. This method treats the intrinsic kinetics properly but can only give insight for processes with slow reactions. It is bound to fail when reactions occur faster than the time scale for homogenization in the system. In such cases we run the risk of overestimating the selectivity and conversion during the design process (a typical problem during reactor scale-up) but completely ignore that a “well-mixed” homogeneous state may never be reached during the entire life of the process (recall Figure 3-6).

Chaotic flows are the only effective route to destroy segregation rapidly in viscous mixing applications, which are particularly prone to remaining inhomogeneous for long times (Lamberto et al., 1996; Avalosse and Crochet, 1997; Hobbs et al., 1997; Unger and Muzzio, 1999). In the past two decades, the effect of chaotic mixing without reactions has been examined in a variety of increasingly complex mixer geometries on a case-by-case basis. However, without a deep understanding of how fluid motion couples with diffusion and molecular kinetics in reactive flows, we cannot yet take the leap to include all transport mechanisms in a realistic geometry. Simplifications can be made by considering 2D model chaotic flows, where the convection–diffusion–reaction mass balance can be solved directly (Muzzio and Ottino, 1988; Metcalfe and Ottino, 1994; Muzzio and Liu, 1996; Zalc and Muzzio, 1999; Neufeld, 2001; Giona et al., 2002).

The sine flow captures many features of 3D chaotic mixing processes accurately. The only parameter that controls the behavior of the system is the flow period  $T$ . As seen in Figure 3-11, this simple sinusoidal velocity field with alternating directions creates complex, layered structures that appear to be a collection of different-sized filaments filling the chaotic region. The two controlling mechanisms of the convective mixing process, stretching and folding, occur similarly in more complex, 3D systems, such as the Kenics mixer (Figure 3-19) or stirred tanks. To understand the effect of hydrodynamics and mixing on reactive flows, in the next section we explore how convective mixing, when coupled with diffusion and reactions, affects the evolution of chemical reactions.

Consider the unit square domain of the sine flow, where the right side is filled with reactant A and the left side contains only B. The initial interface between the two components is a vertical line along the center and one edge of the box. At  $t = 0$  convective mixing is turned on in the model simultaneously with diffusion and reaction. The species balance equation in a dimensionless form for the flow with reaction, diffusion, and convection is

$$\frac{\partial c_i}{\partial t} + \bar{v} \cdot \nabla c_i = \frac{1}{Pe} \nabla^2 c_i + r \quad (3-17)$$

where  $Pe$ , the Peclet number, measures the relative magnitude of the characteristic time for convection to diffusion. Applications usually have values of  $Pe$  in the range  $10^2$  (laminar flames) to  $10^{10}$  (turbulent reactive flows, polymerizations). For problems where convective mixing plays an important role, it is of interest

to choose  $Pe$  as high as possible. If the two time scales were on the same order (i.e.,  $Pe \cong 1$ ), mixing effects would be unimportant because diffusion would erase heterogeneities as quickly as convection creates them. At the other end of the spectrum, where  $Pe$  is very high, diffusion is very slow compared to the convective mixing process. In this case, very fine, partially mixed structures remain intact for long times before diffusion has an effect. The spatial resolution (i.e., maximum distance between neighboring nodes) that is necessary to capture the details of the mixing structure determines the upper bound of the  $Pe$  for practical applications. For the results presented in this chapter, given available computer resources,  $Pe = 2000$  is the highest practical value.

We consider a bimolecular reaction:  $A + B \rightarrow 2P$  and define  $\varphi = c_A - c_B$ . For infinitely fast reactions, since  $A$  and  $B$  cannot coexist, a single equation describes both the reactant and product concentrations:

$$\frac{\partial \varphi}{\partial t} + \bar{v} \cdot \nabla \varphi = \frac{1}{Pe} \nabla^2 \varphi \quad (3-18)$$

To describe the evolution of  $\varphi$ , standard finite-difference methods were employed to solve eq. (3-17) at  $1024 \times 1024$  nodes in the flow. Initially, half of the flow domain was filled with  $A$  and the other half contained only  $B$ . The reactant and product concentrations are computed from  $\varphi$  according to eq. (3-18).

Once the product concentration is known as a function of time, the local reaction rate can be determined from mass conservation:

$$r = \frac{1}{2} \left( \frac{\partial c_P}{\partial t} + v \cdot \nabla c_P - D_f \nabla^2 c_P \right) \quad (3-19)$$

Equation (3-19) in some sense captures the fact that three processes—the local reactivity, diffusive transport, and convective mixing—control the effective reaction rate. We now examine how each of these three components affects the overall evolution of a reactive mixing process.

The reaction rate after the first three periods of the sine flow with  $T = 1.6$  is illustrated on the right-hand side of Figure 3-27. The three figures represent  $r$  after  $n = 1, 2,$  and  $3$ , so its time evolution can be followed from the top to the bottom of the figure. We use a logarithmic scale to illustrate the spatial variations of  $r$ . The colors are relative to the maximum rate after each period, which is 69.82 after  $n = 1$ , 25.70 after  $n = 2$ , and 4.81 after  $n = 3$ . The darkest lines represent the hot zones in the flow, where the instantaneous reaction occurs. The rapid decrease in the maximum rate shows how fast reactants are consumed by the reaction. During the first three periods, the reaction proceeds very rapidly: The conversion is 49.3% at  $n = 1$ , 87.7% at  $n = 2$ , and reaches 96.5% at  $n = 3$ .

Compare the left and right columns of Figure 3-27, where the purely convective flow is compared with the reactive/diffusive case. The hot zones, where the reactive interface is, closely agree with the locations of highest filament density. The landscape of the nonreactive mixture (left side of Figure 3-27) looks almost identical to the landscape of the reactive flow (right side of Figure 3-27).

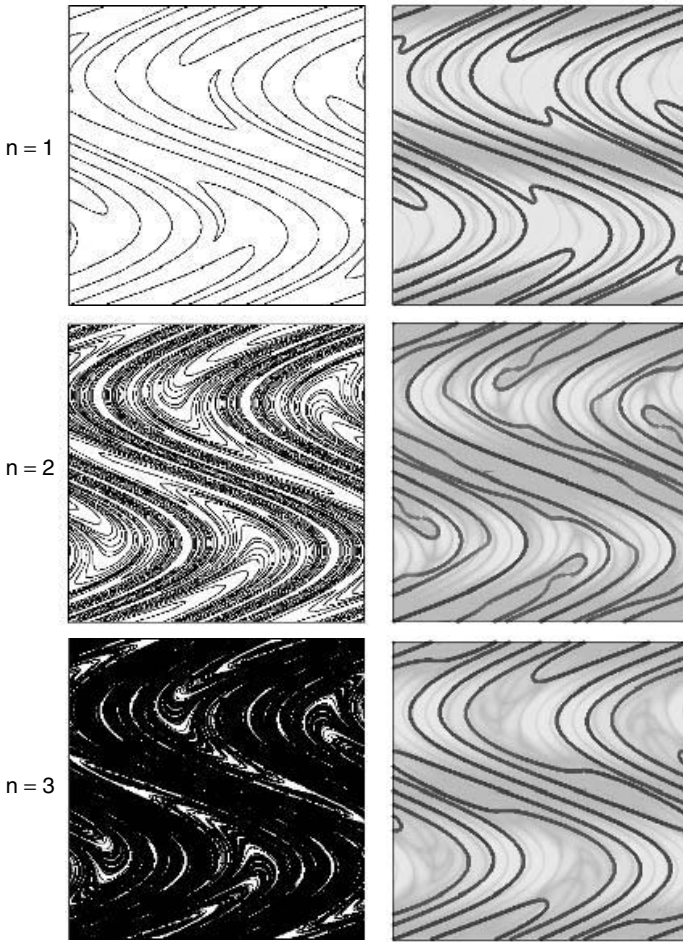


**Figure 3-27** The left-hand side of the figure indicates the distribution of intermaterial contact area in the sine flow with  $T = 1.6$  after  $n = 1, 2,$  and  $3$ . The right-hand side shows the rate of an instantaneous bimolecular reaction ( $A + B \rightarrow 2P$ ) in the same flow. The darkest areas represent the hot zone where the reaction proceeds very rapidly. Its location is almost identical to the landscape of intermaterial contact area.

This similarity is not coincidental; the two sets of figures are highly correlated. The stretching process is the sole determinant of where interface is created and establishes where intimate contact is achieved between fluids A and B. Once the playing field is set by convective stretching, diffusion and reaction follows: The landscape of the reactive zone closely outlines the location of the fluid–fluid interface, which is determined purely by convection. Diffusive transport in each region is proportional to  $\rho$ , the amount of interface at that location. The areas in the flow where striations contain only A or only B remain inactive, because no

reaction takes place there. However, in the areas that contain neighboring striations of A and B (i.e., areas where the A–B interface is), diffusion immediately transports material across the interface, the reaction proceeds, and product begins to accumulate.

There are some differences between the nonreactive and the reactive landscapes (in the left and right columns of Figure 3-27). The thinnest striations contain the least amount of reactants, so they are consumed first by the reaction. As time progresses, these striations become exhausted and the reaction front advances. Early on, convection creates new striations and more interface, so the reaction zone stretches. Then it quickly reaches a balance with diffusion, and reaction proceeds until the area begins to run out of reactant. As a result, the reaction extinguishes and the hot zone migrates. The interplay of two mechanisms—creation of intermaterial area and diffusion—determines how quickly striations are consumed by the reaction. The exponential stretching process controls both of these mechanisms (Szalai et al., 2003).

Next, we examine the spatial distribution of reactants and products as they evolve in time. The left-hand column of Figure 3-28 shows the spatial distribution of reactants after  $n = 1, 2,$  and  $3$ . The right-hand column of Figure 3-28 is the corresponding product distribution in the flow. Similar to previous contour plots, the colors of each figure are based on the relative maximum values of reactants and products, respectively. On the left side, striations of A (red) interpenetrate striations of B (blue) and regions near the reactive interface quickly become exhausted. At the same time, product appears at these locations, following the same landscape as in Figure 3-27. The initially thin product-rich filaments become increasingly thicker until isolated areas of low product concentration remain dispersed in the flow. These islands of low product concentration contain exclusively reactant A or B, as seen in the corresponding left-hand picture. They remain intact until diffusion transports reactants to these regions from the surrounding striations.

Diffusion increasingly smears the boundaries of striations in Figure 3-28. However, the difference is primarily cosmetic. As shown in Figure 3-29, the product concentration field remains statistically self-similar. The product concentration after each period is scaled using standardization. The probability density function of  $c_p$  remains invariant over three flow periods after the mean ( $\langle \log c_p \rangle$ ) is subtracted from each measurement and divided by the standard deviation ( $\sigma_{\log c_p}$ ). Note here that the conversion at the end of the fourth period, corresponding to the pink curve on the plot, is over 96%. By this time the reaction is close to completion; in fact, most areas have become exhausted of reactants, thus demonstrating that self-similar dynamics control the entire evolution of the reactive mixing process even at  $Pe$  as low as  $Pe = 2000$ .

### 3-6.1 Reactions in 3D Laminar Systems

Convective mixing not only affects the progression of reactions in chaotic flows but has governing control on their evolution. The idea that it is sufficient to

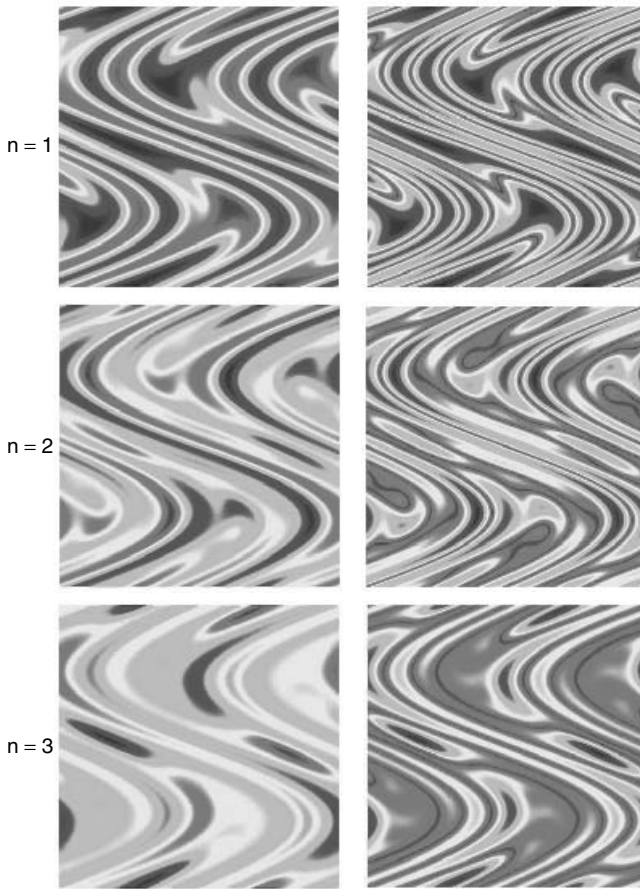


**Figure 3-28** The left-hand side of the figure shows the concentration of reactants A and B after the first three flow periods in the sine flow with  $T = 1.6$ . The right-hand side is the corresponding product concentration. See insert for a color representation of this figure.

have the end result in mind when designing a laminar reactive mixing process must be abandoned. The only route to fast mixing in laminar applications is via chaotic flows, and the mixing intensity in these systems is inherently nonuniform. In such systems, a wide spectrum of stretching intensities distributes material interface along a predefined, invariant template. It establishes intimate contact between mixture components (whether reactive or not) and controls the local rate of diffusion through the intermaterial area density and striation thickness distribution. All chaotic mixing flows share these characteristics.

Understanding the interplay of the three mechanisms—reaction, diffusion, and convection—is essential. In light of what happens in 2D reactive chaotic flows, we can attempt to extend the analysis to 3D reactive mixing applications. Let us take a fresh look at a common 3D example, a mixing tank stirred with three

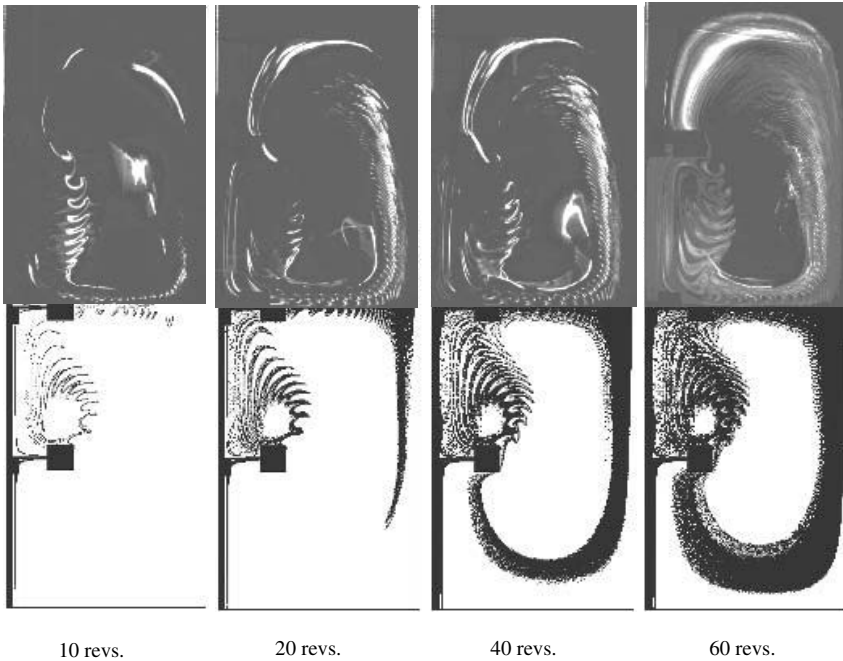


**Figure 3-29** The evolution of a fast reaction in a mixing tank stirred with three Rushton impellers at  $Re = 20$ . The reactive zones in a stirred tank are identical to the location of the intermaterial contact area in a mixing after 10, 20, 40, and 60 impeller revolutions. Each figure shows half of the vertical cross-section, where the shaft and three impeller blades are seen on the left. The upper half is a photograph of the reactive flow and the bottom is the computed chaotic mixing structure.

Rushton impellers. Analytical solutions for stretching and particle positions are not available for 3D flows, so we need to rely on numerical methods to compute the stretching and the filament structure. Figure 3-29 shows a dye filament, initially placed vertically near the impeller shaft, as it is stretched and folded into a complex mixing structure that eventually invades the entire chaotic region. The four pictures in the figure indicate four computational snapshots of the chaotic mixing process at consecutive times. We computed the structure of the filament by placing 200 000 tracer particles in a line along the shaft.

As time increases and convective mixing takes place, the material filament gradually invades portions of the chaotic region. A convoluted, partially mixed structure develops after 60 revolutions, and the location of the filament marks the interface between the mixture components, as indicated in Figure 3-29. An experiment using a pH-sensitive dye is compared to Figure 3-29, where dye was initially injected near the impeller blades. A photograph after 60 impeller revolutions indicates that the filament acquires an identical structure in the experiments as predicted by the computed mixing structure. Since the dye is pH



sensitive, an instantaneous acid–base reaction occurs in the tank at the interface between the mixture components. The mechanism that controls the evolution of the reactive mixing process is largely the same as in the sine flow described earlier. The fluorescent, pH-sensitive dye gives a visual indication of the reaction zones, where the acid–base reaction occurs in the tank. The product-rich areas glow with high illumination and their shape unmistakably coincides with the mixing structure created by the convective flow.

We can go further than qualitative comparisons and measure the probability density function of the reactant and product concentrations in the tank. To measure the product concentrations experimentally, image analysis is used to quantify the level of luminescence in the experimental photograph. The time evolution of the reactive process is monitored by taking a series of pictures similar to those in Figure 3-29. Product concentration is quantified based on the pixel values in each photograph. The entire vessel is divided to equal-sized cells, and the amount of fluorescent dye is measured in each cell. The probability density function of the concentration is computed by counting the number of cells that have concentrations between values of  $c$  and  $(c + \Delta c)$ . The normalized values ( $w$ ) are computed by subtracting the mean and dividing each by the standard deviation on a logarithmic scale. Figure 3-30 indicates the distribution of  $c_p$  in the three-impeller stirred tank at three different times. The evolution of the acid–base

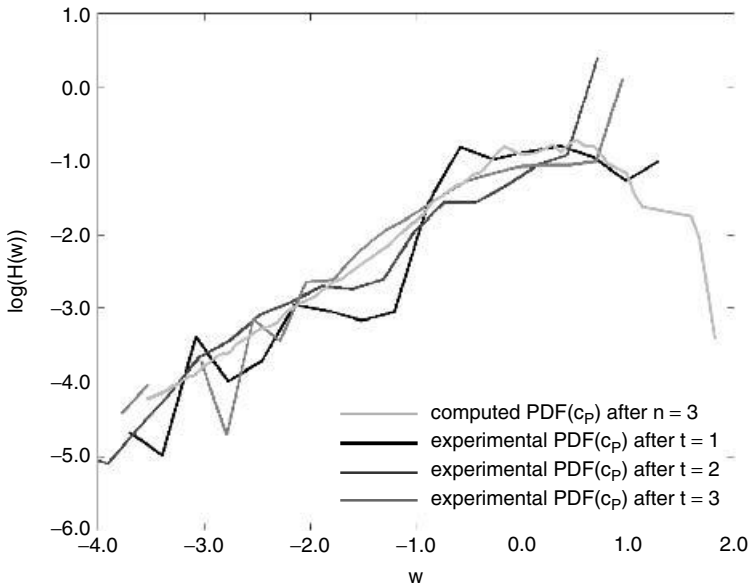


**Figure 3-30** The probability density function of the product concentration [PDF( $c_p$ )] in the tank is calculated from the experimental images after  $t = 1, 2,$  and  $3$  min. The experimental distributions in the 3D chaotic flow are invariant after scaling and match the concentration distribution of the model system. It is shown by overlaying PDF( $c_p$ ) in the tank and in the sine flow at  $n = 3$ .

reaction 1, 2, and 3 min after injecting the dye is captured during the experiments. In light of the self-similarity that occurs in 2D reactive chaotic processes (recall Figure 3-27), we expect the scaled product concentration profiles to show an invariant distribution. Figure 3-30 confirms this expectation for the 3D reactive flow. The distribution of the scaled concentration profiles after 1, 2, and 3 min fall right on top of one another. Remarkably, they also agree closely with the scaled distribution obtained from the 2D model system. The agreement is shown in Figure 3-30 by overlaying the curve from  $n = 3$  from the sine flow with the experimental data. This preliminary result suggests that self-similarity also appears in 3D reactive flows, and implies that the chaotic stretching and orientation process governs the evolution of reactions in 3D systems, indicating a clear conceptual direction pregnant with promise for future progress.

### 3-7 SUMMARY

Fluid mixing takes place by a combination of mechanisms: convection (stirring or macromixing), stretching, folding, and diffusion. Effective mixing processes, whether we think about turbulent flows or chaotic flows, all promote global uniformity by redistributing initially segregated components in space. In the laminar regime, the only efficient route to mix is through chaotic flows. The focus of this chapter was to discuss the nature of these flows through a set of experimental and computational observations. In a general sense, these can be summarized in a few key points:

- Defined geometric patterns and robust statistical properties are evident in chaotic mixing flows. The naive interpretation of chaos, as synonymous with disorder, is misleading. A defined mixing structure is created by each chaotic flow, and the generic geometric features these flows possess all have similar characteristics. We demonstrated this phenomenon on a 2D model flow (the sine flow) as well as on the flow field of an industrial mixer (the Kenics static mixer).
- The highly symmetric, self-similar nature of structures generated by chaotic mixing processes is connected to an intrinsic invariant field of orientations, generated by an invariant manifold structure in these flows. At each location in the domain, this predetermined orientation does not depend on time.
- The evolution of material filaments in chaotic flows can be described by the average intermaterial area density  $\langle \rho \rangle$  at any period in the flow. This single measure, obtained from the elementary stretching of massless tracers, expresses the global time evolution of microstructure in chaotic flows:  $\langle \rho \rangle \sim e^{n\Theta}$ . The accumulation of interface in different areas of the flow domain is highly nonuniform. In some regions the intermaterial area density  $\langle \rho \rangle$  is five orders of magnitude higher than in others. However, since it increases everywhere at the same rate  $\Theta$ , this parameter is a true rate for the overall mixing process.

- Due to the nonuniformity in  $\rho$ , the local rate of transport-controlled reactions (i.e., “fast” reactions) will be much faster in some areas of the flow than in others. In exothermic reactions, this can lead to the creation of “hot spots.”
- The microstructure generated by chaotic periodic flows is very robust. Once the shape of the distribution of striations is determined and the average time evolution is known, the distribution of characteristic lengths can be predicted for any future time, because the striation thickness ( $s$ ) is inversely proportional to  $\rho$ . Striation thickness distributions can be accurately predicted from stretching distributions, and their statistical properties are identical. Therefore, the stretching field provides convenient means of examining the length scales generated by chaotic mixing flows.
- Since stretching controls the location and density of the intermaterial area between mixture components, it has a direct impact on the evolution of reactions. The location of the reactive zones is practically identical to the mixing structure determined only by the chaotic stretching process. Furthermore, since stretching is a self-similar process, the distribution of product concentrations is self-similar as well and can be rendered invariant by statistical methods.

### 3-8 CONCLUSIONS

In this chapter we have discussed methods from dynamical systems theory for characterization of microstructure and topology generated by chaotic periodic flows. In the first half of the chapter, a simple two dimensional model flow, the sine flow, was introduced as an example to illustrate the application of some common and newly developed tools for mixing characterization. In the second half of the chapter we showed how these techniques can be extended to real, three dimensional chaotic flows, and our practical example was the Kenics static mixer. An important shortcoming of methods such as Poincaré sections is that the use of point tracers does not preserve the evolving mixing structure. Thus, understanding and controlling the dynamics of mixing, the very goal in mind when designing a process or equipment, becomes an impossible task.

Convective mechanisms in chaotic flows (stretching and folding) transform portions of materials into elongated striations and reorient these filaments with respect to the direction of deformation. Continuous reorientation creates a sustained exponential rate of increase in intermaterial contact area in chaotic flows. These mechanisms are captured by nontraditional tools, such as computing the stretching field, computing striation thickness distributions directly, or predicting them from stretching.

Another important component of mixing processes, diffusion, remains to be included in the discussion. The ability to measure or predict striation thickness distributions in chaotic flows provides the link between mixing on the macroscopic and microscopic scales. Diffusion and stretching are intimately coupled because as material filaments are stretched by the flow, the rate of diffusion is

increased simultaneously. The increase is due partially to an increase in the interfacial area available for transport (as striation boundaries are increased) and also to a reduction in diffusional length scales (striation thicknesses are decreased everywhere at the same rate). Since stretching is spatially nonuniform in chaotic flows, fluctuations in local diffusional fluxes will also occur. This, in turn, will lead to spatial fluctuations in reaction rate, product concentration, and waste concentration. Continued efforts to incorporate all of the important mechanisms (convection, diffusion, and reactions) within a unified mixing theory is necessary before we can fully understand and predict the behavior of complex real-world industrial systems.

## NOMENCLATURE

$c_i$	concentration of a reactant, where $i = A, B,$ or $P$
$D$	diameter of the housing for a continuous flow mixer
$D_f$	diffusion coefficient
$l$	length of an infinitesimal vector at a later time
$l_0$	initial length of an infinitesimal vector representing a fluid filament
$l_x$	x component of the stretching vector $l$ having initial length of $l_{x0}$
$l_y$	y component of the stretching vector $l$ having initial length of $l_{y0}$
$L$	length of a static mixer element
$L/D$	element length-to diameter ratio, defined as the aspect ratio
$n$	integer representing the periodicity of the flow
$N_\rho$	total number of cells the flow region is divided into
$N_P$	number of fluid tracer particles in a flow
$N_s$	number of fluid striations in a selected region of a flow
$Pe$	dimensionless Péclet number
$r$	local rate of a chemical reaction
$Re$	Reynolds number
$s$	thickness of a fluid striation
$\langle s \rangle$	arithmetic average of the striation thickness, $s$
$t$	time
$t_n$	time after $n$ flow periods
$T$	period of a periodic chaotic flow
$\underline{v}$	velocity field created by a fluid flow
$\langle \underline{v} \rangle$	mean velocity in the main flow direction
$V_x$	x-component of a velocity field
$V_y$	y-component of a velocity field
$w$	scaled variable defined as $w = (\log c_P - \langle \log c_P \rangle) / \sigma_{\log c_P}$
$\underline{X}$	position vector of a fluid tracer particle, equal to $(x, y)$
$x$	x-position of a fluid tracer particle
$y$	y-position of a fluid tracer particle
$x_n$	x-position of a fluid tracer particle after $n$ flow periods
$y_n$	y-position of a fluid tracer particle after $n$ flow periods

### Greek Symbols

$\alpha_n$	enclosed angle between two vector components at time $n$
$\Theta$	topological entropy of a chaotic flow
$\lambda$	ratio of $l/l_0$ is defined as the stretching of a fluid filament
$\Lambda$	Lyapunov exponent of a chaotic flow
$\mu_F$	fluid viscosity
$\rho$	intermaterial area density created by a fluid flow
$\langle \rho \rangle$	average intermaterial area density
$\rho_F$	fluid density
$\sigma_{\log C_P}$	standard deviation of $\log c_P$
$\varphi$	variable defined as the difference of the reactant concentrations, $c_A - c_B$

### REFERENCES

- Alvarez, M. M., F. J. Muzzio, S. Cerbelli, and A. Adrover (1997). Self-similar spatiotemporal structure of material filaments in chaotic flows, *Fractals Eng.*, **1**, 323–335.
- Amanullah, A., L. Serrano-Carreón, B. Castro, E. Galindo, and A. W. Nienow (1998). The influence of impeller type in pilot scale Xanthan fermentations, *Biotech. & Bioeng.*, **57**(1), 95–108.
- Aref, H. (1984). Stirring by chaotic advection, *J. Fluid Mech.*, **143**, 1–21.
- Arnold, V. I. (1963). Small denominators and problems of stability in classical and celestial mechanics, *Russ. Math Surv.*, **18**(6), 85–191.
- Avalosse, Th., and M. J. Crochet (1997). Finite-element simulation of mixing: 2. Three-dimensional flow through a kenics mixer, *AIChE J.*, **43**(3), 588–597.
- Cerbelli, S. (2000). *The topology of chaotic two-dimensional systems*, Ph.D. dissertation, Graduate School of New Brunswick, Rutgers University, New Brunswick, NJ.
- Chaiken, J., R. Chevray, M. Tabor, and Q. M. Tan (1986). Experimental study of Lagrangian turbulence in Stokes flow, *Proc. R. Soc. London*, **A408**, 165–174.
- Chien, W. L., H. Rising, and J. M. Ottino (1986). Laminar mixing and chaotic mixing in several cavity flows, *J. Fluid Mech.*, **170**, 355–377.
- Dong, L., S. T. Johansen, and T. A. Engh (1994). Flow induced by an impeller in an unbaffled tank: I. Experimental, *Chem. Eng. Sci.*, **49**(4), 549–560.
- Franjione, J. G., and J. M. Ottino (1987). Feasibility of numerical tracking of material lines and surfaces in chaotic flows, *Phys. Fluids*, **30**, 3641–3643.
- Giona, M., S. Cerbelli, F. J. Muzzio, and A. Adrover (1998). Non-uniform stationary measure properties of chaotic area-preserving dynamical systems, *Physica A*, **254**, 451–465.
- Giona, M., A. Adrover, F. J. Muzzio, S. Cerbelli, and M. M. Alvarez (1999). The geometry of mixing in time-periodic chaotic flows: I. Asymptotic directionality in physically realizable flows and global invariant properties, *Physica D*, **132**, 298–324.
- Giona, M., S. Cerbelli, and A. Adrover (2002). Geometry of reaction interfaces in chaotic flows, *Phys. Rev. Lett.*, **88**(2), 024501-01.
- Gollub, J. P., and M. C. Cross (2000). Chaos in space and time, *Nature*, **404**, 710–711.

- Hobbs, D. M., and F. J. Muzzio (1998). Optimization of a static mixer using dynamical systems techniques, *Chem. Eng. Sci.*, **53**(18), 3199–3213.
- Hobbs, D. M., M. M. Alvarez, and F. J. Muzzio (1997). Mixing in globally chaotic flows: a self-similar process, *Fractals*, **5**(3).
- Jaffer, S. A., and E. P. Wood (1998). Quantification of laminar mixing in the Kenics static mixer: an experimental study, *Can. J. Chem. Eng.*, **76**, June, pp. 516–521.
- Kim, S. J., and T. H. Kwon (1996). Enhancement of mixing performance of single-screw extrusion process via chaotic flows: II. Numerical study, *Adv. Polym. Technol.*, **15**(1), 55–69.
- Kolmogorov, A. N. (1954). On conservation of conditionally periodic motions under small perturbations of the Hamiltonian, *Dokl. Akad. Nauk. SSSR*, **98**, 527–530.
- Kusch, H. A., and J. M. Ottino (1992). Experiments on mixing in continuous chaotic flows, *J. Fluid Mech.*, **236**, 319–348.
- Lamberto, D. J., F. J. Muzzio, and P. D. Swanson (1996). Using time-dependent rpm to enhance mixing in stirred vessels, *Chem. Eng. Sci.*, **51**(5), 733–741.
- Leong, C. W., and J. M. Ottino (1989). Experiments on mixing due to chaotic advection in a cavity, *J. Fluid Mech.*, **209**, 463–499.
- Ling, F. H., and X. Zhang (1995). A numerical study on mixing in the Kenics static mixer, *Chem. Eng. Commun.*, **136**, 119–141.
- Mandelbrot, B. (1982). *The Fractal Geometry of Nature*, W.H. Freeman, San Francisco.
- Metcalfe, G., and J. M. Ottino (1994). Autocatalytic processes in mixing flows, *Phys. Rev. Lett.*, **72**(18), 2875–2878.
- Middlemann, S. (1977). Mixing, in *Fundamentals of Polymer Processing*, McGraw-Hill, New York.
- Moser, J. (1962). On invariant curves of area-preserving mappings of an annulus, *Nachr. Akad. Wiss. Gottingen Math. Phys. Kl.*, **II**, 1–20.
- Muhr, H., R. David, J. Villermaux, and P. H. Jezequel (1995). Crystallization and precipitation engineering—V. Simulation of the precipitation of silver bromide octahedral crystals in a double jet semi-batch reactor, *Chem. Eng. Sci.*, **50**(2), 345–355.
- Muzzio, F. J., and M. Liu (1996). Chemical reactions in chaotic flows, *Chem. Eng. J.*, **64**, 117–127.
- Muzzio, F. J., and J. M. Ottino (1988). Coagulation in chaotic flows, *Phys. Rev. A*, **38**, Sept., pp. 2516–2524.
- Muzzio, F. J., and J. M. Ottino (1989). Dynamics of a lamellar system with diffusion and reaction: scaling analysis and global kinetics, *Phys. Rev. A*, **40**(12), 7182–7192.
- Muzzio, F. J., and J. M. Ottino (1990). Diffusion and reaction in a lamellar system: self-similarity with finite rates of reaction, *Phys. Rev. A*, **42**(10), 5873–5884.
- Muzzio, F. J., and P. D. Swanson (1991). The statistics of stretching and stirring in chaotic flows, *Phys. Fluids A*, **3**(5), 822–834.
- Muzzio, F. J., M. Tjahjadi, and J. M. Ottino (1991). Self-similar drop size distributions produced by breakup in chaotic flows, *Phys. Rev. Lett.*, **67**(1), 54–57.
- Muzzio, F. J., M. M. Alvarez, S. Cerbelli, M. Giona, and A. Adrover (2000). The inter-material area density generated by time- and spatially periodic 2D chaotic flows, *Chem. Eng. Sci.*, **55**, 1497–1508.
- Neufeld, Z. (2001). Excitable media in a chaotic flow, *Phys. Rev. Lett.*, **87**(10), 108301-1.

- Oseledek, V. I. (1968). A multiplicative ergodic theorem: characteristic Lyapunov exponents of dynamical systems, *Trudy Mosk. Mat. (Obsc.)*, **19**, 179–210.
- Pahl, M. H., and E. Muschelknautz (1982). Static mixers and their applications, *Int. Chem. Eng.*, **22**(2), 197–205.
- Sokolov, I. M., and A. Blumen (1991). Diffusion-controlled reactions in lamellar systems, *Phys. Rev. A*, **43**(6), 2714–2719.
- Souvaliotis, A., S. C. Jana, and J. M. Ottino (1995). Potentialities and limitations of mixing simulations, *AIChE J.*, **41**(7), 1605–1621.
- Swanson, P. D., and J. M. Ottino (1990). A comparative computational and experimental study of chaotic mixing of viscous fluids, *J. Fluid Mech.*, **213**, 227–249.
- Szalai, E. S., and F. J. Muzzio (2002). A fundamental approach to the design and optimization of static mixers, submitted for publication in *AIChE J.*
- Szalai, E. S., J. Kukura, P. Arratia, and F. J. Muzzio (2002). The effect of hydrodynamics on reactive mixing applications, submitted for publication in *AIChE J.*
- Szalai, E. S., and F. J. Muzzio (2003). A fundamental approach to the design and optimization of static mixers, to appear in *AIChE J.*
- Szalai, E. S., and F. J. Muzzio (2003). Predicting mixing microstructure in three dimensional systems, to appear in *Phys. Fluids*.
- Szalai, E. S., J. Kukura, P. Arratia, and F. J. Muzzio (2003). Effect of hydrodynamics on reactive mixing in laminar flows, *AIChE J.*, **49**(1), 168–179.
- Unger, D. R., and F. J. Muzzio (1998). Experimental and numerical characterization of viscous flow in an impinging jet contactor, *Can. J. Chem. Eng.*, **76**(6), 546–555.
- Zalc, J. M., and F. J. Muzzio (1999). Parallel-competitive reactions in a two-dimensional chaotic flow, *Chem. Eng. Sci.*, **54**, 1053–1069.
- Zalc, J. M., M. M. Alvarez, B. E. Arik, and F. J. Muzzio (2001). Extensive validation of computed laminar flow in a stirred tank with three Rushton turbines, *AIChE J.*, **47**(10), 2144–2154.

# Experimental Methods

DAVID A. R. BROWN, PIP N. JONES, and JOHN C. MIDDLETON

*BHR Group Ltd*

GEORGE PAPADOPOULOS

*Dantec Dynamics, Inc.*

ENGIN B. ARIK\*

*VioSense Corporation*

## Part A: Measuring Tools and Techniques for Mixing and Flow Visualization Studies

*David A. R. Brown, Pip N. Jones, and John C. Middleton*

### 4-1 INTRODUCTION

The aim of this chapter is to provide information on some of the tools and techniques available to make qualitative and quantitative measurements of mixing processes. The list of techniques discussed here is not exhaustive. A large number of experimental methods have been employed over the years to quantify mixing processes, and many of those have proved to be unreliable, or reliable only if performed under very specific conditions. Emphasis is placed on providing practical information on techniques that are both reliable and repeatable.

The equipment, instrumentation, and protocols required to perform the various techniques are discussed, with emphasis on the potential errors, inaccuracies, inconsistencies, and limitations of the techniques, as well as any expected

\* Formerly with Dantec Dynamics, Inc.

---

*Handbook of Industrial Mixing: Science and Practice*, Edited by Edward L. Paul, Victor A. Atiemo-Obeng, and Suzanne M. Kresta  
ISBN 0-471-26919-0 Copyright © 2004 John Wiley & Sons, Inc.



deviations between laboratory models and industrial scale operation. Most of the techniques described in this chapter can be applied to stirred tank, jet, and in-line mixed systems with little modification.

#### 4-1.1 Preliminary Considerations

Before beginning any experimentation, a careful assessment should be made of the problem that is being investigated and of the situation in which measurements are to be made. This will help to prevent an inappropriate technique being used for the measurement, and in many cases will lead to a rapid choice of the most suitable experimental method.

Experimental techniques for measuring mixing can be broadly divided into two categories: those that are performed in a laboratory, and those measurements that are performed in actual process plant equipment. The instrumentation and techniques used in each type of measurement are often different, although they can be based on very similar principles.

In the laboratory, experiments are most often carried out on a small scale using transparent vessels or pipe-work. Real process fluids should be used where possible; simulant fluids may be used if the process fluids are difficult to work with. It is straightforward to change the vessel and process configurations in the laboratory, making it possible to investigate a wide range of parameters relatively quickly and easily. The instrumentation that is used will require careful setup and expert operation, but with such treatment will yield precise and accurate data.

Process plant measurements are constrained by the nature of the process plant being used. The vessels are usually much larger than those found in a mixing laboratory, access to the vessels is often difficult, and visual observations of the mixing process are usually very difficult. Making alterations to the plant is costly and time consuming, particularly as a frequent requirement is that production must not be interfered with. In most cases the actual process fluids must be used, which may be difficult or dangerous to handle. The instrumentation used must be extremely robust and must be able to tolerate possible mishandling under the plant conditions. Measurements may have to be made at elevated temperatures or pressures, further increasing the cost and difficulty. The penalty for this robustness is usually a greatly reduced accuracy of measurement.

As a general rule, any extensive investigative or process development work should be performed at the laboratory scale, where a large number of parameters can be investigated easily, leading to rapid process optimization. Scale-up should be investigated using several different sizes of vessel at the laboratory (and pilot) scale, before moving up to the full production plant scale. Experiments with process plant should be carried out very selectively, as confirmation of laboratory work, or to investigate problems with existing process plant.

Before embarking on any series of mixing experiments, it is essential that the relevant published literature be checked to ensure full awareness of the methods and findings of other workers, avoiding unnecessarily repetition of what can be time consuming and costly experiments.

## 4-2 MIXING LABORATORY

In this section we outline the main requirements and considerations in setting up a laboratory with which to perform mixing experiments. Mixing experiments have been performed in the laboratory for many years and a vast array of measurement techniques is available to us. A large proportion of the measurement techniques described have not improved in any fundamental way over the last 10 years. The main improvements have probably come in the following areas:

- Increased data transfer rates, allowing the capture of more data
- Increased data storage capacity
- Increased computer processing power, allowing faster (and sometimes online) signal processing

This means that although we can now generate huge volumes of data, we still need to make sure that we analyze them properly and develop sensible conclusions.

Some other more recent advances that have had a significant effect on the measurements we can make are:

- Digital (or electronic analogue) video imaging and recording, allowing easy visualization of experiments
- Lasers, allowing the use of techniques such as laser Doppler anemometry (LDA) and particle image velocimetry (PIV), described later in this chapter

### 4-2.1 Safety

Safety is of paramount importance in the mixing laboratory. All rigs produced should undergo a safety assessment before use, including (where deemed necessary) a full HAZOP study. The safety assessment should result in a full set of standard operating procedures for the rig, a copy of which should be distributed to all operators. These procedures should include clear instructions as to the rig emergency shutdown procedure. A copy of the procedure should be displayed prominently on the rig. All rigs that include a rotating agitator shaft should have appropriate guards and a prominently displayed emergency stop button.

It is essential that a “Tank Contents” label be attached to each mixing vessel (or indeed, in-line mixing rig), along with relevant Control of Substances Hazardous to Health (COSHH) sheets or Material Safety Data Sheets (MSDSs) for each material present. This ensures that anybody in the laboratory encountering a problem with a rig is aware of the materials present and appropriate safety precautions.

As with all laboratories, it is vital that cleanliness and tidiness be maintained. The mixing laboratory is often subject to spillages of various fluids and particulate

solids, all of which can lead to slip hazards. All mixing vessels and rigs should be placed in a bounding wall or dike to contain any spillage.

## 4-2.2 Fluids

It is often not practical to use actual process fluids in the mixing laboratory, as this can involve the use of expensive and obstructive safety precautions as well as inconvenient temperatures and pressures. To avoid these problems, suitable simulant fluids must be found that will behave in a manner representative of the process fluid in the laboratory mixer. It should be noted that the simulant fluid must have the correct rheological properties *for the scale at which the measurements are to be made*. This is not necessarily the same as simply having the same properties as the fluid in the process: for example, if it is non-Newtonian.

**4-2.2.1 Fluid Rheology<sup>1</sup>**. It is important to model the fluid rheology correctly, particularly when non-Newtonian rheologies are concerned. The rheological properties of liquids handled in industrial processes can often change during the course of the process.

*Definitions.* Considering a small element of a liquid undergoing steady motion between the wall of a stationary cylindrical vessel and that of a rotating coaxial cylinder (Figure 4-1), the stress tensor ( $\tau_{ij}$ ) can be defined by nine components:

$$\tau_{ij} = \begin{bmatrix} \tau_{xx} & \tau_{xy} & \tau_{xz} \\ \tau_{yx} & \tau_{yy} & \tau_{yz} \\ \tau_{zx} & \tau_{zy} & \tau_{zz} \end{bmatrix}$$

$\tau_{xy}$ ,  $\tau_{xz}$ ,  $\tau_{yz}$ ,  $\tau_{yx}$ ,  $\tau_{zx}$ , and  $\tau_{zy}$  are the shearing stresses, and for this configuration

$$\tau_{xz} = \tau_{zx} = 0, \tau_{yz} = \tau_{zy} = 0$$

Since the relative motion between the cylinders is in the x-direction,  $\tau_{xy} = \tau_{yx}$ .  $\tau_{xx}$ ,  $\tau_{yy}$ , and  $\tau_{zz}$  are the normal stresses.  $\tau_{yx}$ , the shear stress, varies in the y-direction and in most texts is denoted simply by  $\tau$ .

The flow curve of a fluid (Figure 4-2) is obtained by plotting the shear stress ( $\tau$ , Pa) as a function of the shear rate ( $\dot{\gamma}$ ,  $s^{-1}$ ; i.e., the change of shear strain per unit time). Shear stress is related to the shear rate by

$$\tau = \mu \dot{\gamma}$$

where  $\mu$  is the liquid viscosity (Pa · s).

<sup>1</sup> Thanks to Gül Özcan-Taşkin for permission to reproduce this section from her Ph.D. thesis (Özcan-Taşkin, 1993).

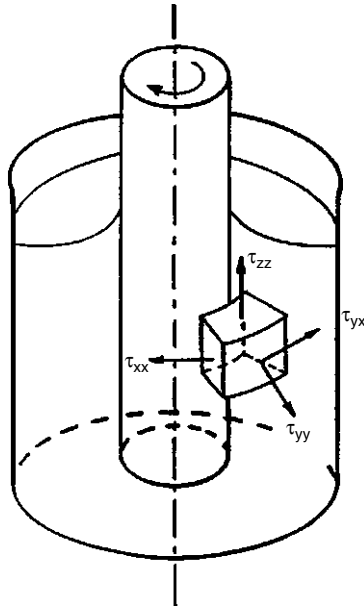


**Figure 4-1** Stress components around a rotating coaxial cylinder.

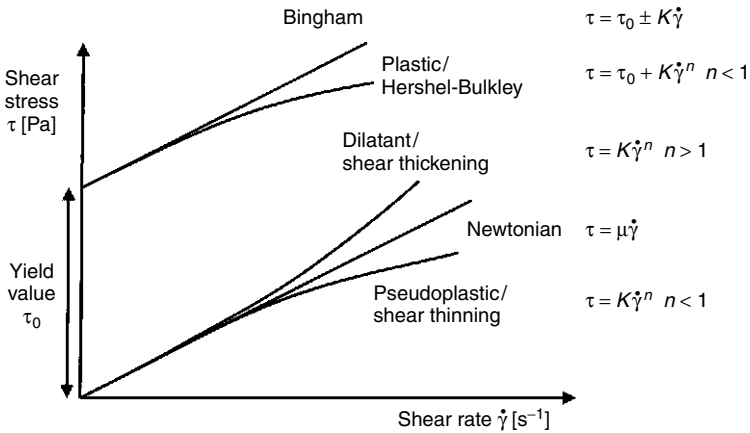


**Figure 4-2** Flow curves of Newtonian and non-Newtonian fluids.

**Newtonian Flow Behavior.** The viscosity of a Newtonian liquid depends only on temperature and pressure. At constant temperature and pressure, Newtonian behavior is characterized as follows (Barnes et al., 1989):

1. The shear stress is the only stress generated in simple shear flow.
2. The shear viscosity is independent of the shear rate.

3. The viscosity does not vary with the time of shearing and the stress in the liquid falls to zero immediately after the shearing is stopped. The viscosity from any subsequent shearing—regardless of the period of time between measurements—is as before.
4. The viscosities measured in different types of deformation (e.g., uniaxial extensional flow and simple shear flow) are always in simple proportion to one another.

Water, oil, glycerol, and sugar solutions are examples of Newtonian liquids. Dilute sludges such as unconcentrated activated and trickling-filter sludges also exhibit Newtonian behavior.

**Non-Newtonian Flow Behavior.** All liquids showing deviations from the behavior above are non-Newtonian. Many liquids encountered in industrial practice, such as paints, emulsions, most mineral slurries, latex, paper pulp, plastic melts, liquid foods, polymeric liquids, and concentrated wastewater sludge, are non-Newtonian.

Some examples of non-Newtonian flow behavior are shown in Figure 4-2. The viscosity of a non-Newtonian fluid is not a coefficient of the shear rate but a function of it and is called the *apparent viscosity* ( $\mu_a$ , Pa · s):

$$\mu_a = \frac{\tau}{\dot{\gamma}}$$

Non-Newtonian fluids can usefully be classified into three main categories (Skelland, 1967) even though sharp distinction between these groups is difficult:

1. *Time-independent fluids.* The shear stress at any point is dependent only on the instantaneous shear rate at that point.
2. *Time-dependent fluids.* The shear stress, and hence the viscosity, either decreases or increases with the duration of the shearing. These changes may be reversible or irreversible.
3. *Viscoelastic fluids.* These fluids have both elastic solid and viscous fluid characteristics. They exhibit partial elastic recovery after a deforming shear stress is removed.

Figure 4-2 shows typical flow curves of Newtonian and non-Newtonian fluids. Figure 4-3 illustrates shear viscosity as a function of shear rate for a pseudoplastic fluid, showing regions of low-shear limiting viscosity ( $\dot{\gamma}_0$ ), high-shear limiting viscosity ( $\dot{\gamma}_\infty$ ) and power law behavior.

**Time-Independent Fluids.** The majority of non-Newtonian fluids in this category are found to be pseudoplastic (Figures 4-2 and 4-3). The viscosity of pseudoplastic fluids decreases with the increase of shear rate over a large range of shear rates. Therefore, they are also called *shear-thinning liquids*. The characteristic of the

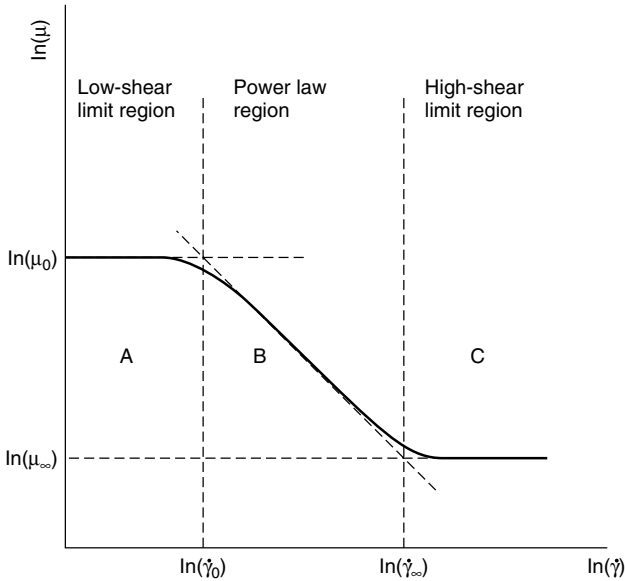


**Figure 4-3** Shear viscosity as a function of shear rate for a typical pseudoplastic fluid.

flow curve (Figure 4-3) is the linearity of the flow curve at very low and very high shear rates where the measured viscosity is constant ( $\mu_0$  and  $\mu_\infty$ ). Most industrial processes take place in the range of shear rates where the viscosity decreases with the shear rate. Therefore, the power law model of Oswald de Waele is widely used to characterize the shear-thinning behavior:

$$\tau = K\dot{\gamma}^n$$

where  $K$  ( $\text{kg/m}^{-1} \cdot \text{s}^{n-2}$ ) is the consistency index and  $n(-)$  is the flow behavior index. The deviation of  $n$  from unity is a measure of the departure from Newtonian behavior. For shear-thinning fluids,  $0 < n < 1$ . The expression for the apparent viscosity is then

$$\mu_a = K\dot{\gamma}^{n-1}$$

where the apparent viscosity is linearly proportional to the shear rate on a logarithmic scale (section B in Figure 4-3). Most polymer solutions exhibit pseudoplastic flow behavior.

For *dilatant fluids*,  $n > 1$ . Rheological dilatancy refers to increasing viscosity with increasing shear rate. Therefore, these fluids are also called *shear-thickening*. Examples include whipped cream and starch slurries. They are rare in industrial practice.

Pseudoplastic and dilatant fluids begin to flow as soon as a stress is applied. For *plastic fluids*, a yield value ( $\tau_y$ ) has to be exceeded before flow occurs (Figure 4-2). Two types of yield stress liquids are Bingham plastic and viscoplastic fluids

(Figure 4-2). Toothpaste, greases, certain mineral slurries such as ground limestone, tomato sauce, and wastewater sludge are some examples of plastic fluids. The Herschel–Bulkley model is used to characterize the behavior of these fluids:

$$\tau = \tau_y + K\dot{\gamma}^n$$

$$\mu = \frac{\tau_y + K\dot{\gamma}^n}{\dot{\gamma}}$$

where  $n = 1$  for Bingham plastics.

**Time-Dependent Fluid Properties.** This category includes thixotropic and rheopectic fluids. When a shear stress is applied to a thixotropic fluid, the viscosity decreases gradually, and when the stress is removed, a gradual recovery is observed. The opposite behavior is observed with rheopectic fluids: a gradual increase of viscosity during shear followed by recovery on the removal of shear-inducing stress.

**Viscoelastic Fluids.** These materials exhibit elastic and viscous properties simultaneously. Under simple shear flow, normal stresses are generated as shown in Figure 4-1. The magnitude of these normal forces varies with the shear rate. It is usual to work in terms of normal stress differences rather than normal stresses themselves:

$$N_1 = A\dot{\gamma}^b$$

where  $N_1$  (Pa) is the first normal stress difference. Polymer solutions exhibit viscoelastic behavior. While mixing viscoelastic fluids, forces generated normal to the plane of shear can lead to flow reversal and the Weissenberg effect where liquid climbs up a rotating shaft (see also Chapter 6).

**4-2.2.2 Simulant Fluids.** When choosing simulant fluids with which to perform experiments, the following must be taken into consideration:

- Is the fluid safe to use in a laboratory?
- Are the physical properties of the simulant fluid correct for the scale at which the experiments are being performed?
- Can the fluids be disposed of safely and economically at the laboratory scale?
- Can the fluid dissolve any ionic or surface active tracer materials?
- Is the fluid rheology sensitive to temperature?
- Will the fluid absorb moisture from the atmosphere?
- How long will the fluid last before decomposing?
- How expensive is the material?
- How must the material be disposed of?

Some common simulant materials are described below.

*Water.* Being cheap and readily available, water is an ideal simulant fluid for Newtonian mixing in the turbulent regime. Its density (and conductivity) can readily be modified by the addition of various salts, although care is required in the study of gas–liquid or liquid–liquid systems that the presence of dissolved salts does not alter the bubble or droplet coalescence properties of the system. Disposal of water is cheap, provided that the concentrations of any dissolved materials are within local discharge regulations.

*Glucose Syrup and Corn Syrup.* Undiluted glucose syrup is an extremely viscous transparent Newtonian material with a viscosity of about 150 Pa · s at room temperature. Corn syrup has similar properties and has a viscosity of about 18 Pa · s in undiluted form. At high viscosities both are extremely stable and will keep for a long period of time (months even). Once diluted with water (to about 1000 cP) biocide and fungicide should be added if solutions are to be kept for more than a day, as fermentation will take place, rendering the fluid unusable and producing an extremely unpleasant odor.

The extremely high viscosity and density of undiluted glucose make it quite difficult to perform the initial dilution required to make solutions of the required viscosity. The best method is to add the glucose slowly to a mixing vessel containing the required amount of water. Where this is not possible, mixing using a high-torque-rated mixer with lots of patience may be the only answer. Glucose affects the polarization of laser beams, so is not suitable for LDA measurements.

*Glycerol.* Glycerol is a viscous Newtonian fluid (99.9% glycerol is about 1.6 Pa · s at room temperature). It is extremely hygroscopic (it absorbs water from the atmosphere), so any free surfaces must be protected from the moist atmosphere to maintain the viscosity. Glycerol is even more transparent than glucose syrup and is good for transitional and laminar flow Newtonian LDA work.

*Silicone Oils.* Silicone oils (Dow Corning 200 fluids generally) are clear Newtonian fluids available in a wide range of viscosities. They are largely used in liquid–liquid dispersion experiments as the dispersed phase (in an aqueous bulk) as they have effectively no solubility in water or aqueous solutions. They are also largely inert and otherwise safe to use in the laboratory (the main danger being if some is spilled on the floor, as it is very difficult to remove and can be slippery). Care must be taken to ensure that any silicone oil purchased for the purpose of liquid–liquid dispersion experiments comes from a “pure” batch. Sometimes different viscosity grades are blended to produce the required final viscosity grade. Some workers have found that these blended oils do not produce consistent droplet size distribution results.

*CMC.* CMC (sodium carboxymethylcellulose) solutions need to be made up from the appropriate grade of powdered CMC. Although specialist equipment can be obtained to perform this mixing duty, a laboratory mixing vessel can also be used for this process. Care must be taken to feed the powder slowly,



with adequate mixing intensity to give reproducible properties and avoid the formation of lumps. Once all the powder has been incorporated, the impeller should be stopped to allow any air ingested to escape before the fluid viscosity has had time to increase. Once the air has escaped, mixing should resume at a lower impeller speed, avoiding air entrainment. It can take up to 12 h of mixing to ensure full hydration of the substance. Newtonian (short-chain) or shear-thinning (long-chain) grades of CMC are available.

CMC solutions are particularly useful for performing mixing experiments because they are inexpensive and the viscosity is relatively insensitive to small changes in temperature and dilution. Significant quantities of salt can be dissolved in a CMC solution without greatly affecting its rheological properties; however, CMC solutions do have a significant background conductivity which can make them unsuitable for experiments using conductivity probes (e.g., blend-time measurements). Once diluted, fungicides must be added; otherwise, the fluids quickly degrade into a foul-smelling fluid with a rheology close to that of water.

CMC solutions tend to be quite cloudy, making them unsuitable for some flow visualization experiments, and useless for LDA and PIV experiments.

*Carbopol.* Carbopol is provided as powder in a manner similar to CMC. It can be obtained in a large number of grades, some of which will produce yield stress fluids. The rheology of most Carbopol solutions is very sensitive to pH.

*Natrosol.* Natrosol is also obtained as powder. It can be obtained in various grades, most of which produce fluids that have shear thinning behavior.

*Versicol.* Versicol (which comes in liquid form) produces acidic solutions with viscosities up to  $5 \text{ Pa} \cdot \text{s}$ . It is little affected by temperature or slight dilution, but rapidly degenerates into an unpleasant-smelling liquid when dilute. Being acidic, it is highly conductive. Care should be taken in its use because its acidic nature means that it can dissolve mild steel and even concrete.

### 4-2.3 Scale of Operation

When a mixing experiment is designed to define a scale-up criterion, experiments should be performed at as large a range of scales as possible. The mechanisms controlling the mixing operation of interest at all scales can then be established with some confidence. It is of vital importance that the mixing system used at laboratory scale is a suitably accurate model of the large scale system. Dimensions must be rigorously scaled according to geometric similarity with the large scale system, even down to details like the thickness of metal sheet used to manufacture small scale impellers or static mixers. The power draw of such devices can be extremely sensitive to such details. The dimensions of baffles and vessel base shapes should also be subject to the same rigorous scaling.

In general, the guidelines in this chapter are applicable to vessels between about 0.2 and 2 m in diameter, although some techniques can be applied at much

larger scales. It is generally not recommended to perform stirred tank-based mixing experiments in a vessel where the diameter is less than about 0.3 m, as maintaining geometric similarity becomes increasingly difficult, as does the manufacture of probes (conductivity, video, etc.) small enough to make only insignificant changes to the flow patterns. Also, the size of drops, particles, or bubbles may become comparable with those of impellers or baffles if the scale is too small. Typical laboratory measurements of in-line systems are made in pipes with diameters between 15 and 100 mm, although measurements in larger systems are not unknown.

Traditionally, mixing experiments in the laboratory are performed at a smaller scale than in a full production system. With a modern process-intensified plant, however, and the increased manufacture of fine chemicals and pharmaceuticals in smaller batches, it is possible to perform laboratory experiments at scales equal to or larger than some production scale facilities.

Care must be taken when developing mixing strategies at a small scale, as it is very easy to use excessively high specific power inputs, which cannot be replicated economically in large scale production systems.

#### 4-2.4 Basic Instrumentation Considerations

In addition to the specialist mixing equipment described later in this section, the following common instruments are extremely useful for a variety of tasks in the mixing laboratory:

- Handheld optical tachometer used to calibrate and check the digital speed readout on most agitators.
- Averaging voltmeters used to measure signals from strain gauges, etc.
- Digital thermometers for monitoring temperature of fluids.
- Temperature-controlled water bath and recirculation system for temperature control of small vessels, usually recirculating the fluid in the surrounding viewing box.
- Digital (or other high-quality) video camera (and tripod) to record visualization experiments.
- Digital camera to photograph experiments.
- Distilled or deionized water supply to provide “clean” water of repeatable quality and low conductivity.
- Electronic balance accurate to 0.001 g for weighing of tracer materials, indicator solutions, density measurements, etc.
- Large balance for weighing large quantities of sand, etc.
- Sieves (and shaker) for crude sizing of solid particles and to help eliminate particular size ranges from a sample.
- *Rheometers*. No mixing laboratory should be without one or more reliable rheometers. There are a large number of different types of rheometer on the market, and one should be specified such that all the relevant rheological

properties can be identified and quantified. Care should be taken that rheology measurements can be and are made at shear rates appropriate to those that will be found in the mixing system being investigated. The instrument should also allow the sensitivity of fluid rheology to temperature (over the range to be experienced in the laboratory) to be investigated. Rheometers should be serviced and calibrated regularly.

#### 4-2.5 Materials of Construction

The materials of construction of the vessel or pipe and all internals (impeller or mixers, shaft, baffles, bearings, seals, and lid) must be compatible with the fluids and any solids that are to be mixed. For most mixing experiments the ability to see clearly what is happening inside the mixer is extremely useful, if not essential. Vessels or pipes made of a transparent material such as polymethylmethacrylate (PMMA; Perspex or Lucite) or glass are ideal, provided that measurements are to be made at temperatures and pressures within the modest limits allowed by such materials (the glue used to seal PMMA vessels tends to fail at about 50°C). PMMA vessels up to about 1 m in diameter can be manufactured relatively simply.

At larger scales, or in situations where elevated or reduced pressures or temperatures are required, the use of completely transparent mixing vessels is unlikely or impossible. For such situations metals such as steel or other metallic alloys or plastics such as polythene can be used. In these situations the addition of windows in the side of the vessel can be extremely useful.

#### 4-2.6 Lab Scale Mixing in Stirred Tanks

The design of mixing vessels to be used in performing experiments depends greatly on the scale of the vessel required. Small vessels can be of relatively simple construction, while larger vessels should undergo the same rigorous design process as production vessels. No matter what the scale of operation, the model should be of suitably accurate geometric scaling in all aspects that affect the mixing process vessel being investigated. When it is not clear if a particular design feature is significant, it is better to err on the side of caution and ensure full geometric similarity.

Small scale PMMA vessels up to about 400 mm can be manufactured by using the appropriate length of PMMA pipe to make the cylindrical section and attaching a base of PMMA that has been formed into the desired shape. Care should be taken to ensure that the base (whether it be flat or dished) is formed according to the relevant standards. A strengthening flange or lip should be added to the top rim of the vessel to increase rigidity.

Larger PMMA vessels (up to 1 m in diameter) are better manufactured in two or more sections (Figure 4-4). One or more cylindrical sections, flanged at the top and bottom to provide strength, can be bolted together to create vessels with a range of aspect ratios. Several base sections of different designs can then be

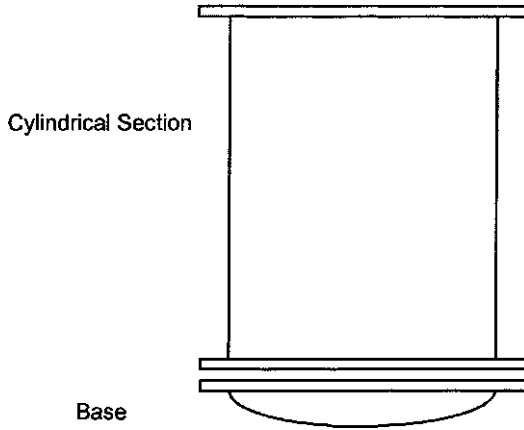


**Figure 4-4** PMMA mixing vessel made from a cylindrical section with a torrispherical base.

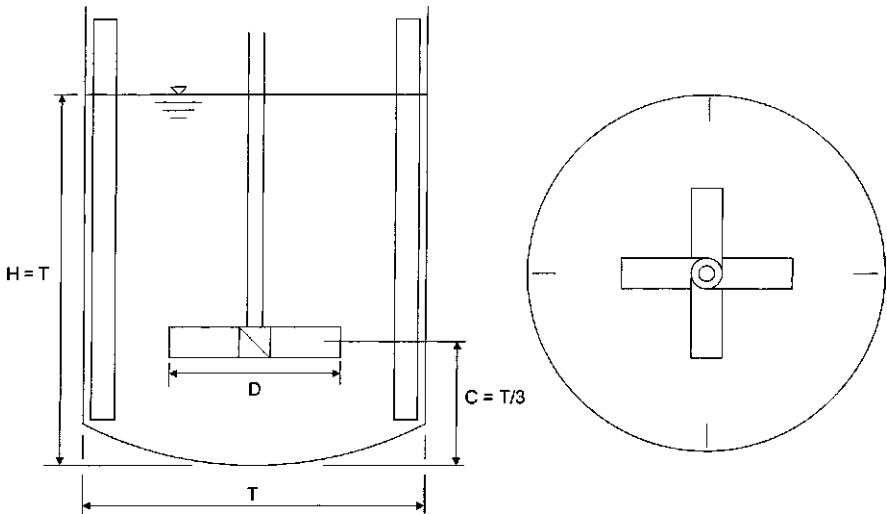


**Figure 4-5** Standard mixing vessel.

manufactured; all of which will fit to the cylindrical sections, allowing a large variety of different vessels to be produced. Double O-ring seals should be used between the flanges.

The standard mixing vessel (Figure 4-5) has a liquid fill depth equal to the tank diameter. To avoid splashing and to cope with a reasonable degree of gas hold-up, it is recommended that the vessel height be at least 30% greater than the fill depth. Laboratory mixers are usually designed without a tightly fitting

lid, as they tend not to be used with particularly hazardous or volatile chemicals. However, when splashing is a problem, a lid made from two sections that fit around the central shaft can be used.

Small to medium scale vessels (up to about 0.6 m in diameter) can be placed in a viewing box as illustrated in Figure 4-6*a*. This is a rectangular box, with walls usually made of PMMA or glass and filled with the same fluid as in the vessel. Viewing boxes are also useful, as the fluid surrounding the vessel can be used to maintain the vessel contents at a constant temperature, or alternatively, can be used to modify the temperature. It is not practical to place larger vessels inside full viewing boxes, but small viewing boxes can be attached to transparent vessels (Figure 4-6*b*) to aid visualization. Where mixing experiments are to include heat transfer, the same rigor should be applied to the design of the heating/cooling coils and/or jacket as to the other aspects of the design.

It may seem convenient to place an outlet and drain valve in the middle of the base of a vessel; however, caution should be applied, as this can significantly affect any solid suspension measurements, and viscous materials added to the vessel may collect in the drain pipe or nozzle. In general, it is better that the vessel contents are removed by pumping through a piece of flexible hose, as this reduces the number of bosses and fittings on the vessel.

Wherever possible, mixing vessels should be supported above the laboratory floor (or benchtop for small vessels), as this provides access for observations of the vessel base. In all situations, the vessel, drive, bounding box, and any other equipment should be mounted in a strong frame that provides support and prevents excessive vibration.

Mixer drives are usually electric, although air motors are used in the presence of hazardous fluids. DC motors with variable speed and belt drive are popular, and direct-drive stepper motors are also recommended. It is generally simplest

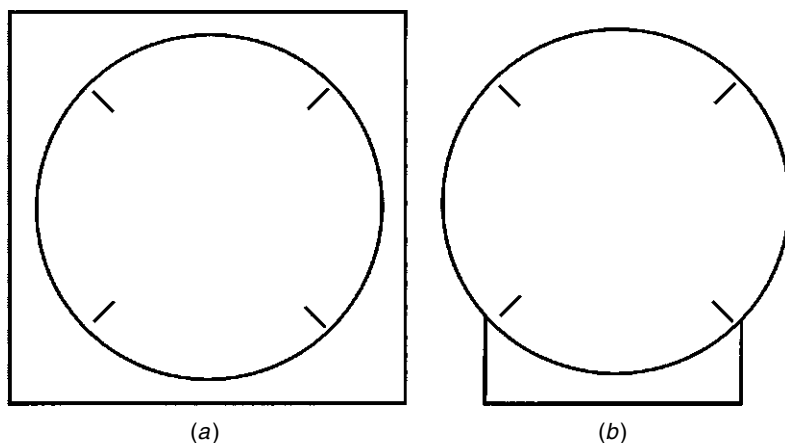


**Figure 4-6** Viewing boxes (*a*) and windows (*b*) to aid observations in transparent vessels.

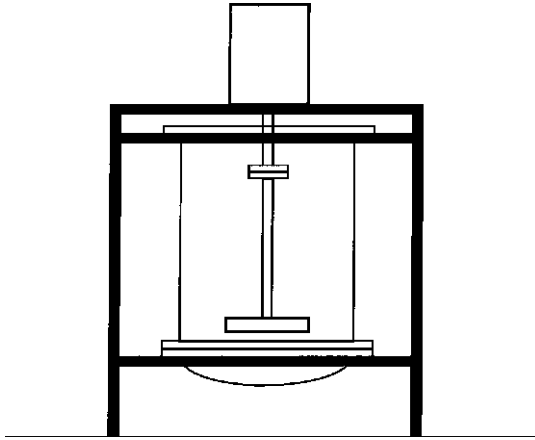


**Figure 4-7** Supported mixing vessel with overhung split shaft.

to have an overhead drive and gearbox in the mixing lab, which means that the shaft is supported from above. This saves dealing with awkward bottom-entry sealing problems and means that with a suitably split shaft (see Figure 4-7), the vessel or impeller can be removed easily.

Care should always be taken to check that the system is running at a speed lower than the first critical oscillation speed of the mixer shaft. The critical speed can be calculated or measured directly (see Chapter 21). In situations where operation close to the critical speed of the unsupported shaft is required, a bottom bearing must be used.

Impellers for use in mixing experiments should be rigorously geometrically scaled relative to the large scale impellers they mimic. Particular care should be made with the following aspects, which are often difficult to reproduce successfully at the small scale:

- *Hub diameter.* Shafts in small vessels tend to be oversized compared with large vessels; consequently, the hubs fitted to small impellers can be excessively large. This can sometimes be important, particularly when investigating the flow patterns generated by the impeller. However, due to the  $D^5$  term in the power draw expression, the effect on the impeller power number may not be significant.
- *Blade edges.* The straightness and sharpness of the blade edges in small impellers must be as good (to scale) as their large scale equivalents.

The correct type of baffles should always be used, again, geometrically scaled down from the full scale and including the correct gap between the baffles and the vessel wall. Baffles are essential to most turbulent and transitional mixing processes with the majority of impellers as they convert the tangential motion into axial motion. Experiments with no baffling should only be performed if this

is what is required at production scale, and with impeller systems specifically designed for use without baffles.

In later sections of this chapter we discuss in some detail the large number of types of probes that may be used to measure some quantity in a mixing vessel (or pipe). When mounting probes in a vessel, it is always desirable to place the probe in the correct position for the measurement while causing as little impact on the flow patterns in the vessel as possible. Consequently, the probe volume should be minimized as far as possible and care should be taken with the probe orientation and mounting supports to reduce disruption to the flow. Large probes designed for large vessels should not be squeezed into small vessels. In situations where measurement probes could cause significant interference with the flows, nonintrusive measurement techniques should be considered, although this may prove to be significantly more expensive. In situations where intrusion effects cannot be eliminated from scale-up experiments, probe size should be scaled geometrically with the vessel.

Probes can be mounted in vessels or pipes using a variety of methods. One common method is to insert the probes through bosses on the side of vessels, although this can, over time, lead to vessels that have so many patches on them that they are no longer transparent. Other good mounting techniques for probes are to attach them to baffles or to the rim of the vessel using rods and clamps. Extreme care must be taken when mounting probes in this way because once the impeller is rotating, the probe may be subject to quite extreme flow-induced vibrations. The various wires and fiber-optic cables commonly attached to probes should also be firmly held in place inside the vessel; otherwise, they may break or get tangled up in the impeller. When probes are mounted toward the base of a vessel but must be inserted into the tank from the top, it is wise to secure supporting rods and wires down behind a baffle, as this protects the probes while minimizing their effect on the flow.

In some situations it is possible to mount probes on the impeller or shaft itself. In these situations, the signal from the probe has to be transmitted either by radio-telemetry equipment or through slip rings on the shaft.

#### **4-2.7 Lab Scale Mixing in Pipelines**

Similar equipment and techniques can be employed for continuous flow experiments using in-line mixing systems. Again, PMMA is an ideal material for the construction of transparent test sections. Most measurements with in-line mixers require accurate measurements of pressure drop and flow rate. Calibrated gear pumps can be useful for small scale work.

Some other general considerations on in-line mixing experiments are:

- Leave enough straight pipe upstream of the measurement position to get fully developed flow if that is what is required for the experiment.
- Make sure that static mixer elements are manufactured correctly at small scale. Sometimes the wrong gauge of sheet or the wrong number of element layers can be used for small scale mixers.

- Often, small scale static mixers do not fit correctly into a circular pipe. Consideration must be made as to how significant this is for the mixing process being investigated.
- It is wise to use a size of static mixer for which manufacturer's friction factor data are available and to ensure confidence in any data of this type before using them in any further correlation. Whenever possible, the friction factor should be measured during the experiment.

### 4-3 POWER DRAW OR TORQUE MEASUREMENT

In a stirred tank mixing system, perhaps the most fundamental measurement one can make is that of the power draw of the system, as many scale-up rules depend heavily on the specific power input. The power draw,  $P$ , of an impeller is characterized by its power number,  $P_o$  (also denoted  $N_p$ ). The following expressions can be used to calculate the power draw of an impeller:

$$P = P_o \cdot \rho N^3 D^5 \quad (4-1)$$

$$P = 2\pi N T_q \quad (4-2)$$

where  $\rho$  is the density,  $N$  the impeller speed,  $D$  the impeller diameter, and  $T_q$  the torque.

All the energy supplied to the fluid by the agitation system must eventually be dissipated as heat, so one possible method of measuring the power draw is to insulate the system and measure the temperature rise over time. In practice, this is extremely difficult to do accurately, due to problems with the effectiveness of the insulation and with the fluid physical properties being a function of temperature. Consequently, the method is rarely used, and methods based on measuring the reaction torque of the system are preferred.

As eq. (4-2) shows, the power input,  $P$ , into the system can be calculated if the impeller speed,  $N$ , and torque,  $T_q$ , are known. If the impeller diameter,  $D$ , and fluid density,  $\rho$ , are also known, the power number,  $P_o$ , for an impeller can be calculated.

There are many methods available to measure the reaction torque. Some allow measurement of the individual torque contribution for each impeller (or any bearings, etc., in the system), while others can only be used to measure the entire system torque. Care should be taken with all methods to ensure that the true impeller torque can be isolated from any frictional torque loads applied by bearings and so on.

It should be remembered that some techniques are practical only over limited ranges of torque and hence scale or impeller speed. No matter what technique is used, extreme care must be taken to ensure that the torque measurement device is well calibrated over the range of torque values being measured, free of errors caused by friction, and compensated for any temperature effects. The calibration



should ideally be checked both before and after the experiments, as some techniques are remarkably sensitive.

### 4-3.1 Strain Gauges

Strain gauges mounted on the mixer shaft (see Figure 4-8) are a popular and reliable method of measuring torque. Generally, strain gauges are used in pairs, with the alignment of the gauges being extremely important in ensuring reliable readings. With careful design and choice of shaft material they can be used to measure a very wide range of strains. With multiple-impeller systems, or where the contribution from a bottom bearing needs to be removed, multiple sets of gauges can be used on the same shaft. Strain gauges generally produce extremely low voltage signals, which must be amplified before the signal can be logged and recorded either in a PC-based data logging system or using an averaging voltmeter. The amplifier must be mounted on the mixer shaft above the water level, with the amplified signal passed to the recording device through either slip rings or a radio-telemetry system.

Extremely careful calibration of the strain gauges is required. Known torques must be applied to the shaft and the response measured. Note that no bending loads should be applied during calibration. If a single strain gauge is to be mounted on the shaft, it should be placed toward the top of the shaft where it will not be submerged and above where any impellers are to be mounted. Where

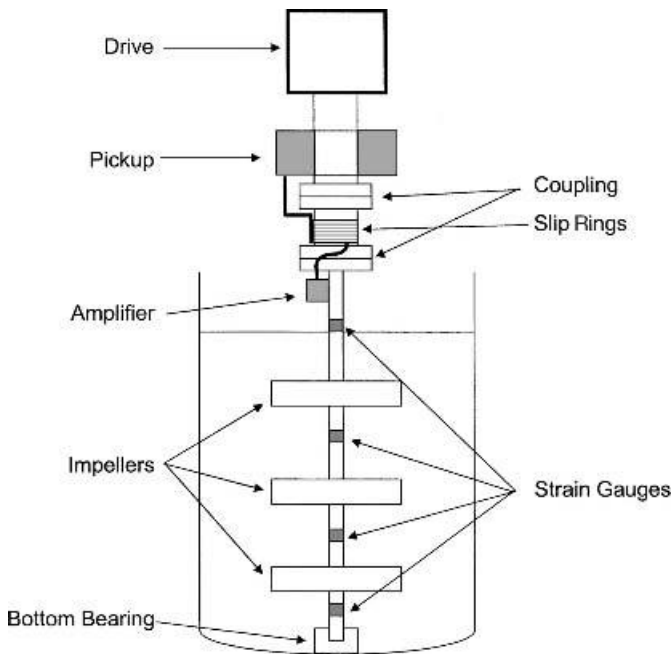


**Figure 4-8** Torque measurement using strain gauges and slip rings.

multiple strain gauges are to be mounted on the shaft, allowing the measurement of torque contributions from individual impellers and bearings, the gauges should be placed in positions that allow reasonable flexibility for impeller position (Figure 4-8).

The gauges are usually placed in turned-down sections of the shaft (which also increases sensitivity), and the connecting wires are best run along a keyway in the shaft or down the centre of a hollow shaft. If very small torques are to be measured, the gauges can be fitted to a special hollow plastic section of the shaft, which will deform more than a steel section, giving greater sensitivity. Gauges of this type are extremely delicate and must be handled and calibrated with extreme care.

Great care must be taken in the waterproofing of any gauges fitted to the shaft. The waterproofing usually consists of several layers of heat-treated wax and adhesive built-up until the surface of the shaft is smooth. Great care should be taken when using a strain-gauged shaft to ensure that the waterproof seal is not ruptured: for example, when the shaft is being removed from or positioned in the tank, or when the impellers are being moved.

Torque transducer units are available that contain strain-gauged sections of shaft that can be fitted in line with the mixer shaft. They must be suitably isolated from any bending moments and axial loads (Figure 4-9). They are generally subject to the same calibration and care during use precautions as are sensitive strain gauges (Chapple et al., 2002).

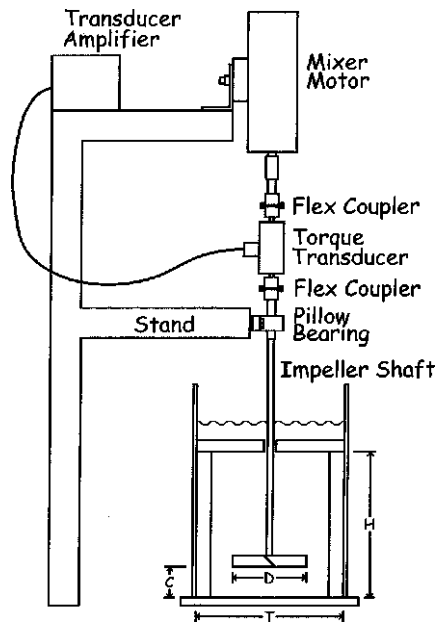


**Figure 4-9** Torque transducer. (From Chapple et al., 2002).

### 4-3.2 Air Bearing with Load Cell

An air bearing can be used to support either the mixing vessel or the motor, allowing rotation without friction. In either case only the total torque can be measured, by a suitably mounted load cell (Figure 4-10). Particular care must be taken when using an air bearing measurement with impellers of small D/T ratio, as the inertia of the tank or motor can become more significant. Air bearings can only be used in practice on vessels up to about 0.6 m (2 ft) diameter. Again, averaging of the signal from the load cell is required.

### 4-3.3 Shaft Power Measurement Using a Modified Rheometer

Some rheometers can be modified to provide accurate torque readings as they are designed to measure shear stresses at known shear rates. This can be a very good method to use in small scale vessels.

### 4-3.4 Measurement of Motor Power

Measurements of the electrical power consumed by the motor can be used to estimate the power delivered to the fluid, provided that the efficiency curves for the motor are known, along with knowledge of the losses in the gearbox and any bearings. In most situations the accuracy of the information on the efficiency and various losses is so poor that this technique is not recommended, particularly at small scale, where the losses tend to be greater than the power delivered to the fluid. Some mixer manufacturers sell small bench scale mixers that have digital torque readout. These almost always use this method and are generally very unreliable—certainly unsuitable for any scientific investigation.

## 4-4 SINGLE-PHASE BLENDING

The main aim of measurements of the single-phase mixing behavior in a stirred tank is to obtain a mixing time for the system under investigation. The mixing

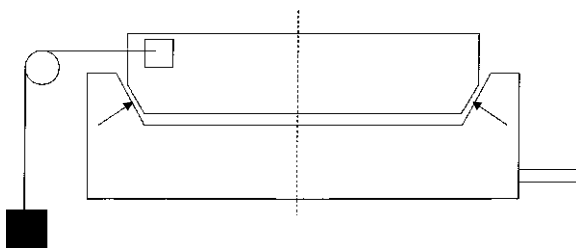


**Figure 4-10** Air bearing used to measure reaction torque.

time is the time taken for a volume of fluid added to a fluid in mixing vessel to blend throughout the rest of the mixing vessel to a pre-chosen degree of uniformity (see Chapter 9 for additional information on mixing time or blend time). Knowledge of the mixing time from experiments, from extrapolation from small scale tests, or from correlations provides confidence that:

- Any sample of product drawn from the vessel will have known chemical concentrations.
- An added species will become well distributed within a certain length of time.
- Any thermal gradients due to chemical reaction or differences in bulk and feed temperatures will be eliminated.
- All regions of the mixing vessel are moving and mixing with all other regions.
- Measurement of the bulk temperature or the concentration of a chemical species is representative of the entire vessel contents.

In an in-line mixing system, one is usually interested in quantifying how well mixed the fluids are at a particular location, or in a manner similar to the batch mixing time, how many mixer elements are required to achieve a given degree of mixedness.

#### 4-4.1 Flow Visualization

Before making measurements of the mixing time for a given process, it is necessary to perform a number of flow visualization studies. These tests are designed not only to help decide how the mixing time should be measured, but also to provide information on flow and to highlight regions of poor fluid motion and flow compartmentalization within the mixing system. The techniques described below are discussed with respect to stirred tank systems; however, it should be made clear that all the techniques can be applied to in-line mixing systems with only a little modification.

The flow patterns of single-phase liquids in tanks agitated by various types of impellers have been widely reported in the literature. The simplest (and cheapest) technique for examining flow patterns within a mixing system is light sheet visualization (Figure 4-11). A narrow light sheet is shone through the mixing vessel, illuminating reflective tracer particles in the bulk fluid. Streak photography or, more commonly, video images of the reflections from the particles show the bulk flow patterns within the stirred tank. The technique can be used in any transparent laboratory mixing vessel, and the light sheet can be either vertical, to provide axial and radial flow information, or horizontal, with a video camera pointing through the bottom of the mixing vessel to provide radial and tangential flow information. Semiquantitative velocity component data can be obtained if the shutter speed or strobe duration is known by measuring the streak lengths. Further refinements to this technique include the use of a laser with a rod prism

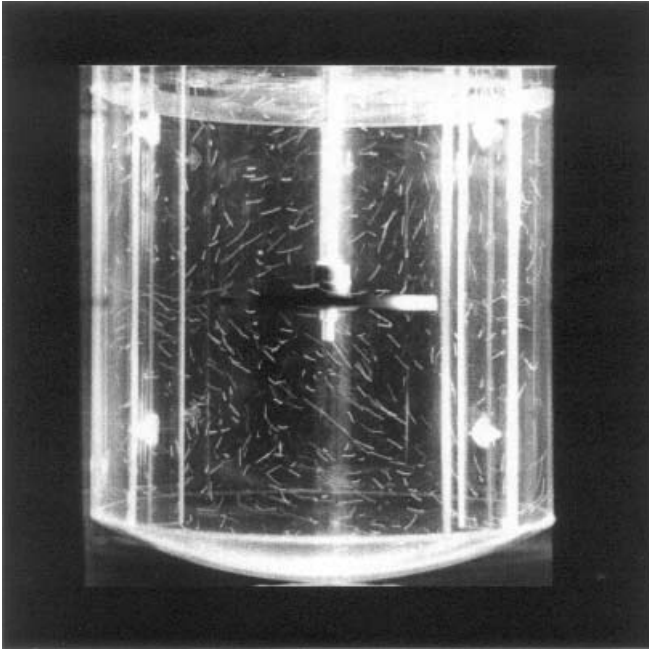


**Figure 4-11** Flow visualization using streak photography.

to give a more intense and uniform light source, and using a polarizing filter to reduce glare from the vessel itself. It is important to minimize the amount of light from other sources within the laboratory to obtain the best possible images.

Video images from this technique have been used to show fluctuations in the discharge angle of impellers, the degree of flow compartmentalization and impeller interaction in multiple impeller systems, and to show the cavern size when mixing yield stress or highly shear thinning liquids.

Other techniques can provide information on local fluid velocities across the whole or parts of the vessel (e.g., PIV) or can measure fluid velocities at a single point with a high degree of accuracy (e.g., LDA/LDV or hot-wire anemometry). These techniques are discussed in Part B of this chapter. It should be stressed, however, that a simple light source and a video camera are substantially cheaper than these other techniques and can often be used as the first step in examining a mixing configuration. It is always useful to look at the flow field as a complement and guide to the use of more quantitative and expensive techniques.

For examination of mixing behavior, light sheet visualization is important, particularly in multiple-impeller systems, to help the experimentalist think about suitable points of addition to study a mixing system, possible choice of feed location, and an initial estimate of suitable probe locations for mixing time experiments. Further tests should be performed to provide more detailed information on suitable choices of probe location.

#### 4-4.2 Selection of Probe Location

Mixing time techniques all work on the principle of adding material to the vessel which has different properties from the bulk. Measurements are then made (usually in a controlled volume within the vessel) that show the presence of the added material. The decay of material property fluctuations is used to measure the mixing time for the system. Many of the devices used for measurement of the added liquid are intrusive, and the experimenter must try to minimize the number of probes installed in the vessel in order to:

- Minimize the perturbation of the bulk flows by the probes and the probe supports.
- Reduce the amount of associated hardware required.
- Minimize the amount of data that need to be collected, stored, and processed.

However, it is important that the probes in the vessel be in the correct positions to provide as much relevant mixing information as possible. There will be certain points in the mixing vessel that will be less intensely agitated and where mixing rates are lower than in the bulk of the tank. These points will be the last points to become mixed and will control and limit the mixing rate for the entire mixing vessel. So if probes are used, one or more should be positioned in these poorly mixed regions to obtain the correct mixing time. Other probe locations should be chosen to indicate whether the bulk of the tank is well mixed. Extra probes could be distributed axially to provide information on flow compartmentalization, particularly in multiple-impeller systems.

#### 4-4.3 Approximate Mixing Time Measurement with Colorimetric Methods

The simplest test of the rate of mixing of the bulk would be to add a dye and see how the dye moves throughout the fluid (Figure 4-13*a*). However, if a colored tracer is added to an agitated vessel, it is not possible to identify the last point of mixing because any dye in front of or behind the poorly mixed region will mask the last mixed pocket (Figure 4-12*a*). What is required is a decolorization technique where the last point to be mixed remains colored or marked while the rest of the tank is stripped of its color.

The technique most commonly used is known as (dye) decolorization. The entire contents of the vessel are colored using one chemical, and then a second chemical is added that removes the color. A poorly mixed region stands out as a pocket of color after the rest of the vessel has cleared (Figure 4-12*b*).

Two of the most common reactions used are pH change with an appropriate indicator (Figure 4-13), and an iodine–iodide change in the presence of starch. The experimenter should check for chemical compatibility when choosing an appropriate decolorization technique. It may be necessary to use a simulant fluid rather than the actual bulk chemical.

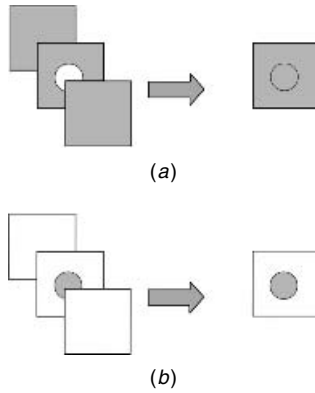


**Figure 4-12** Schematic representation of dye addition and dye decolorization for mixing visualization in three dimensions. (a) A poorly mixed pocket is uncolored, and cannot be seen in two dimensions. (b) A poorly mixed pocket is colored, and can clearly be seen in two dimensions.

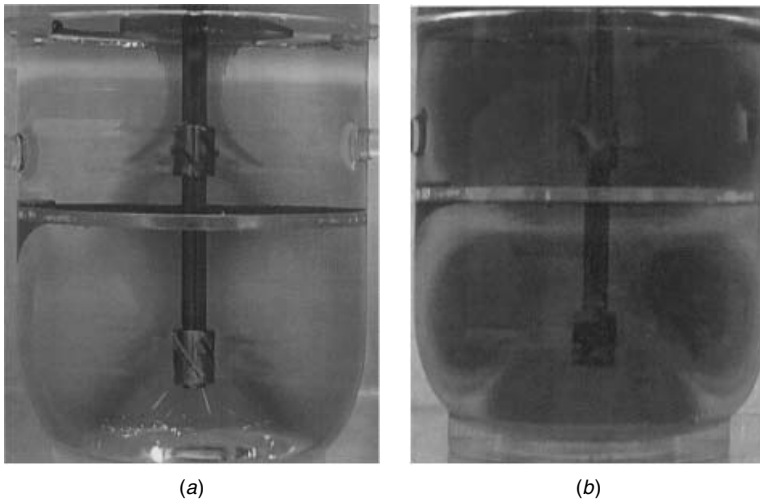


**Figure 4-13** Red dye tracer addition (a) and acid–base decolorization using bromophenol blue (b). (From Clark and Özcan-Taşkin, 2001.) See insert for a color representation of this figure; for a video clip, see the Visual Mixing CD affixed to the back cover of the book.

**4-4.3.1 Acid–Base with Indicator.** An indicator such as bromophenol blue (blue to yellow, Figure 4-13b) or phenolphthalein (pink to colorless) is added to the bulk liquid. Small additions of acid and base can be used to color the entire mixing vessel and then strip out the color. A small excess of the acid–base used for the color change is typically used. The last point to remain colored is easily observed and selected as a suitable probe position. For standard geometries, the

last point of mixing in the transitional regime is generally behind the baffles, where the fluid is protected from the bulk flows by the baffle itself.

Strong acids should always be used to avoid any buffering effects in the presence of salts from the neutralized acids and bases. With this technique, the bulk liquid can be reused repeatedly by re-adding more of the initial reactant.

**4-4.3.2 Iodine–Thiosulfate.** The reaction between sodium thiosulfate and iodine in the presence of starch is a most satisfactory decolorization reaction, with a strong color change from deep blue to clear.

#### *Preparation of Chemicals Required*

- *2 M iodine.* Dissolve 400 g of iodate-free potassium iodide in 0.5 L of distilled water in a 1 L volumetric flask. Add 254 g iodine to the flask and agitate until all the iodine has dissolved. Cool to room temperature, and make up to 1 L. Store in a dark place to prevent deterioration.
- *1 M sodium thiosulfate.* Weigh 248 g of sodium thiosulfate pentahydrate into a 1 L volumetric flask and make up to 1 L with distilled water. Add a small quantity of sodium carbonate (about 0.2 g) to aid preservation.
- *Starch indicator.* Manufacture a paste containing 10 g of soluble starch in a little water. Add this dropwise to a beaker containing 1 L of very hot (but not quite boiling) water while stirring constantly until a clear liquid is obtained. Cool the liquid to ambient temperature and dissolve it in 20 g of potassium iodide. This solution should be protected from the air.

#### *Procedure for Use*

1. Add about 50 mL of starch indicator to the vessel.
2. Add sufficient iodine solution to the vessel to produce an intense black color. Note the quantity used.
3. With the agitator running at the desired speed, quickly incorporate sodium thiosulfate into the vessel at a rate approximately 2.5 times the quantity of iodine solution used. As mixing progresses, the liquid will clarify.
4. After each test, slowly add iodine solution until the neutral point is again reached, demonstrated by a hint of light blue appearing. The test can then be repeated.

It should be noted that this technique must be used with care with solutions of CMC, which have a tendency to decolorize iodine solutions over time, albeit slowly.

#### **4-4.4 Quantitative Measurement of the Mixing Time**

After performing the decolorization technique to provide qualitative understanding of the mixing behavior, the method of mixing time measurement must be



selected. All mixing time techniques are based on addition of a chemical with a different property to the bulk, followed by measurement of the system to infer the presence and uniformity of this marked liquid.

**4-4.4.1 Off-line Sampling.** If an off-line analysis technique is used, a chemical marker such as a particular salt, dye, or acid is added to the mixing vessel, and samples are removed regularly. The concentration of the marker in each sample is measured, and the degree of uniformity is inferred from these measurements. Installation of a suitable sampling system can be difficult, and this technique is not suitable if the mixing time is very short, since there will generally be a finite sampling time.

**4-4.4.2 Schlieren Effect-Based Mixing Measurements.** The Schlieren-based technique relies on the light scattering that occurs when two liquids with different refractive indices are mixed. Light shone through the mixing vessel is scattered by the layers of different liquids and the tank appears cloudy. When the liquid is fully blended, the tank becomes clear once more, giving a mixing time (Van de Vusse, 1955). This technique does, however, require transparent bulk and added liquids, and the liquids must have different refractive indices. The liquids are also, therefore, likely to have different physical properties.

**4-4.4.3 Thermocouple-Based Mixing Time Measurements.** A thermocouple-based mixing time test can be performed by adding a liquid that has a different temperature from the bulk. The temperature at different points in the mixing vessel is monitored over time, and the probe outputs are used to calculate the mixing time. This technique can be used with opaque and/or nonconducting liquids. A disadvantage of this technique is that it may not be suitable if the bulk liquid physical properties are very sensitive to changes in temperature, since the viscosity would then be a function of the temperature (and concentration) of the added liquid.

**4-4.4.4 Conductivity Probe Technique.** The conductivity probe mixing time technique uses an electrolyte in the added liquid as the marker. Conductivity probes monitor the local conductivity as a function of time. If the electrolyte concentration is low, concentration is directly proportional to conductivity. The probe outputs are processed to calculate the mixing time for the system under consideration. This technique is not suitable for measurements in nonconducting systems and cannot be used in systems where the rheological properties of the bulk are sensitive to changes in salt concentration: for example, with certain gums and carrageenans. The technique is, however, cheap and easy to use. Conductivity probes can give very rapid response times, allowing measurements in mixing systems with short mixing times. Further details on probe designs suitable for conductivity-based mixing time measurements are available in Khang and Fitzgerald (1975). The probe itself is made by embedding pieces of platinum

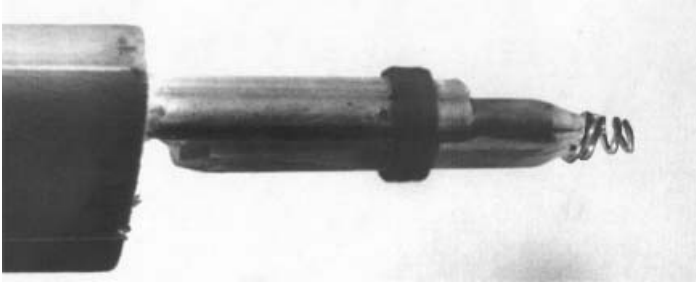


**Figure 4-14** Liquid-phase conductivity probe.

or stainless steel wire, soldered onto the screened signal lead, in a “bullet” of epoxy resin. The diameter of the bullet is approximately 6 mm (Figure 4-14).

All probes have the outer electrode coiled around the probe tip in the shape of a cone. The electrode acts both as an earth for the measuring electrode and as a screen to prevent any interference from other electrodes or earthed objects in the vessel. The probes must be made so that the measuring volume is as small as practically possible, to minimize averaging effects when measuring the fluid conductivity. When placed within the vessel, the probes will affect local mixing by their presence. The position of the probes within the vessel is determined by the point at which a measurement is required and it is not possible to change a probe’s position to minimize the effects on local mixing. The only way in which the effect on local mixing can be minimized is by making the probes as small as possible and arranging the supports in such a way that they intrude as little as possible into the vessel. To this end, the probe supports must, wherever possible, be placed behind baffles.

The typical probe positions used for a single-impeller mixing system are shown in Figure 4-15. Three probes are used and are sited to give as much information as possible about the mixing in the vessel. One probe is sited in the impeller stream, which is the most intensely mixed region of the vessel. The second probe is sited

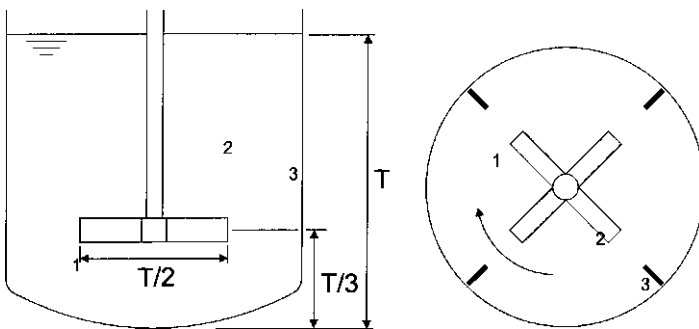


**Figure 4-15** Typical mixing time measurement probe positions.

close to a baffle, which is likely to be a poorly mixed region. The third probe is sited in the middle of the tank approximately halfway around a circulation loop. The position of this probe is particularly important in the transitional regime. It should be checked for new geometries using a decolorization test. The probes are mounted at different heights within the vessel, at different radial distances from the mixer shaft, and on different sides of the tank. These positions are selected so that any deficiencies in vertical convection or tangential convection within the tank will show up in the measured concentration records.

Great care must be taken to prevent unwanted chemical reactions occurring in the mixing vessel. The use of reactive tracers such as nitric acid and sodium hydroxide, rather than common salt, causes some problems. Materials that may normally be regarded as inert, since they react so slowly as not to cause significant drift over the time of the experiments, may start to react more rapidly. Materials that are initially inert may also start to react after a period of time when protective oxide films are broken down.

Care must also be taken to prevent metal objects in the vessel from inadvertently becoming charged. This will lead to electrochemical cells being set up, causing drifting conductivity and a noisy signal. This will also happen if two dissimilar metals, both dipping into the fluid, are allowed to come into contact.

If there is a drain hole in the bottom of the vessel, it should be plugged during experiments. This is done to prevent small amounts of fluid with a different conductivity from the vessel contents, occasionally mixing with the fluid in the vessel. The conductivity meters connected to each probe should use an alternating current-based technique to eliminate polarization or chemical reaction at the probe itself. If measurements are made using more than two probes, each probe should be operated with a different electrical frequency to eliminate probe crosstalk. The output from the conductivity meters is collected on a computer using an analog-to-digital converter card and can then be processed using dedicated software or using a spreadsheet program.

**4-4.4.5 Processing Mixing Time Data.** Data collected by the conductivity, thermocouple, or pH techniques must be processed to obtain a characteristic mixing time for the system under investigation. The analysis is described below in terms of conductivity readings, but is equally applicable to the other data types.

The data must first be normalized to eliminate the effect of different probe gains. The data are normalized between an initial zero value measured before the addition of tracer, and a final stable value measured after the test is complete. These values are typically obtained by measuring the probe outputs over 30 s.

The normalized output is obtained by

$$C'_i = \frac{C_i - C_0}{C_\infty - C_0} \quad (4-3)$$

where  $C'_i$  is the normalized probe output. The normalized responses for three probes in a stirred tank are shown in Figure 4-16.

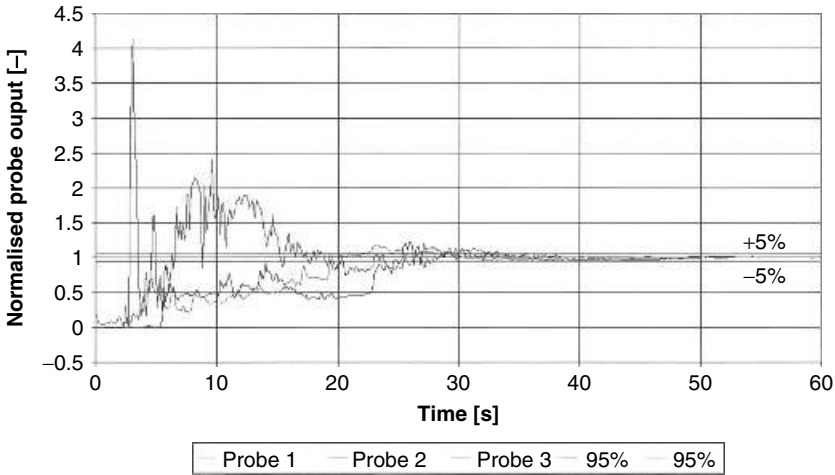


**Figure 4-16** Normalized conductivity probe responses for three probes.

The mixing time is defined as the time required for the normalized probe output to reach and remain between 95 and 105% ( $\pm 5\%$ ) of the final equilibrium value. This value is called the *95% mixing time*. It can be difficult to identify the 95% mixing time accurately from the normalized probe outputs (Figure 4-16) because of the fine scale around the endpoint. Because the probe fluctuations decay exponentially, the data can be conveniently replotted in terms of a probe log variance as a function of time (Figure 4-17):

$$\log \sigma^2 = \log(C'_t - 1)^2 \quad (4-4)$$

This graph is more accurate for obtaining the 95% mixing time. The 95% mixedness line corresponds to the point where  $C' = 0.95$ . To obtain an overall mixing time for the system, the three probe responses must be combined and must be weighted toward the probe showing the largest concentration deviation to ensure that all regions of the vessel are mixed. This is achieved using an RMS variance and is plotted in Figure 4-17:

$$\log \sigma_{\text{RMS}}^2 = \log \left\{ \frac{1}{3} [(C'_{t,1} - 1)^2 + (C'_{t,2} - 1)^2 + (C'_{t,3} - 1)^2] \right\} \quad (4-5)$$

More stringent criteria of 99% or 99.9% mixing time are used in certain applications where a higher degree of uniformity is required (e.g., paint manufacture or pharmaceutical production). These values can also be obtained from the *log variance graph*. The linear response of log variance as a function of time is due to the exponential decay in concentration fluctuations. This relationship also allows one to calculate an arbitrary degree of uniformity from the 95% mixing time:

$$\frac{\theta_n}{\theta_{95}} = \frac{\ln[1.0 - (n/100)]}{\ln(1.0 - 0.95)} \quad (4-6)$$

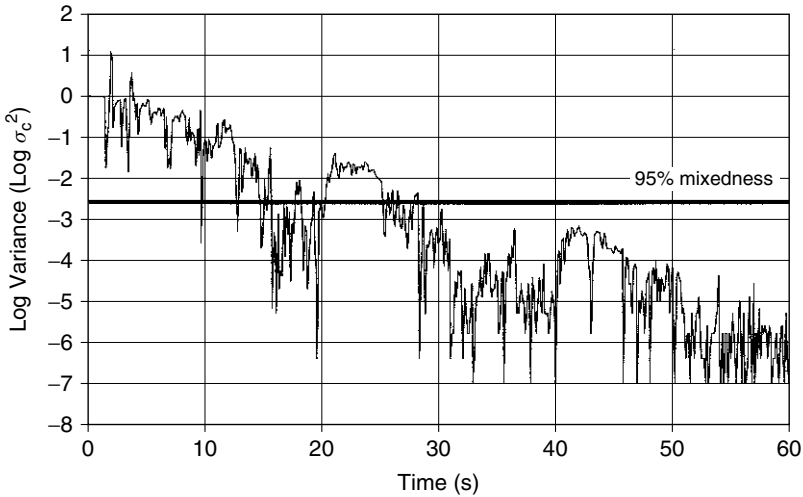


**Figure 4-17** Probe log variance.

where  $n$  represents the desired degree of mixedness. For example, a 99% mixing time can be calculated using

$$\frac{\theta_{99}}{\theta_{95}} = \frac{\ln(1.0 - 0.99)}{\ln(1.0 - 0.95)} = 1.54$$

Papers in the open literature (e.g., Harnby et al., 1992) often refer to a *dimensionless mixing time*,  $N\theta$ . This is the product of the 95% mixing time,  $\theta$ , and the impeller speed,  $N$ . The dimensionless mixing time is equivalent to the number of impeller revolutions required to achieve the desired degree of uniformity.

#### 4-4.5 RTD for CSTR

The conductivity probe technique can also be used to measure the residence time distribution of continuous flow systems by installing probes at the inlet and outlet of the mixing vessel. The probe response can be normalized and interpreted as outlined by Levenspiel (1972) or as discussed in Chapter 1 of this book. Care should be taken to ensure that the data are collected over a sufficiently long time, because the tail can have a large effect on the measured mean residence time and the derived variance.

#### 4-4.6 Local Mixedness

**4-4.6.1 Coefficient of Variation.** The coefficient of variation (CoV) and other measures used to describe mixedness are defined in Chapter 3, where details of the analysis are discussed, and reviewed in the context of pipeline mixing

in Chapter 7. CoV can be measured using a variety of techniques, including laser-induced fluorescence, conductivity probes, and temperature probes.

**4-4.6.2 Reactive Mixing Experiments.** When two reactive fluids are brought together, reaction cannot proceed until the reactive molecules are mixed intimately on a molecular level. If there are several competing reactions occurring simultaneously whose reaction lifetimes are approximately the same as the time scale of the mixing process, the relative progress of the reactions will be governed by the mixing process(es). Generally speaking, the faster (usually desired) reactions will be favored by higher mixing rates and the slower (usually undesired by-product) reactions by slower mixing rates. The product distribution from the reactions will therefore reflect the mixing history; and with the aid of suitable mixing models, these distributions can be used to back-calculate mixing rates.

The overall mixing process occurs within a flow field continuum that covers a wide range of length scales. It is possible to decompose this continuum into several mixing subprocesses or mechanisms, each of which has distinct characteristics. If one of these subprocesses is much slower than the others, it is said to be *rate limiting*. Furthermore, if a system is sensitive to mixing rates (e.g., competitive fast reactions), it is the rate of the slowest mixing step that will influence the process outcome. By focusing on the most important mixing scale, the mixing characterization can be simplified greatly.

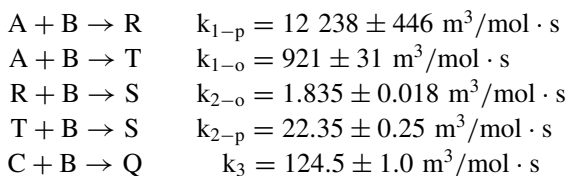
Mixing between two miscible fluids can be broken down into the following steps, where the length scales given are for turbulent mixing of liquids (high  $Sc$ ):

1. Convection of an additive by mean velocities (typical length scale  $10^{-1}$ – $10^{-2}$  m)
2. Turbulent dispersion by fluctuating velocities in large eddies ( $10^{-2}$ – $10^{-3}$  m)
3. Reduction of segregation length scale by breakdown of large eddies ( $10^{-3}$ – $10^{-4}$  m)
4. Fluid engulfment in small eddies ( $10^{-4}$ – $10^{-5}$  m)
5. Lamellar stretching with molecular diffusion ( $10^{-6}$ – $10^{-7}$  m)

These subprocesses occur both in series and (to some extent) in parallel. For the purposes of this discussion, the five processes above can be spilt into three broader categories: steps 1 and 2 are responsible for *macromixing*, step 3 is responsible for *mesomixing*, and steps 4 and 5 are responsible for *micromixing*. The energy to drive these processes comes from the mean flow at the expense of pressure drop or shaft work. This energy is extracted from the flow at large scales (in the form of wakes, vortices, and mean radial velocities) and is dissipated at small scales, where viscosity becomes important. All of this is discussed in far greater detail in Chapter 2 in the context of turbulence and in Chapter 13 in the context of reactive mixing.

**Bourne Azo-Coupling Reactions.** The second Bourne reaction scheme (see Table 13-4) is the most commonly used reactive mixing characterization tool. It is

a fairly robust scheme, with clean, well-defined kinetics that can be made sensitive to mixing rates over a wide range of conditions. The scheme involves the reaction of diazotized sulfanilic acid with 1- and 2-naphthol. The naphthols compete for the sulfanilic acid to produce a range of different-colored dye products according to the following scheme:



where A is 1-naphthol, B is diazotized sulfanilic acid, C is 2-naphthol, R and T are two mono-azo isomers, S is a bis-azo dye, and Q is another mono-azo dye.

The naphthols are generally used in large excess (to ensure that the reaction goes to completion in the mixer) with 2-naphthol present at a greater concentration than the 1-naphthol. The concentrations and relative volumes of the reagent solutions used are varied so that the reaction product distribution is sensitive to mixing intensity in the device used.

Typical concentrations used are  $C_{A0} = 0.03 \text{ mol/m}^3$ ,  $C_{C0} = 0.12 \text{ mol/m}^3$ ,  $C_{B0} = 50.0 \text{ mol/m}^3$ ,  $Q_{A,C}/Q_B = 3000$ .

The product distribution is quantified in terms of product yield relative to the limiting reagent B.

$$\begin{aligned}
 X_Q &= \frac{[Q]}{[R] + [T] + [Q] + 2[S]} \\
 X_S &= \frac{2[S]}{[R] + [T] + [Q] + 2[S]}
 \end{aligned} \tag{4-7}$$

When relatively high mixing intensity conditions are used, very little of the bisubstituted product S is formed. The chemistry then reduces to a competitive-parallel scheme with 1-naphthol (A) competing with 2-naphthol (C) for sulfanilic acid (B), producing R and Q, respectively.

If the B solution was distributed perfectly in the A and C solution at a molecular level before any reaction occurred (“perfect mixing”), the product concentrations would be determined solely by the kinetics of the reactions. At the other extreme, if the mixing is extremely poor, any A and C entering the reaction zone will be consumed before fresh material can be incorporated. The ratio of the products will then be the same as the ratio of the feed reagents (ignoring the consecutive reactions). The actual values of  $X_Q$  will depend on the initial concentration and volume of the B solution.

The Bourne schemes are dealt with in more detail in Chapter 13 and in Table 13-4.

**4-4.6.3 LIF/PLIF.** Laser-induced fluorescence (LIF) techniques are very promising but are still primarily a research tool requiring expert users. They are not discussed in this chapter.

## 4-5 SOLID-LIQUID MIXING

There are a large number of techniques available that can provide both qualitative and quantitative information on the suspension and distribution of solids in a liquid-filled stirred tank. Other techniques can be used to determine the “just suspended” speed (or “just drawn-down” speed with floating solids).

### 4-5.1 Solids Distribution

There is no simple way to describe the distribution of solids in a stirred vessel. The techniques described here either give accurate quantitative data on local concentrations of solids (conductivity probe, optical probe, sampling for external analysis, or process tomography), or provide general observations and semi-quantitative information (e.g., cloud height) on the distribution of solids (visual observation, process tomography). If several local measurements are made using the conductivity, optical, or sampling techniques described below, the relative standard deviation of the data can be used to give a single measure of how well the solids are distributed. The reader is cautioned that this quantity is extremely sensitive to the number and location of the data points used and is of little use without reference to visual observations and a full record of the local data measurement locations used to calculate it.

Two types of probe have commonly been used: conductivity and optical. Both types of probes and the associated instrumentation are commercially available, but care should be taken to ensure that the probe and instrumentation are suitable for a particular application. The dimensions of the measuring volume should be at least an order of magnitude greater than the dimensions of the solid particles, and the probe should allow free flow through the measuring volume. If these criteria cannot be met, inaccurate measurements will result, and a custom-built probe may have to be used.

Attempts to close a solids mass balance using these approaches generally fail unless the solids are very well distributed throughout the vessel. It is very difficult to measure accurately the quantity of any unsuspended solids on the vessel base. This problem is most acute if visual observations are not possible. The number of locations in the vessel at which measurements are made will usually be limited for practical reasons. This lack of spatial resolution will lead to inaccurate measurements being made in regions where there are high solids concentration gradients.

**4-5.1.1 Visual Observations.** Visual observations are most commonly used to determine the minimum speed for suspension of solids ( $N_{js}$ ) as discussed in Section 4-5.2. Visual observations can also be an extremely useful tool to give a rough estimate of the degree of homogeneity in a mixing vessel. Where a range of geometries is being optimized, this enables a rapid choice to be made of the two or three most efficient geometries. At this point further testing may be carried out. Observations of the multiphase flow are necessary in order to choose



suitable positions for mounting instruments in the vessel and can be used to rapidly identify problem areas such as stagnant areas where solids may collect. Such observations of the flow patterns also help in choosing sampling points in the vessel, and cloud height observations will help in selecting vessel outlet locations and in estimating how well mixed the vessel is. Visual observations also help to identify any unusual phenomena that may cause problems with the process (e.g., drop-out of solids at intermediate impeller speeds) and help in interpreting the data obtained by other means.

At high solids concentrations, visual observations become difficult: The solids screen most of the vessel from view. If a process with a high solids concentration is being investigated, observations at lower solids concentrations will aid in understanding the mixing mechanisms. However, observations should still be carried out at high solids concentration since the flow patterns in the vessel often vary considerably with solids concentration.

The addition of a colored dye (food dye works very well in aqueous systems) to the vessel, which is taken up preferentially by either the liquid phase or the solid phase, may assist with visualizing the flows. The addition of a small quantity of solids of a contrasting color (with the other relevant physical properties held constant) may help flow visualization, as will the use of a high intensity spotlight to allow light to penetrate as far into the vessel as possible. Where photographs or video are required, a polarizing filter can be extremely helpful in removing unwanted reflections. A ruler or some other scale attached to the side of the vessel can be very helpful for providing some quantitative information on cloud height observations.

**4-5.1.2 Conductivity Probe.** If the suspending fluid is conducting (e.g., water) and the suspended solids nonconducting, a conductivity probe (Figure 4-18) can be used to measure the local solids concentration precisely and accurately. The conductivity probe will only measure an overall solids concentration in the measurement volume, and cannot discriminate between particles of different sizes. Any probe placed within the vessel has the disadvantage of being intrusive and hence altering the flows and possibly the solids concentration at the measuring point. The probes can be designed to minimize their effect on local flows, but some level of intrusiveness will have to be tolerated. Since the probe is intrusive, it is desirable to check for separation of the solids from the liquid near the probe. This may be done by rotating the probe. If no separation is taking place, the measured solids concentration will not change. If problems are occurring due to flow separation, the measured value of solids concentration will generally be too low, so the highest value of solids concentration should be taken as the true value.

The measured electrical conductivity of the probe volume will vary as the solids concentration in the probe volume changes. Generally, the measured conductivity is linearly related to the volume fraction of solids over a wide range of solids concentrations:

$$\frac{\kappa}{\kappa_0} = 1 - A\varepsilon_S \quad (4-8)$$

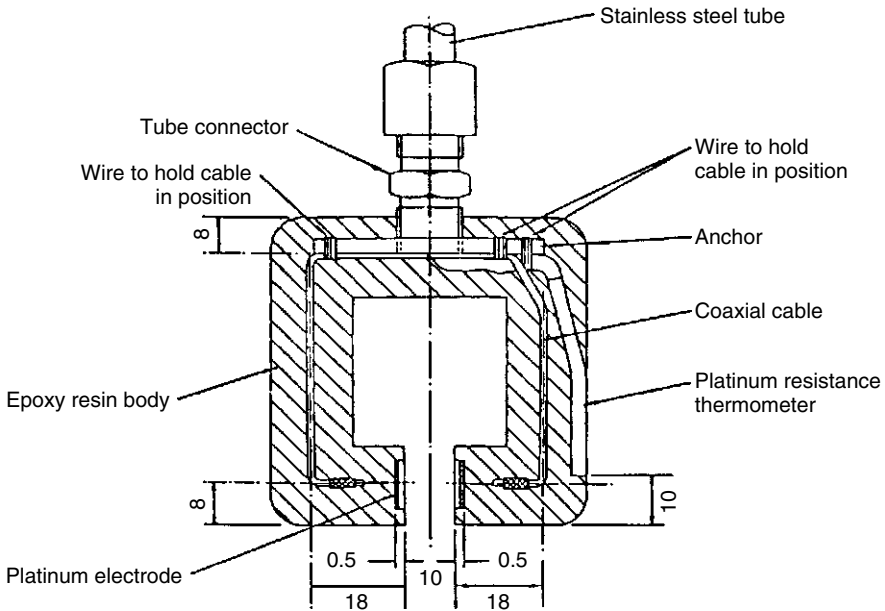


**Figure 4-18** Conductivity probe for measuring solid concentration.

where  $\kappa$  is the measured conductivity,  $\kappa_0$  is the conductivity with no solids present,  $\varepsilon_s$  is the volume fraction of solids, and  $A$  is a calibration factor.

The probes require calibration with the liquid and solids that are to be measured. For solids that are easily suspended, calibration may be carried out in a small vessel fitted with a laboratory stirrer. The suspension is agitated sufficiently to ensure homogeneity and allow measurement of the solids concentration with the probe being calibrated. Solids that are difficult to suspend may be calibrated using a fluidized bed, although it will be necessary to use solids of a very narrow size distribution for accurate calibration. Calibration using a laboratory stirrer is generally limited to low concentrations, as it is difficult to maintain homogeneity at high solids concentrations. Calibrations using a fluidized bed are generally limited to high solids concentrations, since the bed becomes unstable at low solids concentrations. It may be necessary to use a combination of the two techniques. There is some evidence that the calibration factor is a weak function of particle size and shape, but this can be ignored in most practical applications.

The fluid used for suspending the solids must be conducting but must not contain any electrolytes. Any electrolytes will cause polarization at the electrodes, leading to problems with noisy and drifting signals. Most commercially available probes have a platinum-black coating to prevent polarization. Care should be taken, as the solids present in the vessel often rapidly erode this coating. Before making any measurements, checks should be made to ensure that the solids contain no soluble impurities, which may cause the conductivity signal to drift,

and that all the vessel internals are inert. Solids containing soluble impurities that may affect the conductivity must be washed thoroughly before use to remove the impurities.

The measured conductivity may change not only as a result of solids concentration, but also due to changes in the fluid temperature and to impurities dissolving in the fluid. During use it is essential to measure temperature accurately and to correct for any changes. The following expression can be used:

$$\kappa_C = \kappa_M \frac{\kappa_{OR}}{\kappa_{OM}} \quad (4-9)$$

where  $\kappa_C$  is the conductivity corrected to the reference temperature,  $\kappa_M$  the measured conductivity,  $\kappa_{OR}$  the fluid conductivity at the reference temperature, and  $\kappa_{OM}$  the fluid conductivity at the measured temperature.

Where more than one probe is used to make measurements, care should be taken that no crosstalk occurs between probes. A conductivity meter applies an AC voltage (approximately 1 to 2 kHz) across the probe, and the voltage applied to one probe may be detected by another probe. To prevent this, the probes must either be multiplexed, so that only one probe at a time has a voltage applied to it, or different AC frequencies, with bandpass filtering, must be used for each probe.

The conductivity probe is best suited to work under laboratory conditions, although if exceptional precautions are taken, it may be used in industrial process plant. Care must be taken to ensure that the probe(s) are mounted securely in the vessel. Measurements made with probes of this type are typically averages of several minutes' worth of data.

**4-5.1.3 Optical Probe.** Optical probes can also be used to measure solid concentration and are generally of two types: light absorption or light scattering. In both cases the amount of light absorbed or scattered is related to the solids concentration. For absorption, *Beer's law* applies:

$$\log \frac{I_0}{I} = E\varepsilon_S \ell \quad (4-10)$$

where  $I_0$  is the intensity of the incident light,  $I$  the intensity of the light after absorption,  $E$  the extinction coefficient for the system,  $\varepsilon_S$  the volume fraction of solids, and  $\ell$  the optical path length.

The extinction coefficient is a function of particle size and light wavelength. The relative amounts of light absorbed and scattered will depend on both the particle size and light wavelength used, and it is essential that a calibration is carried out with the same solids and same light source which will be used in the mixing vessel. Calibration is carried out in a similar manner to the conductivity probes mentioned earlier.

The probe response becomes nonlinear as the solids concentration is increased, and measurements are extremely difficult at solids concentrations greater than 2 to 3 vol %. by volume. The upper limit on the instrument range is also dependent

on the particle size of the solids. Reducing the gap between the light source and light receiver may extend the range, but this may cause problems with poor flow through the measuring volume.

Although the probe response is a function of both particle size and solids concentration, it is not possible to distinguish between the two effects. If the particle size distribution in the mixing vessel changes during the course of the experiment due to degradation of the solids, the probe response will drift. This problem is especially acute where the solids contain friable particles such as clay, which degrade easily to give a turbid suspension. Problems will also occur if solids with a very wide size distribution are used. The particle size distribution will vary with position in the vessel, and hence the probe response will become a function of position in the vessel.

Optical probes are insensitive to changes in temperature and to impurities that do not absorb or scatter light. An optical probe will give an accurate and precise measure of the concentration of solids for which a prior calibration has been carried out. The probes are generally less susceptible to interference than conductivity probes. They should be used under laboratory conditions, although in some cases they may be used in industrial process plant. Optical probes can normally be used only to measure low solids concentrations (up to 2 to 3 vol %). Care should be taken to avoid errors due to changes in particle size distribution during measurement.

**4-5.1.4 Sampling.** In many situations probes may be unsuitable for measuring local solids concentration, particularly if information on the particle size distribution is required. In such cases a sample must be taken from the vessel while it is in operation, and analyzed using standard laboratory methods. The laboratory analytical techniques are usually straightforward (e.g., sieve analysis), and generally no major problems are encountered with their use. The chief difficulty lies in obtaining a sample that is representative of the local conditions at the sampling point.

Two means are generally available for removing a sample from a mixing vessel: pumping the sample out through a pipe, or taking a grab sample. In both cases the sampling process may cause classification of the solids, or separation of the solids and liquid. When removing a sample through a pipe, the arrangement used must ensure that the sample is removed isokinetically; that is, the velocity at which the sample enters the pipe must match the local fluid velocity, and the pipe must be aligned in the local direction of flow. In a mixing vessel with its complex three dimensional turbulent flows, this is very difficult, but with care an approach can be made. A sharp-edged pipe should be used to prevent classification of the solid, and care should be taken to ensure that the solids do not separate out in the pipe. In practice there are few locations in the vessel where the flows are steady enough for the flow velocity and direction to be matched. Some flow visualization experiments must be carried out before sampling to ensure optimum matching of sampling flows with local flows in the vessel.

Grab sampling involves lowering a container fitted with a lid into the vessel, remotely opening the lid to fill the container, closing the lid and withdrawing

the sample. Open-topped containers are unsuitable for this purpose, since they will tend to collect a sample from the surface of the vessel as they are lowered in. The measured solids concentration will also be a function of time unless the container allows a completely free flow of fluid while it is open.

Sampling is the most robust and most generally applicable technique for measuring solids concentration and is the only practical technique that will give information on particle size distribution [except, perhaps, phase Doppler anemometry (PDA), but that works only at very low concentrations]. Great care must be taken when sampling to ensure that representative samples are taken. The lack of commercially available equipment means that equipment will usually have to be designed and built for each job.

**4-5.1.5 Tomography.** Electrical resistance tomography is very much an emerging technology (see Section 4-8.1) Measurement of solids distribution is one area where the technique is likely to be extremely useful.

#### 4-5.2 Solids Suspension: Measurement of $N_{js}$

$N_{js}$  is defined as the minimum impeller speed at which all the solids in the vessel are suspended. This is the speed at which the surface area of all the solids in the vessel are in complete contact with the liquid and hence is an optimal operating point for mass transfer rate in the vessel (Figure 4-19). Solid suspension measurements are very sensitive to the precise shape of the vessel base. Measurements should not be made in a vessel with a drain in the middle

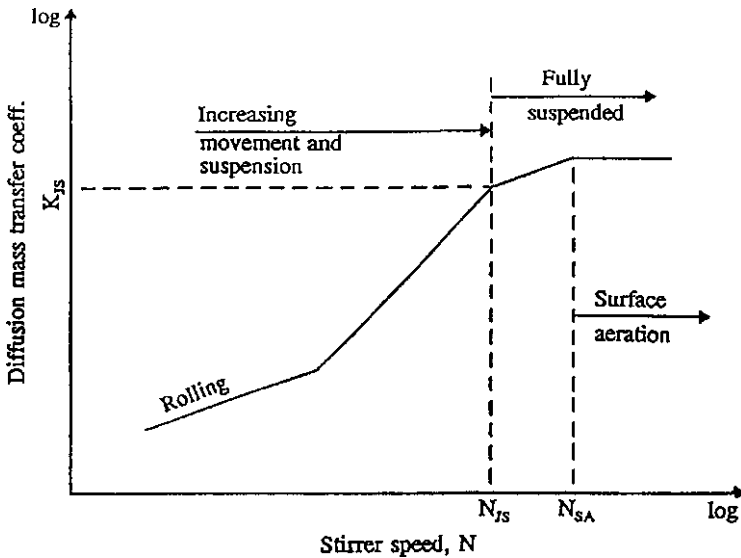


Figure 4-19 Solid-liquid mass transfer coefficient over a range of impeller speeds.

of the vessel base unless they are done to model a particular production facility where this occurs.

The measurement (indeed, the existence of) of the “just suspension” speed is subject to the assumption that there exists a speed where there is equilibrium between the particles lifted from the vessel base and those settling back onto the base. This assumption is reasonable with fast settling particles but becomes more and more dubious as the settling velocity of the particles decreases.

**4-5.2.1 Visual Technique.** The most common way of determining  $N_{js}$  is by making visual observations through the base of the vessel (provided that the vessel is equipped with a transparent base). This is a difficult technique, as there is generally no sharp endpoint at  $N_{js}$ , but a gradual transition from the partly suspended to the just suspended condition. This transition becomes more gradual as the solids concentration is increased. The problem is still further compounded, since many workers have used different criteria for defining the just suspended state. At various times, criteria such as “no solids remain stationary on the vessel base for more than 1 to 2 seconds,” “no solids remain stationary on the vessel base for more than 2 to 4 seconds,” and “no solids remain on the vessel base for more than 1 to 2 seconds” have been used. It is important to select an  $N_{js}$  criterion relevant to the process under investigation, and one that is consistent with any other data that are being referenced.

Different workers, even when working with the same system and using the same suspension criterion, often obtain different values of  $N_{js}$ . Where possible, the entire set of measurements should be made by one person. When this is not possible, care should be taken to ensure that each operator trained in the technique produces consistent results.

On a practical level, transparent-based vessels designed for  $N_{js}$  measurements should be mounted on a sturdy frame with the base raised several feet above the ground (Figure 4-7). In this way an operator can either lie on his or her back underneath the vessel, or can view a reflection of the base in a mirror. Care should be taken to ensure that a large enough section of the vessel base can be observed. With small vessels ( $T < 0.6$  m) it should be possible to observe the entire base at once, while with larger vessels this may not be possible and a section (say, one quadrant) of the vessel base will have to be observed. If the decision is made to observe only a section of the vessel base, it should be noted that the eye does tend to wander, and it may help to hide the other sections from view.

The operator should have access to the impeller speed controller and a digital readout from the position in which he or she makes the measurements. Several repeat measurements should be made by slowly stepping up the impeller speed and observing the vessel base for stagnant particles. Sufficient time should be allowed for steady state to be reached before checking to see if the chosen “just suspension” criterion has been reached. If not, the impeller speed should be stepped up and the observation repeated. With fast-settling particles in a reasonably small vessel (say  $T < 1.0$  m), the time required to reach steady state is

not generally longer than about 1 min, although a longer period of measurement is required to test if the criterion has been reached. With much slower settling particles (either very small particles and/or a viscous liquid phase) the time to reach steady state and the measurement time may be large compared to the time it takes for a particle to settle back onto the vessel base. In these situations the entire measurement is meaningless, as the system is not in equilibrium and the concentration at the base is changing with time.

When making visual  $N_{js}$  measurements, it is important to note not only the speed required to meet the chosen just suspended criterion but also the location of the point of last suspension. Some impeller and vessel geometry combinations tend to produce a point of last suspension in the middle of the base of the vessel; other combinations tend to leave a ring of settled solids around the base next to the vessel walls.

Similar visual techniques can be used to measure the equivalent speed for systems with floating particles, the “just drawn-down” criterion. The visual observations are subject to exactly the same issues and problems as the just suspended measurements; however, access to see the particles on the free surface of the fluid is generally easier to obtain than at the base of the vessel, as no transparent vessel parts are required.

In many situations, measurement of  $N_{js}$  by direct observation is impractical. Other means must be resorted to, and two methods are available: detecting the movement of solids by means of an ultrasonic flowmeter, and inferring  $N_{js}$  from measurements of solids concentration. Both techniques are difficult to use, and neither should be used without making visual observations in a geometrically similar vessel. It is in these situations that the knowledge of the location of the last point of suspension is vital.

**4-5.2.2 Ultrasonic Doppler Flowmeter Probe.** The ultrasonic Doppler flowmeter (UDF) instrument measures the velocity of a fluid by measuring the Doppler shift in an ultrasonic signal reflected from particles being carried by the fluid (Figure 4-20). This type of meter is normally used for measuring flows in pipes, but when mounted beneath the vessel base can be used to measure

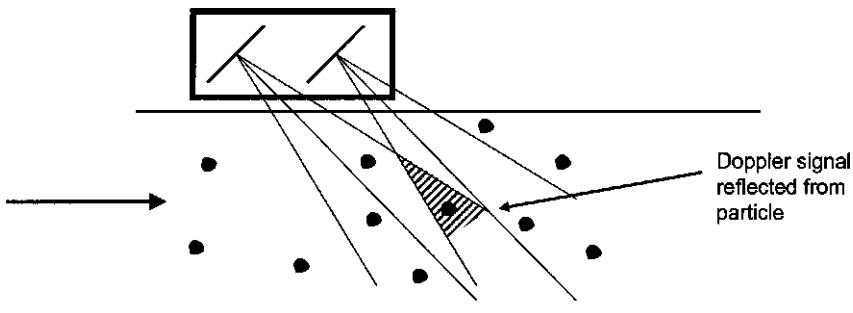


**Figure 4-20** Ultrasonic Doppler flowmeter: principles of operation.

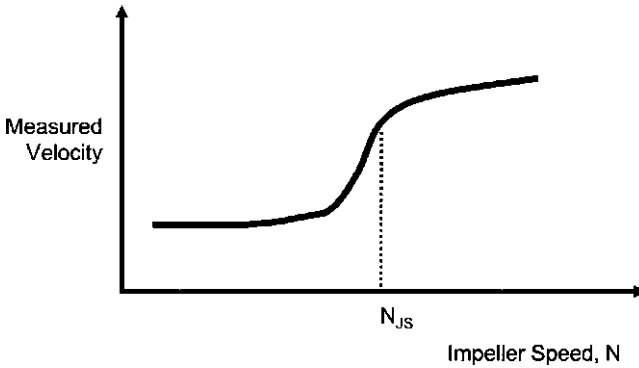


**Figure 4-21** Ultrasonic Doppler flowmeter: output signal.

$N_{js}$ . At low impeller speeds the meter will indicate a zero velocity, since there will be an immobile bed of solids on the vessel base. As the impeller speed is increased, there will be a large increase in the indicated velocity at the point where the bed of solids becomes fully mobile. As impeller speed is increased beyond  $N_{js}$ , the indicated velocity will continue to increase, but at a much slower rate (Figure 4-21).

The meter does not require accurate calibration, since it is only necessary to measure relative velocities at different impeller speeds, and the position of the endpoint is taken as an indication of  $N_{js}$ . For successful operation a fairly high solids concentration is needed, at least 2 to 3 vol %. At lower concentrations the instrument can “see” right through the bed of solids and does not detect an endpoint. Several different types of sensing heads are available which measure velocities at various distances from the vessel wall. A head with as small a measuring distance as possible should be used to prevent this problem.

It is extremely important that the sensing head is positioned underneath the vessel base in the place where suspension occurs last. If visual observations are not possible in the vessel being used, some preliminary work must be carried out in a geometrically scaled transparent vessel. Placing the sensing head in an inappropriate position will result in erroneous and misleading measurements being made. Some correlation of meter response against visual observation must be made.

The ultrasonic Doppler flowmeter has the advantage of being mounted externally on the vessel and is capable of measuring  $N_{js}$  where visual measurements are impossible. This makes it especially suitable for use in a process plant, where the process fluids may be aggressive, access to the vessel may be difficult, and visual observations cannot usually be made. The instrument is, however, unusable at low solids concentrations and still requires some visual observations to be made before installation.

**4-5.2.3 Conductivity Probe.** As described earlier, a probe that responds to changes in solids concentration may be placed at a point inside a vessel to



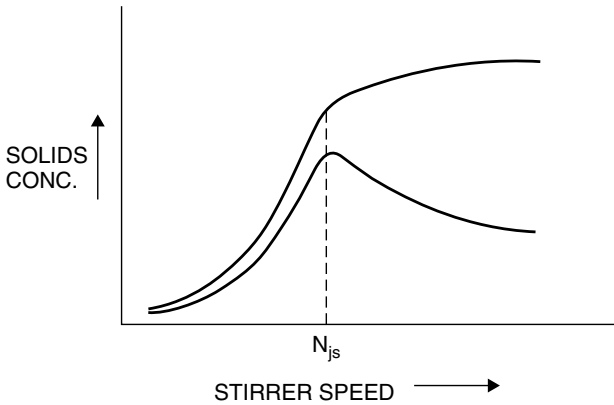


**Figure 4-22** Determination of  $N_{js}$  from solids concentration measurement.

obtain information on the local solids concentration. From measurements of local solids concentration,  $N_{js}$  may also sometimes be inferred. To infer  $N_{js}$  from solids concentration measurements, there must be some feature of the solids concentration versus speed curve that can be correlated with  $N_{js}$  (Figure 4-22).

The assumed mechanism here is that as the impeller speed is increased while the solids are partly suspended, the solids concentration near the vessel base will increase due to the increase in the quantity of solids removed from the immobile bed on the vessel base. Once  $N_{js}$  has been reached, the solids concentration will start to fall, since the solids near the base are being redistributed to other regions of the vessel, and no more solids are available on the base to take their place.

In many cases such an idealized behavior has not been reported, and workers have observed only a kink in the solids concentration curve at  $N_{js}$ . It is extremely difficult to get reliable, reproducible results with this technique. The shape of the solids concentration versus speed curve is very sensitive to changes in the position of the measuring point. Often, there are no salient features that can be correlated with  $N_{js}$ , or worse still, there is a feature that is located at a speed far below  $N_{js}$ —hence the need for parallel visual observations. The technique does have the advantage that it is not prone to subjective interpretations by different observers. However, it should not be attempted unless there is a great deal of time available to develop the experimental method further.

Visual observations of the flows in the vessel, or in a geometrically similar small scale vessel, should be made to assist in probe positioning. Even in a well-mixed vessel the solids concentration can vary greatly between different parts of the vessel. A misleading interpretation of the results may occur if the solids in the vessel are incompletely suspended and measurements are made in regions of the vessel with relatively high solids concentrations.

## 4-6 LIQUID-LIQUID DISPERSION

### 4-6.1 Cleaning a Liquid-Liquid System

All experimentalists who work with immiscible liquid-liquid systems must be concerned about the cleanliness of the system. Liquid-liquid experiments, particularly drop size measurements, are notoriously sensitive to changes in the cleanliness of the fluids, the vessel, and the mixers. The concern is that any trace of impurity, be it surfactant or greasy fingerprint, can alter the interfacial tension, alter the dynamics of the interface (repressing coalescence), or if preferentially wetted by the dispersed phase, act as a center for coalescence.

Two approaches may be taken to cleanliness. The one that is more popular with industrial workers is to swamp the interface with a known contaminant. This gives a reproducible system that is completely stabilized, or *noncoalescing*, and this method is thus suitable only for study of such systems. The other technique, more popular with academic researchers, is to strive for a base case with a very high level of cleanliness. For this approach a range of extremely draconian, though very necessary cleaning regimes have been developed to ensure that vessels and pipes are at least uniformly clean. Most of these procedures involve the repeated scrubbing of all wetted mixer parts in copious quantities of hot water and surfactant, followed by several rinses with deionized water. Some procedures also stipulate flushing with chromic acid, but the present authors do not recommend the use of this substance. Further details of the cleaning procedures are presented in Chapter 12.

When moving to larger scale systems, things may get easier. At larger scales there is less surface area of mixer and vessel per unit volume available to contaminate, and at higher dispersed phase concentrations there is more interfacial area of dispersion per volume of contaminant. However, performing large scale experiments (anything at  $T = 0.6$  m or over is considered large scale) is extremely difficult because of the high cost of materials and cleaning and the scarcity of vessels that can be cleaned to the degree required to give reproducible results.

The reader is strongly cautioned that a number of issues other than cleanliness may contribute to the variability often seen in liquid-liquid dispersion experiments. These include:

- *Materials of construction.* The fluids have different tendencies to wet the surfaces of different materials of construction, and this can lead to coalescence of one liquid at a surface, which distorts the results of the experiment. Glass and steel vessels are hydrophilic, while Perspex vessels are hydrophobic. These properties can be modified if surfaces become coated (typically with oil) over time.
- *Temperature.* The material properties, particularly interface tension, viscosity, and density, that influence liquid-liquid dispersions are functions of temperature.

- *Slight geometry changes.* Small differences in impeller or vessel geometry can affect the power number of the impeller and hence the breakup and coalescence of drops. It may also be postulated that details such as blade sharpness or baffle thickness affect drop size in some cases.

#### 4-6.2 Measuring Interfacial Tension

One of the key variables governing droplet breakup is the interfacial tension between phases. The pendant drop apparatus can be used to measure either the surface tension between a liquid and air or the interfacial tension between two liquids. The pendant drop method should be used in preference to the du Nüoy ring, as it is easier to use and gives more reliable results.

The apparatus consists of a glass microsyringe with a calibrated volume scale. The end of the syringe has a stainless steel hypodermic needle attached. The entire apparatus is clamped to a stand to eliminate vibrations (Figure 4-23). For interfacial tension measurements, a small PMMA or glass cell is positioned beneath the needle tip. The syringe is charged with the more dense fluid, and the cell is charged with the less dense fluid. The tip of the syringe needle is lowered to a position below the surface of the less dense fluid and a droplet is slowly squeezed out through the needle until it detaches and sinks to the base of the cell.

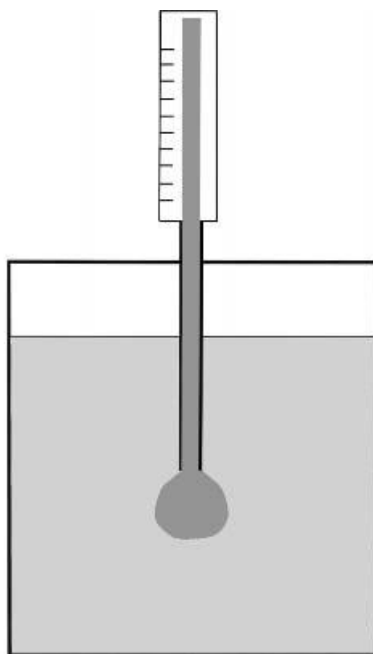


**Figure 4-23** Pendant drop technique for interfacial tension measurement.

The method works on the principle that the volume that the droplet reaches within another liquid is related to the interfacial tension between the two liquids by the following expression:

$$\sigma = \frac{\theta V_d \Delta \rho g}{2\pi r} \quad (4-11)$$

where  $\sigma$  is the interfacial tension,  $V_d$  the volume of the detached drop,  $\Delta \rho$  the difference in density between the two phases,  $g$  the acceleration due to gravity, and  $r$  the radius of the hypodermic needle.  $\theta$  is a correction factor that allows for the amount of liquid left inside the needle tip after the drop has detached.

Great care must be taken when making these measurements to ensure that all equipment is scrupulously clean and that the temperature of the fluids and equipment is monitored and constant. The interfacial tension should be calculated based on the average droplet size of a large number of droplets. If repeatable measurements are not obtainable and suitable care has been taken in the performance of the experiment, it is possible that some form of contamination has occurred.

#### 4-6.3 $N_{jd}$ for Liquid-Liquid Systems

Various techniques have been employed to try to measure the speed required to disperse successfully, to the conditions of “just drawdown,” one immiscible phase in another (Skelland and Seksaria, 1978; Penney et al., 1999; Yamamura and Takahashi, 1999). These have included several variations on the use of conductivity probes (zero conductivity behind the baffle, indicating the presence of a pocket of organic phase), along with visual measurements. Measurements of this type are fraught with difficulty and it is extremely difficult to relate the results obtained using one technique with those obtained using another technique. There is a large difference between “just dispersed,” where no continuous layer of the dispersed phase remains in the vessel, and “completely dispersed,” where the liquid-liquid dispersion is distributed uniformly throughout the vessel. In a liquid-liquid dispersion system this can be quite difficult to detect. Figure 4-24 shows an immiscible liquid-liquid stirred tank system at impeller speeds below the full drawn-down condition.

#### 4-6.4 Distribution of the Dispersed Phase

Most measurements on the distribution of a dispersed phase in a liquid-liquid system have been made using the “local” techniques of measuring the conductivity or light transmittance. The probes used for these measurements are practically identical to those discussed in Sections 4-5.1.2 and 4-5.1.3 with reference to solid-liquid mixing. The conductivity-type probe can, however, suffer from the added complication of the electrode(s) becoming completely coated with a layer of the nonconductive (organic) phase, which causes the instrument to fail. Sampling techniques are subject to the same problems discussed in Section 4-5.1.4.

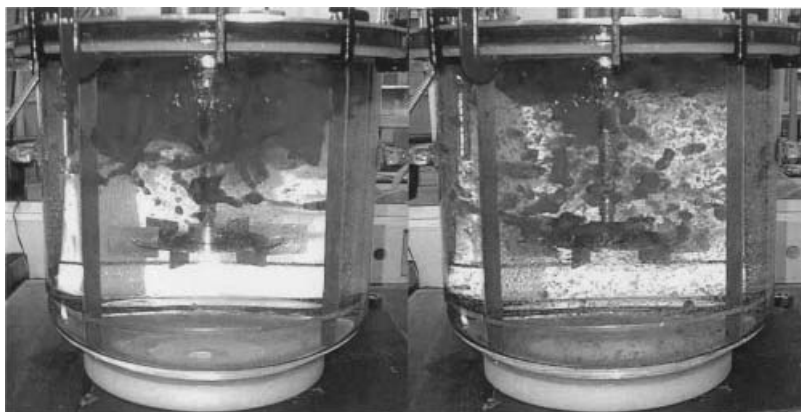


**Figure 4-24** Immiscible liquid–liquid system at a speed below that required for complete dispersion. See insert for a color representation of this figure.

#### 4-6.5 Phase Inversion

The point of phase inversion (where the continuous phase becomes dispersed and the dispersed phase becomes continuous) is generally best detected using a conductivity technique, provided that one phase is a good conductor (e.g., an aqueous solution) and the other is not (most organic liquids).

#### 4-6.6 Droplet Sizing

Many efforts have been made to measure the size of liquid dispersed droplets. The techniques can be divided into those that require a sample to be withdrawn from the vessel (or pipe) and those that take the measurement in situ. Pulling a sample is generally considered to be acceptable if the system has been suitably stabilized using a surfactant. Significant care still needs to be taken to ensure that the resulting droplet size distribution is not affected by the sampling method itself (i.e., no droplet breakup, coalescence, or preferential sampling occurs).

The other main consideration when selecting a measurement technique is whether the system is to be dilute or high concentration. Large numbers of investigations into droplet size distributions (or simply  $d_{32}$ ) have focused on extremely dilute dispersions, where it is assumed that coalescence can be eliminated. “High concentration” can actually mean anything from about 1 vol % to the point of phase inversion. Great care should be taken with any droplet size measurement system to ensure that a suitably large number of droplets have been sampled to provide a meaningful result. This means at least 500 drops for a unimodal distribution or for each peak of a multimodal distribution.

**4-6.6.1 Microscope Analysis.** Once a sample has been taken, perhaps the simplest way to measure the droplet size distribution is to place the sample on

a microscope slide and take photographs of it. The photographs can either be taken digitally or conventionally, but in either case suitable calibration images will have to be collected so that the droplet sizes can be determined. Microscope slide cover slips should not be used, as they can “squash” the droplets flat, making them appear larger than they actually are.

**4-6.6.2 Laser Diffraction.** There are now a large number of laser diffraction instruments on the market. This is an excellent technique, provided that a representative sample can be obtained and placed in the instrument. A key difficulty is sampling successfully (i.e., without altering the droplet size) and representatively, particularly at high concentrations when stabilization and dilution are often required.

**4-6.6.3 Video Probe Methods.** Various commercial models of video probes are now available, and the components can easily be bought to produce a tailor-made system. A diagram of a typical probe (in situ in a stirred tank) is shown in Figure 4-25. A photograph of the same probe is shown in Figure 4-26. All probe surfaces that come into contact with the dispersion are made from stainless steel or glass. Other designs of probe are available. A typical image produced by probes of this type is shown in Figure 4-27. Video records are provided on the Visual Mixing CD affixed to the back cover of the book.

Some comments about the components of the video system:

- *Lens.* A compact lens with a suitable magnification should be chosen. The size of the droplets to be measured is the governing factor. The measurement

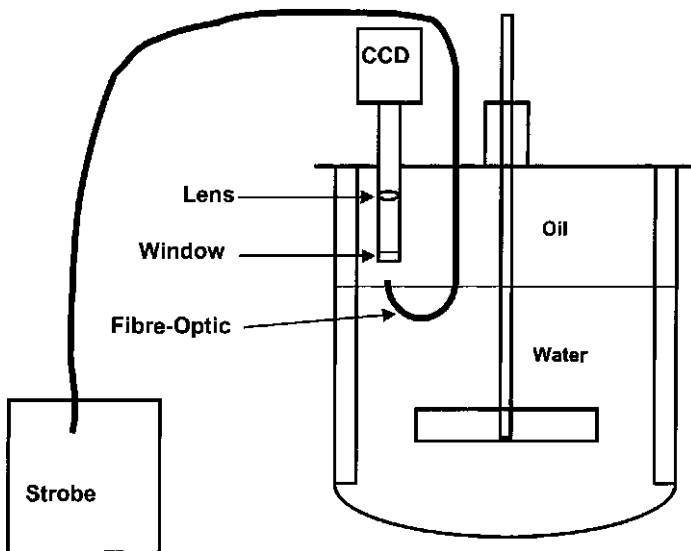
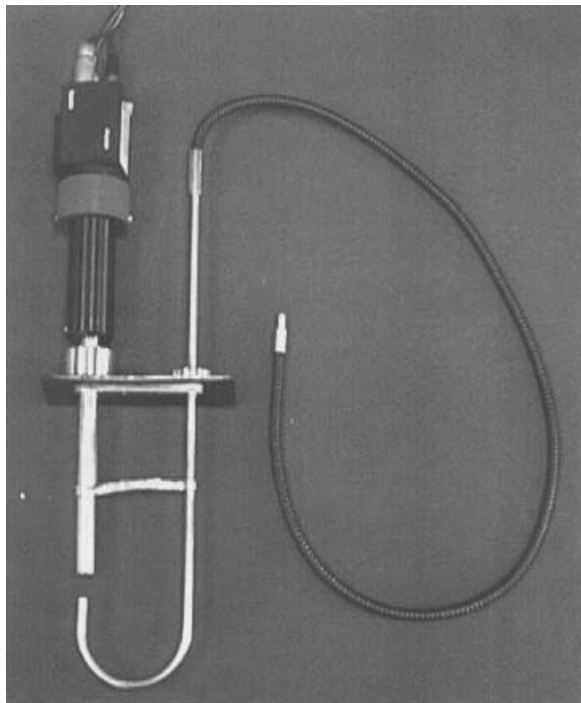
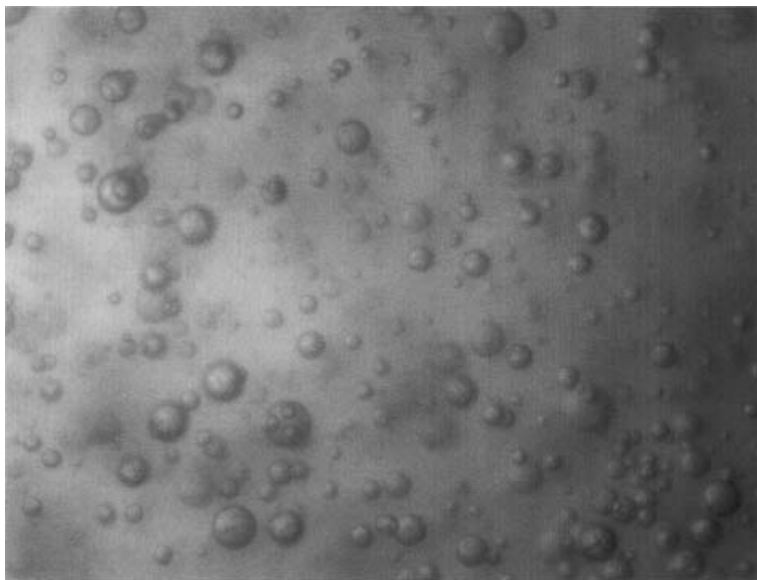


Figure 4-25 Liquid-liquid drop size video probe in stirred tank.



**Figure 4-26** Video probe for use in a STR.



**Figure 4-27** Typical liquid-liquid droplet image.

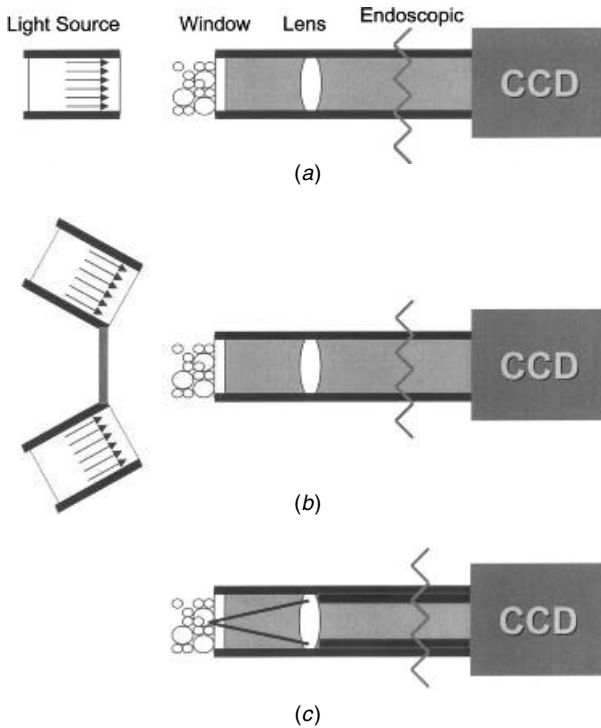


**Figure 4-28** Video probe lighting methods: (a) back lighting; (b) dark field; (c) ring lighting.

of a droplet that has a diameter less than  $1/100$  the image width is not recommended.

- *Lighting.* Backlighting produces the best images, although application of dark-field illumination and front lighting can prove useful in some situations (Figure 4-28). Great care is required in optimizing the lighting for a given measurement condition, as the lighting is critical in obtaining good-quality images but is sensitive to variables such as droplet size and dispersed phase fraction.
- *Shutter.* Most cameras have a controllable shutter. When a constant light source is used, the shutter should be set to as fast a speed as possible without the images appearing too dark, in order to give the clearest images with “stopped” droplets. A high-speed strobe (one with a short pulse width) running at the frequency of the camera can be used as an alternative to an electronic shutter. If the strobe is fast enough, it will “stop” the images of the droplets.
- *Capture.* Image capture uses either a digital video system, or an analog CCD camera, fed into a computer with an image capture card.



- *Analysis of images.* Various commercial software packages are now available that analyze images automatically and measure the size of the droplets. The quality of the results from these packages is variable and depends on a number of variables, including the quality of the initial images. Custom software can be written to incorporate previously validated image processing algorithms. Software is also available that allows the “manual” measurement of droplet images on computer. This process is extremely time consuming but generally considered essential for producing accurate results as well as checking the performance of automatic software.

#### **4-6.6.4 Chord Length Measurement Using Laser and Rotating Mirror.**

A device is available that uses a rotating mirror to pass a laser beam across a measurement area. The reflected light of the laser can be converted into chord lengths of droplets, and from this the droplet size distribution can be calculated, assuming that the droplets are spherical.

**4-6.6.5 Phase Doppler Anemometry.** Phase Doppler anemometry (PDA) is discussed in Section 4-11. At the time of writing, it is only useful for very low dispersed phase concentrations.

## **4-7 GAS-LIQUID MIXING**

### **4-7.1 Detecting the Gassing Regime**

The regime describes the degree of dispersion of the gas and its flow patterns around the vessel (see Chapter 11; and Smith et al., 1987). Detecting the regime is best done by visual observation through the side of a transparent vessel using the real system or a good model system. If this is not possible, the appearance of the top surface gives an indication of the most important condition: If the gas is seen to be arriving at the center of the surface in large bubbles, this indicates that it is not being dispersed. Some clue to the regime may also be obtained by measuring the variation of local gas fraction between locations using a local void fraction probe (see Section 4-7.4).

### **4-7.2 Cavity Type**

Direct observation is the best way to observe the type of blade cavity (refer to Chapter 11 for a description of cavities), although, of course, this requires that the vessel have a transparent base or bottom window. One method of capturing an image of the rotating cavity system involves observing or videoing through a derotational prism (Dove prism) mounted underneath the vessel (Figure 4-29). Another method involves a video camera mounted on a turntable underneath the vessel and rotated synchronously with the impeller. Early work (e.g., War-moeskerken et al., 1984) used slip rings to transmit the signal to a stationary

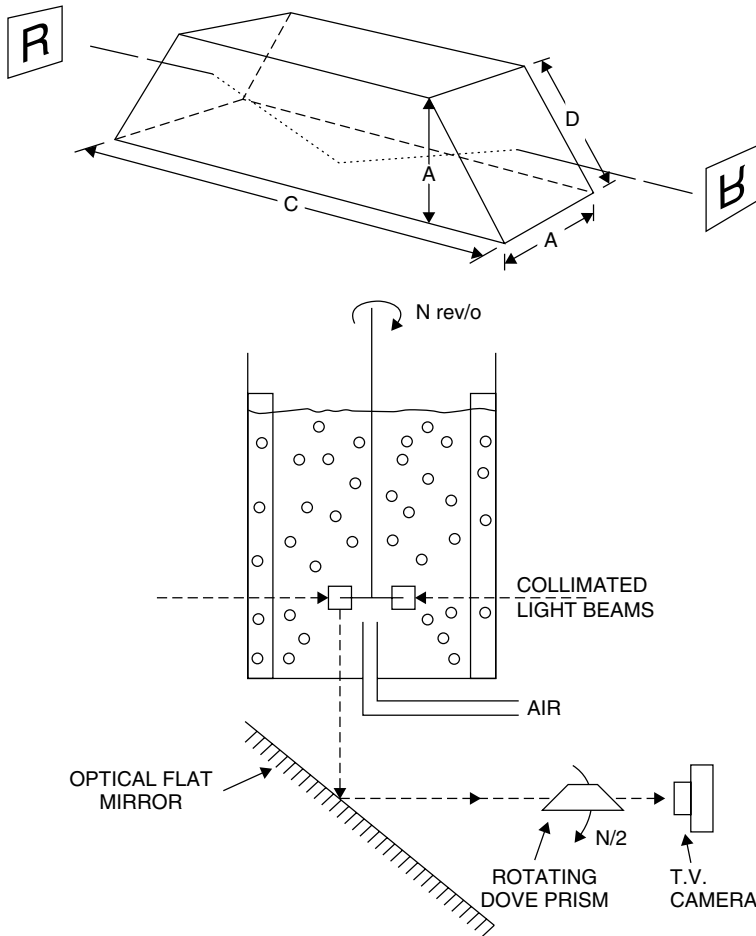


**Figure 4-29** Derotational prism. (Modified from Kuboi et al., 1983.)

recorder, which limited the speed and reliability. Self-contained camcorders are now available. Care is required (as always) with the lighting.

If a sufficiently powerful stroboscopic lamp is available, this can be used, flashing at  $N$  times the number of blades, with a stationary video camera (Nienow and Wisdom, 1974). For better-quality single shots, a high-speed flash can be used with a still camera.

The vane probe (Smith, 1985) has been used with success to detect cavity type. A probe with a small vane fitted with strain gauges is mounted in the turbine discharge stream, and the different cavity types are indicated by characteristic frequency spectra of the strain gauge signals. Cavity type can also be implied from power draw measurements if the ungasged power number of the impeller and the power losses in the motor and drive are known.

### 4-7.3 Power Measurement

The gassed power draw should be measured using the techniques described in Section 4-3.

### 4-7.4 Gas Volume Fraction (Hold-up)

Either local gas volume fraction or the vessel average fraction (*gas hold-up*) may be measured. Where the amount of surface motion in the gas–liquid system is not excessive, an estimate of the vessel average gas hold-up may be made by visual observation of the level change (possibly aided by video analysis).

A more reliable technique, and one that can be used where there are larger surface fluctuations, is to use an ultrasonic radar probe (Machon et al., 1991). Such probes are commercially available, from, for example, Endress and Hauser. The probe is mounted above a representative part of the fluctuating surface and measures the distance to the surface. Care must be taken in the calibration (especially if any foam is present) to ensure that the true surface is detected and that an adequate range of fill levels is covered. Some foams will not be penetrated by the ultrasonic beam. Calibration with a moving liquid surface is recommended.

A cruder but effective method for overall gas hold-up in batch vessels is the spillover technique. The vessel is filled to the overflow before gassing; then the gas displaces its own volume of liquid, which is collected and measured.

Local gas fraction is measured using conductivity probes or optical probes. These conductivity probes typically measure the conductivity across two parallel plates about 10 mm square and 10 mm apart. The optical probes are the same as those used in solid–liquid work. Both types require careful calibration with the liquid under study.

### 4-7.5 Volumetric Mass Transfer Coefficient, $k_L a$

Gas–liquid mass transfer and  $k_L a$  are described in Chapter 11.

Dynamic absorption (usually of oxygen into aqueous liquids) has been a popular method for measuring  $k_L a$ , although it suffers from the need for rapid response, robust dissolved oxygen probes, which although being available (the polarographic type with thin membrane and small electrolyte path length) were not always used. The probes are temperature sensitive, and their response lag must be deconvoluted from the overall response signal. More important, the dynamic methods are subject to gross errors with systems containing small bubbles, which become exhausted quickly in oxygen-lean zones then act as an extra oxygen sink in oxygen-rich zones (Heijnen et al., 1980). For these reasons, steady-state methods are preferred.

Among the steady-state methods, the hydrogen peroxide–catalase method of Hickman (1988a) is the most commonly used. It can be used at any scale with aqueous systems at pH around 7, but not with ionic solutes such as NaCl, KCl, or  $K_2SO_4$  (sometimes used to render the liquid noncoalescing). Air is the usual gas feed, and the liquid contains the enzyme catalase in excess. Hydrogen

peroxide is fed at a steady rate such that dissolved oxygen concentration remains constant while the excess catalase decomposes the peroxide to water and oxygen. Thus at a steady state the oxygen transfer rate is obtained from the peroxide feed rate. Some precautions are necessary (Cooke et al., 1991):

- The catalase concentration must be in excess of stoichiometric by a factor of at least 15.
- For  $k_{La} > 0.5 \text{ s}^{-1}$ , catalase may deposit on surfaces and may affect coalescence properties.
- The pH must be maintained near 7 to minimize degradation of the catalase.
- The dissolved oxygen level must not exceed 300% saturation (otherwise, extraneous bubbles may be formed) but should be greater than 130% saturation to avoid large errors arising from small driving forces.
- The dissolved oxygen probe membrane must be resistant to peroxide attack (check by constancy of repeating measurements at different peroxide addition rates).
- Constant volume should be maintained by using concentrated peroxide feed and, for long experiments, withdrawing some liquid.
- Liquid mixedness should be checked by using several dissolved oxygen probes at various locations in the vessel.
- A high concentration of catalase will minimize the standing concentration of peroxide (thus minimize the risk of membrane damage) but will enhance spatial variations of concentration. Therefore, the catalase concentration must be optimized for the degree of mixing in each case.
- The decomposition of peroxide is exothermic, so temperatures must be checked before and after the measurement.
- The water produced could affect the viscosity of some model fluids.

One disadvantage of the catalase method for larger scales is the cost of the enzyme. A similar method involving manganese dioxide in place of catalase (Muller and Davidson, 1992; Martin et al., 1994; Vasconcelos et al., 1997) alleviates this problem and allows operation with noncoalescing electrolyte solutions. Although fine (20  $\mu\text{m}$ ) particles are involved, the concentration is low (0.8 g/l) and it is found (Vasconcelos et al., 1997) that they do not affect the coalescence properties of the system or the result obtained. However, manganese dioxide can absorb and degrade some solutes, such as carbohydrates (corn syrup, glucose, etc.) or polyhydroxy compounds (such as polypropylene glycol) often used in experiments.

A number of steady-state methods involving oxygen absorption with an oxygen sink dissolved in the liquid have been proposed. Among the oxygen sinks, sodium sulfite was used widely in older work but is very sensitive to conditions and catalysis (usually, copper or cobalt) and renders the solution noncoalescing. Active yeast has also been used as an oxygen sink (Hickman and Nienow, 1986) for work with fermenters.

Another method that has been suggested for plant vessels (especially, e.g., fermenters) where no additives are tolerated is the *pressure jump method* (Hickman, 1988b). The vessel pressure is rapidly dropped by a small amount, and the dissolved gas concentration in the liquid is monitored against time.

Chemical methods can also be used to measure  $k_L a$ . Robinson and Wilke (1974) describe an ingenious method to obtain  $k_L a$  and  $a$  simultaneously, by desorption of oxygen (rate  $\propto k_L a$ ) and reaction-enhanced absorption of carbon dioxide (regime III; see Chapter 11) into potassium hydroxide solution (rate  $\propto a$ ).

All the methods above require the correct gas flow pattern (plug flow, well back-mixed, or intermediate) to convert the transfer rate to a correct  $k_L a$  value unless the degree of depletion of the gas phase is very low. This can be very important, as discussed in Chapter 11. Gas flow patterns can be determined from measurements of the gas residence time distribution using tracer gas (see Section 4-7.8). Two dynamic methods avoid this problem: the double response method (Chapman et al., 1982), in which the dynamic responses of both liquid and gas phases are measured, and the initial response method (Gibilaro et al., 1985).

All methods also assume that the liquid is well mixed. This can be checked by comparing the 90% mixing time (measured by the methods described earlier, but see Section 4-7.10) to the measured 90% mass transfer time ( $= 2.3/k_L a$ ). If the liquid is not well mixed, an interlinked zone model (see, e.g., Figure 4-30

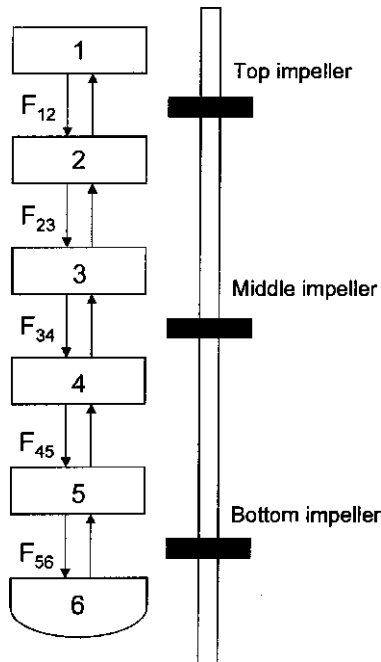


Figure 4-30 Network of zones model.

and Whitton et al., 1997) can be used to describe and scale-up mass transfer, with the fluid volume divided into zones, chosen with regard to the flow patterns so as to be well mixed. The interzone flow rates to be used in the model are fitted from liquid residence time distribution measurements (see Section 4-7.9) or from zone-to-zone dye tracing experiments using the area between the normalized response traces of probes in neighboring zones.

#### 4-7.6 Bubble Size and Specific Interfacial Area

Surface volume mean bubble size,  $d$ , and specific interfacial area,  $a$ , are linked via the local gas fraction,  $\phi$ :

$$a = \frac{6\phi}{d} \quad (4-12)$$

Thus, measurements of any two will give the third. Direct photography, either through the walls (Machon et al., 1997) (which may not give representative samples) or with an optical probe (see Section 4-6.6.3) with image analysis is the most direct method, yielding local size distributions and gas fractions.

Other probes have been used for measuring bubble size, often using arrays of optical fibers (Cochrane and Burgess, 1985; Frijlink, 1987) or electrodes [e.g., the Burgess-Calderbank five-point probe (Burgess and Calderbank, 1975), or the radio-frequency probe of Abuaf et al. (1979)] to register the gas-liquid interfaces as they pass over or between (Cochrane and Burgess, 1985) the probe tips. An array of probes enables shape and velocity to be detected also. Such probes are somewhat fragile and cannot measure bubbles smaller than about 1 mm in diameter.

Light transmittance methods for interfacial area have been widely employed in gas-liquid systems. Sridhar and Potter (1978) describe one of the more successful versions. The techniques are described in more detail in the liquid-liquid section. Chemical methods can be used to measure interfacial area, as described above (Section 4-7.5; Robinson and Wilke, 1974). Sampling methods are not suitable since it is impossible to withdraw a sample isokinetically. Generally, the results from chemical and physical methods do not agree. Chemical methods tend to have a bias toward the smaller bubbles of the distribution, whereas these may be missed by physical methods.

The method of dynamic gas disengagement (Sriram and Mann, 1977; Patel et al., 1989) to obtain an estimate of bubble size distribution is worthy of mention since it is convenient to use, sometimes even in real systems, especially for lower gas fractions. The impeller is stopped and the trend in the level measured against time. This trend indicates the bubble size distribution if terminal rise velocities are known and if coalescence is negligible.

#### 4-7.7 Coalescence

The best test of whether a system is coalescing or noncoalescing is to set it up in a vessel of standard configuration and impeller speed, in which overall gas

fraction can be measured. The gas fraction is compared with those of known coalescing and noncoalescing liquids and solutions.

Reith and Beek (1970) measured net coalescence rates in a vessel by injecting two gases separately and measuring concentrations in the leaving bubbles using a sampling probe. They also used a chemical method based on absorption in cobalt-catalyzed sulfite solution. The reaction, being second order in oxygen, proceeds at different rates for separate or mixed bubbles.

Several more fundamental measurements of quasi-static two-bubble coalescence times are reported; Machon et al. (1997) give a summary.

#### **4-7.8 Gas-Phase RTD**

Commonly, helium is used as a tracer gas in air or nitrogen, in the usual method for measuring RTD with a step change or pulse in the input gas stream. The tracer gas must exhibit the following properties:

- Very low solubility
- Safe to use
- Nonreactive
- Inexpensive
- Easy to sample
- Easily measurable at low concentration
- Easy to obtain

The method is described in Section 4-4.5. It is important to ensure that the dead spaces (gas volumes between the liquid surface and the exit gas concentration detector) are deconvoluted from the measured response. Gas-phase RTD has been measured by Hanhart et al. (1963) and Gal-or and Resnick (1966) and is often in between the ideal limits of plug flow and perfectly backmixed.

#### **4-7.9 Liquid-Phase RTD**

The method is the same as described in Section 4-4.5. The probes must be mounted or shielded such that the gas bubbles do not interfere with the readings.

#### **4-7.10 Liquid-Phase Blending Time**

Liquid-phase mixing time measurements can be made using the techniques described in the single-phase mixing section. Again the probes must be protected from interference from the gas bubbles.

#### **4-7.11 Surface Aeration**

Mass transfer by surface aeration is measured in the same ways as described in Section 4-7.5. If it is necessary to measure the gas induction rate in a closed

batch vessel (e.g., with a surface aerator or self-inducing agitator), this can be done directly by measuring the gas flow rate into the sealed vessel required to maintain the head-space pressure. This gas flow can be corrected to compensate for the pressure drop of the entry into the vessel. Another method (Chapman et al., 1980) involves sampling and analyzing gas bubbles within the dispersion. This method was extended to measure surface aeration in the presence of sparged gas.

## 4-8 OTHER TECHNIQUES

### 4-8.1 Tomography

Tomography is the nonobtrusive localized measurement of velocity, density, concentration, and so on, in three dimensions. An image is built up from the responses of an array of sensors around the periphery of the domain. A variety of signals have been used in mixing vessels, including light, x-ray,  $\gamma$ -ray, ultrasonic, positron, magnetic resonance, and electrical resistance and capacitance.

The simplest form of tomography uses crossed light beams or sheets and cameras, and has been used to measure (plane-by-plane) velocities in the impeller stream (Takashima and Mochizuki, 1971), and concentration (pH) fields in acid-base-indicator mixing experiments (All-Saeedi, 1995). Lübke (1982) used elaborate holographic interferometry equipment to measure the real-time dynamics of temperature fields in stirred vessels. Mewes and Ostendorf (1986) review this and other methods such as X-ray and  $\gamma$ -ray tomography. Ultrasonic tomography basically responds to density (and elastic modulus) differences and has been used successfully in gas-liquid pipe flow systems (including metal pipes). In theory it has a spatial resolution of about 1 mm and a temporal resolution of 16 ms (for a 200 mm pipe with multiple transmitters), but the stream velocity for imaging is limited to a maximum of about 0.5 m/s (Hoyle, 1996). Positron emission tomography (Parker and McNeil, 1996) provides high resolution but requires long times for data acquisition (e.g., 30 min). It has been used (McKee et al., 1994) for measuring solid particle concentration fields, and (Fangary et al., 1992) for velocity measurements ( $<0.5$  m/s) in stirred vessels.

Electrical tomography (Dickin et al., 1992; McKee et al., 1994) is the most widely explored for stirred vessels, and probably the lowest-cost method, in cases where modest resolution is sufficient. Resistance tomography is used for conducting liquids and capacitance for nonconducting liquids. A typical capacitance system has a temporal resolution of 10 to 100 frames per second and a spatial resolution (radially) of  $\frac{1}{20}$  of the vessel diameter. Several (typically eight) rings, each of typically 16 electrodes, are positioned on the vessel wall, and readings from all pairs on a ring are taken in turn and fed to an image reconstruction algorithm. A typical probe cage is shown in Figure 4-31. It can detect solids, gases, immiscible liquids, or ionic tracer solutions, and has been used in mixing studies in pilot scale stirred vessels (2.3 m<sup>3</sup>) (Stanley et al., 2002). Resolution very near the base and surface is poor and deteriorates toward the axis of the



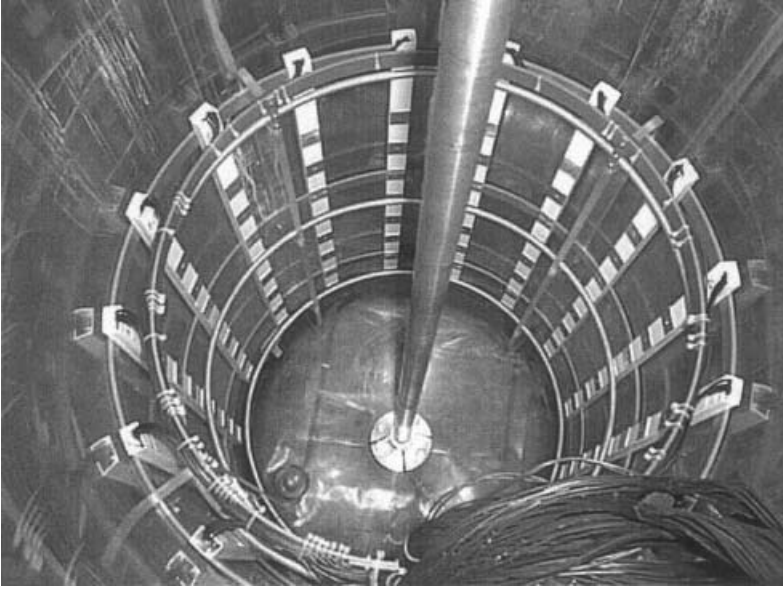


**Figure 4-31** Tomography cage. (From Cooke et al., 2001.)

vessel unless a central electrode is added. It is possible to use the method with metal vessels (Wang et al., 1993) using a modified reconstruction algorithm.

## **Part B: Fundamental Flow Measurement**

*George Papadopoulos and Engin B. Arik*

### **4-9 SCOPE OF FUNDAMENTAL FLOW MEASUREMENT TECHNIQUES**

Early emphasis in turbulence research was on the statistical analysis and description of turbulent flow fields. Theoretical advances in the field have been complemented by experiments that included pressure measurements and by the point measurement technique of hot wire anemometry (HWA). The intrusive nature of this latter technique has precluded its use in some experiments, whereas in others, corrections have been introduced to the measurement results.

Optical diagnostic techniques are desirable for fluid flow measurements due to their nonintrusive nature. Soon after the invention of the laser in the 1960s, the technique of laser Doppler anemometry (LDA) was developed. During the last three decades, the LDA technique has witnessed significant advancements. Three-component fiber optic-based LDA systems with frequency-domain signal

processors are currently the state of the art and are used in numerous facilities. The addition of a second photodetector to the first component LDA receiving optics gives the system the capability of size measurement, in addition to velocity, through phase difference analysis of the scattered light. The particle dynamics analyzer or phase Doppler anemometer (PDA) is an extension of the LDA and is a valuable tool for size determination of spherical particles.

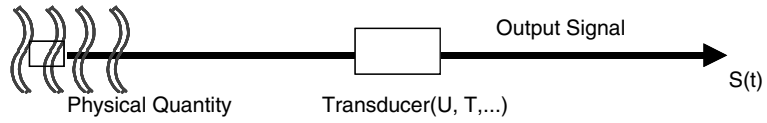
Since the early 1960s, the investigation of three dimensional coherent structures has been of significant interest for turbulence researchers. Flow visualization techniques have been around since the days of Prandtl. Flow markers, such as seeding particles, dyes, smoke, and so on, are typically used, and the techniques have been improved, with new ones being developed over the years. The evolution of these whole field flow visualization techniques has led to quantification of the visualized results, especially during the last 10 years with the advent of digital imaging and fast growth of computational power. Particle image velocimetry (PIV) has evolved to be a highly powerful technique for 2D and 3D whole field velocity measurements, while planar laser-induced fluorescence (PLIF) is also becoming a powerful technique in the mixing research community for quantitative concentration measurements.

#### **4-9.1 Point versus Full Field Velocity Measurement Techniques: Advantages and Limitations**

Hot wire anemometry (HWA) or constant temperature anemometry (CTA), laser Doppler anemometry (LDA) or laser Doppler velocimetry (LDV), and particle image velocimetry (PIV) are currently the most commonly used and commercially available diagnostic techniques to measure fluid flow velocity. The great majority of the HWA systems in use employ the constant temperature anemometry (CTA) implementation. A quick comparison of the key transducer properties of each technique is shown in Table 4-1, with expanded details on spatial resolution, temporal resolution, and calibration provided in the following sections.

**4-9.1.1 Spatial Resolution.** High spatial resolution is a must for any advanced flow diagnostic tool. In particular, the spatial resolution of a sensor should be small compared to the flow scale, or eddy size, of interest. For turbulent flows, accurate measurement of turbulence requires that scales as small as two to three times the Kolmogorov scale be resolved. Typical CTA sensors are a few micrometers in diameter, and a few millimeters in length, providing sufficiently high spatial resolution for most applications. Their small size and fast response make them the diagnostic of choice for turbulence measurements.

The LDA measurement volume is defined as the fringe pattern formed at the crossing point of two focused laser beams. Typical dimensions are 100  $\mu\text{m}$  for the diameter and 1 mm for the length. Smaller measurement volumes can be achieved by using beam expansion, larger beam separation on the front lens, and shorter focal length lenses. However, fewer fringes in the measurement volume increase the uncertainty of the measurement.

**Table 4-1** Transducer Comparison of Commonly Used Velocity Measurement Diagnostics


	CTA (HWA)	LDA	PIV
Proportionality of output signal $S(t)$	Nonlinear	Linear	Linear
Spatial resolution	Single point typically $\sim 5 \mu\text{s}$ ; multiwires: measurement volume	Single point $\sim O(100 \mu\text{s})$	Multipoint varies depending on field magnification (measurement volume)
Frequency distortion	Sensor in contact with flow—very high frequency response, follows flow behavior	Good frequency response—tracer particles assumed to follow flow (particle lag)	Particle motion frozen at two instants in time; assumes linear displacement (particle lag)
Dynamic range; resolution	Depends on analog-to-digital conversion; 12- and 16 bit typical; can be higher	16 bit digitization of Doppler frequency within selected bandwidth	Depends on subpixel resolution of particle displacement; 6 to 8 bit typical
Interference with physical process	Yes	No	No
Influence of other variables	Yes	No	No

A PIV sensor is the subsection of the image, called an *interrogation region*. Typical dimensions are  $32 \times 32$  pixels, which would correspond to a sensor having dimensions of  $3 \times 3$  mm by the light sheet thickness ( $\sim 1$  mm) when an area  $10 \times 10$  cm is imaged using a digital camera with a pixel format of  $1000 \times 1000$ . Spatial resolution on the order of a few micrometers has been reported by Meinhart et al. (1999), who have developed a micrometer resolution PIV system using an oil immersion microscopic lens. What makes PIV most interesting is the ability of the technique to measure hundreds or thousands of flow vectors simultaneously.

**4-9.1.2 Temporal Resolution.** Due to the high-gain amplifiers incorporated into the Wheatstone bridge, CTA systems offer a very high frequency response, reaching into the range of hundreds of kilohertz. This makes CTA an ideal instrument for the measurement of spectral content in most flows. A CTA sensor

provides an analog signal, which is sampled using analog-to-digital converters at the appropriate rate obeying the Nyquist sampling criterion.

Commercial LDA signal processors can deal with data rates in the range of hundreds of kilohertz, although in practice, due to measurement volume size and seeding concentration requirements, validated data rates are typically in the 10 kHz or kHz range. This update rate of velocity information is sufficient to recover the frequency content of many flows.

The PIV sensor, however, is quite limited temporally, due to the framing rate of the cameras and pulsing frequency of the light sources used. Most common cross-correlation video cameras in use today operate at 30 Hz. These are used with dual-cavity Nd:Yag lasers, with each laser cavity pulsing at 15 Hz. Hence, these systems sample the images at 30 Hz and the velocity field at 15 Hz. High-framing-rate CCD (charge-coupled device) cameras are available that have framing rates in the 10 kHz range, albeit with lower pixel resolution. Copper vapor lasers offer pulsing rates up to the range 50 kHz, with energy per pulse around a fraction of 1 mJ. Hence, in principle, a high-framing-rate PIV system is possible with this camera and laser combination. But in practice, due to the low laser energy and limited spatial resolution of the camera, such a system is suitable for a limited range of applications. Recently, however, CMOS (complementary metal-oxide semiconductor)-based digital cameras have been commercialized with framing rates of 1 kHz and a pixel resolution of  $1\text{ K} \times 1\text{ K}$ . Combined with Nd:Yag lasers capable of pulsing at several kHz with energies of 10 to 20 mJ/pulse, the latter system brings us one step closer to measuring complex, 3D turbulent flow fields globally with high spatial and temporal resolution. The vast amount of data acquired using a high-framing-rate PIV system, however, still limits its common use due to the computational resources needed in processing the image information in nearly real time, as is the case with current low-framing-rate commercial PIV systems.

**4-9.1.3 Calibration.** The CTA voltage output,  $E$ , has a nonlinear relation with the input cooling velocity impinging on the sensor,  $U$ . Even though analytical treatment of the heat balance on the wire sensor shows that the transfer function has a power law relationship of the form  $E^2 = A + BU^n$  (King's law), with constants  $A$ ,  $B$ , and  $n$ , it is most often modeled using a fourth-order polynomial relation. Moreover, any flow variable that affects the heat transfer from the heated CTA sensor, such as the fluid density and temperature, affects the sensor response. Hence, CTA sensors need to be calibrated for their velocity response before use. In many cases, they also need to be calibrated for angular response. A common case such as gradually increasing ambient temperature can be dealt with either by performing a range of velocity calibrations for the range of ambient temperatures, or by performing analytical temperature corrections for the measured voltages.

The LDA measurement principle is given by the relation  $V_x = d_f \cdot f_d$ , where  $V_x$  is the component of velocity in the plane of the laser beams and perpendicular to their bisector,  $d_f$  is the distance between fringes, and  $f_d$  is the Doppler

frequency. The fringe spacing is a function of the distance between the two beams on the front lens and the focal length of the lens, given by the relation  $d_f = \lambda/[2 \sin(\theta/2)]$ , where  $\lambda$  is the laser wavelength and  $\theta$  is the beam crossing angle. Since  $d_f$  is a constant for a given optical system, there is a linear relation between the Doppler frequency and velocity. The calibration factor (i.e., the fringe spacing) is constant, calculable from the optical parameters, and mostly unaffected by other changing variables in the experiment. Hence, the LDA requires no physical calibration prior to use.

The PIV measurement is based on the simple relation  $V = d/\Delta t$ . Seeding particle velocities, which approximate the flow field velocity, are given by the particle displacement,  $d$ , obtained from particle images in at least two consecutive times, divided by the time interval between the images,  $\Delta t$ . Hence, the PIV technique also has a linear calibration response between the primary measured quantity (i.e., particle displacement) and particle velocity. Since the displacement is calculated from images, commonly using correlation techniques, PIV calibration involves measuring the magnification factor for the images. In the case of 3D stereoscopic PIV, calibration includes documenting the perspective distortion of target images obtained in different vertical locations by the two cameras situated off normal to the target.

**4-9.1.4 Summary of Transducer Comparison.** In summary, the point measurement techniques of CTA and LDA can offer good spatial and temporal response. This makes them ideal for measurements of both time-independent flow statistics, such as moments of velocity (mean, RMS, etc.) and time-dependent flow statistics such as flow spectra and correlation functions at a point. Although rakes of these sensors can be built, multipoint measurements are limited due primarily to cost.

The primary strength of the global PIV technique is its ability to measure flow velocity at many locations simultaneously, making it a unique diagnostic tool to measure 3D flow structures and transient phenomenon. However, since the temporal sampling rate is typically 15 Hz with today's commonly used 30 Hz cross-correlation cameras, the PIV technique is normally used to measure instantaneous velocity fields from which time-independent statistical information can be derived. Cost and processing speed are the main limiting factors that influence the temporal sampling rate of PIV, but such limitations are quickly disappearing.

## 4-9.2 Nonintrusive Measurement Techniques

Most emphasis in recent times has been in the development of nonintrusive flow measurement techniques for measuring vector as well as scalar quantities in the flow. These techniques have been mostly optically based, but when fluid opaqueness prohibits access, other techniques are available. A quick overview of several of these nonintrusive measurement techniques is given for completeness in the next few sections. More extensive discussion on these techniques can be found in the references cited.

#### **4-9.2.1 Particle Tracking Velocimetry and Laser Speckle Velocimetry.**

Just like PIV, PTV and LSV measure instantaneous flow fields by recording images of suspended seeding particles in flows at successive instants in time. An important difference among the three techniques comes from the typical seeding densities that can be dealt with by each technique. PTV is appropriate with low seeding density experiments, PIV with medium seeding density, and LSV with high seeding density. The issue of flow seeding is discussed later in the chapter.

Historically, LSV and PIV techniques have evolved separately from the PTV technique. In LSV and PIV, fluid velocity information at an interrogation region is obtained from many tracer particles, and it is obtained as the most probable statistical value. The results are obtained and presented in a regularly spaced grid. In PIV, a typical interrogation region may contain images of 10 to 20 particles. In LSV, larger numbers of particles in the interrogation region scatter light, which interferes to form speckles. Correlation of either particle images or speckles can be done using identical techniques and result in the local displacement of the fluid. Hence, LSV and PIV are essentially the same technique, used with different seeding density of particles. In the rest of the chapter the acronym PIV is used to refer to either technique.

In PTV, the acquired data provide a time sequence of individual tracer particles in the flow. To be able to track individual particles from frame to frame, the seeding density needs to be small. Unlike PIV, the PTV results in sparse velocity information located in random locations. Guezennec et al. (1994) have developed an automated three dimensional particle tracking velocimetry system that provides time-resolved measurements in a volume.

**4-9.2.2 Image Correlation Velocimetry.** Tokumaru and Dimotakis (1995) introduced image correlation velocimetry (ICV) for the purpose of measuring imaged fluid motions without the requirement for discrete particles in the flow. Schlieren-based image correlation velocimetry was recently implemented by Kegrise and Settles (2000) to measure the mean velocity field of an axisymmetric turbulent free-convection jet. Papadopoulos (2000) demonstrated a shadow image velocimetry (SIV) technique which combined shadowgraphy with PIV to determine the temperature field of a flickering diffusion flame. Image correlation was also used by Bivolaru et al. (1999) to improve on the quantitative evaluation of Mie and Rayleigh scattering signal obtained from a supersonic jet using a Fabry–Perot interferometer. Although such developments are novel, we are still far from being able to fully characterize a flow by complete simultaneous measurements of density, temperature, pressure, and flow velocity.

## **4-10 LASER DOPPLER ANEMOMETRY**

Laser Doppler anemometry is a nonintrusive technique used to measure the velocity of particles suspended in a flow. If these particles are small, in the order of micrometers, they can be assumed to be good flow tracers following the flow

with their velocity corresponding to the fluid velocity. The LDA technique has some important characteristics that make it an ideal tool for dynamic flow measurements and turbulence characterization.

#### 4-10.1 Characteristics of LDA

Laser anemometers offer unique advantages in comparison with other fluid flow instrumentation:

- *Noncontact optical measurement.* Laser anemometers probe the flow with focused laser beams and can sense the velocity without disturbing the flow in the measuring volume. The only necessary conditions are a transparent medium with a suitable concentration of tracer particles (or seeding) and optical access to the flow through windows or via a submerged optical probe. In the latter case the submerged probe will to some extent, of course, disturb the flow, but since the measurement takes place some distance away from the probe itself, this disturbance can normally be ignored.
- *No calibration—no drift.* The laser anemometer has a unique intrinsic response to fluid velocity—absolute linearity. The measurement is based on the stability and linearity of optical electromagnetic waves, which for most practical purposes can be considered unaffected by other physical parameters such as temperature and pressure.
- *Well-defined directional response.* The quantity measured by the laser Doppler method is the projection of the velocity vector on the measuring direction defined by the optical system (a true cosine response). The angular response is thus defined unambiguously.
- *High spatial and temporal resolution.* The optics of the laser anemometer are able to define a very small measuring volume and thus provides good spatial resolution and yields a local measurement of Eulerian velocity. The small measuring volume, in combination with fast signal processing electronics, also permits high-bandwidth time-resolved measurements of fluctuating velocities, providing excellent temporal resolution. Usually, the temporal resolution is limited by the concentration of seeding rather than by the measuring equipment itself.
- *Multicomponent bidirectional measurements.* Combinations of laser anemometer systems with component separation based on color, polarization, or frequency shift allow one-, two-, or three-component LDA systems to be put together based on common optical modules. Acoustooptical frequency shift allows measurement of reversing flow velocities.

#### 4-10.2 Principles of LDA

**4-10.2.1 Laser Beam.** The special properties of the gas laser that make it so well suited for the measurement of many mechanical properties are spatial and temporal coherence. At all cross-sections along the laser beam, the intensity has

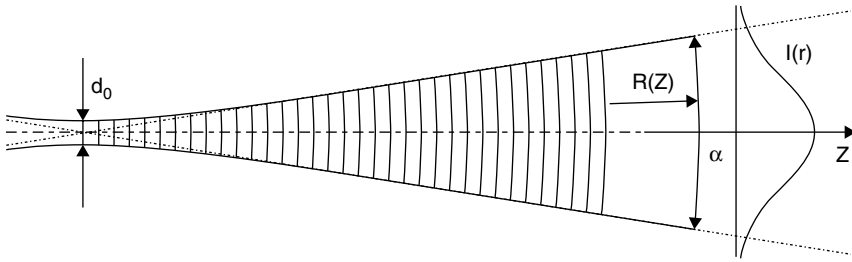


Figure 4-32 Laser beam with Gaussian intensity distribution.\*

a Gaussian distribution and the width of the beam is usually defined by the edge intensity being  $1/e^2 = 13\%$  of the core intensity. At one point the cross-section attains its smallest value, and the laser beam is uniquely described by the size and position of this *beam waist*.

With a known wavelength  $\lambda$  of the laser light, the laser beam is described uniquely by the size  $d_0$  and position of the beam waist, as shown in Figure 4-32. With  $z$  describing the distance from the beam waist, the following formulas apply:

beam divergence: 
$$\alpha = \frac{4\lambda}{\pi d_0} \tag{4-13}$$

beam diameter: 
$$d(z) = d_0 \sqrt{1 + \left(\frac{4\lambda z}{\pi d_0^2}\right)^2} \rightarrow \alpha z \quad \text{for } z \rightarrow \infty \tag{4-14}$$

wavefront radius: 
$$R(z) = z \left[ 1 + \left(\frac{\pi d_0^2}{4\lambda z}\right)^2 \right] \begin{cases} \rightarrow \infty & \text{for } z \rightarrow 0 \\ \rightarrow z & \text{for } z \rightarrow \infty \end{cases} \tag{4-15}$$

The beam divergence  $\alpha$  is much smaller than indicated in Figure 4-32, and visually the laser beam appears to be straight and of constant thickness. It is important, however, to understand that this is not the case since measurements should take place in the beam waist to get optimal performance from any LDA equipment. This is due to the wavefronts being straight in the beam waist and curved elsewhere. According to the previous equations, the wavefront radius approaches infinity for  $z$  approaching zero, meaning that the wavefronts are approximately straight in the immediate vicinity of the beam waist, thus letting us apply the theory of plane waves and greatly simplify calculations.

**4-10.2.2 Doppler Effect.** Laser Doppler anemometry utilizes the Doppler effect to measure instantaneous particle velocities. When particles suspended in a flow are illuminated with a laser beam, the frequency of the light scattered (and/or refracted) from the particles is different from that of the incident beam.

\* Figure schematics and photographs in Part B of this chapter are courtesy of Dantec Dynamics A/S, unless otherwise stated.



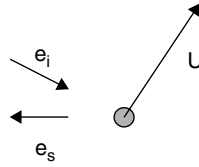


**Figure 4-33** Light scattering from a moving seeding particle.

This difference in frequency, called the *Doppler shift*, is linearly proportional to the particle velocity.

The principle is illustrated in Figure 4-33, where the vector  $\mathbf{U}$  represents the particle velocity, and the unit vectors  $\mathbf{e}_i$  and  $\mathbf{e}_s$  describe the direction of incoming and scattered light, respectively. According to the Lorenz–Mie scattering theory, the light is scattered in all directions at once, but we consider only the light reflected in the direction of the LDA receiver. The incoming light has the velocity  $c$  and the frequency  $f_i$ , but due to the particle movement, the seeding particle “sees” a different frequency,  $f_p$ , which is scattered toward the receiver. From the receiver’s point of view, the seeding particle acts as a moving transmitter, and the movement introduces additional Doppler shift in the frequency of the light reaching the receiver. Using Doppler theory, the frequency of the light reaching the receiver can be calculated as

$$f_s = f_i \frac{1 - \mathbf{e}_i \cdot (\mathbf{U}/c)}{1 - \mathbf{e}_s \cdot (\mathbf{U}/c)} \quad (4-16)$$

Even for supersonic flows the seeding particle velocity  $|\mathbf{U}|$  is much lower than the speed of light, meaning that  $|\mathbf{U}/c| \ll 1$ . Taking advantage of this, eq. (4-16) can be linearized to

$$f_s \cong f_i \left[ 1 + \frac{\mathbf{U}}{c} \cdot (\mathbf{e}_s - \mathbf{e}_i) \right] = f_i + \frac{f_i}{c} \mathbf{U} \cdot (\mathbf{e}_s - \mathbf{e}_i) = f_i + \Delta f \quad (4-17)$$

With the particle velocity  $\mathbf{U}$  being the only unknown parameter, then in principle the particle velocity can be determined from measurements of the Doppler shift  $\Delta f$ .

In practice, this frequency change can only be measured directly for very high particle velocities (using a Fabry–Perot interferometer). This is why in the commonly employed fringe mode, the LDA is implemented by splitting a laser beam to have two beams intersect at a common point so that light scattered from two intersecting laser beams is mixed, as illustrated in Figure 4-34. In this way both incoming laser beams are scattered toward the receiver, but with slightly different frequencies due to the different angles of the two laser beams. When two wavetrains of slightly different frequency are superimposed, we get the well-known phenomenon of a beat frequency due to the two waves intermittently interfering with each other constructively and destructively. The beat frequency

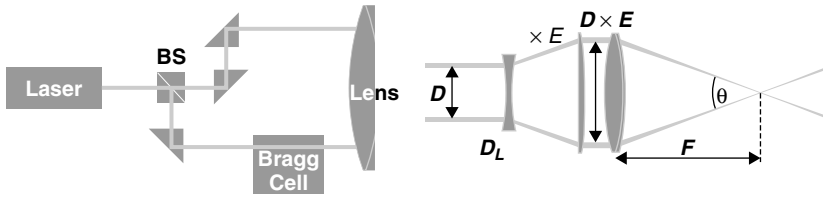


**Figure 4-34** LDA setup: left schematic shows beam splitter (BS) arrangement for creating two separate beams; right schematic shows the use of a beam expander to increase beam separation prior to focusing at a common point.

corresponds to the difference between the two wave frequencies, and since the two incoming waves originate from the same laser, they also have the same frequency,  $f_1 = f_2 = f_I$ , where the subscript I refers to the incident light:

$$\begin{aligned}
 f_D &= f_{s,2} - f_{s,1} \\
 &= f_2 \left[ 1 + \frac{\mathbf{U}}{c} \cdot (\mathbf{e}_s - \mathbf{e}_2) \right] - f_1 \left[ 1 + \frac{\mathbf{U}}{c} \cdot (\mathbf{e}_s - \mathbf{e}_1) \right] \\
 &= f_I \left[ \frac{\mathbf{U}}{c} \cdot (\mathbf{e}_1 - \mathbf{e}_2) \right] \\
 &= \frac{f_I}{c} (|\mathbf{e}_1 - \mathbf{e}_2| \cdot |\mathbf{U}| \cdot \cos \varphi) \\
 &= \frac{1}{\lambda} \cdot 2 \sin(\theta/2) \cdot u_x = \frac{2 \sin(\theta/2)}{\lambda} u_x
 \end{aligned} \tag{4-18}$$

where  $\theta$  is the angle between the incoming laser beams and  $\varphi$  is the angle between the velocity vector  $\mathbf{U}$  and the direction of measurement. Note that the unit vector  $\mathbf{e}_s$  has dropped out of the calculation, meaning that the position of the receiver has no direct influence on the frequency measured. (According to the Lorenz–Mie light scattering theory, the position of the receiver will, however, have considerable influence on signal strength.) The beat frequency, also called the Doppler frequency  $f_D$ , is much lower than the frequency of the light itself, and it can be measured as fluctuations in the intensity of the light reflected from the seeding particle. As shown in eq. (4-18), the x-component of the particle velocity is directly proportional to the Doppler frequency and thus can be calculated directly from  $f_D$ :

$$u_x = \frac{\lambda}{2 \sin(\theta/2)} f_D \tag{4-19}$$

Further discussion on LDA theory and different modes of operation may be found in the classic texts of Durst et al. (1976) and Watrasiewicz and Rudd (1976).

### 4-10.3 LDA Implementation

**4-10.3.1 Fringe Model.** Although the description of LDA above is accurate, it may be intuitively difficult to quantify. To handle this, the fringe model is commonly used in LDA as a reasonably simple visualization producing the correct results. When two coherent laser beams intersect, they will interfere in the volume of the intersection. If the beams intersect in their respective beam waists, the wave fronts are approximately plane, and consequently, the interference will produce parallel planes of light and darkness as shown in Figure 4-35. The interference planes are known as *fringes*, and the distance,  $\delta_f$ , between them depends on the wavelength and the angle between the incident beams:

$$\delta_f = \frac{\lambda}{2 \sin(\theta/2)} \quad (4-20)$$

The fringes are oriented normal to the  $x$ -axis, so the intensity of light reflected from a particle moving through the measuring volume will vary with a frequency proportional to the  $x$ -component,  $u_x$ , of the particle velocity:

$$f_D = \frac{u_x}{\delta_f} = \frac{2 \sin(\theta/2)}{\lambda} u_x \quad (4-21)$$

If the two laser beams do not intersect at the beam waists but elsewhere in the beams, the wavefronts will be curved rather than plane, and as a result the fringe spacing will not be constant but depend on the position within the intersection volume. As a consequence, the measured Doppler frequency will also depend on the particle position, and as such it will no longer be directly proportional to the particle velocity, hence resulting in a velocity bias.

**4-10.3.2 Measuring Volume.** Measurements take place in the intersection between the two incident laser beams, and the measuring volume is defined as the volume within which the modulation depth is higher than  $e^{-2}$  times the peak core value. Due to the Gaussian intensity distribution in the beams, the measuring

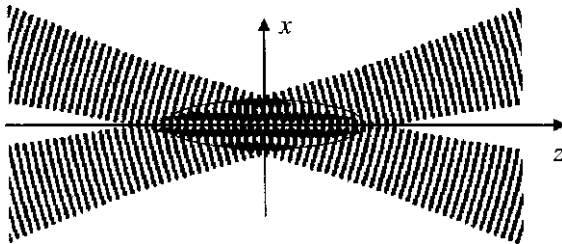


**Figure 4-35** Fringes at the point of intersection of two coherent beams.

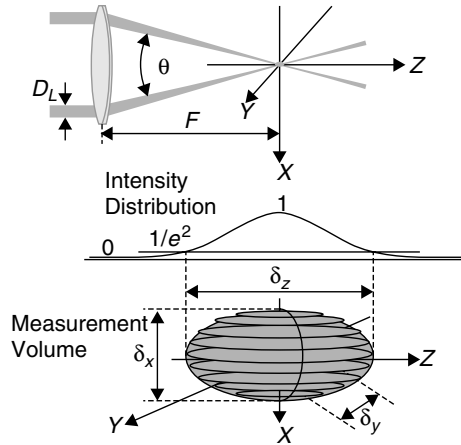


Figure 4-36 LDA measurement volume.

volume is an ellipsoid, as indicated in Figure 4-36. Its dimensions are as follows:

$$\text{length: } \delta_z = \frac{4F\lambda}{\pi ED_L \sin(\theta/2)} \tag{4-22}$$

$$\text{width: } \delta_y = \frac{4F\lambda}{\pi ED_L} \tag{4-23}$$

$$\text{height: } \delta_x = \frac{4F\lambda}{\pi ED_L \cos(\theta/2)} \tag{4-24}$$

where  $F$  is the focal length of the lens,  $E$  the beam expansion (see Figure 4-34), and  $D_L$  the initial beam thickness ( $e^{-2}$ ).

As important are the fringe separation and number of fringes in the measurement volume. These are given by:

$$\text{fringe separation: } \delta_f = \frac{\lambda}{2 \sin(\theta/2)} \tag{4-25}$$

$$\text{Number of fringes: } N_f = \frac{8F \tan(\theta/2)}{\pi ED_L} \tag{4-26}$$

This number of fringes applies for a seeding particle moving straight through the center of the measuring volume along the  $x$ -axis. If the particle passes through the outskirts of the measuring volume, it will pass fewer fringes, and consequently there will be fewer periods in the recorded signal from which to estimate the Doppler frequency. To get good results from the LDA equipment, one should ensure a sufficiently high number of fringes in the measuring volume. Typical LDA setups produce between 10 and 100 fringes, but in some cases reasonable results may be obtained with less, depending on the electronics or technique

used to determine the frequency. The key issue here is the number of periods produced in the oscillating intensity of the reflected light, and while modern processors using FFT technology can estimate particle velocity from as little as one period, the accuracy will improve with more periods.

**4-10.3.3 Backscatter versus Forward Scatter.** A typical LDA setup in the *forward scatter mode* is shown in Figure 4-37. The figure also shows the important components of a modern commercial LDA system. The majority of light from commonly used seeding particles is scattered in a direction away from the transmitting laser, and in the early days of LDA, forward scattering was commonly used, meaning that the receiving optics was positioned opposite the transmitting aperture [consult the text by Hulst (1981) for a discussion of light scattering].

A much smaller amount of light is scattered back towards the transmitter, but advances in technology have made it possible to make reliable measurements even on these faint signals, and today backward scatter is the usual choice in LDA. This *backscatter LDA* allows for the integration of transmitting and receiving optics in a common housing (as seen in Figure 4-38), saving the user a lot of tedious and time-consuming work aligning separate units.

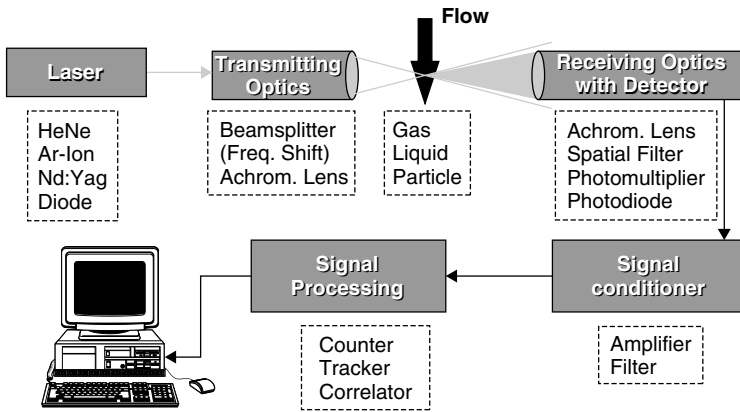


Figure 4-37 Schematic of components for a typical LDA system.

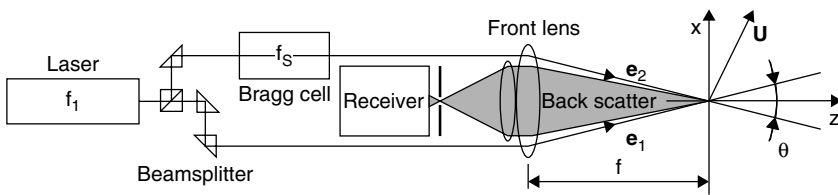


Figure 4-38 Principles of a backscatter LDA system.

Forward scattering LDA is not completely obsolete, however, since in some cases its improved signal-to-noise ratio makes it the only way to obtain measurements at all. Experiments requiring forward scatter might include:

- High-speed flows, requiring very small seeding particles, which stay in the measuring volume for a very short time, and thus receive and scatter a very limited number of photons.
- Transient phenomena which require high data rates in order to collect a reasonable amount of data over a very short period of time.
- Very low turbulence intensities, where the turbulent fluctuations might drown in noise if measured with backscatter LDA.

Forward and backscattering is identified by the position of the receiving aperture relative to the transmitting optics. Another option is *off-axis scattering*, where the receiver is looking at the measuring volume at an angle. Like forward scattering, this approach requires a separate receiver and thus involves careful alignment of the different units, but it helps to mitigate an intrinsic problem present in both forward and backscatter LDA. As indicated in Figure 4-36, the measuring volume is an ellipsoid, and usually the major axis  $\delta_z$  is much bigger than the two minor axes  $\delta_x$  and  $\delta_y$ , rendering the measuring volume more or less cigar-shaped. This makes forward and backscattering LDA sensitive to velocity gradients within the measuring volume, and in many cases also disturbs measurements near surfaces due to reflection of the laser beams.

Figure 4-39 illustrates how off-axis scattering reduces the effective size of the measuring volume. Seeding particles passing through either end of the measuring volume will be ignored since they are out of focus, and as such contribute to background noise rather than to the actual signal. This reduces the sensitivity to velocity gradients within the measuring volume, and the off-axis position of the receiver automatically reduces problems with reflection. These properties make off-axis scattering LDA very efficient, for example, in boundary layer or near-surface measurements.

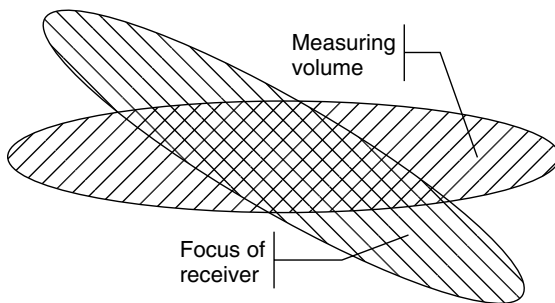


**Figure 4-39** Off-axis scattering.

**4-10.3.4 Optics.** In modern LDA equipment the light from the beamsplitter and the Bragg cell is sent through optical fibers, as is the light scattered back from seeding particles. This reduces the size and the weight of the probe itself, making the equipment flexible and easier to use in practical measurements. A photograph of a pair of commercially available LDA probes is shown in Figure 4-40. The laser, beamsplitter, Bragg cell, and photodetector (receiver) can be installed stationary and out of the way, while the LDA probe can be traversed between different measuring positions.

It is normally desired to make the measuring volume as small as possible. According to the formulas above, this means that the beam waist,

$$d_f = \frac{4F\lambda}{\pi ED_L} \quad (4-27)$$

should be small. The laser wavelength  $\lambda$  is a fixed parameter, and focal length  $F$  is normally limited by the geometry of the model being investigated. Some lasers allow for adjustment of the beam waist position, but the beam waist diameter  $D_L$  is normally fixed. This leaves beam expansion as the only remaining way to reduce the size of the measuring volume. When no beam expander is installed,  $E = 1$ .

A beam expander is a combination of lenses in front of or replacing the front lens of a conventional LDA system. It converts the beams exiting the optical system to beams of greater width. At the same time, the spacing between the two laser beams is increased, since the beam expander also increases the aperture. Provided that the focal length  $F$  remains unchanged, the larger beam spacing will thus increase the angle  $\theta$  between the two beams. According to the formulas in Section 4-10.3.2, this will further reduce the size of the measuring volume.



**Figure 4-40** Modern commercial fiber optic-based LDA probes.

In agreement with the fundamental principles of wave theory, a larger aperture is able to focus a beam to a smaller spot size and hence generate greater light intensity from the scattering particles. At the same time the greater receiver aperture is able to pick up more of the reflected light. As a result, the benefits of the beam expander are threefold:

- Reduce the size of the measuring volume at a given measuring distance.
- Improve the signal-to-noise ratio at a given measuring distance, or
- Reach greater measuring distances without sacrificing the signal-to-noise ratio.

**4-10.3.5 Frequency Shift.** A drawback of the LDA technique described so far is that negative velocities  $u_x < 0$  will produce negative frequencies  $f_D < 0$ . However, the receiver cannot distinguish between positive and negative frequencies, and as such, there will be a directional ambiguity in the measured velocities. To handle this problem, a Bragg cell is introduced in the path of one of the laser beams (as shown in Figure 4-34). The Bragg cell shown in Figure 4-41 is a block of glass. On one side, an electromechanical transducer driven by an oscillator produces an acoustic wave propagating through the block generating a periodic moving pattern of high and low density. The opposite side of the block is shaped to minimize reflection of the acoustic wave and is attached to a material absorbing the acoustic energy.

The incident light beam hits a series of traveling wavefronts that act as a thick diffraction grating. Interference of the light scattered by each acoustic wavefront causes intensity maxima to be emitted in a series of directions. By adjusting the acoustic signal intensity and the tilt angle,  $\theta_B$ , of the Bragg cell, the intensity balance between the direct beam and the first order of diffraction can be adjusted. In modern LDA equipment this is exploited, using the Bragg cell itself as the

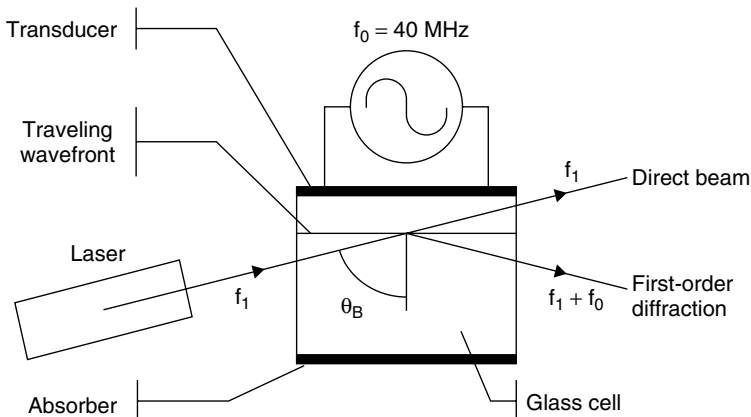


**Figure 4-41** Principles of operation of a Bragg cell.



beamsplitter. Not only does this eliminate the need for a separate beamsplitter, but it also improves the overall efficiency of the light-transmitting optics, since more than 90% of the lasing energy can be made to reach the measuring volume, effectively increasing the signal strength.

The Bragg cell adds a fixed frequency shift  $f_0$  to the diffracted beam, which then results in a measured frequency off a moving particle of

$$f_D \simeq f_0 + \frac{2 \sin(\theta/2)}{\lambda} u_x \quad (4-28)$$

and as long as the particle velocity does not introduce a negative frequency shift numerically larger than  $f_0$ , the Bragg cell with thus ensure a measurable positive Doppler frequency  $f_D$ . In other words, the frequency shift  $f_0$  allows measurement of velocities down to

$$u_x > -\frac{\lambda f_0}{2 \sin(\theta/2)} \quad (4-29)$$

without directional ambiguity (Figure 4-42). Typical values might be  $\lambda = 500$  nm,  $f_0 = 40$  MHz,  $\theta = 20^\circ$ , allowing of negative velocity components down to  $u_x > -57.6$  m/s. Upward, the maximum measurable velocity is limited only by the response time of the photomultiplier and the signal-conditioning electronics. In modern commercial LDA equipment, such a maximum is well into the supersonic velocity regime.

**4-10.3.6 Signal Processing.** The primary result of a laser anemometer measurement is a current pulse from the photodetector. This current contains the frequency information relating to the velocity to be measured. The photocurrent also contains noise, with sources for this noise being:

- Photodetection shot noise
- Secondary electronic noise
- Thermal noise from preamplifier circuit
- Higher-order laser modes (optical noise)
- Light scattered from outside the measurement volume, dirt, scratched windows, ambient light, multiple particles, etc.
- Unwanted reflections (windows, lenses, mirrors, etc.)

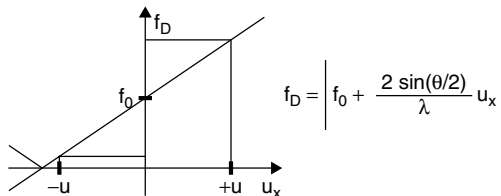


**Figure 4-42** Resolving directional ambiguity using frequency shift.

The primary source of noise is the photodetection shot noise, which is a fundamental property of the detection process. The interaction between the optical field and the photo-sensitive material is a quantum process, which unavoidably impresses a certain amount of fluctuation on the mean photocurrent. In addition, there is mean photocurrent and shot noise from undesired light reaching the photodetector. Much of the design effort for the optical system is aimed at reducing the amount of unwanted reflected laser light or ambient light reaching the detector.

A laser anemometer is most advantageously operated under such circumstances that the shot noise in the signal is the predominant noise source. This shot noise-limited performance can be obtained by proper selection of laser power, seeding particle size, and optical system parameters. In addition, noise should be minimized by selecting only the minimum bandwidth needed for measuring the desired velocity range by setting low- and high-pass filters in the signal processor input. Very important for the quality of the signal, and the performance of the signal processor, is the number of seeding particles present simultaneously in the measuring volume. If on average much less than one particle is present in the volume, we speak of a burst-type Doppler signal. Typical Doppler burst signals are shown in Figure 4-43. Figure 4-43a shows the filtered signal which is actually input to the signal processor. The DC part, which was removed by the high-pass filter, is known as the *Doppler pedestal*, and it is often used as a trigger signal, which starts sampling of an assumed burst signal. The envelope of the Doppler-modulated current reflects the Gaussian intensity distribution in the measuring volume.

If more particles are present in the measuring volume simultaneously, we speak of a multiparticle signal. The detector current is the sum of the current bursts from each individual particle within the illuminated region. Since the particles are located randomly in space, the individual current contributions are added with random phases, and the resulting Doppler signal envelope and phase will fluctuate. Most LDA processors are designed for single-particle bursts, and with a multiparticle signal, they will normally estimate the velocity as a weighted average of the particles within the measuring volume. One should be aware, however, that the random-phase fluctuations of the multiparticle LDA signal

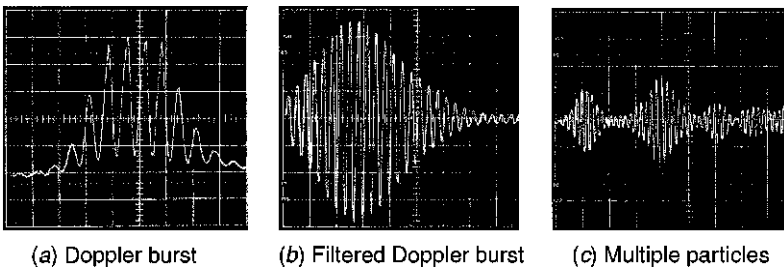


**Figure 4-43** Typical single- and multiple-particle Doppler bursts.

add a phase noise to the detected Doppler frequency which is very difficult to remove.

To better estimate the Doppler frequency of noisy signals, frequency-domain processing techniques are used. With the advent of fast digital electronics, the fast Fourier transform of digitized Doppler signals can now be performed at a very high rate (hundreds of kHz). The power spectrum  $S$  of a discretized Doppler signal  $x$  is given by

$$S_k = \left| \sum_{n=0}^{N-1} x_n \exp\left(\frac{-j2\pi kn}{2N}\right) \right|^2 \quad (4-30)$$

where  $N$  is the number of discrete samples, and  $K = -N, -N + 1, \dots, N - 1$ . The Doppler frequency is given by the peak of the spectrum.

**4-10.3.7 Data Analysis.** In LDA there are two major problems faced when making a statistical analysis of the measurement data: velocity bias and the random arrival of seeding particles to the measuring volume. Although velocity bias is the predominant problem for simple statistics, such as mean and RMS values, the random sampling is the main problem for statistical quantities that depend on the timing of events, such as spectrum and correlation functions (see Tropea, 1995).

Figure 4-44 illustrates the calculation of moments, correlation, and spectra on the basis of measurements received from the processor. The velocity data coming from the processor consist of  $N$  validated bursts, collected during the time  $T$ , in a flow with the integral time scale  $\tau_1$ . For each burst the arrival time  $a_i$  and the transit time  $t_i$  of the seeding particle is recorded along with the non-Cartesian velocity components  $(u_i, v_i, w_i)$ . The different topics involved in the analysis are described in more detail in the open literature and will be touched upon briefly in the following section.

## 4-10.4 Making Measurements

**4-10.4.1 Dealing with Multiple Probes (3D Setup).** The non-Cartesian velocity components  $(u_1, u_2, u_3)$  are transformed to Cartesian coordinates  $(u, v, w)$  using the transformation matrix  $C$ :

$$\begin{Bmatrix} u \\ v \\ w \end{Bmatrix} = \begin{Bmatrix} C_{11} & C_{12} & C_{13} \\ C_{21} & C_{22} & C_{23} \\ C_{31} & C_{32} & C_{33} \end{Bmatrix} \cdot \begin{Bmatrix} u_1 \\ u_2 \\ u_3 \end{Bmatrix} \quad (4-31)$$

A typical 3D LDA setup requiring coordinate transformation is depicted in Figure 4-45, where 3D velocity measurements are performed with a 2D probe

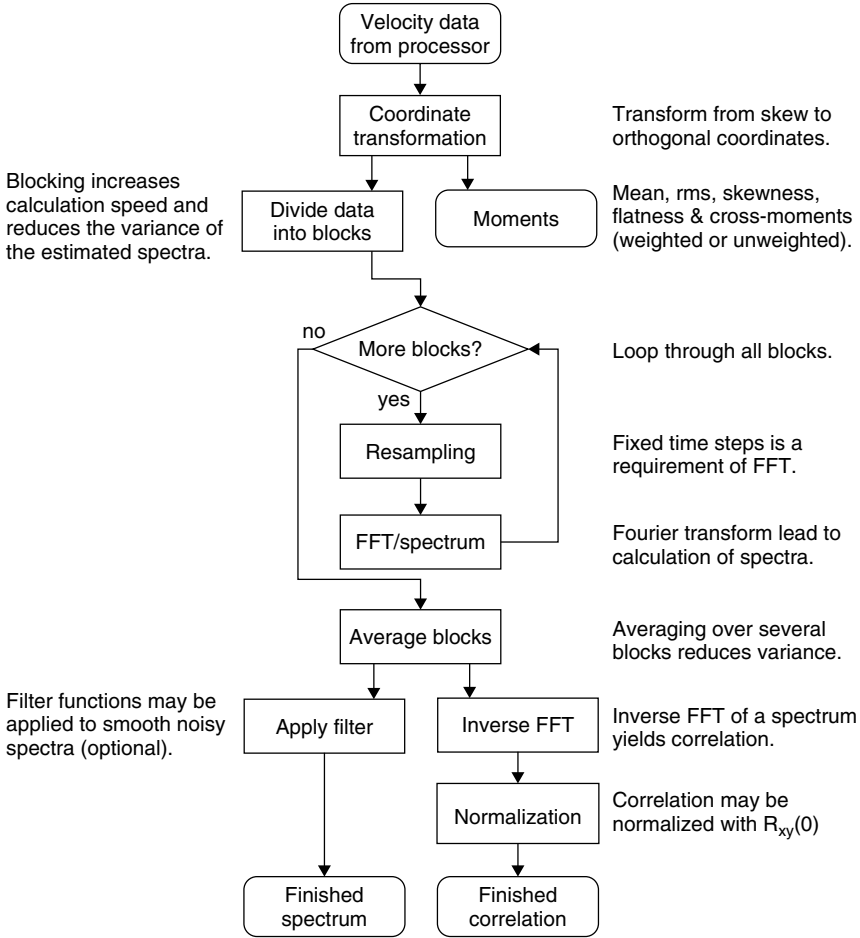


**Figure 4-44** Block diagram of data analysis and calculation from velocity estimate received from LDA processor.

positioned at off-axis angle  $\alpha_1$  and a 1D probe positioned at off-axis angle  $\alpha_2$ . The transformation for this case is

$$\begin{Bmatrix} u \\ v \\ w \end{Bmatrix} = \begin{Bmatrix} 1 & 0 & 0 \\ 0 & -\frac{\sin \alpha_2}{\sin(\alpha_1 - \alpha_2)} & \frac{\sin \alpha_1}{\sin(\alpha_1 - \alpha_2)} \\ 0 & \frac{\cos \alpha_2}{\sin(\alpha_1 - \alpha_2)} & \frac{\cos \alpha_1}{\sin(\alpha_1 - \alpha_2)} \end{Bmatrix} \cdot \begin{Bmatrix} u_1 \\ u_2 \\ u_3 \end{Bmatrix} \quad (4-32)$$

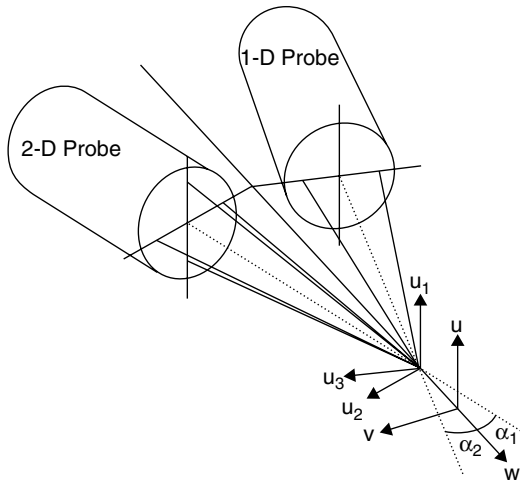


**Figure 4-45** Typical configuration of 3D LDA system.

**4-10.4.2 Calculating Moments.** Moments are the simplest form of statistics that can be calculated for a set of data. The calculations are based on individual samples, and the possible relations between samples are ignored, as is the timing of events. This leads to moments sometimes being referred to as one-time statistics, since samples are treated one at a time.

Table 4-2 lists the formulas used to estimate the moments. The table operates with velocity components  $x_i$  and  $y_i$ , but this is just examples, and could of course be any velocity component, Cartesian or not. It could even be samples of an external signal representing pressure, temperature, or something else. George (1978) gives a good account of the basic uncertainty principles governing the statistics of correlated time series with emphasis on the differences between equal-time and Poisson sampling (LDA measurements fall in the latter). Statistics treated by George include the mean, variance, autocorrelation, and power spectra. A recent publication by Benedict and Gould (1996) gives methods of determining uncertainties for higher-order moments.

**4-10.4.3 Velocity Bias and Weighting Factor.** Even for incompressible flows where the seeding particles are statistically uniformly distributed, the sampling process is not independent of the process being sampled (i.e., the velocity field). Measurements have shown that the particle arrival rate and the flow field are strongly correlated (McLaughlin and Tiedermann, 1973; Erdmann and Gellert, 1976). During periods of higher velocity, a larger volume of fluid is swept through the measuring volume, and consequently, a greater number of velocity samples will be recorded. As a direct result, an attempt to evaluate the statistics of the flow field using arithmetic averaging will bias the results in favor of the higher velocities.

**Table 4-2** Definition of Statistical Measures Often Used for Turbulence Characterization

Mean	$\bar{u} = \sum_{i=0}^{N-1} \eta_i u_i$
Variance	$\sigma^2 = \sum_{i=0}^{N-1} \eta_i (u_i - \bar{u})^2$
RMS	$\sigma = \sqrt{\sigma^2}$
Turbulence	$Tu = \frac{\sigma}{\bar{u}} \cdot 100\%$
Skewness	$S = \frac{1}{\sigma^3} \sum_{i=0}^{N-1} \eta_i (u_i - \bar{u})^3$
Flatness	$F = \frac{1}{\sigma^4} \sum_{i=0}^{N-1} \eta_i (u_i - \bar{u})^4$
Cross-moments	$\overline{uv} - \bar{u}\bar{v} = \sum_{i=0}^{N-1} \eta_i (u_i - \bar{u})(v_i - \bar{v})$

There are several ways to deal with this issue:

- *Ensure statistically independent samples.* The time between bursts must exceed the integral time scale of the flow field at least by a factor of 2. Then the weighting factor corresponds to the arithmetic mean,  $\eta_i = 1/N$ . Statistically independent samples can be accomplished by using very low concentration of seeding particles in the fluid.
- *Use dead-time mode.* The dead time is a specified period of time after each detected Doppler burst, during which further bursts will be ignored. Setting the dead time equal to two times the integral time scale will ensure statistically independent samples, while the integral time scale itself can be estimated from a previous series of velocity samples, recorded with the dead-time feature switched off.
- *Use bias correction.* If one plans to calculate correlations and spectra on the basis of measurements performed, the resolution achievable will be greatly reduced by the low data rates required to ensure statistically independent samples. To improve the resolution of the spectra, a higher data rate is needed, which, as explained above, will bias the estimated average velocity. To correct this velocity bias, a nonuniform weighting factor is introduced:

$$\eta_i = \frac{t_i}{\sum_{j=0}^{N-1} t_j} \quad (4-33)$$

The bias-free method of performing the statistical averages on individual realizations uses the transit time,  $t_i$ , weighting (see George, 1976). Additional information on the transit time weighting method can be found in George (1978), Buchhave et al. (1979), Buchhave (1979), and Benedict and Gould (1999). In the literature, transit time is sometimes referred to as *residence time*.

#### 4-10.5 LDA Applications in Mixing

**4-10.5.1 Experimental Considerations.** There are several important experimental issues specific to the application of LDA to mixing experiments, particularly in stirred tanks.

*Curvature.* As the laser beams travel through curved surfaces, they are deflected due to changes in the refractive index. This produces a lensing effect that moves the measuring volume away from its expected location. The problem can be addressed in two ways: by refractive index matching of the fluid with the vessel, or by performing beam tracing calculations to correct for the displacement (see Kresta and Wood, 1993).

*Use of Vessel Symmetry to Obtain Three Velocity Components.* The velocity component measured is perpendicular to the interference fringes shown in Figure 4-35. When the plane defined by the beams is vertical and the beam angle bisector is horizontal, the vertical velocity component ( $z$ -component) is measured. When the beams are in a horizontal plane, two velocity components can be measured, depending on the location of the beams in the tank. If the beam angle bisector intercepts the shaft, the angular velocity ( $\theta$ -component) is measured. If a traverse at  $90^\circ$  to this is used, the radial velocity ( $r$ -component) is measured. Looking into the tank from the laser, moving forward and backward in front of the shaft axis (toward the six o'clock position from the top of the tank) will give the angular or tangential velocity. Moving sideways (toward the three o'clock or the nine o'clock position) will give the radial velocity. This assumes  $90^\circ$  symmetry of the tank, an assumption that has been validated for several tank geometries.

*Reflections from the Shaft and Impeller.* Signal quality close to the shaft or impeller can be improved by minimizing reflections. This can be done with black matte paint or by anodizing the parts after fabrication.

*Impeller Geometry.* The impeller geometry must be exactly scaled down from full scale dimensions. Thickness of blades, hub size, hub thickness, and placement of blades can all have significant effects on power draw, velocity profiles, and turbulence characteristics.

*Shaft Encoding.* LDV measurements in stirred vessels are typically combined with shaft encoding so that the velocity can be analyzed either as a long-time

average at a fixed position in the tank, or as ensemble-averaged data relative to a specific angular position of the impeller. This is particularly important if the trailing vortices leaving the impeller blades are the feature of greatest interest. Many papers have been published that use this method (e.g., Yianneskis et al., 1987; Schaffer et al., 1997).

#### **4-10.5.2 Uses of LDV Data**

*Impeller Characterization.* The first stage of characterization of a new impeller will typically involve measurement of the mean velocity and RMS velocity profiles very close to the impeller. The position of the traverses relative to the impeller is crucial, as the velocity gradients are very steep in this region. The velocity drops quickly as one moves away from the impeller. These velocity traverses are used to define the flow number and the momentum of the fluid leaving the impeller and to characterize the turbulence intensity close to the impeller. The reader should note that streak photography is typically undertaken before LDV. This qualitative method will show the average user a great deal about the flow field without the full expense of LDV measurements. Quantitative full field measurements can be obtained using particle image velocimetry as an alternative to LDV.

*CFD Validation.* LDV measurements are widely used for validation of CFD codes. Velocity measurements can be compared directly with the results of simulations. There are some subtleties here as the simulations become more complex. When steady simulations are performed using velocity boundary conditions around the impeller, mean velocity measurements are used to validate circulation patterns and the RMS velocity components are combined for comparison with the simulated turbulent kinetic energy  $k$ . If trailing vortices dominate, as they do for the Rushton turbine, shaft-encoded LDV data are compared with the results of sliding mesh simulations, which are ensemble averaged. If macroinstabilities are of interest, large eddy simulations offer the next step of resolution in the time-varying flow. The definition of turbulence quantities for the second and third cases is still a topic of active research. When considering CFD validation, the reader will benefit from careful consideration of how best to characterize the flow: What are the key characteristics to be replicated, and how will they be validated?

*Turbulence Characterization.* LDV has been widely used to characterize the turbulence close to impellers. This work requires careful reflection and detailed experimental work. Approaches range from estimates (Zhou and Kresta, 1996) to full turbulent energy balances (Escudie, 2001) and direct measurements of the dissipation (Michelet, 1998). The best way to treat regular frequencies due to blade passages and macroinstabilities is still a topic of active investigation. Further discussion and references are given in Chapter 2 and by Kresta (1998).

*Application of Results.* It has often been noted that velocity fields, no matter how detailed, do not provide any direct information about process performance.



This is true. The power of LDV and other velocity measurement methods lies in the interpretation of the results for the improvement of process performance. Velocity field measurements close to the base of vessels can be used to clarify mechanisms of solids suspension which depend on the shape of the bottom. Velocity measurements close to the top of the vessel can be used to probe dead zones and examine the effect of changing geometry on the size of these dead zones. These measurements are very targeted and can provide very powerful information to the user. This must be balanced with consideration of the costs of purchasing and supporting LDV equipment.

## 4-11 PHASE DOPPLER ANEMOMETRY

### 4-11.1 Principles and Equations for PDA

In the LDA system discussed previously there was only one photodetector. If one considers the situation shown in Figure 4-46, two photodetectors spaced a certain distance apart will both receive the light scattered from the surface of a reflecting spherical particle. However, the difference in the optical path length for the reflections from the two incident beams changes with the position of the photodetector. This means that when the particle passes through the measuring volume, both photodetectors receive a Doppler burst of the same frequency, but the phases of the two bursts vary with the angular position of the detectors. This phenomenon was first utilized as an indication of the size of a particle by Durst and Zaré (1975).

Again it is convenient to introduce the fringe model as a first order of approximation. Figure 4-47 illustrates the intensity fluctuation in each of the photodetectors and the time lag,  $\Delta t$ , separating the wavefronts reaching the two

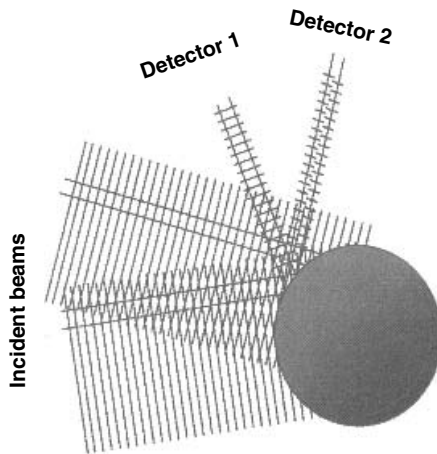


**Figure 4-46** Interference patterns at two photodetectors will differ by a certain phase.

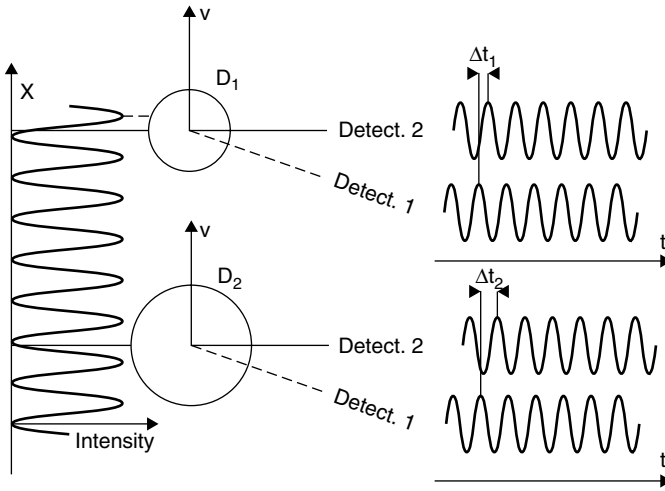


Figure 4-47 Increasing phase difference with increasing particle diameter.

photodetectors. The corresponding phase difference for reflection would be

$$\Phi = \frac{2\pi d_p}{\lambda} \frac{\sin \theta \sin \psi}{\sqrt{2(1 - \cos \theta \cos \psi \cos \phi)}} \tag{4-34}$$

given the angular position of the detectors as illustrated in Figure 4-48. The property that is of foremost importance is that the phase difference between the two Doppler bursts depends on the size of the particle, provided that all other geometric parameters of the optics remain constant. Figure 4-47 shows

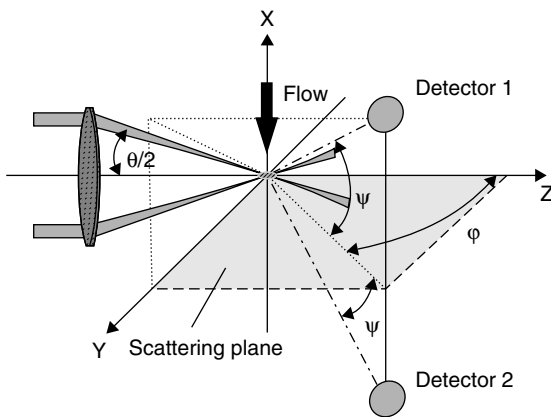


Figure 4-48 Detector setup and general coordinate system used for PDA.

two particles of different size, illustrating how the phase difference between the Doppler bursts from the large particle exceeds that of the smaller particle.

Mathematically, the phase of a Doppler burst received at detector  $i$  can be expressed as

$$\Phi_i = \alpha \cdot \beta_i \quad (4-35)$$

where the size parameter is

$$\alpha = \pi \frac{n_1}{\lambda} d_p \quad (4-36)$$

and where  $n_1$  is the refractive index of the scattering medium,  $\lambda$  the laser wavelength in vacuum, and  $d_p$  the particle diameter.

Thus, a linear relationship between particle size and phase exists. The geometrical factor,  $\beta_i$ , depends on the scattering mode and the three angles,  $\theta$ ,  $\varphi_i$ , and  $\psi_i$ . The full intersection angle between the two incident beams,  $\theta$ , determines the fringe separation, while  $\varphi_i$  and  $\psi_i$  define the direction toward the (centroid of the) photodetector from the measuring volume. The angle of intersection between the two incident beams is determined by the beam separation and the focal length of the transmitting lens. The scattering angle,  $\varphi_i$ , is measured from the axis of the transmitting optics (the bisector of the two incident beams; the Z-axis), while the azimuth angle,  $\psi_i$ , gives the rotational position about the Z-axis.

The factor  $\beta_i$  between particle diameter and phase shift also depends on the scattering mode. This is illustrated in Figure 4-49, in which ray tracing has been used to depict how incident light will scatter from a spherical particle. Three main contributions are included in the representation; reflection from the outer surface of the particle, refraction through the particle (first-order refraction), and refraction with one internal reflection (second-order refraction). The formulas expressing the geometrical factor are given below for reflection and (first-order) refraction.

*Reflection:*

$$\beta_i = \sqrt{2} \left( \sqrt{1 + \sin \frac{\theta}{2} \sin \varphi_i \sin \psi_i - \cos \frac{\theta}{2} \cos \varphi_i} - \sqrt{1 - \sin \frac{\theta}{2} \sin \varphi_i \sin \psi_i - \cos \frac{\theta}{2} \cos \varphi_i} \right) \quad (4-37)$$

Note in eq. (4-37) that the refractive index of the particle,  $n_2$ , does not appear. Hence, in practice this means that the reflection mode is a useful scattering mode to employ in situations where the exact value of the refractive index is not known.

*First-order refraction:*

$$\beta_i = 2 \left( \sqrt{1 + n_{\text{rel}}^2 - \sqrt{2} n_{\text{rel}} \sqrt{f_{i+}}} - \sqrt{1 + n_{\text{rel}}^2 - \sqrt{2} n_{\text{rel}} \sqrt{f_{i-}}} \right) \quad (4-38)$$

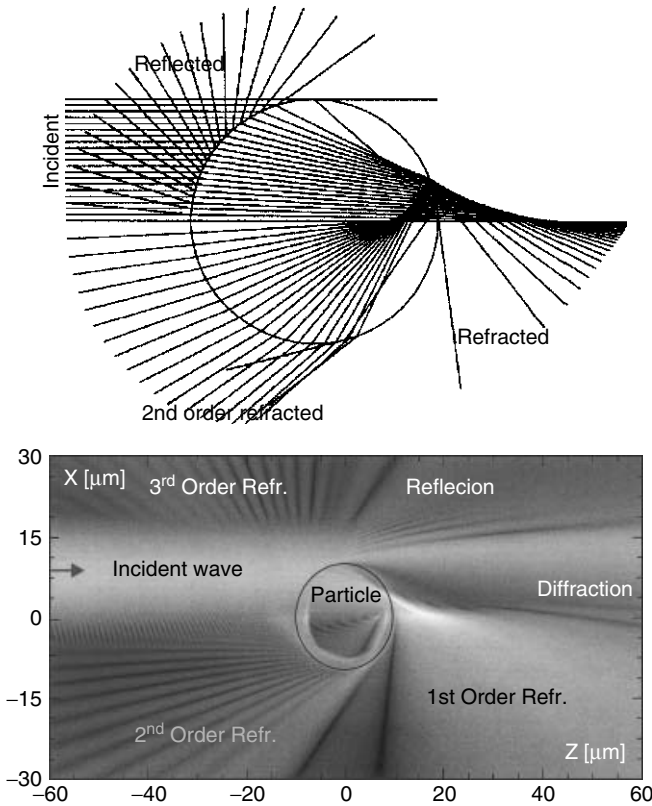


**Figure 4-49** Ray traces indicating the three significant modes of scattering—reflection and first- and second-order refraction—for a water droplet (top); light scattering of a Gaussian beam from a water droplet, simulated using the Fourier Lorenz–Mie theory (bottom; courtesy of C. Tropea and N. Damaschke, Technische Universität Darmstadt, Germany).

where

$$n_{rel} = \frac{n_2}{n_1} \tag{4-39}$$

$n_2$  is the particle refractive index, and

$$f_{i\pm} = 1 \pm \sin \frac{\theta}{2} \sin \varphi_i \sin \psi_i + \cos \frac{\theta}{2} \cos \varphi_i \tag{4-40}$$

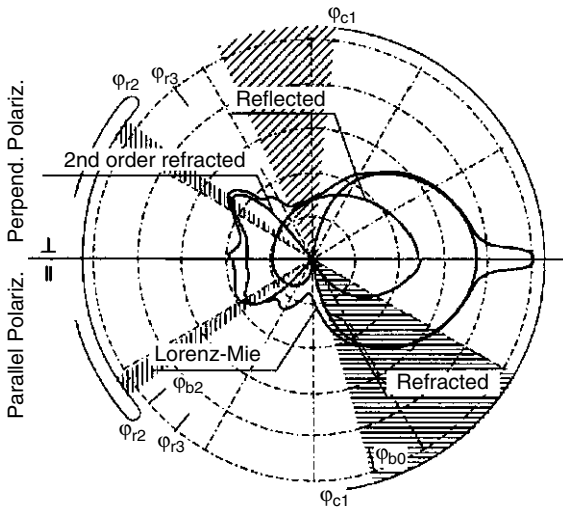
For second-order refraction,  $\beta_i$  cannot be given as a closed-form solution but must be solved for numerically by an iterative process. In this mode, small inaccuracies in the value of the refractive index of the particle may result to large errors in its diameter estimation; hence care should be used when employing this scattering mode.

### 4-11.2 Sensitivity and Range of PDA

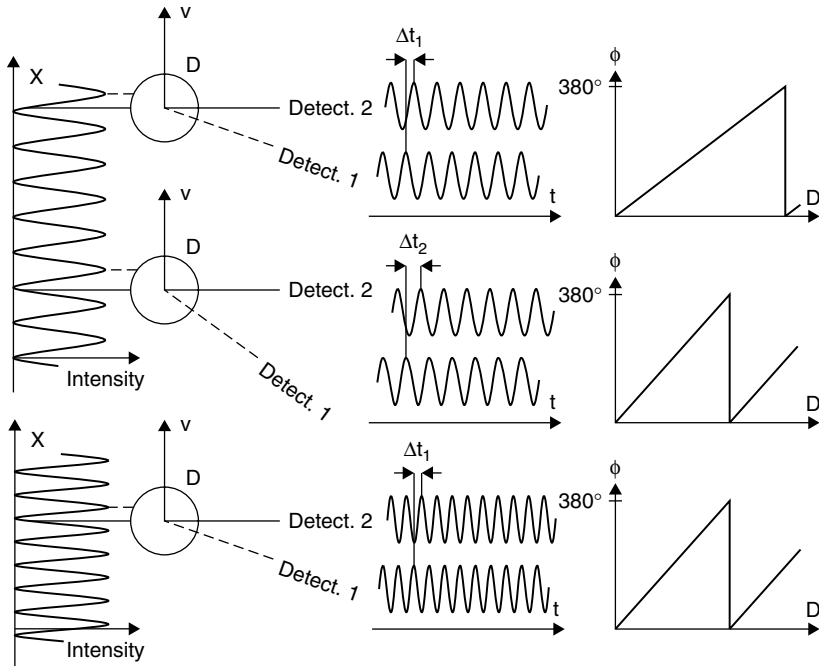
The geometric factor, and hence the sensitivity and range of the PDA, can be altered by changing any of the angles,  $\theta$ ,  $\varphi_i$ , or  $\psi_i$ . However, in practice the three angles cannot be chosen freely. Typically, the selection of the scattering angle is quite restricted, either to ensure a particular mode of scattering (see Figure 4-50) or a sufficient signal-to-noise ratio, or from practical considerations of the measurement situation. The required working distance to the measurement point also affects the possible range of  $\theta$  and  $\psi_i$ .

Figure 4-51 illustrates the increase in the slope of the diameter–phase relationship when the angular separation between the photodetectors is increased (i.e., increasing  $\psi_{12}$  in the middle), and when the fringe separation is reduced by increasing the angle  $\theta$  between the incident beams. Changing  $\psi_{12}$  only affects the slope of the diameter–phase relationship (i.e., the sensitivity and range of the sizing) and has no effect on the velocity–frequency relationship. Changing  $\theta$  affects both the slope of the diameter–phase curve and the velocity–frequency relationship. This is done in two ways: (1) by changing the focal length of the front lens of the transmitting optics, and (2) by changing the beam separation.

**4-11.2.1 Handling the  $2\pi$  Ambiguity.** Figure 4-52 shows the phase difference for three different particles of increasing size. While the phase difference for the first two particles is within  $2\pi (= 360^\circ)$ , the third particle falls beyond this range. Thus, from measuring the phase difference between the Doppler bursts



**Figure 4-50** Light intensity distribution of a water droplet (log scale, one decade between each circle) for each of the scattering modes is shown in a polar plot for scattering angles from 0 to  $180^\circ$  and for two polarizations, the upper half at  $90^\circ$  to the scattering plane and the lower half parallel to the scattering plane.



**Figure 4-51** Effect of changing the azimuth angle,  $\psi$ , and the angle between the incident beams,  $\theta$ , on the slope of the diameter–phase relationship.

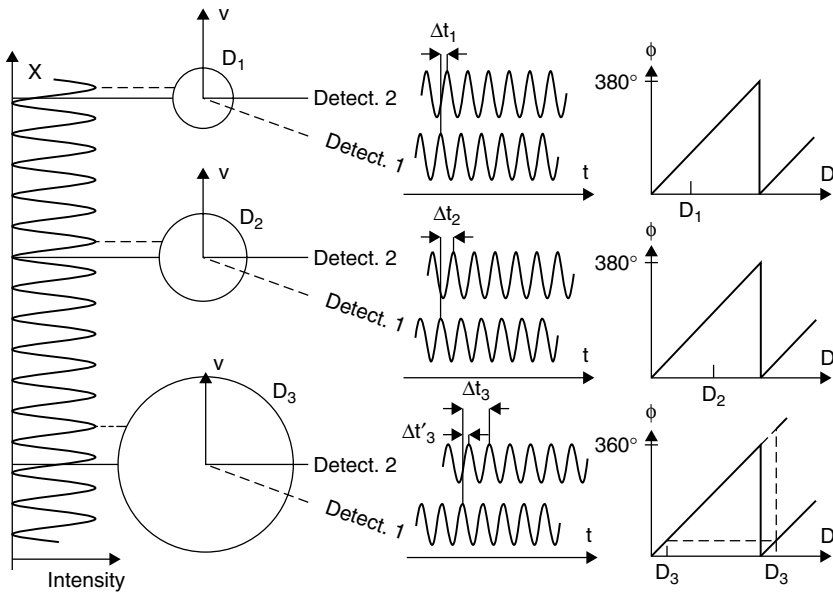


**Figure 4-52** The  $2\pi$  ambiguity in PDA.

received by the two detectors alone there is no way to tell whether the diameter is  $D_3$  or  $D'_e$  (corresponding to the phase difference of  $-2\pi$ ). This uncertainty is referred to as the  $2\pi$  ambiguity in PDA. Under such conditions, a compromise is necessary between either high sensitivity and small measurement size range, or a larger measurement size range at the expense of sensitivity.

The solution to this problem is to use additional detectors. In conventional PDA a third detector is introduced so that the three are symmetrically positioned. Two detectors, U1 and U2, form the more distant pair giving the greater slope of the diameter–phase relationship and hence higher resolution and smaller working range. The detectors U1 and U3 form another pair, less separated and therefore giving a smaller slope to the diameter–phase relationship. This corresponds to a larger measurement size range but lower resolution. By comparing the phase differences from the two detector pairs, one can achieve at the same time, the high resolution and the large measurement range (see Figure 4-53).

**4-11.2.2 Particle Sphericity.** The two-detector-pair arrangement has another useful feature, and that is to give information with regard to the curvature over a certain arc of the particle surface. If the curvature measured at two different locations on the surface (phase difference) is identical, the particle is said to be *spherical*. If the two local curvatures differ,  $\Phi_{12}$  and  $\Phi_{13}$  will point at diameter values differing by  $\Delta D$ . Consequently, a measure of the deviation from sphericity is available, and if  $\Delta D$  exceeds a certain limit set by the user, the particle is said to be invalid. The underlying equations of size determination using the PDA technique assume that the particle is spherical, and hence any deviation from this assumption will introduce errors in the absolute determination of the particle size.

Ideally, the sum of the phase differences,  $\Phi_{12}$ ,  $\Phi_{23}$ , and  $\Phi_{31}$ , is zero. However, due to the uncertainty of the phase measurements, this measured sum will deviate from zero. The absolute value of this deviation is the closed-loop phase error, which must not be greater than a certain value (to be set by the user in the software) for the particle to be accepted. This value should be typically set in the range  $10$  to  $15^\circ$ .

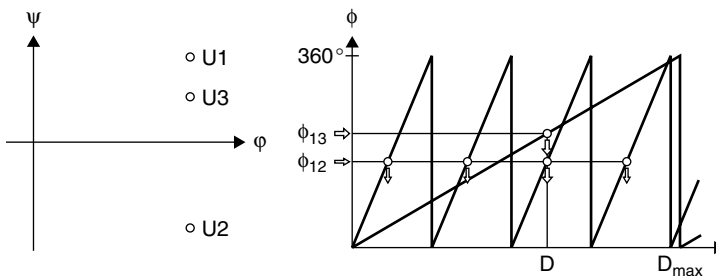


**Figure 4-53** Different slopes of the diameter–phase relation obtained in a conventional PDA setup with two pairs of photodetectors at different separations.

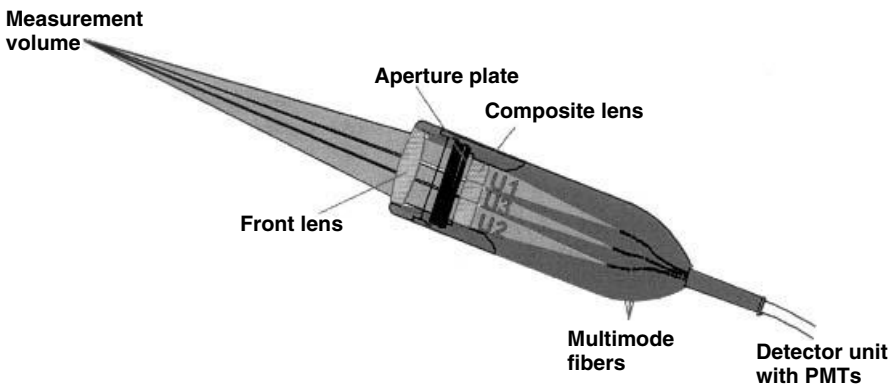
### 4-11.3 Implementation of PDA

There are three different optical configurations that can be used for size measurements using a PDA. These configurations are determined by the different modes of light scattering (see Figure 4-49):

- (First-order) refraction
- Reflection
- Second-order refraction

The majority of PDA applications make use of light scattered by first-order refraction. However, there can be several reasons for choosing one of the other two modes of light scattering. In any case, you should make sure that the selected mode of light scattering is dominating (i.e., the intensity of light scattered by one of the other modes is at least one order of magnitude smaller than the mode selected). Utilization of light scattering analysis codes is generally recommended for this purpose. A typical result of a light-scattering analysis computation is shown in Figure 4-50. Table 4-3 summarizes the application of the three modes.

**4-11.3.1 PDA Receiver Optics.** As with the LDA probes, commercial PDA equipment implements a fiber optic design to integrate all detectors in a single portable unit, as shown in Figure 4-54. Such units feature the flexibility of adjustable azimuthal positions (by means of exchangeable aperture plates) in combination with the convenience of alignment through a single common front lens. The front lens works as a collimator creating a beam of parallel light. This beam passes through an aperture plate, which divides the parallel light beam into three segments corresponding to the photodetectors U1, U2, and segmented lens then focuses each beam onto one of three slit-shaped spatial filters in front of an optical fiber that transmits the scattered light to the photodetectors.

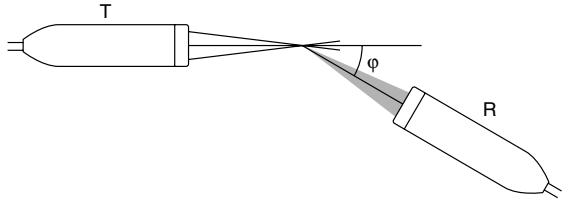


**Figure 4-54** Basic layout of a typical fiber optic-based PDA receiving probe.

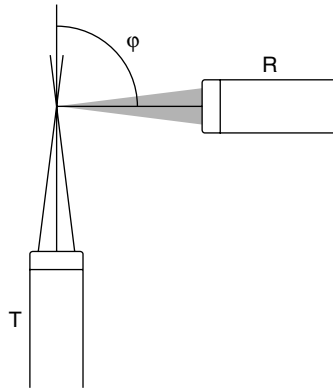


**Table 4-3** Summary of PDA Measuring Modes<sup>a</sup>*First-order refraction*

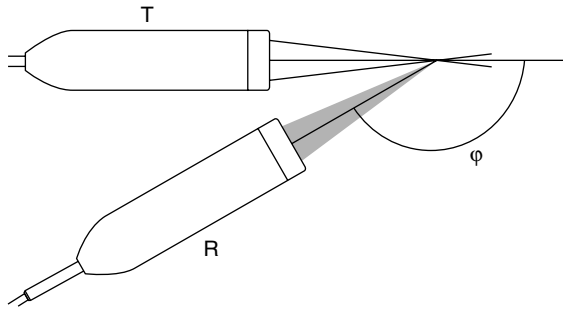
Transparent droplets: water or oil. Moderately great scattering angle (around  $70^\circ$ ) is favored since the measured size will be independent of small changes of refractive index. Smaller angle ( $30^\circ$ ) is good when the signal-to-noise ratio is poor, due to higher scattered light intensity.

*Reflection*

Reflective particles or bubbles ( $n_{\text{rel}} < 1$ ). For bubbles, scattering angle should be slightly less than  $90^\circ$ . Useful when the exact value of the relative refractive index is not known.

*Second-order refraction*

Transparent droplets. Scattering angle should be chosen carefully to yield a linear diameter-phase relationship. Accurate knowledge of the refractive index is required. Should be used only when physical restrictions, such as limited optical access, make it mandatory.



<sup>a</sup>Schematics show configuration with T and R labeling transmitting and receiving optics, respectively (the direction of flow is perpendicular to the plane of the illustrations). (Courtesy of Dantec Dynamics A/S.)

The measurable size range is determined by the following parameters:

- Beam intersection angle of the transmitting optics (defined by the beam separation and the front lens focal length)
- Focal length of the receiving front lens
- Aperture plate (controls azimuth angle)
- Selected scattering mode
- Scattering angle

All these parameters can be varied independently from one another to achieve a variety of size ranges that can be measured. As mentioned earlier, the working distance and optical access may fixate many of the parameters and thus limit implementation variability. One should be aware of the size range under investigation in order to best optimize the system. If not, setting parameters such as to achieve a large size range is a good first step toward optimizing the system configuration for the best measurement scenario. Typically, a PDA system can measure particles sizes of less than 1  $\mu\text{m}$  micron to several millimeters.

**4-11.3.2 PDA Configurations.** The PDA principle is implemented using one of three configurations (Figure 4-55):

- *Conventional PDA:* three-detector system with detectors located off the scattering plane
- *Planar PDA:* three-detector system with detectors located in the scattering plane
- *Dual PDA:* four-detector system that combines a conventional two-detector PDA with a planar two-detector PDA

While the conventional and the planar PDA systems perform similar measurements, the dual PDA combines both configurations to make two simultaneous independent measurements of size to eliminate two common effects when measuring in refraction mode that potentially lead to incorrect size measurements when particles are more than one-third the size of the measurement volume. This error in size can translate to significant bias of the volume-weighted flux and concentration, since the volume is proportional to the third power of the diameter. The two effects are:

- The trajectory effect (or Gaussian beam effect)
- The slit effect

Both effects arise when the PDA system is set up to receive refractively scattered light, as is typical in spray applications, but instead receives reflectively scattered light. These signals are then processed with the phase–diameter relationship based on refraction and thus lead to incorrect size measurements.

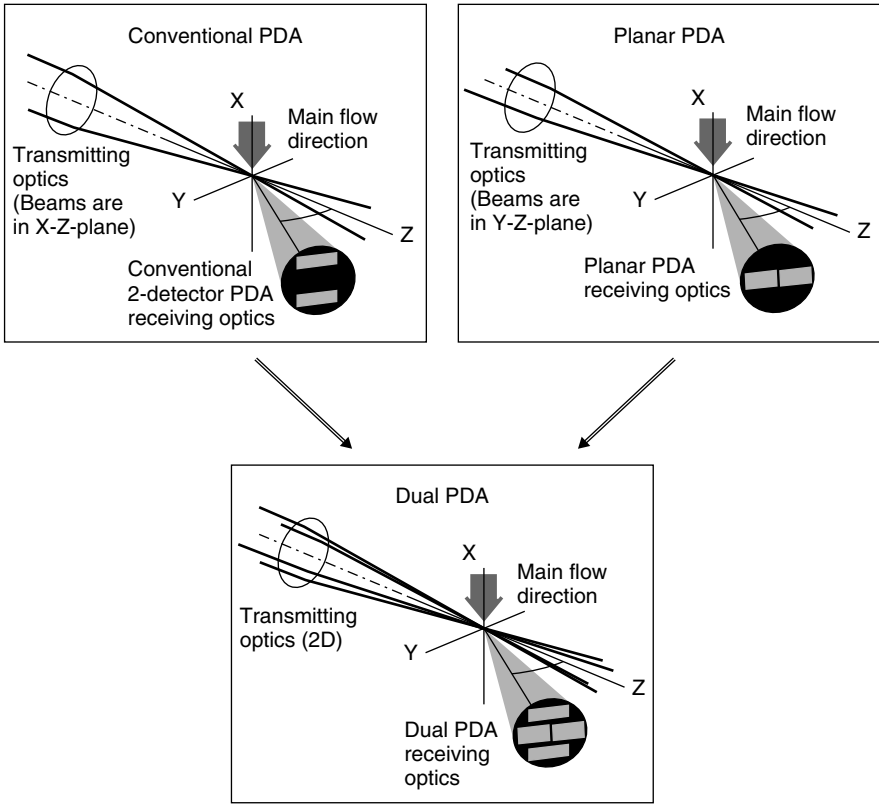


Figure 4-55 PDA probe configurations.

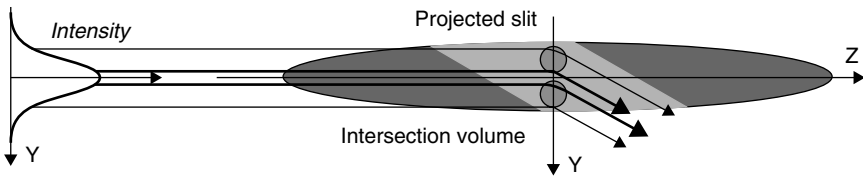
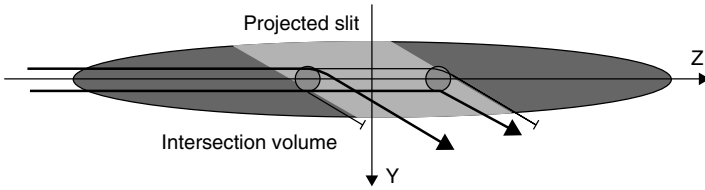


Figure 4-56 Trajectory effect expressed in terms of geometric optics.

The two effects are illustrated in Figures 4-56 and 4-57, respectively. As indicated in Figure 4-56, there exist particle positions within the volume (trajectories) where reflection may become the dominant scattering mode due to the much higher intensity of the incident light, in particular on the negative Y-axis. On the other hand, in Figure 4-57 the scattering light from particles in certain positions may be suppressed because they lie outside the slit aperture, and hence unwanted reflections will overwhelm the signal.



**Figure 4-57** Suppression of scattered light due to the slit aperture (slit effect).

By making two independent measurements, one using conventional PDA and the other using planar PDA, the same result regarding size is obtained only if the light received in both configurations is refractively scattered and the particle is spherical. Thus, both these effects that may result to significant errors in size and especially in volume estimation are eliminated using this redundancy.

**4-11.3.3 Optimizing Measurement Conditions in PDA.** In setting up any phase Doppler anemometer system for making reliable size measurements, some basic understanding of a few scattering phenomena is of great help. All three modes of scattering can be used with the PDA. There is, however, one crucial point that it is imperative to keep in mind. The PDA estimates the particle size from the phase differences of the Doppler bursts received by the three photodetectors in the receiving optics. Since the three modes of scattering give rise to different conversion factors (phase factors), receiving light from more than one scattering mode is likely to give rise to errors. Therefore, one should always set up a phase Doppler system so that only one mode of scattering dominates the light received by the receiving optics.

To assist in achieving a linear relationship between phase and diameter, Table 4-4 lists some typical scenarios and optical configurations that work best.

## 4-12 PARTICLE IMAGE VELOCIMETRY

### 4-12.1 Principles of PIV

PIV is a velocimetry technique based on images of tracer “seeding” particles suspended in the flow. In an ideal situation, these particles should be perfect flow tracers, homogeneously distributed in the flow, and their presence should not alter the flow properties. In that case, local fluid velocity can be measured by measuring the fluid displacement (see Figure 4-58) from multiple particle images and dividing that displacement by the time interval between the exposures. To get an accurate instantaneous flow velocity, the time between exposures should be small compared to the time scales in the flow; and the spatial resolution of the PIV sensor should be small compared to the length scales in the flow.

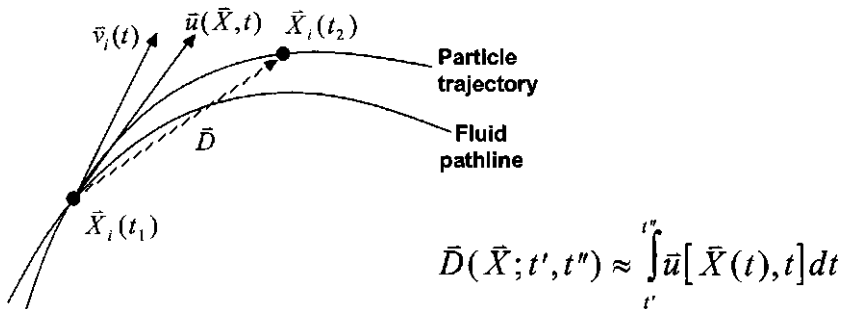
Principles of PIV have been covered in many papers, including Lourenco et al. (1989), Adrian (1991), and Willert and Gharib (1991). A more recent book by Raffel et al. (1998) is an excellent source of information on various aspects of PIV. The principal layout of a modern PIV system is shown in Figure 4-59.

**Table 4-4** Effect of Particle Type on Scattering Angle for PDA Measurements

Particle Type	Scattering Angle	Polarization Relative to Scattering Plane
$n_{rel} > 1$ (bubbles)	Near forward scatter	Parallel or perpendicular
$n_{rel} > 1$ (droplets)	Near forward scatter	Must be parallel
	Side scatter	Must be perpendicular
	Near backscatter	Perpendicular (best) or parallel
Reflecting particles	Near forward or backscatter	Parallel or perpendicular
	Side scatter	Must be perpendicular

Particle Type	Scattering Type	Scattering Angle
Totally reflecting	Reflection	Any angle except forward diffraction region; angle must be larger than $\arcsin(1.4/D_{min})$
Air bubbles in liquid	Reflection	Optimum near $\phi_{\infty} - 10^{\circ}$ ; in liquid can be used from $\phi_{\infty} - 15^{\circ}$ to $\phi_{\infty} - 5^{\circ}$
Air bubbles in water	Reflection	Optimum near $+70^{\circ}$ ; in water can be used from $+65^{\circ}$ to $+5^{\circ}$
Liquid droplets in air	Refraction	Optimum at $\phi_b$ ; second-order refraction can be used at $\phi_r + 5^{\circ}$ to $\phi_r + 10^{\circ}$
Water droplets in air	Refraction	Optimum at Brewster's angle = $73.7^{\circ}$ ; can be used from $37$ to $10^{\circ}$ ; second-order refraction can be used from $145$ to $150^{\circ}$
Two-phase flow	Reflection	Optimum near $\phi_{\infty} - 10^{\circ}$ ; can be used from $\phi_{\infty} - 15^{\circ}$ to $\phi_{\infty} - 5^{\circ}$



**Figure 4-58** Determination of particle displacement and its relationship to actual fluid velocity. (From Keane and Adrian, 1993.)

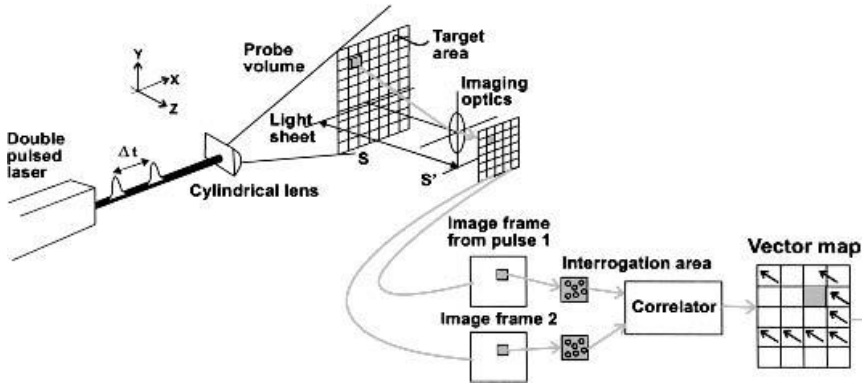


Figure 4-59 Principal of operation for a PIV system.

The PIV measurement includes illuminating a cross-section of the seeded flow field, typically by a pulsing light sheet, recording multiple images of the seeding particles in the flow using a camera located perpendicular to the light sheet, and analyzing the images for displacement information.

The recorded images are divided into small subregions called *interrogation regions*, the dimensions of which determine the spatial resolution of the measurement. The interrogation regions can be adjacent to each other, or more commonly, have partial overlap with their neighbors. The shape of the interrogation regions can deviate from square to better accommodate flow gradients. In addition, interrogation areas A and B, corresponding to two different exposures, may be shifted by several pixels to remove a mean dominant flow direction (DC offset) and thus improve the evaluation of small fluctuating velocity components about the mean.

The peak of the correlation function gives the displacement information. For double or multiple exposed single images, an autocorrelation analysis is performed. For single exposed double images, a cross-correlation analysis gives the displacement information.

#### 4-12.2 Image Processing

If multiple images of the seeding particles are captured on a single frame (as seen in the photograph of Figure 4-60), the displacements can be calculated by autocorrelation analysis. This analysis technique has been developed for photography-based PIV, since it is not possible to advance the film fast enough between the two exposures. The autocorrelation function of a double-exposed image has a central peak and two symmetric side peaks, as shown in Figure 4-61. This poses two problems: (1) although the particle displacement is known, there is an ambiguity in the flow direction, and (2) for very small displacements, the side peaks can partially overlap with the central peak, limiting the measurable velocity range. To overcome the directional ambiguity problem, image shifting techniques using

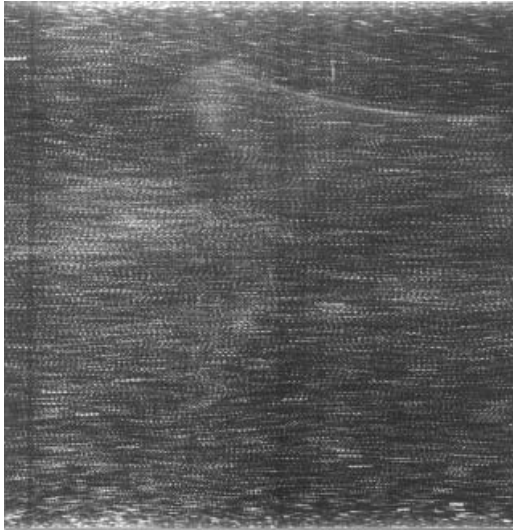


**Figure 4-60** Multiple-exposure image captured for PIV autocorrelation analysis. (From Stanislas et al., 2000, p. 65.)

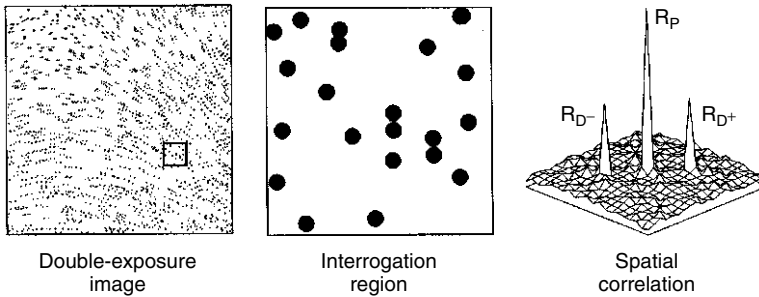


**Figure 4-61** Autocorrelation analysis of a double-exposed image. (From Westerweel, 1993.)

rotating mirrors (Landreth et al., 1988) and electrooptical techniques (Landreth and Adrian, 1988b; Lourenco, 1993) have been developed. To leave enough room for the added image shift, larger interrogation regions are used for autocorrelation analysis. By displacing the second image at least as much as the largest negative displacement, the directional ambiguity is removed. This is analogous to frequency shifting in LDA systems to make them directionally sensitive.

The preferred method in PIV is to capture two images on two separate frames and perform cross-correlation analysis. This cross-correlation function has a single peak,

$$R(\vec{s}) = \int W_1(\vec{x})I_1(\vec{x})W_2(\vec{x} + \vec{s})I_2(\vec{x} + \vec{s}) d\vec{x} \quad (4-41)$$

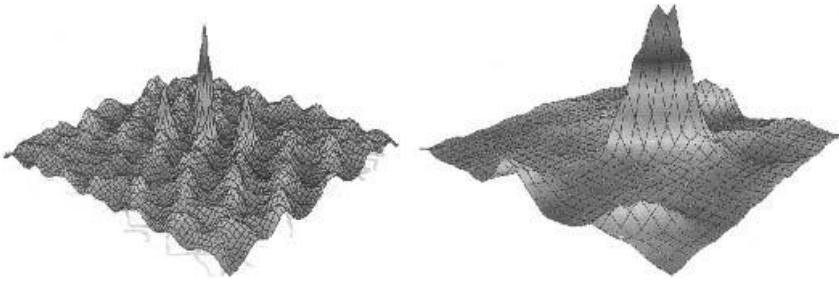


**Figure 4-62** Autocorrelation (left) versus cross-correlation (right) analysis result.

providing the magnitude and direction of the flow without ambiguity (Figure 4-62).

Common particles need to exist in the interrogation regions, which are being correlated; otherwise, only random correlation or noise will exist. The PIV measurement accuracy and dynamic range increase with increasing time difference  $\Delta t$  between the pulses. However, as  $\Delta t$  increases, the likelihood of having common particles in the interrogation region decreases and the measurement noise goes up. A good rule of thumb is to ensure that within time  $\Delta t$ , the in-plane components of velocity  $V_x$  and  $V_y$  carry the particles no more than a third of the interrogation region dimensions, and the out-of-plane component of velocity  $V_z$  carries the particles no more than a third of the light sheet thickness.

Most commonly used interrogation region dimensions are  $64 \times 64$  pixels for autocorrelation, and  $32 \times 32$  pixels for cross-correlation analysis. Since the maximum particle displacement is about a third of these dimensions, to achieve reasonable accuracy and dynamic range for PIV measurements, it is necessary to be able to measure the particle displacements with subpixel accuracy.

Fast Fourier transform (FFT) techniques are used for the calculation of the correlation functions. Since the images are digitized, the correlation values are found for integral pixel values, with an uncertainty of  $\pm 0.5$  pixel. Different techniques, such as centroids, Gaussian, and parabolic fits, have been used to estimate the location of the correlation peak. Using 8 bit digital cameras, peak estimation accuracy of 0.1 to 0.01 pixel can be obtained. For subpixel interpolation techniques to work properly, it is necessary for particle images to occupy multiple (2 to 4) pixels. If the particle images are too small (i.e., around 1 pixel), these subpixel estimators do not work properly, since the neighboring values are noisy. In such a case, slight defocusing of the image improves the accuracy.

Digital windowing and filtering techniques can be used in PIV systems to improve the results. Top-hat windows with zero padding, or Gaussian windows, applied to interrogation regions are effective in reducing the cyclical noise, which is inherent to FFT calculation. A Gaussian window also improves measurement accuracy in cases where particle images straddle the boundaries of the interrogation regions. A spatial frequency high-pass filter can reduce the effect of low-frequency distortions from optics, cameras, or background light variations.



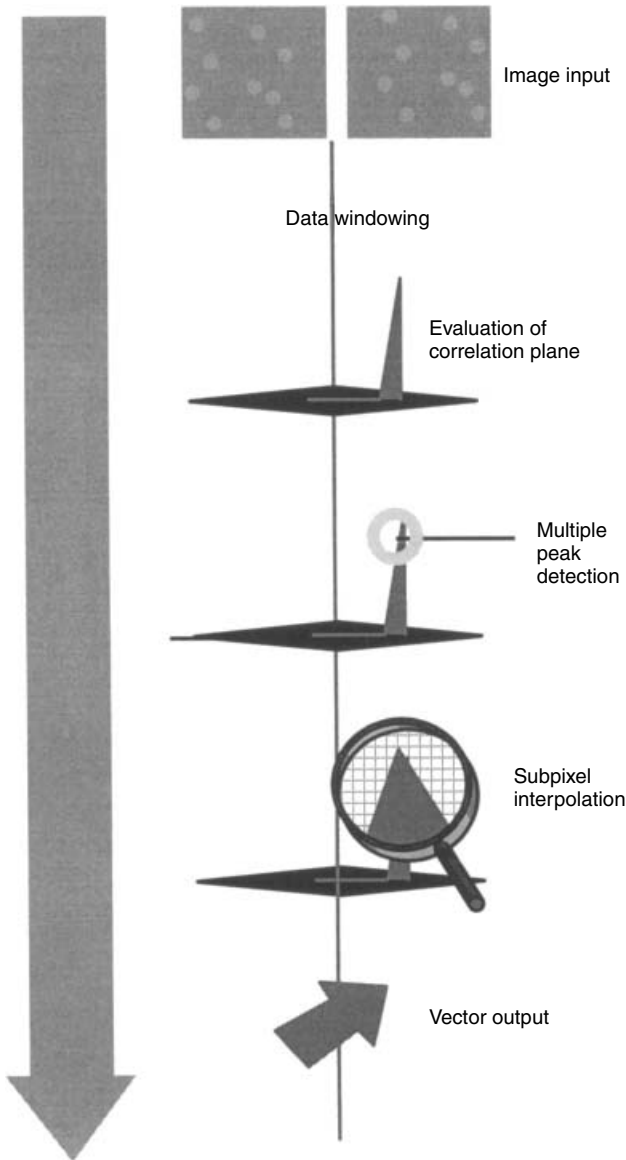


**Figure 4-63** Image to vector processing sequence.

A spatial frequency low-pass filter can reduce the high-frequency noise generated by the camera, and ensure that the subpixel interpolation algorithm can still work in cases where the particles in the image map are less than 2 pixels in diameter. Typical image to vector processing sequence is shown in Figure 4-63.

The spatial resolution of PIV can be increased using multipass correlation approaches. Offsetting the interrogation region by a value equal to the local

integer displacement, a higher signal-to-noise ratio can be achieved in the correlation function, since the probability of matching particle pairs is maximized. This idea has led to implementations such as adaptive correlation *Dantec*, 2000), superresolution PIV (Keane et al., 1995), and hybrid PTV (Cowen and Monosmith, 1997).

#### 4-12.3 Implementation of PIV

The vast majority of modern PIV systems today consist of dual-cavity Nd : Yag lasers, cross-correlation cameras, and processing using software or dedicated FFT-based correlation hardware. In this section we review the typical implementation of these components to perform a measurement process (as shown in the flowchart of Figure 4-64) and address concerns regarding proper seeding, light delivery, and imaging.

**4-12.3.1 Seeding Particles.** Rather than relying on naturally existing particles, it is common practice to add particles to the flow to have control over their size, distribution, and concentration. In general, these particles should be small enough to be good flow tracers and large enough to scatter sufficient light for imaging. They should also be nontoxic, noncorrosive, and chemically inert, if possible. Melling (1997) reviews a wide variety of tracer materials that have been used in liquid and gas PIV experiments. Methods of generating seeding particles and introducing them into the flow are also discussed.

Possibilities for liquid applications include silver-coated hollow glass spheres, polystyrene, polymers, titanium dioxide ( $\text{TiO}_2$ ), aluminum oxide ( $\text{Al}_2\text{O}_3$ ), conifer pollen, and hydrogen bubbles. Furthermore, fluorescent dyes are used in conjunction with polystyrene or polymer particles to generate particles that will absorb the incident laser radiation and emit at another wavelength band. A common dye for Nd : Yag lasers operating in the 532 nm spectral range is Rhodamine-B, which when

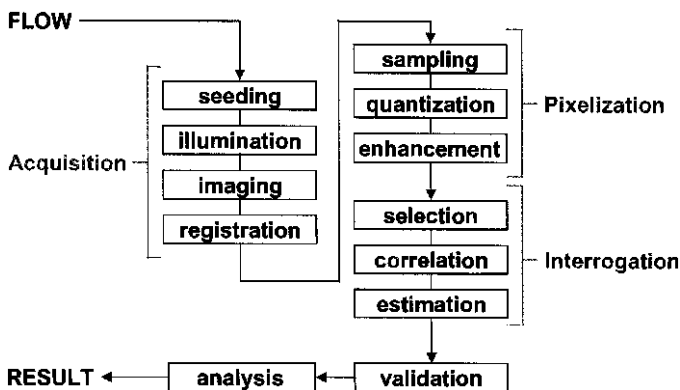


**Figure 4-64** Flowchart of the PIV measurement and analysis process. (From Westerweel, 1993.)

excited emits at wavelengths above 560 nm. Hence, for applications where many reflections exist from geometric boundaries (e.g., stirred tanks), the use of fluorescent particles is greatly advantageous (see Hammad and Papadopoulos, 2001).

For gas flow applications, theatrical smoke, different kinds of atomized oil,  $\text{TiO}_2$ , and  $\text{Al}_2\text{O}_3$  have been used. Typical theatrical smoke generators are inexpensive, and they generate plenty of particles. Oil can be atomized using devices such as a Laskin nozzle, generating particles in the micrometer to submicrometer range, which are particularly useful for high-speed applications.  $\text{TiO}_2$  and  $\text{Al}_2\text{O}_3$  are useful for high-temperature applications such as combustion and flame measurements.

**4-12.3.2 Light Sources and Delivery.** In PIV, lasers are used only as a source of bright illumination and are not a requirement. Flash lamps and other white light sources can also be used. Some facilities prefer these nonlaser light sources because of safety issues. However, white light cannot be collimated as well as coherent laser light, and their use in PIV is not widespread.

PIV image acquisition should be completed using short light pulses to prevent streaking. Hence, pulsed lasers are naturally well suited for PIV work. However, since many labs already have existing continuous-wave (CW) lasers, these lasers have been adapted for PIV use, especially for liquid applications.

Dual-cavity Nd:Yag lasers, also called PIV lasers, are the standard laser configuration for modern PIV systems. Nd:Yag lasers emit infrared radiation whose frequency can be doubled to give 532 nm green wavelength. Minilasers are available with power up to 200 mJ/pulse, and larger lasers provide up to 1 J/pulse. Typical pulse duration is around 10 ns, and the pulse frequency is typically 5 to 30 Hz. To achieve a wide range of pulse separations, two laser cavities are used to generate a combined beam. Control signals required for PIV Nd:Yag lasers are shown in Figure 4-65.

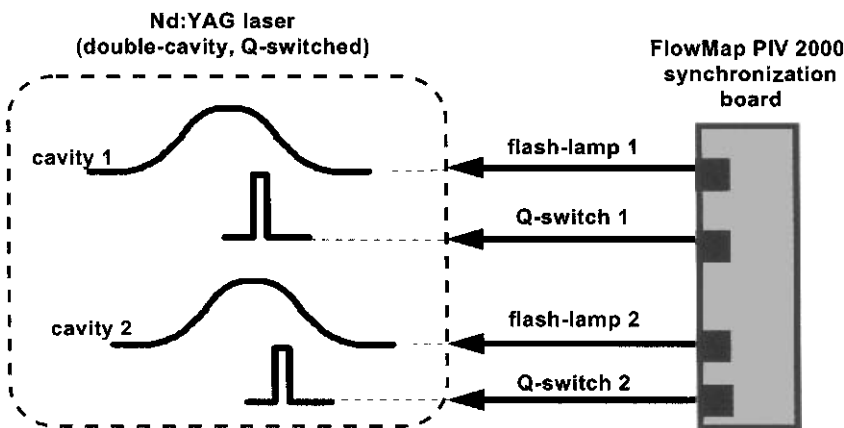


Figure 4-65 Control signals required for PIV Nd:Yag lasers.

Argon-ion lasers are CW gas lasers whose emission is composed of multiple wavelengths in the green–blue–violet range. Air-cooled models emitting up to 300 mW and water-cooled models emitting up to 10 W are quite common in labs for LDA use. They can also be used for PIV experiments in low-speed liquid applications, in conjunction with shutters or rotating mirrors.

Copper-vapor lasers are pulsed metal vapor lasers that emit green (510 nm) and yellow (578 nm). Since the repetition rates can reach up to 50 kHz, energy per pulse is a few millijoules or less. They are used with high-framing-rate cameras for flow visualization and some PIV applications. High pulse rate Nd : Yag lasers have also been recently used to make time resolved PIV measurements (see Papadopoulos and Hammad, 2003).

Ruby lasers have been used in PIV because of their high-energy output. But their 694 nm wavelength is at the end of the visible range where typical CCD (charge-coupled diode) chips and photographic film are not very sensitive.

Fiber optics are commonly used for delivering Ar-ion beams conveniently and safely. Single-mode polarization-preserving fibers can be used for delivering up to 1 W of input power, whereas multimode fibers can accept up to 10 W. Although use of multimode fibers produces nonuniform intensity in the light sheet, they have been used in some PIV applications.

The short-duration high-power beams from pulsed Nd : Yag lasers can instantly damage optical fibers. Hence, alternative light guiding mechanisms have been developed, consisting of a series of interconnecting hollow tubes and flexible joints where high-power mirrors are mounted. Light sheet optics located at the end of the arm can be oriented at any angle and extended up to 1.8 m. Such a mechanism can transmit up to 500 mJ of pulsed laser radiation with 90% transmission efficiency at 532 nm, offering a unique solution for safe delivery of high-powered pulsed laser beams.

The main component of light sheet optics is a cylindrical lens. To generate a light sheet from a laser beam with small diameter and divergence, such as one from an Ar-ion laser, using a single cylindrical lens can be sufficient. For Nd : Yag lasers, one or more additional cylindrical lenses are used, to focus the light sheet to a desired thickness and height. For light sheet optics designed for high-power lasers, a diverging lens with a negative focal length is used first to avoid focal lines.

**4-12.3.3 Image Recorders.** Cross-correlation cameras are the preferred method of sampling data for PIV. The cross-correlation cameras use high-performance progressive-scan interline CCD chips. Such chips include  $m \times n$  light-sensitive cells and an equal number of storage cells (blind cells). Figure 4-66 is a schematic illustration of the light-sensitive pixels and storage cell layout for these cameras.

The first laser pulse is timed to expose the first frame, which is transferred from the light-sensitive cells to the storage cells immediately after the laser pulse. The second laser pulse is then fired to expose the second frame. The storage cells now contain the first camera frame of the pair with information about the initial positions of seeding particles. The light-sensitive cells contain the second camera

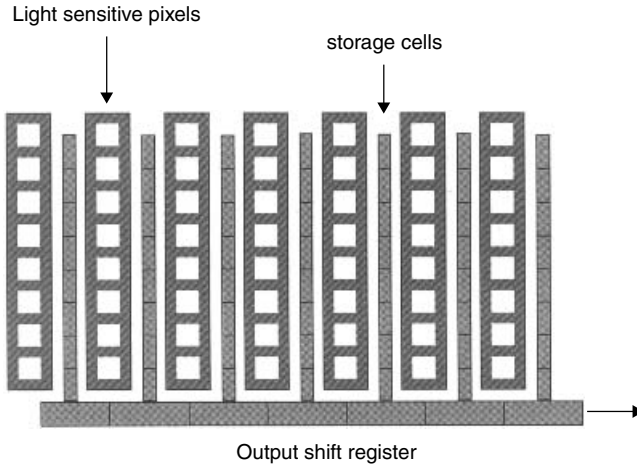


**Figure 4-66** Schematic illustration of light-sensitive pixels and storage cell layout of cross-correlation PIV cameras.

frame, which has information on the final positions of the seeding particles. These two frames are then transferred sequentially to the camera outputs for acquisition and cross-correlation processing.

Cross-correlation cameras are available with resolutions up to  $2\text{ k} \times 2\text{ k}$  pixels, and framing rates up to 30 Hz; 8 bit cameras are sufficient for most purposes. However, 12 bit cameras are becoming common, especially for applications such as planar laser-induced fluorescence (PLIF), where extra sensitivity and dynamic range are required.

Flow fields with velocities ranging from micrometers per second to supersonic speeds can be studied since interframe time separations down to few hundred nanoseconds can be obtained. One interesting feature of the cameras is that they can be reset asynchronously. This is particularly useful in conjunction with the special triggering options for synchronizing the measurements to external events, such as rotating machinery.

#### 4-12.4 PIV Data Processing

Typically, the raw PIV data obtained from the cross-correlation of two images need to be validated and optionally smoothed before statistical values are calculated or various derived quantities are computed.

The following are various data validation techniques that are commonly used:

- *Correlation peak-height validation* works based on the height of the peaks in the correlation plane. If  $P_1$  is the highest peak and  $P_2$  is the second highest peak, the most common approach, called the *detectability criterion*, validates vectors for which  $P_1/P_2 \geq k$ , where  $k$  is typically around 1.2 (Keane and Adrian, 1992).

- *Velocity-range validation* rejects vectors whose magnitude or components are outside a given range. Normally, the user has an idea about the range of velocities in the flow. This information is used as validation criteria.

$$V_{\min} \leq |\mathbf{V}| \leq V_{\max} \quad (\text{length})$$

$$V_{x,\min} \leq |V_x| \leq V_{x,\max} \quad (\text{x-component})$$

$$V_{y,\min} \leq |V_y| \leq V_{y,\max} \quad (\text{y-component})$$

Hence, if the vector does not satisfy the required relations above, it is rejected.

- *Moving-average validation* is a special case of the general class of iterative filtered validation, described by Host-Madsen and McCluskey (1994). Since the vector field is oversampled by the PIV technique, there is a correlation between neighboring vectors, and there is not too much change from one vector to its neighbor. If a vector deviates too much from its neighbors, it must be an outlier. Hence, in this technique, the average of the vectors neighboring a given vector is calculated and compared with the vector. If the difference is larger than a certain acceptance factor, that vector is rejected. The rejected vector may be substituted by a local average of its neighbors.
- *Moving-average filter* substitutes each vector with the uniformly weighted average of the vectors in a neighborhood of a specified size  $m \times n$ . Here,  $m$  and  $n$  are an odd number of vector cells symmetrically located around each vector. This filter takes out the high-frequency jitter in the PIV results.

After validation and optional filtering, the user is ready to calculate derived quantities and statistical values. Following are the commonly calculated derived quantities from PIV data:

- *Vorticity* is the curl of the 3D velocity vector. From 2D PIV calculations, the normal component of the vorticity vector can be calculated.
- *Streamlines* are curves parallel to the direction of the flow. They are defined by the equation  $v_x dy = v_y dx$ . They represent the path that a particle would follow if the flow field were constant with time. Hence, the streamlines calculated from PIV measurements are correct only if the flow is 2D in the plane of the light sheet.

The commonly employed statistical properties that are calculated from PIV measurements include the mean of each velocity component, the standard deviation of the mean, and the covariance coefficient.

#### 4-12.5 Stereoscopic (3D) PIV

Conventional 2D planar PIV technique measures projections of 3D velocity vectors onto the 2D plane defined by the light sheet. It is not capable of measuring

the third component of the flow normal to the light sheet. In fact, if that normal component is large, the planar PIV technique can give wrong results even for the in-plane components of velocity, due to parallax error. This error gets increasingly large from the center to the edges of the image. In these situations, the problem is normally minimized by having a large-focal-length lens so that the distance from the camera to the image is large compared to the image area.

Since there are many applications where it is important to measure the third component of velocity normal to the light sheet, various approaches have been proposed to recover that third component. The most common technique, *stereoscopic PIV*, involves using an additional camera and viewing the flow from two different angles. It is based on the same principle as human stereosight. The two eyes see slightly different images of the objects around us. The differences of the images are compared in the brain and interpreted as the 3D perception.

**4-12.5.1 Stereoscopic Imaging Basics: Scheimpflug Condition.** Stereoscopic PIV is a planar PIV technique for measuring all three components of velocity. Instead of having a single camera normal to the light sheet, two cameras are used, each looking at the same flow field at different angles. Due to different orientations, each camera records a different image. 3D displacements and hence velocities on the plane can be derived by proper calibration of the camera views of a target, and combining 2D results from each camera.

The principle of stereo PIV is indicated in Figure 4-67. When each camera views the measurement volume illuminated by the light sheet at an angle, the CCD chip in each camera needs to be tilted so that the entire field of view

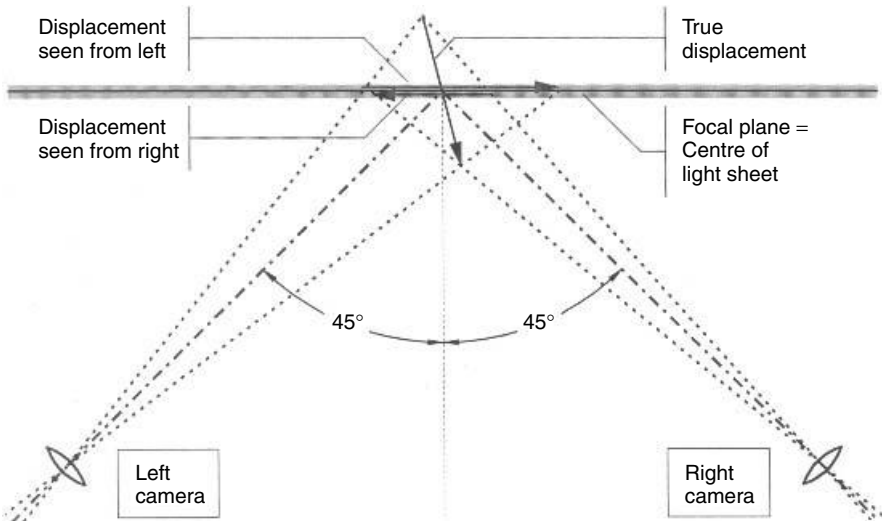


**Figure 4-67** Stereo vision.

of the camera can be focused. In fact, for each camera to be focused properly, the object (light sheet), camera lens, and image (CCD chip) planes should all intersect along a common line (Prasad and Jensen, 1995). This is called the *Scheimpflug condition*. When the Scheimpflug condition is satisfied, a perspective distortion is introduced into the two images as a side effect. Hence, the magnification factor is not constant across the image any more and needs to be evaluated via calibration.

**4-12.5.2 Calibration and 3D Reconstruction.** To reconstruct the true 3D ( $X, Y, Z$ ) displacements from two 2D ( $x, y$ ) displacements as observed by the two cameras, a numerical model is necessary that describes how each of the two cameras image the flow field onto their CCD chips. Using the camera imaging models, four equations (which may be linear or nonlinear) with three unknowns are obtained.

Instead of a theoretical model that requires careful measurements of distances, angles, and so on, an experimental calibration approach is preferred. The experimental calibration estimates the model parameters based on the images of a calibration target as recorded by each camera. A linear imaging model that works well for most cases, the *pinhole camera model*, is based on geometrical optics. This leads to the following direct linear transform equations, where  $x, y$  are image coordinates, and  $X, Y, Z$  are object coordinates. This physics-based model cannot describe nonlinear phenomena such as lens distortions.

$$\begin{bmatrix} kx \\ ky \\ k \end{bmatrix} = \begin{bmatrix} A_{11} & A_{12} & A_{13} & A_{14} \\ A_{21} & A_{22} & A_{23} & A_{24} \\ A_{31} & A_{32} & A_{33} & A_{34} \end{bmatrix} \cdot \begin{bmatrix} X \\ Y \\ Z \\ 1 \end{bmatrix} \quad (4-42)$$

In experiments involving significant lens distortion, refraction, and so on, higher-order nonlinear imaging models can be used (Soloff et al., 1997). These models are based not on a physical mapping of the geometry but on a least-squares fitting of the image–object pairs using adjustable parameters. Imaging parameters such as image magnification and focal length do not need to be determined, and higher-order terms can compensate for nonlinear effects.

#### 4-12.6 PIV Applications in Mixing

*Stirred tanks* are used commonly in various mixing industries. These dynamic devices typically consist of a circular tank with a rotating shaft containing impellers of various geometries. There are also *static mixers*, where the mixing occurs as the fluid is forced through a complex geometry in a conduit. These devices have been adapted for use in such industries as pharmaceutical, chemical, personal care products, food and beverages, biotechnology, polymer, plastic, paper and pulp, oil, rubber, and waste disposal.

The use of computational fluid dynamics (CFD) to predict the flow fields in various industrial mixers has increased substantially during the last few years.



Time-dependent mixing flows, coupled with complex geometry, bring uncertainty to the CFD predictions, especially for turbulent flows. This has also increased the interest in experimental verification of the simulations.

Hence, in addition to the traditional experimentalist who obtains the mixing information experimentally, more and more CFD users are turning to PIV to measure the initial and boundary conditions in their mixer and to verify the results of their simulations.

Although the flow fields in stirred tanks have been measured by the LDA technique by many researchers since the mid-1970s, the use of PIV is more recent. Bakker et al. (1996) were early users of PIV to study the 2D flow pattern along the center plane of a stirred vessel. Sheng et al. (1998) have investigated methods for validating CFD simulations against PIV measurements. They have extracted the mean velocity, turbulent kinetic energy, Reynolds stresses, and dissipation rate from the PIV data and investigated the effect of boundary conditions on CFD simulation results using PIV and LDA data. More recently, Zalc (2000) has developed CFD tools to investigate mixing in a static mixer and a three-Rushton turbine stirred tank, where PIV was used to validate the stirred tank simulations.

## NOMENCLATURE

$D_{\min}$	minimum particle diameter to be measured ( $\mu\text{m}$ )
$n_1$	index of refraction of external medium
$n_2$	index of refraction of particle
$n_{\text{rel}}$	relative index of refraction, $n_1/n_2$

### Greek Symbols

$\phi_{\infty}$	critical angle for particles with $n_{\text{rel}} < 1$ (the largest scattering angle for reflection is $2 \arccos n_{\text{rel}}$ )
$\phi_b$	Brewster's angle for particles with $n_{\text{rel}} > 1$ [the angle at which reflection is zero for polarization parallel to the scattering plane is $2 \arctan(1/n_{\text{rel}})$ ]
$\phi_{\text{cl}}$	critical angle for particles with $n_{\text{rel}} > 1$ [the largest scattering angle for refraction is $2 \arccos(1/n_{\text{rel}})$ ]
$\phi_r$	rainbow angle for particles with $n_{\text{rel}} > 1$ (the angle where second-order refraction is strongest is $4 \arccos[\cos(\gamma)n_{\text{rel}}] - 2\gamma$ , where $\gamma = \arcsin\sqrt{(n_{\text{rel}}^2 - 1)/3}$ )

## REFERENCES

- Abuaf, N., T. P. Felerabend, G. A. Zimmer, and O. C. Jones (1979). Radio-frequency probe for bubble size and velocity measurements, *Rev. Sci. Instrum.*, **50**(10), 1260–1263.

- Adrian, R. J. (1991). Particle imaging techniques for experimental fluid mechanics, *Annu. Rev. Fluid Mech.*, **23**, 261–304.
- All-Saeedi, J. N., M. O. Kirkpatrick, and R. W. Pike (1995). Optical tomography for measurement of concentration distributions in a stirred tank, *Paper 11.5*, presented at Mixing XVI, Banff, Alberta, Canada.
- Bakker, A. K., J. Myers, R. W. Ward, and C. K. Lee (1996). The laminar and turbulence flow pattern of a pitched blade turbine, *Trans. Inst. Chem. Eng.*, **74**, 485–491.
- Barnes, H. A., J. F. Hutton, and K. Walters (1989). *An Introduction to Rheology*, Elsevier, New York.
- Benedict, L. H., and R. D. Gould (1996). Towards better uncertainty estimates for turbulence statistics, *Exp. Fluids*, **22**, 129–136.
- Benedict, L. H., and R. D. Gould (1999). Understanding biases in the near-field region of LDA two-point correlation measurements, *Exp. Fluids*, **26**, 381–388.
- Bivolaru, D., M. V. Ötügen, A. Tzes, and G. Papadopoulos (1999). Image processing for interferometric Mie and Rayleigh scattering velocity measurements, *AIAA J.*, **37**(6), 688–694.
- Buchhave, P. (1979). The measurement of turbulence with the burst-like laser-Doppler-anemometer-errors and correction methods, *Tech. Rep. TRL-106*, State University of New York–Buffalo.
- Buchhave, P., W. K. George, and J. L. Lumley (1979). The measurement of turbulence with the laser-Doppler anemometer, *Annu. Rev. Fluid Mech.*, **11**, 443–503.
- Burgess, J. M., and P. H. Calderbank (1975). The measurement of bubble parameters in two-phase dispersions: I, *Chem. Eng. Sci.*, **30**, 743–750. [See also Raper, J. A., D. C. Dixon, and C. J. D. Fell (1978). Limitations of Burgess–Calderbank probe technique for characterization of gas liquid dispersions on sieve trays, *Chem. Eng. Sci.*, **33**, 1405–1406; and J. M. Burgess and P. H. Calderbank, Limitations of Burgess–Calderbank probe technique for characterization of gas liquid dispersions on sieve trays, authors’ reply, p. 1407.]
- Chapman, C. M., A. W. Nienow, and J. C. Middleton (1980). Surface aeration in a small agitated and sparged vessel, *Biotechnol Bioeng.*, **22**, 981–993.
- Chapman, C. M., L. G. Gibilaro, and A. W. Nienow (1982). A dynamic response technique for the estimation of gas–liquid mass transfer coefficients in a stirred vessel, *Chem. Eng. Sci.*, **37**(6), 891–896.
- Chapple, D., S. M. Kresta, A. Wall, and A. Afacan (2002). The effect of impeller and tank geometry on power number for a pitched blade turbine, *Trans. Inst. Chem. Eng. A (Chem. Eng. Res. Des.)*, **80**, 364–372.
- Clark, H. and Özcan-Taşkin, N. G. (2001). A study of drop break up and deformation in the laminar regime, *AIChE Meeting*, November, Reno, NV.
- Cochrane, D. R., and J. M. Burgess (1985). A new method for the measurement of the properties of two-phase gas–liquid dispersions, *Proc. Chemeca’85 Conference, Paper CIA*, pp. 263–268.
- Cooke, M., M. K. Dawson, A. W. Nienow, G. Moody, and M. J. Whitton (1991). Mass transfer in aerated agitated vessels: assessment of the NEL/Hickman steady state method, *Proc. 7th European Conference on Mixing, KVIV*, Bruges, Belgium, pp. 409–418.
- Cooke, M., G. T. Bolton, D. H. Jones, and D. Housley (2001). Demonstration of a novel retrofit tomography baffle cage for gas–liquid mixing studies under intense operating

- conditions, *Proc. 2nd World Congress on Industrial Process Tomography*, Hanover, Germany, Aug. 29–31.
- Cowen, E. A., and S. G. Monosmith (1997). A hybrid digital particle tracking velocimetry technique, *Exp. Fluids*, **22**, 199–211.
- Dantec (2000). Adaptive correlation, *Dantec Product Information*, Dantec Dynamics, Inc., Mahwah, NJ.
- Dickin, F. J., T. Dyakowski, R. A. Williams, R. C. Waterfall, C. G. Xie, and M. S. Beck (1992). Process tomography for improving the design and control of multiphase systems: its current status and future prospects, presented at the ECAPT Conference, Manchester, Lancashire, England.
- Durst, F., and M. Zaré (1975). Laser-Doppler measurements in two-phase flows, *Proc. LDA Symposium*, Copenhagen, pp. 403–429.
- Durst, F., A. Melling, and J. H. Whitelaw (1976). *Principles and Practice of Laser-Doppler Anemometry*, Academic Press, London.
- Erdmann, J. C., and R. I. Gellert (1976). Particle arrival statistics in laser anemometry of turbulent flow, *Appl. Phys. Lett.*, **29**, 408–411.
- Escudie, R. (2001). Ph.D. dissertation, INSA, Toulouse, France.
- Fangary, Y. S., J. P.K. Seville, and M. Barigou (1992). Flow studies in stirred tanks by positron emission particle tracking (PEPT), *Proc. Fluid Mixing 6 Conference*, Bradford, Yorkshire, England. *Inst. Chem. Eng. Symp. Ser.*, **146**, 23–34.
- Frijlink, J. J. (1987). *Physical aspects of gassed suspension reactors*, Ph.D. dissertation, Technical University of Delft, The Netherlands.
- Gal-or, B., and W. Resnick (1966). Gas residence time in agitated gas–liquid contactor: experimental test of mass transfer model, *Ind. Eng. Chem. Process. Des. Dev.*, **5**(1), 15–19.
- George, W. K. (1976). Limitations to measuring accuracy inherent in the laser Doppler signal, in *The Accuracy of Flow Measurements by Laser Doppler Methods: Proceedings of the LDA–Symposium Copenhagen 1975*, P. Buchhave, J. M. Delhaye, F. Durst, W. K. George, K. Refslund, and J. H. Whitelaw (eds.), Hemisphere Publishing Corporation, pp. 20–63.
- George, W. K. (1978). Processing of random signals, *Proc. Dynamic Flow Conference*, Skovlunde, Denmark.
- Gibilaro, L. G., S. N. Davies, M. Cooke, P. M. Lynch, and J. C. Middleton (1985). Initial response analysis of mass transfer in a gas sparged stirred vessel, *Chem. Eng. Sci.*, **40**(10), 1811–1816.
- Guezennec, Y. G., R. S. Brodkey, N. T. Trigue, and J. C. Kent (1994). Algorithms for fully automated three-dimensional particle tracking velocimetry, *Exp. Fluids*, **17**, 209–219.
- Hammad, K. J., and G. Papadopoulos (2001). Phase-resolved PIV measurements within a triple impeller stirred-tank, *ASME 2001 Fluids Engineering Division Summer Meeting*, FEDSM2001-18224, May 29–June 1, New Orleans, LA.
- Hanhart, J., H. Kramers, and K. R. Westerterp (1963). The residence time distribution of the gas in an agitated gas–liquid contactor, *Chem. Eng. Sci.*, **18**, 503–509.
- Harnby, N., M. F. Edwards, and A. W. Nienow (Eds.) (1992). *Mixing in the Process Industries*, Butterworth-Heinemann, Wolburn, MA.

- Heijnen, J. J., K. van't Riet, and A. J. Wolthuis (1980). Influence of small bubbles on the dynamic  $k_L$  a measurement in viscous gas–liquid systems, *Biotechnol. Bioeng.*, **22**, 1945–1956.
- Hickman, A. D. (1988a). Gas–liquid oxygen transfer and scale-up: a novel experimental technique with results for mass transfer in aerated mixing vessels, *Proc. 6th European Conference on Mixing, Pavia, Italy*, p. 369.
- Hickman, A. D. (1988b). The measurement of oxygen mass transfer coefficients using a simple novel technique, *Proc. 3rd Bioreactor Project Research Symposium, NEL, East Kilbride, Glasgow, Scotland, May 4*.
- Hickman, A. D., and A. W. Nienow (1986). Mass transfer and hold-up in an agitated simulated fermentation broth as a function of viscosity, *Proc. First International Conference on Bioreactor Fluid Dynamics, BHRA, Cambridge, Paper 22*, p. 301.
- Host-Madsen, A., and D. R. McCluskey (1994). On the accuracy and reliability of PIV measurements, *Proc. 7th International Symposium on Applications of Laser Techniques to Flow Measurements*, Lisbon.
- Hoyle, B. S. (1996). Process tomography using ultrasonic sensors, *Meas. Sci. Technol.*, **7**, 272–280.
- Hulst, H. C. (1981). *Light Scattering by Small Particles*, Dover, New York.
- Keane, R. D., and R. J. Adrian (1992). Theory of cross-correlation analysis of PIV images, *Appl. Sci. Res.*, **49**, 191–215.
- Keane, R. D., and R. J. Adrian (1993). *Flow Visualization and Image Analysis*, Kluwer, Norwell, MA, pp. 1–25.
- Keane, R. D., R. J. Adrian, and Y. Zhang (1995). Super-resolution particle image velocimetry, *Meas. Sci. Technol.*, **6**, 754–768.
- Kegrise, M. A., and G. S. Settles (2000). Schlieren image-correlation velocimetry and its application to free-convection flows, *Proc. 9th International Symposium on Flow Visualization*, G. M. Carlomagno and I. Grant, eds., Henriot-Watt University, Edinburgh, pp. 380: 1–13.
- Khang, S. J., and T. J. Fitzgerald (1975). A new probe and circuit for measuring electrolyte conductivity, *Ind. Eng. Chem. Fundam.*, **14**(3), 208–211.
- Kresta, S. M. (1998). Turbulence in stirred tanks: anisotropic, approximate, and applied, *Can. J. Chem. Eng.*, **76**, 563–576.
- Kresta, S. M., and P. E. Wood, 1993. The flow field produced by a 45 degree pitched blade turbine: changes in the circulation pattern due to off bottom clearance, *Can. J. Chem. Eng.*, **71**, 42–53.
- Kuboi, R., A. W. Nienow, and K. V. Allsford (1983). Using a derotational prism for studying gas dispersion processes, *Chem. Eng. Commun.*, **22**, 29.
- Landreth, C. C., and R. J. Adrian (1988). Electro-optical image shifting for particle image velocimetry, *Appl. Opt.*, **27**, 4216–4220.
- Landreth, C. C., R. J. Adrian, and C. S. Yao (1988). Double-pulsed particle image velocimeter with directional resolution for complex flows, *Exp. Fluids*, **6**, 119–128.
- Levenspiel, O. (1972). *Chemical Reaction Engineering*, 2nd ed., Wiley, New York.
- Lourenco, L. M. (1993). Velocity bias technique for particle image velocimetry measurements of high speed flows, *Appl. Opt.*, **32**, 2159–2162.
- Lourenco, L. M., A. Krothopalli, and C. A. Smith (1989). Particle image velocimetry, in *Advances in Fluid Mechanics Measurements*, Springer-Verlag, Berlin, p. 127.

- Lübbe, D. (1982). Thesis, University of Hanover, Germany.
- Machon, V., C. M. McFarlane, and A. W. Nienow (1991). Power input and gas hold-up in gas liquid dispersions agitated by axial flow impellers, *Proc. 7th European Conference on Mixing, KVIV*, Bruges, Belgium, p. 242.
- Machon, V., A. W. Pacek, and A. W. Nienow (1997). Bubble sizes in electrolyte and alcohol solutions in a turbulent stirred vessel, *Trans. Inst. Chem. Eng.*, **75A**, 339–348.
- Martin, T., C. M. McFarlane, and A. W. Nienow (1994). The influence of liquid properties and impeller type on bubble coalescence behaviour and mass transfer in sparged, agitated reactors, *Proc. 8th European Conference on Mixing, Chem. Eng. Symp. Sers.*, **136**, 57–64.
- McKee, S. L., R. A. Williams, F. J. Dickin, R. Mann, J. Brinkel, P. Ying, A. Boxman, and G. McGrath (1994). Measurement of concentration profiles and mixing kinetics in stirred tanks using a resistance tomography technique, *Proc. 8th European Conference on Mixing, Inst. Chem. Eng. Symp. Ser.*, **136**, 9–16.
- McLaughlin, D. K., and W. G. Tiedermann, Jr. (1973). Biasing correction for individual realization of laser anemometer measurements in turbulent flow, *Phy. Fluids*, **16**(12), 2082–2088.
- Meinhart, C. D., S. T. Werely, and J. G. Santiago (1999). PIV measurements of a micro-channel flow, *Exp. Fluids*, **27**, 414–419.
- Melling, A. (1997). Tracer particles and seeding for particle image velocimetry, *Meas. Sci. and Technol.* **8**(12), 1406–1416.
- Mewes, D., and W. Ostendorf (1986). Application of tomographic measurement techniques for process engineering studies, *Int. Chem. Eng.*, **26**(1), 11–21.
- Michelet, St. (1998). Ph.D. dissertation, INPL, CNRS, Nancy, France.
- Muller, F. L., and J. F. Davidson (1992). On the contribution of small bubbles to mass transfer in bubble columns containing highly viscous liquids, *Chem. Eng. Sci.*, **47**(13/14), 3525–3532.
- Nienow, A. W., and D. J. Wisdom (1974). Flow over disc turbine blades, *Chem. Eng. Sci.*, **29**, 1994–1997.
- Özcan-Taşkin, N. G. (1993). On the effects of viscoelasticity in stirred tanks, Ph.D Thesis, Birmingham University.
- Papadopoulos, G. (2000). Inferring temperature by means of a novel shadow image velocimetry technique, *J. Thermophys. Heat Transfer*, **14**(4), 593–600.
- Papadopoulos, G., and K. J. Hammad (2003). Time-resolved PIV measurements within a triple impeller stirred-tank. *ASME/JSME Joint Fluids Engineering Summer Meeting, FEDSM2003-45295*, July 6–11, Honolulu, HI.
- Parker, D. J., and P. A. McNeil (1996). Positron emission tomography for process applications, *Meas. Sci. Technol.*, **7**(3), 287–296.
- Patel, S. A., J. Daly, and D. B. Bukur (1989). Holdup and interfacial area measurements using dynamic gas disengagement, *AIChE J.*, **35**(6), 931–942.
- Penney, W. R., M. Myrick, P. Popejoy and R. Goff (1999). Liquid–liquid suspension using six-blade disk impellers in agitated vessels: an experimental and correlational study, presented at the AIChE Meeting, Dallas, TX.
- Prasad, A. K., and K. Jensen (1995). Scheimpflug stereo camera for particle image velocimetry in liquid flows; *Appl. Opt.*, **34**(30), 7092–7099.

- Raffel, M., M. Willert, and J. Kompenhans (1998). *Particle Image Velocimetry: A Practical Guide*, Springer-Verlag, Berlin.
- Reith, T., and W. J. Beek (1970). Bubble coalescence rates in a stirred contactor, *Trans. Inst. Chem. Eng.*, **48**, T63–T68, T76.
- Robinson, C. W., and C. R. Wilke (1974). Simultaneous measurement of interfacial area and mass transfer coefficients for a well-mixed gas dispersion in aqueous electrolyte solutions, *AIChE J.*, **20**(2), 285–294.
- Schaffer, M., M. Hofken, and F. Durst (1997). Detailed LDV measurements for visualization of the flow field within a stirred-tank reactor equipped with a Rushton turbine, *Chem. Eng. Res. Des.*, **75**, 729–736.
- Sheng, J., H. Meng, and R. O. Fox (1998). Validation of CFD simulations of a stirred tank using particle image velocimetry data, *Can. J. Chem. Eng.*, **76**, 611–625.
- Skelland, A. H. P. (1967). *Non-Newtonian Flow and Heat Transfer*, Wiley, New York.
- Skelland, A., and R. Seksaria (1978). Minimum impeller speeds for liquid–liquid dispersion in baffled vessels, *Ind. Eng. Chem. Process. Des. Dev.*, **17**, 56–61.
- Smith, J. M. (1985). Dispersion of gases in liquids, *Chapter 5 in Mixing of Liquids by Mechanical Agitation*, J. J. Ulbrecht, and G. K. Patterson, eds., Gordon & Breach, New York.
- Smith, J. M., M. M.C. G. Warmoeskerken, and E. Zeef (1987). Flow conditions in vessels dispersing gases in liquids, *Biotechnol. Prog. AIChE*, **3**, 107–115.
- Soloff, S. M., R. J. Adrian, and Z. C. Liu (1997). Distortion compensation for generalized stereoscopic particle image velocimetry, *Meas. Sci. and Technol.*, **8**, 1441–1454.
- Sridhar, R., and O. E. Potter (1978). Interfacial area measurements in gas–liquid agitated vessels: comparison of techniques, *Chem. Eng. Sci.*, **33**, 1347–1353.
- Sriram, K., and R. Mann (1977). Dynamic gas disengagement: a new technique for assessing the behaviour of bubble columns, *Chem. Eng. Sci.*, **32**, 571–580.
- Stanislas, M., J. Kompenhans, and J. Westerweel (eds.) (2000). *Particle Image Velocimetry: Progress Toward Industrial Applications*, Kluwer, Dordrecht, The Netherlands.
- Stanley, S. J., R. Mann, and K. Primrose (2002). Tomographic imaging in three dimensions for single-feed semi-batch operation of a stirred vessel, *Trans. Inst. Chem. Eng. A (Chem. Eng. Res. Des.)*, **80**, 903–909.
- Takashima, I., and M. Mochizuki (1971). Tomographic observations of the flow around an agitator impeller, *J. Chem. Eng. Jpn.*, **4**(1), 66–72.
- Tokumaru, P. T., and P. E. Dimotakis (1995) Image correlation velocimetry, *Exp. Fluids*, **19**(1), 1–15.
- Tropea, C. (1995). Laser Doppler anemometry: recent developments and future challenges, *Meas. Sci. Technol.*, **6**, 605–619.
- Van de Vusse, J. G. (1955). Mixing by agitation of miscible liquids. *Chem. Eng. Sci.*, **4**, 178–200.
- Van den Hulst, H. C. (1981). *Light Scattering by Small Particles*, Dover, New York.
- Vasconcelos, J. M.T., A. W. Nienow, T. Martin, S. S. Alves, and C. M. McFarlane (1997). Alternative ways of applying the hydrogen peroxide steady state method of  $K_L a$  measurement, *Trans. Inst. Chem. Eng.*, **75A**, 467–472.
- Wang, M., F. J. Dickin, R. A. Williams, R. C. Waterfall, and M. S. Beck (1993). Electrical resistance tomography on metal walled vessels, presented at the ECAPT Conference, Karlsruhe, Germany.

- Warmoeskerken, M. M. C. G., J. Speur, and J. M. Smith (1984). Gas–liquid dispersion with pitched-blade turbines, *Chem. Eng. Commun.*, **25**, 11–29.
- Watrasiwics, B. M., and M. J. Rudd (1976). *Laser Doppler Measurements*, Butterworth, London.
- Westerweel, J. (1993). *Digital Particle Image Velocimetry—Theory and Application*, Delft University Press, Delft, The Netherlands.
- Whitton, M. J., S. Cropper, and N. G. Özcan-Taşkin (1997). Mixing of liquid phase in large vessels equipped with multiple impellers, Proc. 4th International Conference on Bioreactor and Bioprocess Fluid Dynamics, BHRG, Edinburgh, Scotland, pp. 277–294.
- Willert, C. E., and M. Gharib (1991). Digital particle image velocimetry, *Exp. Fluids*, **10**, 181–193.
- Yamamura, H., and K. Takahashi (1999). Minimum impeller speeds for complete liquid–liquid dispersion in a baffled vessel, *J. Chem. Eng. Jpn.* **32**(4), 395–401.
- Yianneskis, M., Z. Popiolek, and J. H. Whitelaw (1987). An experimental study of the steady and unsteady-flow characteristics of stirred reactors, *J. Fluid Mech.*, **175**, 537–555.
- Zalc, J. M. (2000). Computational fluid dynamic tools for investigating flow and mixing in industrial systems: the koch–Glitsch SMX static mixer and a three Rushton turbine stirred tank, Ph.D. dissertation, Rutgers, The State University of New Jersey.
- Zhou, G., and S. M. Kresta (1996). Impact of geometry on the maximum turbulence energy dissipation rate for various impellers, *AIChE J.*, **42**, 2476–2490.